Gallium Nitride and Silicon Based Photoelectrodes for High Efficiency and Highly Stable Solar Water Splitting

Srinivas Vanka

Department of Electrical and Computer Engineering

Faculty of Engineering, McGill University, Montréal

August 2019

A thesis submitted to McGill University in partial fulfillment of the requirements of the degree of Doctor of Philosophy

To my Parents and Loved Ones

Table of Contents

Abstract

Artificial photosynthesis on semiconductor photoelectrodes is a clean and eco-friendly method for the generation of solar fuels, including hydrogen and hydrocarbons directly from sunlight, water, and carbon dioxide, which can address the challenges associated with energy demands and storage. Simultaneously achieving high efficiency (solar-to-hydrogen efficiency > 15%) and stability (> 1000 h) for unassisted photoelectrochemical water splitting is the "holy grail" in the field of clean, renewable energy. III-nitride semiconductors are promising materials to realize high-efficiency photoelectrodes: their energy bandgap can be varied across nearly the entire solar spectrum by changing the alloy compositions, and the energy band edge positions straddle water oxidation and reduction potentials under deep visible and near-IR light irradiation. In this study, we report the development of high quality (In)GaN nanostructures on Si, using molecular beam epitaxy, for high efficiency and ultrahigh stable photoelectrochemical water splitting photoelectrodes. We have designed InGaN alloy photoanodes having indium content ~ 50%, corresponding to an energy bandgap of ~1.7 eV, for high-efficiency solar water oxidation. This study lays a solid foundation for the development of a tandem device with InGaN as top light absorber stacked on Si bottom absorber to achieve solar-to-hydrogen efficiency > 25%.

Furthermore, we demonstrated the use of multifunctional N-terminated GaN nanowires protection layer on Si photocathode with Pt catalyst, which enhances light absorption and reduces interfacial charge transfer losses, to achieve high half-cell conversion efficiency ~ 12% and the longest stability of 3000 h, for any photoelectrode operating at a similar efficiency level, under AM 1.5G one-sun illumination for solar water splitting. We further showed the first demonstration of low-cost, earth-abundant and few monolayers thick $MoSe_2$ as a protection layer on Si photoanode for hydrogen production under AM 1.5G one-sun illumination. In the end, we have

also presented the growth of tunnel junction nanowires to monolithically integrate the p^+-InGaN nanowires (top cell) on Si solar cell (bottom cell) to form a double-junction photocathode. This photocathode, with optimized surface modifications, can achieve a high solar-to-hydrogen efficiency of ~ 10.1% and high stability of 100 h for unassisted water splitting under AM 1.5G one-sun illumination. These results are significantly superior compared to other state-of-the-art photoelectrodes for unassisted solar water splitting. The III-nitride nanostructures presented in this work bring us one step closer in achieving high efficiency, long-term stability and low-cost photoelectrochemical water splitting systems required for large-scale applications.

Résumé

La photosynthèse artificielle utilisant des photoélectrodes semiconductrices est une méthode propre et environnementalement favorable pour la génération de combustibles solaires, notamment l'hydrogène et les hydrocarbures, et cela directement à partir de la lumière solaire, de l'eau et du dioxyde de carbone. Ceci permet de relever les défis liés à la demande croissante et au stockage d'énergie. Atteindre simultanément un rendement élevé (efficacité de la conversion solaire-hydrogène > 15%) et une stabilité (> 1000 h) pour un fractionnement photoélectrochimique sans assistance de l'eau est le but ultime dans le domaine des énergies propres et renouvelables. Les semiconducteurs à base des matériaux du groupe III-N sont prometteurs pour la réalisation de photoélectrodes à haute efficacité: leur bande interdite d'énergie peut être modifiée pour couvrir presque l'entièreté du spectre solaire en modifiant la composition de l'alliage de ces matériaux. De plus, les positions de la bande énergétique chevauchent les potentiels d'oxydation et de réduction par irradiation lumineuse avec des longueurs d'onde dans le spectre visible et infrarouge. Dans cette étude, nous avons dévelopé des nanostructures en (In)GaN de haute qualité sur substrats en Si, en utilisant l'épitaxie par jet moléculaire, pour former des photoélectrodes ultra-stables et à haute efficacité pour la séparation photoélectrochimique de l'eau. Nous avons conçu des photoanodes en InGaN ayant une composition d'indium d'environ 50%, correspondant à une bande interdite d'énergie d'environ 1,7 eV, permettant ainsi l'oxydation solaire de l'eau avec haute efficacité. Cette étude représente la base fondamentale pour le développement d'un dispositif tandem avec une couche en InGaN comme absorbeur de lumière au-dessus du Si pour atteindre un rendement de conversion solaire-hydrogène > 25%.

De plus, nous avons démontré que l'utilisation d'une couche protectrice à base de nanofils en GaN à terminaison N sur une photocathode en Si avec catalyseur au Pt améliore l'absorption de

la lumière et réduit les pertes liées au transfert de charge interfaciale. Ceci a permis d'atteindre un rendement de conversion élevé des cellules d'environ 12% et une stabilité maximale de 3000 h, pour n'importe quelle photoélectrode, sous un éclairage avec correspondance spectrale d'un soleil avec une irradiance spectrale AM 1,5 G pour la séparation solaire de l'eau. Cette thèse présente également la première démonstration de l'usage du $MoSe_2$ en tant que couche protectrice au-dessus de la photoanode en Si pour la production d'hydrogène sous un éclairage avec correspondance spectrale d'un soleil avec une irradiance spectrale AM 1,5 G. Enfin, nous présentons la croissance de nanofils à jonction tunnel pour intégrer monolithiquement les nanofils p^+-InGaN (cellule supérieure) sur une cellule solaire en Si (cellule inférieure) pour former une photocathode à jonction double. Cette photocathode, avec certaines optimisations de sa surface, peut atteindre un rendement de conversion solaire-hydrogène d'environ 10,1% et une stabilité de longue durée de 100 h pour la séparation de l'eau non-assistée sous un éclairage avec correspondance spectrale d'un soleil et une irradiance spectrale AM 1,5 G. Ces résultats sont nettement supérieurs à d'autres photoélectrodes pour la séparation solaire non-assistée de l'eau. Les nanostructures à base des matériaux du groupe III-N présentées dans cette thèse nous rapprochent de la réalisation de systèmes de fractionnement photoélectrochimique de l'eau à haute efficacité, avec une stabilité à long terme, et à faible coût pour des applications à grande échelle.

Acknowledgment

All glories to the Supreme Lord Sri Krishna for giving me the enthusiasm, physical and mental well-being, and fortitude to face various situations during my Ph.D. pursuit. Many amazing people have helped me during this wonderful journey, and I am thankful to every one.

First, I would like to thank my supervisor, Professor Zetian Mi. It is indeed a great privilege and an honor to work under his supervision. I want to express my most sincere gratitude to him for providing me with the opportunity to work in well-established and organized research facilities. I am genuinely grateful for his patience, continuous support, suggestions, and valuable time in discussing various research topics. I am fortunate to have him as my supervisor, who was available every day to provide feedback and suggestions for my research work.

I want to express my gratitude to my co-supervisor Prof. Thomas Szkopek for his continuous support and suggestions towards my research. Special thanks to my Ph.D. committee members Prof. Kirk Bevan and Prof. Hong Guo for their suggestions. I thank my Ph.D. oral defence committee members: Prof. Jun Song, Prof. Janine Mauzeroll and Prof. Odile Liboiron-Ladouceur for their constructive comments and suggestions to improve the quality of this thesis. I would also like to thank collaborative groups from Boston College (Prof. Dunwei Wang), Michigan State University (Prof. Thomas Hamann) and the University of Toledo (Prof. Yanfa Ya) for their insightful discussions on the electrochemical analysis of solar water splitting devices.

I am grateful to my colleagues: Mr. David Laleyan, Dr. Shizhao Fan, Prof. Songrui Zhao, and Dr. Faqrul Chowdhury for explaining the basics and operation of MBE tool. I want to thank Prof. Bandar AlOtaibi, Prof. Md Golam Kibria, Dr. Baowen Zhou, Dr. Sheng Chu, Dr. Yichen Wang, Dr. Yongjie Wang, Mr. Nick Pant, Mr. Ronglei Fan and Ms. Alexa Robert for their valuable help and suggestions. I am also grateful to all the previous and present group members: Dr. Sharif

Sadaf, Dr. Yong-Ho Ra, Ms. Roksana Tonny Rashid, Dr. Binh Le, Ms. Nhung Tran, Dr. Renjie Wang, Dr. Xianhe Liu, Prof. Li Lu, Mr. Yuanpeng Wu, Mr. Anthony Aiello, Mr. Ayush Pandey, Mr. Eric Reid, Dr. Yi Sun, Dr. Ping Wang, Mr. Kishwar Mashooq, Ms. Pegah Ghamari, Mr. Yongbum Park and Mr. Walter Shin. Special thanks to Mr. David Laleyan for translating the abstract to French. I am also grateful to the Lurie Nanofabrication Facility (LNF) staff at the University of Michigan and McGill Nanotools cleanroom staff for their support towards this research work.

In the end, I am also grateful and indebted to my parents for giving me this opportunity to pursue my dreams. My heartfelt thanks to my elder brother for showing enduring love and affection.

I sincerely acknowledge the McGill Engineering Doctoral Awards program for giving me financial support. This work is supported by the HydroGEN Advanced Water Splitting Materials Consortium, established as part of the Energy Materials Network under the U.S. Department of Energy, Office of Energy Efficiency and Renewable Energy, Fuel Cell Technologies Office and Emissions Reduction Alberta.

Contribution of Authors

This work includes the contribution of the candidate and other individuals. The candidate and his supervisor Prof. Zetian Mi had conceived the ideas, designed and established the setup of the photoelectrochemical experiment, and written the manuscripts. The candidate did the Si samples' cleaning and loading into the MBE machine with some help from Mr. Nick Pant. The MBE growths were carried out by the candidate under the direct supervision of Prof. Zetian Mi. The candidate carried the fabrication of Si solar cell substrates with some help from Dr. Yichen Wang, Ms. Pegah Ghamari, Mr. Ronglei Fan and Mr. Nick Pant. Initially, the candidate worked closely with Prof. Bandar AlOtaibi and Dr. Shizhao Fan to understand the photoelectrochemical water splitting experiments setup and analysis. Subsequently, the candidate performed all the experiments including electrochemical studies with some help from Dr. Sheng Chu and Dr. Baowen Zhou.

Dr. Sheng Chu and the candidate have equally contributed to work mentioned in Chapter-3. Specific contributions of the authors for Chapter-3 are as follows: Dr. Sheng Chu, the candidate, and Prof. Zetian Mi designed the study. The candidate and Prof. Zetian Mi conducted the InGaN nanowire growth. Dr. Sheng Chu and the candidate prepared, characterized the sample and performed PEC test. The candidate carried out the Si substrate cleaning and preparation with some assistance from Dr. Yichen Wang. Dr. Sheng Chu, the candidate, and Prof. Zetian Mi contributed to the result analysis and discussions. The manuscript was written by Dr. Sheng Chu and Prof. Zetian Mi with contributions from other co-authors. The candidate has taken consent from Dr. Sheng Chu to include the manuscript in this thesis.

The XPS measurements in Chapter-4 were carried out by Dr. Glenn Teeter and Dr. Elisabetta Arca from National Renewable Energy Laboratory (NREL) on the samples grown by

the candidate. STEM analysis in Chapter-3 was done by Prof. Robert Hovden and Mr. Jiseok Gim from the University of Michigan. Furthermore, the STEM analysis in Chapter-4 (for Figure 4.3) was done by Prof. Gianluigi A. Botton and Dr. Shaobo Cheng from McMaster University. The TEM analysis in Chapter-4 (for Figure 4.2(c)) and Chapter-5 were measured by Dr. Kai Sun along with the candidate in Michigan Centre for Materials Characterization (University of Michigan). SEM images were primarily done by the candidate along with some help from Dr. Xianhe Liu, Dr. Sheng Chu, and Mr. Kishwar Mashooq. The candidate conducted the photoluminescence experiments with some assistance from Mr. Yuanpeng Wu during the initial training.

This thesis work produced significant scientific outcomes, through multiple projects, in the design of materials and setting new benchmark standards for photoelectrochemical water splitting research. There are three primary achievements from this work: 1) MBE growth of defect-free In-rich InGaN photoanode for high efficiency water oxidation; 2) monolithic integration of InGaN and Si double junction photocathode for unbiased water splitting; 3) GaN protection layer on low cost Si photocathode to achieve ultra-high stability for photoelectrochemical water splitting.

List of Figures

List of Tables

List of Acronyms

ABPE	Applied Bias Photon-to-Current Efficiency
AEC	Alkaline Electrolysis Cells
BEP	Beam Equivalent Pressure
BHF	Buffered Hydrofluoric acid
Btu	The British Thermal Unit
CA	Chronoamperometry
CB	Conduction Band
CBM	Conduction Band Minimum
CV	Cyclic-Voltammetry
CVD	Chemical Vapor Deposition
DFT	Density Function Theory
EELS	Electron Energy Loss Spectroscopy
EIS	Electrochemical Impedance Spectroscopy
EQE	External Quantum Efficiency
FID	Flame Ionization Detector
GC	Gas Chromatograph
HDAAF	High Angle Annular Dark Field
HF	Hydrofluoric Acid
HRTEM	High Resolution Transmission Electron Microscopy
IPCE	Incident Photon-to-Current Conversion Efficiency
IR	Infrared
LED	Light Emitting Diode

LSV	Linear Scan Voltammetry
MBE	Molecular Beam Epitaxy
MOCVD	Metal Organic Chemical Vapor Deposition
MQW	Multi Quantum Well
NHE	Normal Hydrogen Electrode
OCP	Open Circuit Potential
PC	Photochemical
PEC	Photoelectrochemical
PEMEC	Proton Exchange Membrane Electrolysis Cells
PL	Photoluminescence
PV	Photovoltaic
PV-EL	Photovoltaic-Electrolyser
PV-PEC	Photovoltaic-Photoelectrochemical
RF	Radio Frequency
RHE	Reversible Hydrogen Electrode
SEM	Scanning Electron Microscopy
SHE	Saturated Hydrogen Electrode
SOEC	Solid Oxide Electrolysis Cells
STH	Solar-to-Hydrogen
STEM	Scanning Transmission Electron Microscopy
TCD	Thermal Conductivity Detector
TEM	Transmission Electron Microscopy
UV	Ultraviolet

VB	Valence Band
VBM	Valence Band Maximum
VLS	Vapor-Liquid-Solid
VPE	Vapor Phase Epitaxy

Chapter 1: Introduction

Motivation for Sustainable and Eco-friendly Energy Resources

The over-reliance on coal, crude oil and natural gas (fossil fuels) for energy requirements to accommodate the ever-increasing population has resulted in the generation of greenhouse gases, which are harmful to the environment. Over the last century, the concentrations of dangerous greenhouse gases have dramatically increased. It is estimated that the worldwide CO_2 emissions would increase from 32.2 billion metric tons in 2012 to 43.2 billion metric tons in 2040 [1]. This rise of CO_2 concentration will undoubtedly lead to catastrophic transformations to the climate. Different climate models by the World Climate Research Programme have simulated that there will be an increase of earth's surface temperature by a couple of degrees [2a]. One of the significant goals of the Paris Agreement [2b] is to keep the increase of the global average temperature below the temperature threshold of 2 °C and further restrict the growth to only 1.5 °C. From Figure 1.1 [1], the increasing use of coal and natural gas for future energy needs is one of the major causes for global warming and other catastrophic consequences.

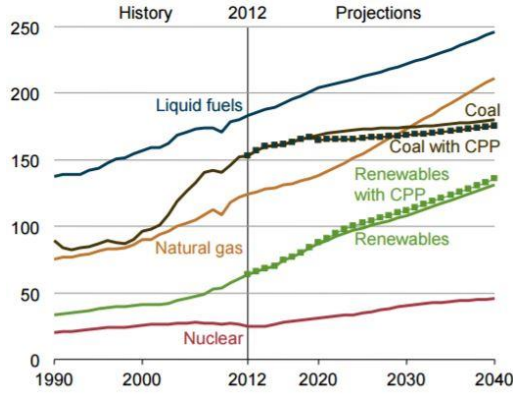

Figure 1.1. Energy consumptions and projections for different energy sources from 1990-2040 [1].

As the population increases, there is a drastic growth in energy consumption that leads to energy famine in the world. As per the predictions, the world energy consumption will increase from 549 quadrillions British thermal unit (Btu) in 2012 to about 629 quadrillions Btu in 2020, and in 2040 it may breach the 800 quadrillion Btu mark. These predictions show an increase of ~ 48% (1.4%/year) over the next few decades, as shown in Figure 1.2 [1]. Thus, the consumption of natural resources has increased because of the increasing energy demands. It is to be noted that renewable energy is one of the fastest-growing energy sources with an increased rate of 2.6%/year, as shown in Figure 1.1 [1]. Henceforth, investigating new alternative clean renewable energy resources is an important responsibility of all researchers, in the field of sustainable energy, to mitigate the catastrophic effects of greenhouse emissions.

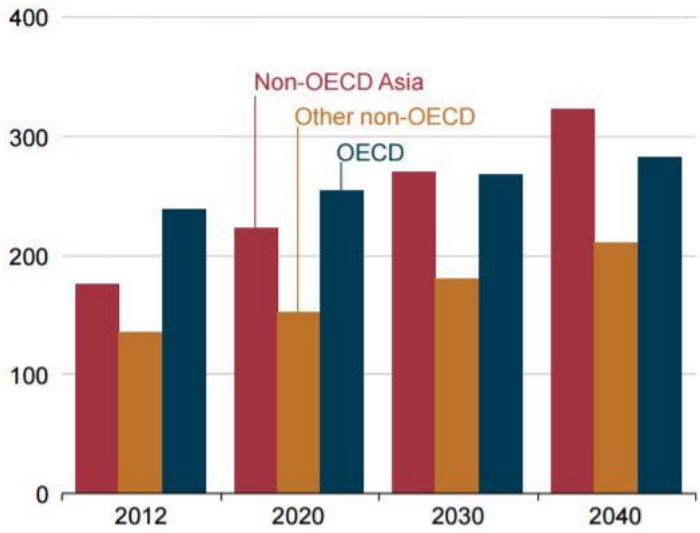

Figure 1.2. History and projections of world energy consumption (in quadrillion Btu for y-axis) between 2012-2040 [1].

1.2 Advantages and Challenges of Solar Energy

By the continuous stream of sunlight energy propagated through outer space, life on Earth has naturally evolved to maintain its existence through photosynthesis. It is the most abundant renewable resource available on the planet for energy conversion. The energy contained in most traditional fossil fuels has come from sunlight. It is to be noted that the energy received on the Earth in one hour from the sun is more than what the entire globe requires in a year. Therefore, the technology and processes to harness the sun's energy to make it usable are of critical importance for all humankind. A significant obstacle in realizing the full potential of solar energy is the intermittency—we cannot get a steady supply of solar energy. There are many ways to convert and store sunlight into different useful outputs; one of which is chemical fuels. The current methods of saving solar energy, including potential energy (electric charge in capacitors), kinetic energy (flywheels) and thermal energy (concentrated solar thermal, geothermal). These methods have a high cost of deployment, short time storage, low energy density, and efficiency to be implemented for large-scale applications. However, the energy stored in chemical forms has tremendous advantages regarding high energy density, storage time and facile mobility. A comparison of different energy storage techniques had been discussed in the previous publication [3]. Solar fuels help in providing massive grid-scale storage which compensates for the intermittency of solar power and an abundant source of liquid fuels which are readily needed to run trucks, ships, and aircraft as these vehicles cannot run on batteries alone. Solar fuels technologies use water, carbon dioxide, and nitrogen from the air along with sunlight to produce fuels (see Figure 1.3). These are sustainable and produce no net emissions of carbon dioxide.

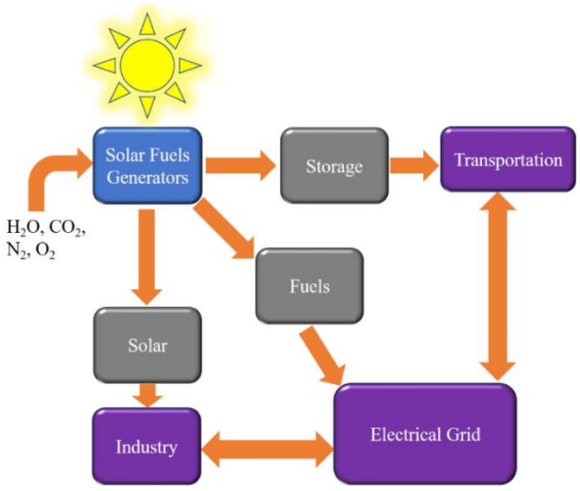

Figure 1.3. Solar fuels production using sunlight along with water, carbon dioxide and nitrogen for transportation, industry and electrical demands.

One of the most critical chemical fuels or solar fuels is hydrogen. Hydrogen (H_2) is an excellent candidate as a substantial energy carrier. It has the highest calorific value of ~150 KJ/g. H_2 is also considered a high efficiency, the low polluting fuel used for transportation, heating, and power generation (Figure 1.3) in places where it is difficult to use electricity. The process of obtaining energy from H_2 is clean without CO_2 emission through an oxidation reaction. This reaction is described as follows in Eqn. (1.1),

$$H_2 + \frac{1}{2}O_2 \rightarrow H_2O \qquad \text{eq. (1.1)}$$

This reaction can be converted to electricity using fuel cells (as shown in Figure 1.3). In contrast to other low-efficiency fossil fuel engines, the efficiency of H_2-based fuel cells can reach a maximum of up to ~65% considering all conversion losses.

1.3 Hydrogen Production Processes

1.3.1 Non-Renewable Processes

Commercial H_2 is mainly produced by using non-renewable raw materials. Figure 1.4 shows that 48% of commercial H_2 production is coming from methane/natural gas, 30% from petroleum fractions in refineries (primarily through steam reforming) and 18% from coal gasification [4a]. The H_2 production from water electrolysis is merely 4% which is the lowest compared to other processes.

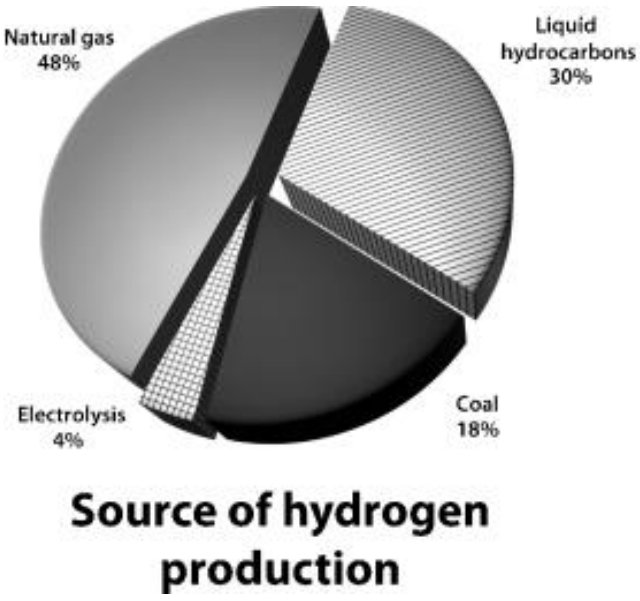

Figure 1.4. Sources of hydrogen generation used in the world; total production is ~50 million tonnes [4a].

In steam-methane reforming process, methane reacts with steam under high temperature (700-1000 ^{0}C) and 3–25 bar pressure in the presence of a catalyst to produce H_2, carbon monoxide, and carbon dioxide as shown in Eqns. (1.2) and (1.3).

$$CH_4 + H_2O \rightarrow CO + 3H_2 \qquad \Delta H = 206.2\ KJ/mol \qquad \text{eq. (1.2)}$$

$$CH_4 + 2H_2O \rightarrow CO_2 + 4H_2 \qquad \Delta H = 164.9\ KJ/mol \qquad \text{eq. (1.3)}$$

Steam methane reforming is an endothermic process, i.e., it requires heat for the reaction to proceed. This process generates many greenhouse gases like CO and CO_2 which are not eco-friendly. Therefore, it is imperative to investigate alternate renewable sources for H_2 production which can overcome the problems of conventional methods used in industries.

1.3.2 Renewable Processes

Renewable H_2 production can be achieved directly and indirectly from solar energy, as shown in Figure 1.5 [4b]. For example, wind/hydro/tidal energies can be transformed into mechanical energy and then to electricity. This electricity can further be used to electrolyze water for H_2 production. However, the efficiency of these indirect H_2 production methods is severely limited. Therefore, it is more attractive to use the direct conversion of solar energy to H_2 or other chemical fuels.

Biomass is abundant, environmentally friendly and renewable. Hence, the production of H_2 from biomass represents a promising approach. Consequently, H_2 production from biomass has drawn much attention among some researchers. The efficiency of this method is between 45-50%. One of the significant disadvantages with biomass is the difficulty in handling the H_2 gas compared to liquid fuels. The low production rates and large energy consumptions are the major impediments of this process for producing cost-effective H_2 [4c].

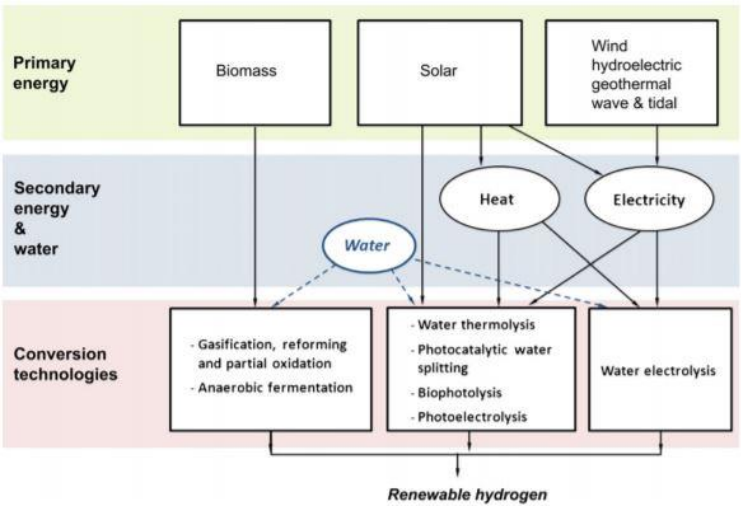

Figure 1.5. Different schemes for renewable hydrogen generation [4b].

Water electrolysis is one of the best methods to generate pure H_2. This process is driven by the continuous movement of electrons supplied through an external circuit. The unit in which the water-splitting reaction takes place is called an electrolyzer. Electrolyzer cells can be of different sizes, ranging from small to large production facilities to cater to small-scale H_2 distribution to large-scale respectively. The electrolyzers generally consist of an anode and a cathode separated by an electrolyte. The three main technologies used for water electrolysis are alkaline electrolysis cells (AEC), proton exchange membrane electrolysis cells (PEMEC) and solid oxide electrolysis cells (SOEC). AEC electrolysis is the most widely used method with a maximum efficiency of ~70%. Some of the disadvantages of this method are low current density and operating pressure which impact the H_2 production costs. PEMEC method has advantages such as high-power density, gas purity, and cell efficiency. However, the use of an expensive platinum catalyst and high system complexity are the disadvantages of this method. SOEC is still under research phase, and it is not yet commercialized. Therefore, it is quintessential that research needs to be focused on other

techniques such as solar water splitting which uses the two most abundant resources on the planet, water and sunlight, to produce sustainable H_2.

There are three main processes for solar water splitting: photovoltaic-electrolysis (PV-EL), photoelectrochemical (PEC) cell and photochemical (PC). In PV-EL systems, light absorption and initial charge transfer occur within the PV, and these processes are physically separated from the electrolyte and fuel production. In theory, PV-EL systems could achieve up to 90-95% of the PV efficiency which in turn translates, in theory, into PV-EL efficiencies of ~ 57% for 3J cell and ~ 62% for 4J or 5J cell [5a]. The highest solar-to-hydrogen (STH) conversion efficiency (see Chapter-2 for definition and details) for PV-EL system reported so far in the literature is ~ 30% for GaInP/GaAs 3J cell [5b]. Although PV-EL systems have demonstrated high STH efficiencies, the technology requires high capital costs for the current electrolyzers which adds to H_2 production costs. PC system is a simple and low-cost way to produce solar H_2, but the STH efficiency is very low compared to PV-EL and PEC systems. It also produces a mixture of H_2 and O_2, which requires additional steps for separation and in turn adds to the production costs. On the other hand, PEC cells are the complete and single monolithic integrated version of PV-EL systems. Both systems require three main steps: light absorption, charge carrier separation, and catalysis. PEC system is different from PV-EL that the light absorbers are in direct contact with the electrolyte which reduces cost. It has a distinct advantage over PC that the H_2 and O_2 evolution half-reactions occur on two different electrodes whereby the gases are physically separated which eliminates unnecessary steps to reduce the overall H_2 production cost. It is vital for any economically feasible system for solar hydrogen production must also compete with the price of H_2 generated from conventional sources (US$ 2−3 kg^{-1} for the steam reforming of natural gas). Therefore, the major challenge for any system converting solar energy to chemical fuels is to find a balance between

minimizing system complexity (i.e., device cost) and maximizing device performance (i.e., energy conversion efficiency and device longevity) given the relatively low energy density of solar irradiation.

1.4 Hydrogen Production from Photoelectrochemical Water Splitting

1.4.1 Fundamentals of Water Splitting

After the first direct water splitting demonstration using *n*-TiO2 in 1972 by Fujishima and Honda [6a], there has been tremendous progress in photoelectrolysis field with emphasis on the development of new materials for photoanode and photocathode for efficient and stable H_2 generation. In PEC water splitting reaction, solar energy is transformed into chemical energy in the form of H_2 and O_2 as shown in the below Eqn. (1.4),

$$H_2O \rightarrow \frac{1}{2}O_2 + H_2 \qquad \Delta G = +237.178\ KJ/mol \qquad \text{eq. (1.4)}$$

The positive sign for Gibbs free energy indicates that the reaction is not spontaneous. From the Nernst equation, we get,

$$\Delta G = -zFE_{cell} \qquad \text{eq. (1.5)}$$

where z is the number of electrons transferred in the cell reaction and for water splitting it is 2, F is the Faraday Constant (i.e., 96485 C/mol) and $E_{cell} = E_{cathodic} - E_{anodic}$. From the above ΔG value, the E_{cell} for water splitting is -1.23 V.

The half reactions for reduction and oxidation for water splitting are as follows:

Reduction reaction at the cathode:

$$2H^+ + 2e^- \rightarrow H_2 \qquad E_{cathodic} = 0 - (0.059 \times (pH))V\ vs.RHE \qquad \text{eq. (1.6)}$$

Oxidation reaction at the anode:

$$H_2O \rightarrow \frac{1}{2}O_2 + 2h^+ + 2H^+ \qquad E_{anodic} = -1.23 - \big(0.059 \times (pH)\big)V\ vs.RHE \qquad \text{eq. (1.7)}$$

The most crucial thermodynamic requirement for water splitting is that the semiconductor photoelectrodes must have a potential more than 1.23 V between the anode and cathode to drive the reaction forward. While a difference in the bias of only 1.23 V should be sufficient to split water into H_2 and O_2, the overpotentials required for the oxygen (overpotential of 300-400 mV) and hydrogen (overpotential of 50-100 mV) evolution reactions, add up to a total potential of 1.6-1.8 V for water splitting. Therefore, modern alkaline electrolyzers usually operate at voltages above 1.8 V. For hydrogen evolution reaction (HER) half reaction, the conduction band minimum (CBM) of the semiconductor photocathode must be more negative than water reduction potential (0 V *vs.* RHE at pH=0). For the oxygen evolution reaction (OER) half reaction, the valence band maximum (VBM) of the semiconductor photoanode must be more positive than water oxidation potential (1.23 V *vs.* RHE at pH=0). Unassisted PEC water splitting, and PC system requires the semiconductor photoelectrode to at least have its band edge positions straddling the water redox potentials. From Eqns. (1.6) and (1.7), it is to be noted that OER is the rate determining step which requires four holes for oxidation, whereas HER requires two electrons for reduction. Therefore, water oxidation is a slower reaction than water reduction. In Chapter-2, further details are discussed for kinetic and thermodynamic challenges involved in PEC water splitting.

In the next sub-section, we will discuss the bio-inspiration for solar water splitting via artificial photosynthesis and the limitations of natural photosynthesis for meeting the energy demands.

1.4.2 Inspiration for Artificial Photosynthesis

Natural photosynthesis gives the inspiration for catalytic conversion of CO_2 into useful fuels using solar energy. There are four significant steps in natural photosynthesis: light harvesting, charge separation, water oxidation, and fuel production. For light harvesting, chlorophyll and

carotenes absorb sunlight and transfer the energy among themselves and eventually to the reaction center (see Figure 1.6) where charge separation takes place. In this way, energy from sunlight is used to separate holes and electrons from each other. Photosystem II absorbs photons and splits water molecules into oxygen and protons. Then the photogenerated electrons are transferred from photosystem II via cytochrome b_6f and mobile electron carriers to photosystem I where they are excited again and used to produce carbohydrate fuel.

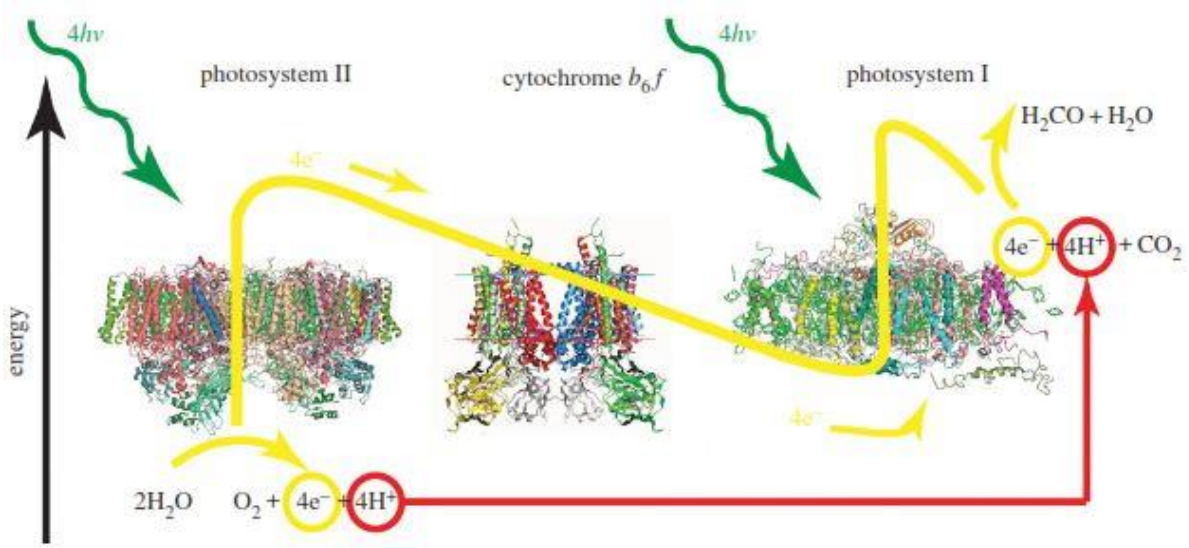

Figure 1.6. Schematic of natural photosynthesis showing light absorption, charge separation and redox reactions for water splitting and fuel production [6].

The following are the half-reactions involved in the photosynthesis process:

$$2H_2O \xrightarrow{4h\upsilon} O_2 + 4e^- + 4H^+ \qquad \text{eq. (1.16)}$$

$$CO_2 + 4H^+ + 4e^- \xrightarrow{4h\upsilon} (H_2CO) + H_2O \qquad \text{eq. (1.17)}$$

These two reactions add up to give the complete chemical reaction:

$$CO_2 + H_2O \xrightarrow{8h\nu} (H_2CO) + O_2 \quad \text{eq. (1.18)}$$

From the half reactions, four photons are required to drive each of the reactions. In total eight electrons are necessary to carry out the total chemical reaction. As four electrons are carried over (yellow arrows in Figure 1.6), and eight photons are used (green arrows in Figure 1.6), thus the process proceeds with two photons per electron. The natural photosynthesis uses two photosystems in tandem to drive the two chemical reactions of water splitting and fuel production. This arrangement of the tandem systems is known as *Z-scheme* of photosynthesis. Parts of the natural photosynthetic process are highly efficient, but the overall solar-to-carbohydrate efficiency is very low (<1%). Another issue with the natural system is that the two photosystems (I and II) absorb the light of approximately the same energy, so the two systems are competing for the same photons while the infrared photons remain unused. In an artificial system, it is possible to have a tandem photo absorber where one can absorb the visible part of the spectrum, and the other can absorb the infrared. Therefore, natural photosynthesis cannot directly serve humanity's purposes for fuel production, but it can serve as a blueprint for developing high efficiency and stable artificial photosynthesis.

1.5 Metal-Nitride Nanostructures for Photoelectrochemical Water Splitting

1.5.1 Advantages of III-Nitrides

In the past few decades, research has been focused on III-nitride materials, e.g., GaN, InN, and their ternary alloys due to their unique electrical, optical, and structural properties [7]. From Figure 1.7, the E_g of III-nitride material system can be tuned to cover nearly the entire solar spectrum by varying In composition [8], thereby increasing light absorption and providing promising multi-band solar-to-hydrogen conversion devices using a single alloy material like $In_xGa_{1-x}N$.

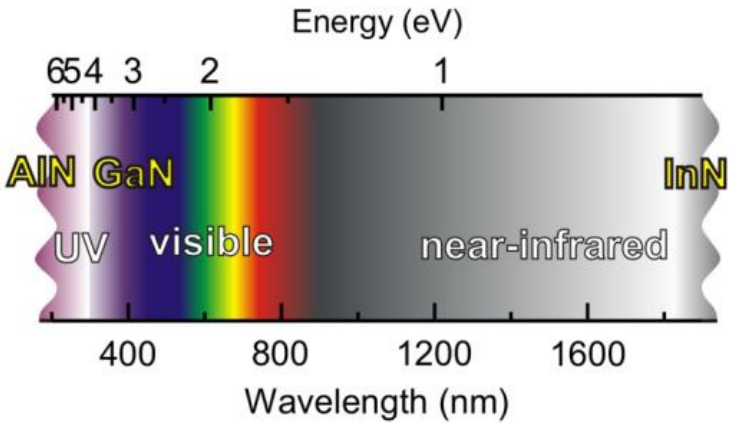

Figure 1.7. Optical spectrum showing the wavelength (in nm) coverage by III-nitride compound semiconductors from ultraviolet (UV) to near-infrared (IR) [8].

Further, from Figure 1.8, it is clear that by tuning In composition to ~ 50%, the band edges of InGaN can straddle the water redox reactions (with overpotentials) for up to 1.6-1.8 eV [7]. III-nitrides compared to metal oxide materials have a narrow E_g to absorb the visible light, due to the negative potential of the N_{2p} orbital compared to the O_{2p} orbital, while still straddling the redox potentials of water splitting and CO_2 reduction (see Figure 1.8). Nitrides also possess a high absorption coefficient and large charge carrier mobility, leading to excellent photon absorption and charge carrier extraction for efficient solar-fuel conversion [8, 9].

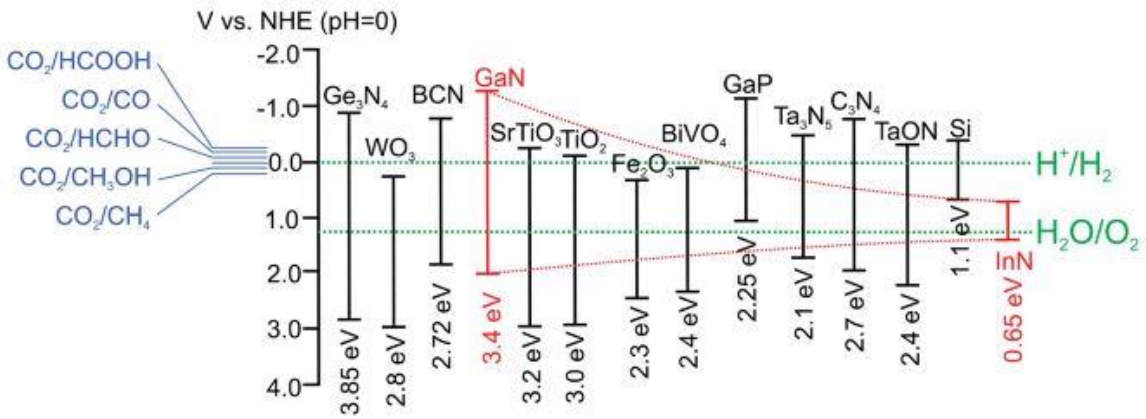

Figure 1.8. Band-edge positions (*vs*. RHE) of III-nitride photocatalysts compared to conventional semiconductor photocatalysts. The green dotted lines represent the water redox potentials. Red dotted lines represent the band edge positions of $In_xGa_{1-x}N$ with x increasing from left to right (0–1). The CO_2 reduction products are shown on the left side [7].

Compared to other III–V compounds, wherein the chemical bonds are mostly covalent, the chemical bonds in III-nitrides are strongly ionic [10]. Due to this strong ionicity of nitrides, the surface states and states associated with dangling bonds in edge dislocations are located mostly near the band edges, which prevent them from being non-radiative recombination centers. Also, the Fermi level is unpinned in the energy gap of III-nitrides, thereby reducing the participation of surface states in the self-oxidation process and resulting in photostability of electrode [10]. Recent studies show high photostability for near defect-free and N-terminated III-nitride photocatalysts against photo-corrosion in different electrolytes [11, 12]. High crystalline quality and defect free III-nitrides can function as high-efficiency photoanodes and photocathodes [13-15]. But due to the low electronegativity of nitrogen compared to oxygen, the III-nitrides are not stable against anodic photo-corrosion. Therefore, III-nitrides are more suitable as photocathodes [16].

1.5.2 Advantages of III-Nitride Nanostructures

As shown in Figure 1.9 [7], the use of nanostructures as photoelectrodes can offer further advantages for water splitting and CO_2 reduction. Such 1-D nanostructure semiconductors are nearly free of dislocations and provide a large surface area for reaction sites. For the nanowires, the lattice dislocation densities will be much reduced with the absence of strain field, thereby leading to lesser nonradiative recombination sites for the carriers. The nanowire arrays help in improving the light absorption significantly due to light trapping and scattering effects. For 2-D epitaxial films, the light trapping efficiency is very low as most of the light is lost due to reflection phenomena. Therefore, nanowires morphology helps to reduce material cost by absorbing the same amount of light with less material. These 1-D nanowires can lead to significantly enhanced light absorption and rapid electron-hole separation (see Figure 1.9), thereby improving solar-to-fuel conversion efficiency [17]. The photogenerated charge carriers are likely to recombine if there are no suitable active sites available on the photocatalyst surface. By surface modification, with the incorporation of proper cocatalysts on the III-nitride semiconductors, it is possible to provide active reaction sites and further reduce kinetic losses. Therefore, III-nitride photocatalysts satisfy the three significant steps for the artificial photosynthesis (shown in Figure 1.9): light capturing, charge separation and transportation of charges for electrochemical reaction.

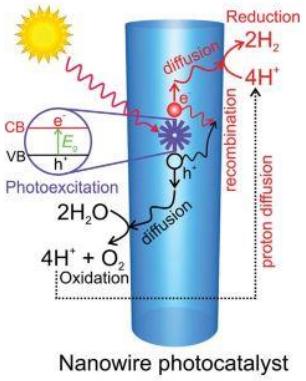

Figure 1.9. Schematic is showing light absorption, charge separation, diffusion, recombination, water reduction, and oxidation on semiconductor (III-nitride) nanowire photocatalyst [7].

In 1995, Turner et al. first reported high-quality III-nitride (*n*-GaN) as a viable photoelectrode material for solar water splitting [18]. Over the past few decades, detailed PEC studies reveal that GaN photocatalyst can split water without any external bias in different electrolytes [12, 19-21]. Many researchers reported epitaxial growth of crystalline III-nitride nanostructures on large area Si for high-efficiency photocatalysts for water splitting [7, 11, 13-15, 22-25]. This technology is scalable with established fabrication processes. Kibria et al. showed growth of defect-free N-terminated GaN nanowires on Si using molecular beam epitaxy (MBE) technique for high efficiency and stable PC water splitting [26]. The Ga-terminated GaN surfaces can be easily oxidized (to Ga_2O_3) in the air and aqueous electrolytes. The high stability of MBE grown GaN nanowires is attributed to the N-rich surfaces of GaN nanowire structures compared to Ga-rich grown GaN, which protects against photocorrosion and oxidation [27]. These advancements in the epitaxial growth technique of high crystalline quality and unique photocatalytic properties of III-nitrides gives future researchers an excellent opportunity to develop high efficiency and stable PEC/PC systems for artificial photosynthesis.

1.6 Molecular Beam Epitaxy (MBE) Growth of III-Nitride Nanostructures

1.6.1 MBE Equipment Details

MBE is one of the most controllable bottom-up approaches to grow high quality, defect-free nanowire growth on lattice-mismatched foreign substrates like Si, Al_2O_3, diamond or SiC [28-31]. Nanowires and planar structures can be grown under ultra-high vacuum (UHV) conditions (typical base pressure ~ 10^{-10} torr) in the MBE growth chamber. The UHV conditions in the growth chamber are maintained by using cryopump and an ion pump. This UHV helps to eliminate any impurities in the growth chamber and minimizes interactions between the molecular beam and the impurities. As shown in Figure 1.10, an MBE growth chamber is equipped with Knudsen effusion cells, a substrate heater along with holder, viewports, and reflection high- energy electron diffraction (RHEED) gun. The effusion cells consist of crucibles (see Figure 1.10) which are usually made up of pyrolytic boron nitride. These crucibles can withstand high temperatures up to ~ 1400 ℃, but the standard effusion cells operate at a temperature ~1200 ℃. The RHEED gun is a powerful tool to monitor the in-situ oxide desorption of the substrate surface. RHEED pattern is susceptible to the uppermost layers of the sample rather than the bulk structure. During the nanowire growth, spotty patterns (an array of dots) are observed on the RHEED screen. The general information of the nanowires, including the size, shape, orientation, and density can be derived from the size, shape, and density of the dots on the RHEED screen. It is important to note that diffraction from an amorphous layer, such as an oxide on the top surface, gives no diffraction patterns at all. The substrate heater is designed with a continuous azimuthal rotation (CAR) to provide excellent uniformity for deposition of materials on the substrate.

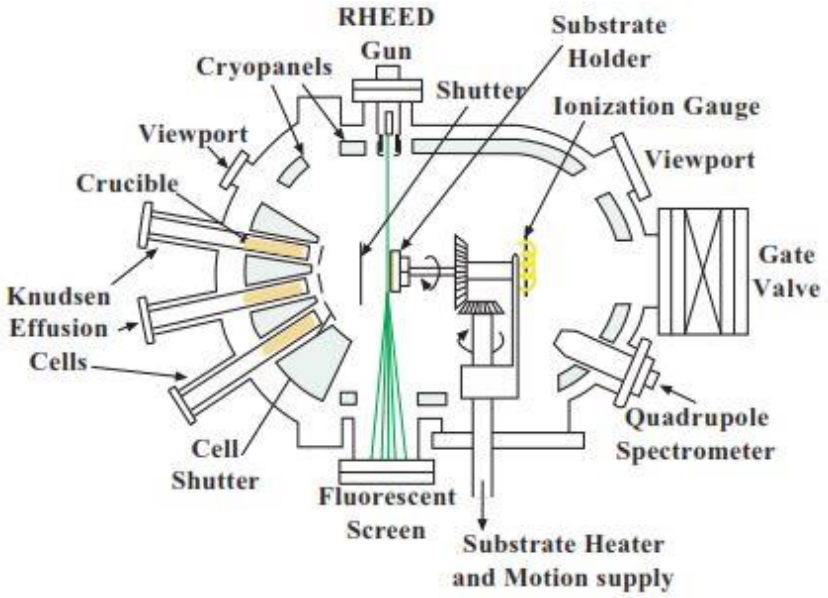

Figure 1.10. Schematic showing MBE growth chamber with all the effusion cells with crucibles and shutters, RHEED gun, a substrate holder, viewports, ionization gauge, and gate valves [32a].

For the growths in this thesis, a Veeco Gen II (shown in figure 1.11(a)) and Veeco GenXplor (shown in figure 1.11(b)) MBE systems, equipped with an integrated radio-frequency (RF) plasma source are used for the growth of nanowires. Both MBE systems are equipped with Ga, Al, In, Mn, Mg, Si, and Ge Knudsen effusion cells. The MBE systems consist of three main vacuum chambers, an intro chamber (or load lock chamber), a buffer chamber, and a growth chamber. For the GenXplor MBE, an electron beam gun is mounted to evaporate refractory metals like Mo, W, Ta, and Nb. This MBE additionally has Se and Te sources to grow 2-D transition metal dichalcogenides (TMDCs) like $MoSe_2$, WSe_2, WTe_2, and $MoTe_2$. The growth conditions, structural characterization and PEC application of the first-time demonstration of 2-D $MoSe_2$ protection layer on Si for water splitting are discussed in Chapter-6.

All the growths are done on *n*-Si substrate. Before loading into the MBE chamber, the Si substrate is cleaned with acetone and methanol to remove any organic contaminants. Subsequently, Si substrate is immersed in 10% buffered hydrofluoric acid to remove native oxide. The cleaned Si substrate is loaded into the intro chamber and baked at 200 ℃ for 1.5 h. Subsequently, the substrate is transferred to the buffer chamber where it is baked at 450 ℃ for 2.5 h. In the growth chamber, the substrate is put on the substrate holder and thermally treated to obtain well-ordered surfaces after the oxide (SiO_x) removal from the substrate at high temperature.

During the surface reconstruction of Si (100), a 2 × 2 pattern was observed on the RHEED screen at ~ 770 ℃ (thermocouple reading). To completely remove SiO_x from the Si surface, the substrate temperature is further increased by ~ 50 ℃ and outgassed at the same temperature for 10 min. After this *in-situ* thermal treatment, before starting growth, the ion pump is isolated from the growth chamber. The typical growth chamber pressure is ~10^{-5} torr with the cryopump. A RF plasma source power of ~350-420 W and constant ultrahigh pure N_2 flow of 0.45-1 standard cubic centimeter per minute (sccm) are used for InGaN and GaN nanowire growths. The RF power supply dissociates stable N_2 molecules into nitrogen species (neutral atoms, ions, and active molecules).

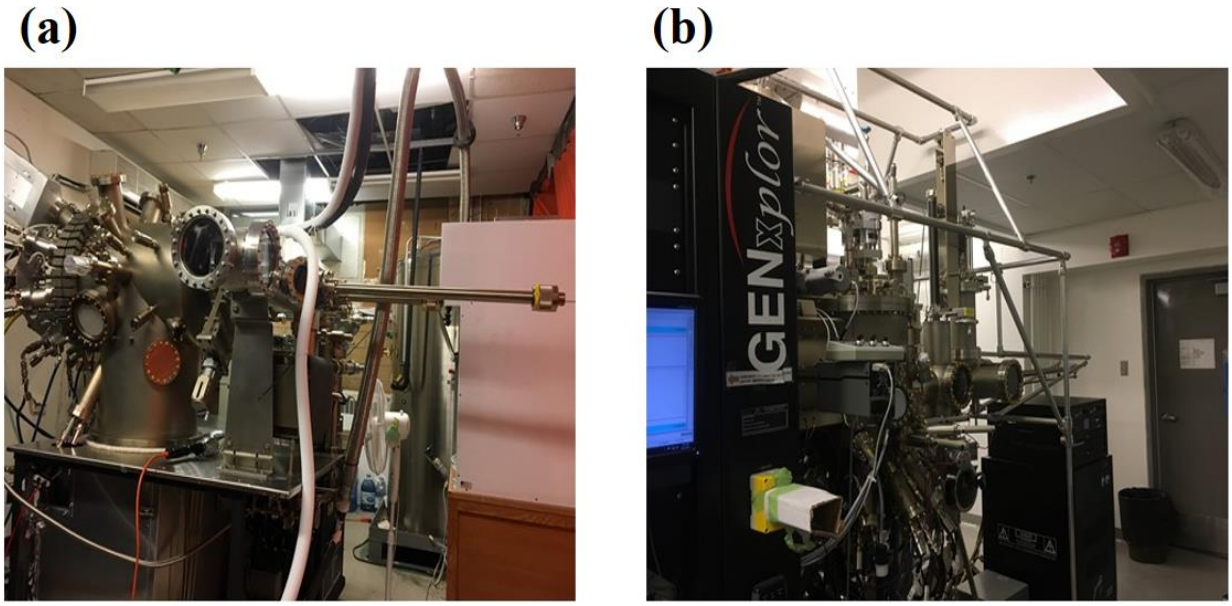

Figure 1.11. Images of (a) Veeco Gen II and (b) Veeco GenXplor - PA-MBE systems.

1.6.2 MBE Growth Mechanism

Wagner and Ellis from Bell Laboratory [32b] illustrated the formation of NW through a technique known as vapor-liquid-solid (VLS) growth. In this mechanism, a metal particle like Au is used as a catalyst (see Figure 1.12) to serve as nucleation sites and assist in NW formation. There are four main steps for VLS growth as illustrated in Figure 1.12: 1) deposition of metal particles, 2) formation liquid alloy (Au-Ga), 3) crystal nucleation, 4) precipitation of excess material from the metal droplet to promote axial growth of the NW. The length and diameter of VLS grown NW are determined size and position of metal particles, as well as growth parameters like pressure and temperature. A significant issue with the VLS growth process is that the metal catalyst particles remain on the tip of the NW after growth. These metal particles on the material lead to unintentional defects and impurities in the NW.

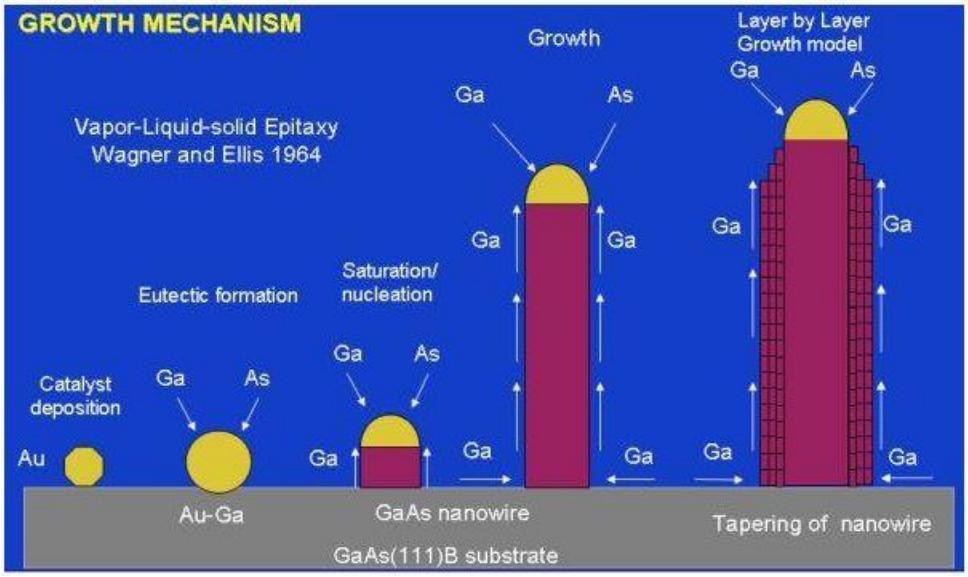

Figure 1.12. Schematic illustrations of GaAs nanowire grown by VLS growth process [33].

In contrast to the VLS growth, GaN/InGaN NW can be spontaneously grown on Si under nitrogen-rich conditions in MBE, without any external metal catalysts required for the nucleation. As illustrated in Figure 1.13, for self-catalytic growth of GaN NW by MBE, there are three main processes: 1) adsorption, 2) desorption and 3) diffusion. A major advantage for MBE grown GaN NW over VLS growth process is the absence of Ga droplets after growth on the tip of the NW, which eliminates defects arising from liquid alloy. The growth is initiated by a nucleation step, where stable nuclei are formed after reaching a critical radius. This step needs to be controlled to determine the nanowire dimensions (length and diameter), density and morphology. Ristic et al. [34] proposed the model that Ga atoms on the substrate surface can undergo adsorption, diffusion, and desorption while forming the stable nucleus required for NW propagation. Some of the factors affecting the formation of stable nuclei are substrate temperature, source atoms' (Ga) affinity to

the substrate and Ga flux. It is observed that as soon as RF plasma source is turned on to start the growth, a thin (~1-3 nm) amorphous Si_xN_y layer is unintentionally formed on Si substrate.

The NW propagation is determined by differences in surface energy states, adatom diffusion and sticking coefficients on different crystal planes [35]. The sticking coefficient for Ga atoms at the top is much larger than the sidewalls of NW. As seen from Figure 1.13, the Ga atoms impinging at the very tip or near diffusion length of the tip will be incorporated and help in axial growth of NW. However, Ga atoms impinging farther down the sidewalls are likely to be desorbed and do not contribute to the NW growth. Therefore, the adatoms diffuse to the NW top from its lateral sides as a result of lower chemical potential at the top surface of NW. The factors affecting the sticking coefficient and surface diffusion for NW growth are growth temperature and N_2 flow.

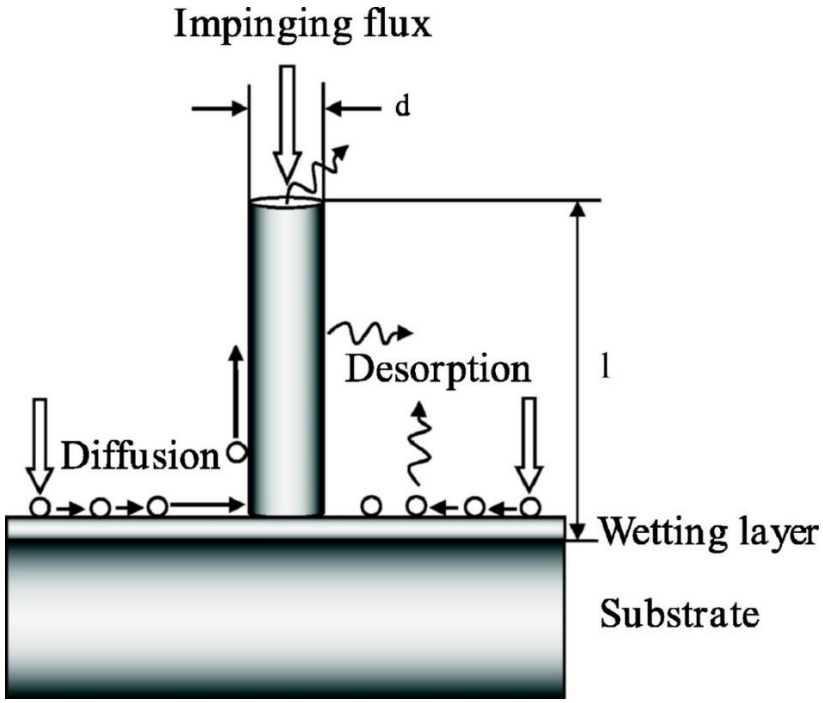

Figure 1.13. Schematic representation of different processes involved in MBE growth: adsorption, desorption, and surface diffusion [36].

The catalyst-free growth of GaN NW by PA-MBE takes place within a broad range of growth conditions. Fernández-Garrido et al. studied MBE growth morphology as a function of impinging Ga flux and growth temperature [31,37]. As seen from Figure 1.14, the label "No growth" indicates no growth of GaN due to the high Ga desorption and GaN decomposition. Depending on the specific flux and temperature conditions, the morphology can be varied from compact layers to nanocolumns. These studies clearly establish that it is possible to accurately control the GaN morphology using MBE. In Chapters 3 and 4, we will discuss the growth of N-terminated In-rich InGaN photoanode and GaN/Si photocathode respectively for high efficiency PEC water splitting.

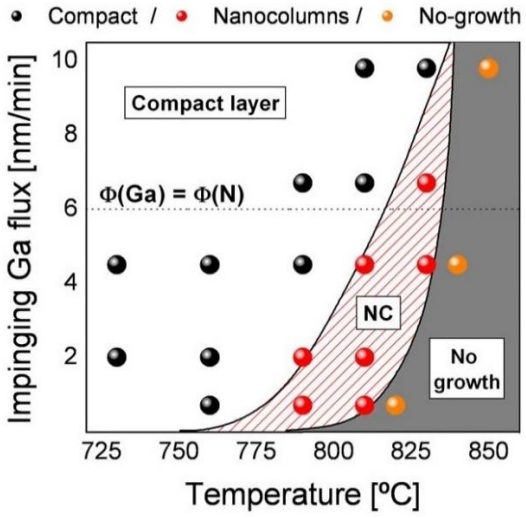

Figure 1.14. Growth diagram showing a variation of nanostructure morphology as a function of Ga flux and growth temperature at a fixed N_2 plasma condition [37].

Therefore, the MBE growth process can achieve superior quality III-nitride NW heterostructures with well-controlled structural and optical properties which lead to highly efficient photocatalysts for PEC/PC water splitting.

1.7 Tandem Photoelectrodes for Photoelectrochemical Water Splitting

Tandem water splitting cell is a combination of small bandgap semiconductor and large bandgap semiconductor connected in series to achieve a high photovoltage (generally in the range of 1.7-2.0 V), which is required for unassisted PEC water splitting. This design can effectively utilize most of the solar spectrum to produce high efficiency devices. The tandem photoelectrodes can be divided into two broad categories: III-V based, and non-III-V based photoelectrodes. In the following sub-sections, we will discuss the design, current status and the challenges for tandem devices.

1.7.1 Design Principles

The tandem device consists of a top light absorber cell, bottom light absorber cell and tunnel junction to connect the two cells [38]. As discussed earlier, the practical photovoltage required for water splitting is 1.6-1.8 V. Therefore, it is essential that the top and bottom cells should produce a photovoltage of 1.6-1.8 V for unassisted photoelectrochemical water splitting. In *Section 2.5*, we discussed the optimized energy band-gap requirements for both top and bottom cells to achieve an STH > 25%. In the literature (as shown in Figure 1.15), III-V compound semiconductors and their alloys are ideal choices for the top cell. The bottom cell is commonly a p-n junction PV device. It is to be noted that the tunnel junction plays a crucial role in connecting the top and bottom cells with negligible loss in the photovoltage and photocurrent density. The working mechanism for a tunnel junction is as follows. The tunnel junction consists of degenerate p^{++} and n^{++} doping levels. Due to such heavy doping concentrations, the thickness of the space charge region reduces which creates band bending at the junction to align the valence band edge on p^{++}-side with conduction band edge on n^{++}-side. Tunnel junctions consisting of heterostructures of highly polar materials, such as III-nitrides, have significantly higher tunneling

probability due to a high electric field generated over a small region with substantial band bending. Furthermore, it had been demonstrated that InGaN tunnel junction devices could achieve superior optoelectronic performances due to the piezoelectrically induced polarization effect [39-41]. Therefore, the polarization induced III-nitride structures are attractive alternatives to the conventional tunnel junctions for building PEC tandem devices.

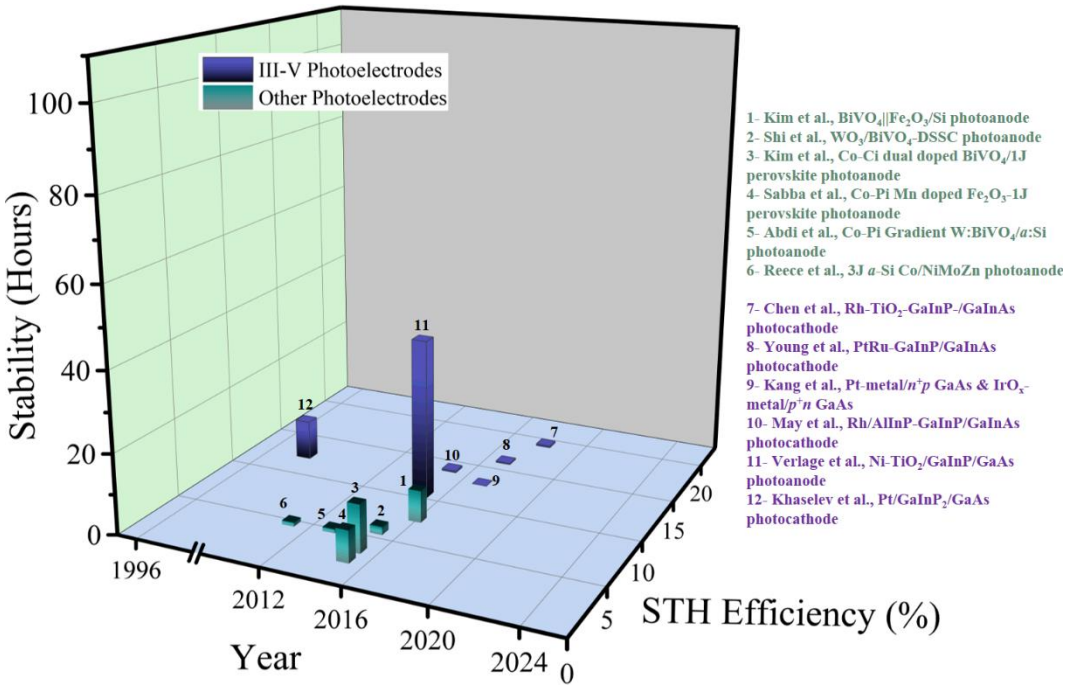

Figure 1.15. Graphical representation of state-of-the-art photoelectrodes for III-V photoelectrodes and non-III-V photoelectrodes in terms of STH and stability.

1.7.2 Current State-of-the-Art Tandem Photoelectrodes

The major challenge for current PEC water splitting is to achieve high efficiency and stable solar-to-H_2 conversion. Most of the research from the 1970s [43a] was focused on wide bandgap (E_g) materials as photocatalysts and photoelectrodes (both anode and cathode) as the wide bandgap can

readily drive unassisted water splitting. However, to achieve high efficiencies, the photoelectrode materials need to absorb the visible light part (400-750 nm) of the solar spectrum. The conventional metal oxide-based materials suffer from very low efficiency under direct solar irradiation, due to the large E_g and they absorb only the UV portion (<400 nm) of the solar spectrum. Therefore, in the recent past researchers have been focusing on other materials such as III-V compound semiconductors and their alloys (especially as photocathodes) to achieve high efficiencies.

As shown in Figure 1.15, Turner et al. [43b] first reported a high STH efficiency of 12.4% using GaInP/GaAs tandem photocathode. In 2016 Turner et al. [43c] broke their previous record by publishing one of the highest STH efficiency of 16% with GaInP/GaInAs tandem photocathode. Recently, Chen et al. reported the highest STH of 19.3% using III-V photoelectrodes [43d]. Most of the III-V photoelectrodes are generally employed as photocathodes. As discussed earlier, OER is the kinetic bottleneck for overall water splitting, and therefore the reported efficiencies of photoanode tandem devices in the literature are always lower than photocathode tandem devices.

The high-efficiency non-III-V photoelectrodes (especially photoanodes), shown in Figure 1.15, generally consists of one or two junction Si/perovskite PV devices electrically connected in series with a top light absorber (bandgap, E_g, of 2-2.6 eV) to overcome the overpotential for water oxidation and earth-abundant co-catalysts such as cobalt-based catalysts to enhance reaction kinetics. From the band-gap requirements for those mentioned above top light absorbers, $BiVO_4$ ($E_g \sim 2.6$ eV) and hematite (α-Fe_2O_3) ($E_g \sim 2.0$ eV) are good candidates which can absorb photons of $\lambda < 510$ nm and $\lambda < 620$ nm, respectively. Therefore, hetero-type dual photoelectrodes with Si solar cell showed the best STH efficiency of 7.7% [43e].

As shown in Figure 1.15, the stability of III-V photoelectrodes is less than 1 h for unassisted PEC water splitting. The highest stability reported for the III-V photoelectrodes with an extra

protection layer is ~ 40 h [43f]. It is to be noted that even the non-III-V photoelectrodes also suffer from low stability < 8 h. Further details about the stability of different photoelectrodes are discussed in Chapter-5.

1.7.3 Challenges

Much research is still on-going to reduce the bandgap for top light absorber and meet the current matching conditions (further discussed in *Section 2.5*) for a tandem PV+PEC, which in theory can give a maximum STH of >25%. As shown in Figure 1.15, in all the high-efficiency photocathodes and photoanodes, one of the major issues is the stability (< 50 h), which is often measured in terms of photocurrent density variations over a specified duration of time. There are no reports so far, to the best of our knowledge, for a high-efficiency PEC device having high stability (measured in two-electrode, unassisted solar water splitting condition) > 100 h simultaneously. Therefore, stability is a significant requirement along with STH >10% for PEC approach to be commercialized for H_2 production. A significant issue with non-III-V photoelectrodes consisting of metal oxides, such as $BiVO_4$ and Fe_2O_3, is their low efficiencies because of the limitations in bulk transport of charge carriers and their wide band gaps. In Chapter-7, we will discuss the design and implementation of InGaN/Si tandem photocathode with a unique polarization induced tunnel junction to address the conundrum of simultaneously achieving high efficiency and high stability for PEC water splitting.

1.8 Organization of Thesis

Chapter-1 illustrates the present global energy crisis and the need for alternate clean and eco-friendly renewable sources of energy. We discussed the importance of solar H_2 generation over conventional methods by using two of the most abundant sources (sunlight and water) on earth. PEC has been considered by many as the best method to achieve high efficiency and low-

cost H_2 generation to meet energy demands. The advantages and MBE growth of III-nitride nanostructures are elaborated in *Sections 1.5 and 1.6*.

Chapter-2 discusses the fundamentals of PEC water splitting by taking the example of a photoanode to illustrate the thermodynamic and kinetic factors and their challenges. Crucial figures of merit for PEC are also discussed. Different PEC configurations and efficiency limitations are discussed in *Section 2.5*. Lastly, the importance of photoelectrode stability is discussed.

Chapter-3 reports high-efficiency In-rich InGaN nanowires photoanode (with E_g ~ 1.7 eV) with IrO_2 nanoparticles catalyst in 0.5M H_2SO_4 under AM 1.5G one-sun illumination. The maximum applied bias photon-to-current efficiency (ABPE) achieved by the photoanode is ~3.6% at 0.75 V *vs.* NHE. Furthermore, in the presence of hole scavengers like H_2O_2, InGaN photoanode reached the theoretical maximum photocurrent density of ~ 20 mA/cm^2 for E_g ~ 1.7 eV. These results lay the foundation for the development of a tandem device with InGaN as top light absorber stacked on a bottom absorber with E_g – 1.1 eV which can achieve a theoretical maximum STH >25%.

Chapter-4 reports growth and water splitting performance of GaN nanostructures on n^+-p Si photocathode. In this chapter, detailed XPS measurements reveal that the conduction band edge of GaN and Si are near-perfectly aligned, which enables efficient extraction of photo-generated electrons from the underlying Si wafer to GaN nanowires. With the incorporation of Pt co-catalyst nanoparticles on GaN surface, we have demonstrated solar water splitting on GaN/Si photocathode with a maximum current density of >35 mA/cm^2, ABPE >10% and a very high stability of >100 h in 0.5 M H_2SO_4 under AM1.5G one-sun illumination. This work shows the use of GaN nanowires

as a multi-functional protection layer as well as excellent charge extraction of the photogenerated electrons from the underlying Si wafer.

Chapter-5 is a further demonstration of the GaN/Si platform, shown in chapter-4, for ultrahigh long-term stability. We report that Pt-decorated GaN nanostructures on n^+-p Si photocathode can achieve ultrahigh stability of 3000 h (i.e., over 500 days for usable sunlight ~5.5 hr per day) at a large photocurrent density (> 35 mA/cm^2) under AM 1.5G one-sun illumination with frequent Pt catalyst regeneration. The best performing platinized n^+-GaN NWs/n^+-p Si photocathode also showed excellent onset potential (V_{on}) ~0.56 V *vs.* RHE with high photocurrent density of ~37 mA/cm^2 and a high applied bias photon-to-current efficiency (ABPE) of 11.88% under AM 1.5G one-sun illumination in 0.5M H_2SO_4. This study provides a new outlook for the design and development of semiconductor photoelectrodes for high efficiency and ultrahigh stable PEC water splitting.

Chapter-6 demonstrates the use of earth-abundant $MoSe_2$ as a surface protection layer for Si-based photoanodes, which has transformed, for the first time, Si into a highly stable and high-efficiency photoanode. Detailed structural analysis of $MoSe_2$ layers using Raman spectroscopy, X-ray photoelectron spectroscopy (XPS) and atomic force microscopy (AFM) are discussed. The $MoSe_2$/Si photoanode produces a nearly light-limited current density of ~30 mA/cm^2 in 1M HBr under AM 1.5G one sun illumination. The half-cell solar energy conversion efficiency (ABPE) reaches up to 13.8%. Chronoamperometry studies revealed a high photocurrent density of 26 mA/cm^2 for 1 h at an applied bias of 0.6 V *vs.* RHE under AM 1.5G one sun illumination in 1M HBr.

Chapter-7 reports the design and implementation of the double-junction InGaN/Si photocathode for unassisted water splitting. The best performing surface modified InGaN/Si

double-junction photocathode, in three-electrode measurements, shows an excellent onset potential (V_{on}) ~2.3 V *vs.* RHE with a high applied bias photon-to-current efficiency (ABPE) of 9.6% under AM 1.5G one-sun illumination in 0.5M H_2SO_4. The PEC performance in the two-electrode configuration of the double-junction photocathode also shows an excellent photocurrent density ~ 8.2 mA/cm^2 and STH of ~ 10.1%. Chronoamperometry analysis for the photocathode shows a stable photocurrent density of ~8 mA/cm^2 for 100 h under AM 1.5G one-sun illumination in 0.5M H_2SO_4. This work is a stepping stone towards the development of low-cost and industry-ready semiconductor materials, like III-nitrides and Si, for PEC systems providing high efficiency > 10% and long-term stability > 1000 h.

Chapter-8 summarizes the work presented in this thesis. Future research directions are also proposed, to realize artificial photosynthesis via solar-to-fuel conversion on III-nitride nanostructures for high efficiency and stability.

Chapter-2: Fundamentals of Photoelectrochemical Water Splitting

2.1 Introduction

The history of PEC experiment started in 1839 when Becquerel found a photovoltaic effect at an illuminated silver chloride electrode [44]. In 1954, Brattain and Garrett showed that the electrochemical reactions occurring at Ge electrodes were influenced by changing the semiconductor properties of Ge through light excitation [44, 45]. This work was followed up by many works on several other semiconductor electrodes. These studies lead to the first principle calculations for the nature of charge distribution, kinetics and thermodynamics of charge transfer involved in the semiconductor-liquid interface. The pioneering work for PEC was started by Boddy in 1969 showing OER using TiO_2 [46]. It was later in 1972, Fujishima and Honda who demonstrated PEC water splitting for HER using TiO_2 [47]. As discussed in *Section 1.8.2*, a lot of progress was made by researchers over the past few decades to show the potential application of PEC systems to solar energy conversion with high efficiency. PEC water splitting systems use the combination of sunlight and water to convert the solar energy into electrical energy, as well as to produce a chemical fuel such as H_2 [48]. H_2 is a valuable energy carrier and it can be more easily stored than electricity. PEC technology enables energy storage in a transportable fuel like H_2 and O_2 [48].

The basic operation of a PEC cell can be explained, in Figure 2.1, by using the example of a dual-tandem system having a single absorber photoanode and a single absorber photocathode connected wirelessly. The photochemistry involved in this system is divided into three steps. First step is capturing the photons from the light source. In the tandem system, the solar spectrum is absorbed by the two complementary photo-absorbers with $E_{g1} > E_{g2}$; E_{g1} is band-gap of photoanode and E_{g2} is band-gap of photocathode. The second step is the creation of electron-hole

pairs which needs to be separated. Finally, once the electron-hole pair is spilt, it is essential for the electron and hole to move in different directions to reach chemically active sites in the device. The holes drive the OER at the surface of the photoanode semiconductor. The electrons move through the ohmic contact end and travel across the electrical connection to the surface of the photocathode semiconductor where the HER takes place.

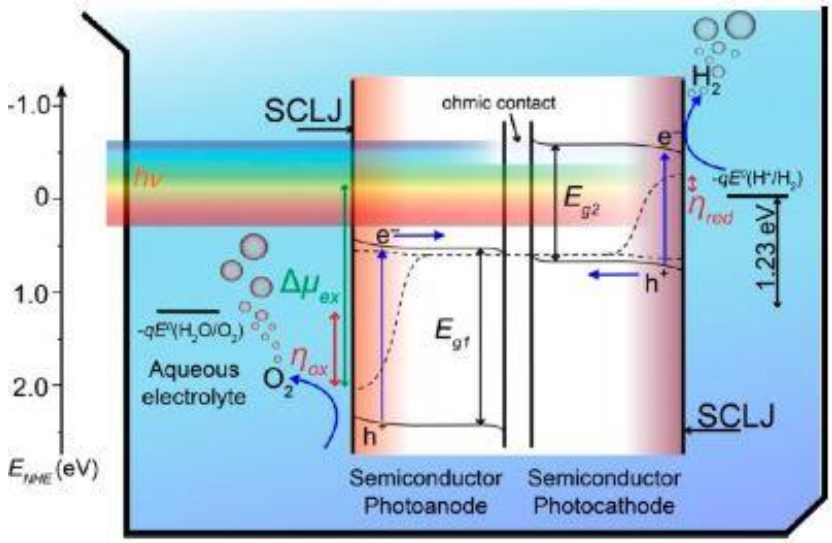

Figure 2.1. Schematic representation of dual-tandem PEC water splitting system showing charge carriers' generation, separation, and extraction from semiconductor photoanode and photocathode, including overpotentials for oxidation and reduction reactions [38].

The concept of semiconductor–liquid junction (SCLJ) makes these systems highly attractive alternatives to costly all-solid-state solar conversion devices. From Eqn. (1.4), Eqn. (1.6) and Eqn. (1.7), the theoretically minimum E_g for water splitting is 1.23 eV which corresponds to a wavelength ~ 1000 nm. However, the overall E_g requirement rises to 1.5–2.5 eV which includes overpotentials of entropic losses, OER and HER overpotentials, and other parasitic losses. Upon

illumination, the light absorber must generate electron-hole pairs and under appropriate band bending conditions near the SCLJ, these electrons and holes can be separated to drive the reduction and oxidation, respectively, generating H_2 and O_2. Therefore, understanding SCLJ is very important in designing high efficiency PEC systems for H_2 generation.

2.2 Electrostatic Analysis of Semiconductor Liquid Junction

The unique advantage of a semiconductor is the ability to vary the doping by using impurities known as dopants. For Si material, trivalent dopants (group III), which have more electron deficiency, accept electrons from the valence band and produce more mobile holes than electrons in Si. Such an impurity dopant gives rise to *p*-type doping in Si. Whereas electron-rich pentavalent dopants (group V) give *n*-type doping by increasing the concentration of mobile electron [49]. For other semiconductors, like III-nitrides, the *p*-type and *n*-type dopants will be different.

The concentrations of the mobile electrons and holes in a semiconductor with respective to Fermi level are given by:

$$n \approx N_C(T)\, e^{-\frac{q}{kT}(\phi_{CB}-\phi_F)};\ N_C(T) = 2\frac{(2\pi m_e^* kT)^{\frac{3}{2}}}{h^3} \qquad \text{eq. (2.1)}$$

$$p \approx N_V(T)\, e^{-\frac{q}{kT}(\phi_F-\phi_{VB})};\ N_V(T) = 2\frac{(2\pi m_h^* kT)^{\frac{3}{2}}}{h^3} \qquad \text{eq. (2.2)}$$

where $N_C(T)$ and $N_V(T)$ are charge carrier concentrations, and ϕ_{CB} and ϕ_{VB} are the potentials for CBM and VBM, respectively, m_e^* and m_h^* are the effective masses of electrons and holes, and ϕ_F is the Fermi level potential. k is Boltzmann's constant and T is temperature.

For a non-intrinsic semiconductor, these values are related to the intrinsic concentration by:

$$np = N_C(T)N_V(T)\, e^{-\frac{q}{kT}(\phi_{CB}-\phi_{VB})} = n_i^2 \qquad \text{eq. (2.3)}$$

where n_i is the material's intrinsic carrier concentration and $\phi_{CB} - \phi_{VB} = E_g$ (which will not change with doping). The above Eqns. (2.1) and (2.2) can be written in terms of n_i, ϕ_i (intrinsic Fermi level) as

$$n \approx n_i \, e^{-\frac{q}{kT}(\phi_i - \phi_F)} \qquad \text{eq. (2.4)}$$

$$p \approx n_i \, e^{-\frac{q}{kT}(\phi_F - \phi_i)} \qquad \text{eq. (2.5)}$$

$$\phi_i = \frac{(\phi_{CB} + \phi_{VB})}{2} + \frac{1}{2} \, kT \, ln\left(\frac{N_V}{N_C}\right) \qquad \text{eq. (2.6)}$$

The ϕ_F in semiconductor is the electrochemical potential of electrons in a solid. The electrochemical potential of electrons in a redox electrolyte is given by:

$$E_{redox} = E^o_{redox} + \frac{RT}{nF} \ln \frac{c_{oxd}}{c_{red}} \qquad \text{eq. (2.7)}$$

where c_{red} and c_{oxd} are concentrations of the reduced and oxidized species respectively in the redox reaction, R is the gas constant, F is Faraday constant, E^o_{redox} is the standard cell potential and n is the number of electrons involved in the reaction. In the case of an electrolyte, the electrochemical potential in a redox system is equivalent to Fermi level $\phi_{F,redox}$:

$$\phi_{F,redox} = E_{redox} \qquad \text{eq. (2.8)}$$

The redox potentials are given in a conventional scale, using the normal hydrogen electrode (NHE) or the saturated hydrogen electrode (SHE) or the reversible hydrogen electrode (RHE) as a reference electrode. Therefore, redox potential E_{redox} (*vs.* RHE) with the $\phi_{F,redox}$, expressed versus vacuum reference ($E_{ref} = 4.5 \; eV$) is given as:

$$\phi_{F,redox} = -4.5 \; eV - e_o E_{redox} \qquad \text{eq. (2.9)}$$

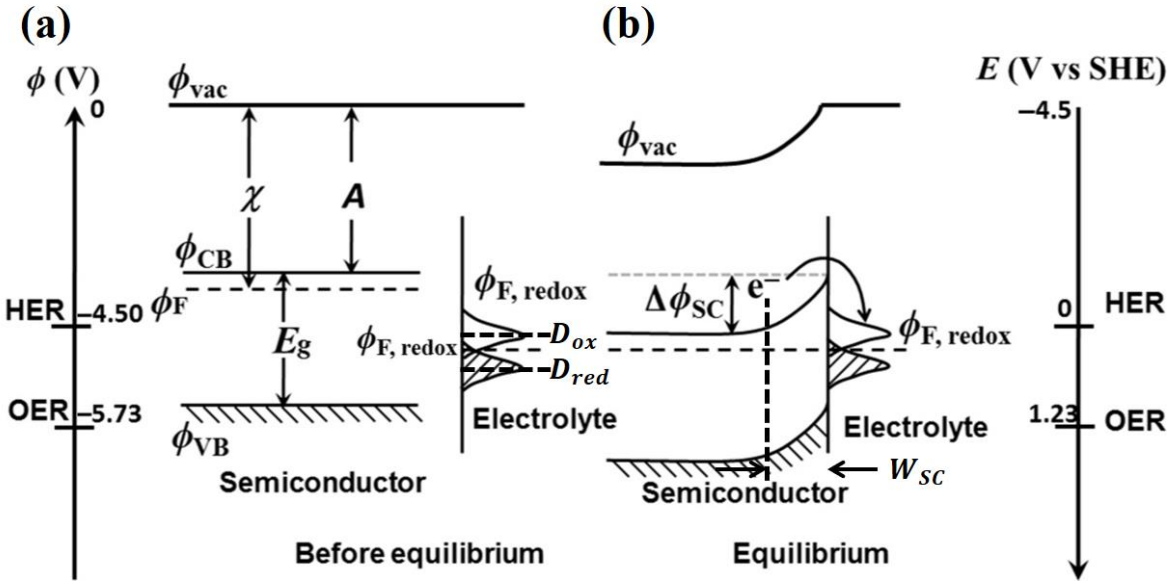

Figure 2.2. Band diagram of semiconductor (a) before and (a) after contact with electrolyte versus SHE (right) and relative energy levels to vacuum (left). The drawings are for an *n*-type semiconductor. $A = -q\phi_{CB}$ is electron affinity and $\chi = -q\phi_F$ is work function of the semiconductor. This figure has been edited using previous reference [50].

Gerischer's model [51-53] leads to a Gaussian distribution of the redox states (*vs.* SHE) in an electrolyte as shown on the right side of Figure 2.2a. The distribution functions for the states are given as follows:

$$D_{ox} = c_{oxd} e^{-\frac{(\phi - \phi_{F,redox} - \lambda)^2}{4kT\lambda}} \quad \text{eq. (2.10)}$$

$$D_{red} = c_{red} e^{-\frac{(\phi - \phi_{F,redox} + \lambda)^2}{4kT\lambda}} \quad \text{eq. (2.11)}$$

where λ is the reorganization energy of electron transfer theory [52]. The corresponding distributions shown in Figure 2.2 (a) and (b) are for equal concentrations ($c_{ox} = c_{red}$). This model further states that an electron transfer can occur from an occupied state in the metal or the semiconductor to an

empty state in the redox system in the electrolyte. Therefore, the rate of electron transfer depends on the density of energy states on both sides of the interface irrespective of solid/liquid/electrolyte states.

When a semiconductor is placed in direct contact with an electrolyte, the semiconductor's ϕ_F (Fermi level is unpinned) equilibrates with the oxidation/reduction potential of the electrolyte. During the system equilibration, the electrons flows from higher free energy to lower free energy until the compensating field is sufficient to stop the flow (see Figure 2.4a), which gives

$$\phi_F = \phi_{F,redox} \qquad \text{eq. (2.12)}$$

It is to be noted that the semiconductor interacts with the molecules of the electrolyte and forms a double layer. As shown in Figure 2.3, the solution side consists of several layers. The first layer is formed by solvent molecules and specifically adsorbed ions. This layer is called the inner Helmholtz layer or plane (IHP) [54]. The next layer consists of solvated ions, and the center of the charges is called the outer Helmholtz layer or plane (OHP).

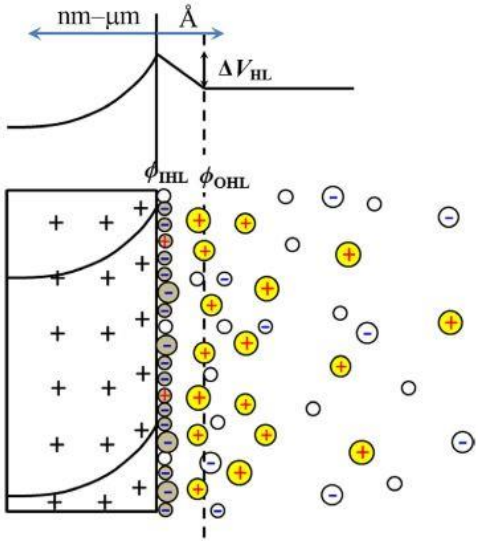

Figure 2.3. Schematic showing Helmholtz layers at the SCLJ for *n*-type semiconductor [50].

A concentration profile of solvated ions exists over a relatively large length depending on the electrolyte concentration. The region from OHP to the bulk of the electrolyte is called Gouy or diffuse layer. Under dark condition, Fermi level of the semiconductor aligns with the electrochemical potential of the redox species in the electrolyte which leads to surface band-bending (BB). From Figure 2.2b, there is a Fermi level difference between semiconductor and electrolyte ($\phi_{F,redox} < \phi_F$) as *n*-type semiconductor encounters the electrolyte. The electrons flow from semiconductor to the electrolyte during equilibration. This leads to an accumulation of positive charges or holes near the surface, moving the Fermi level further away from the CBM and towards VBM. It has been found that a space charge region (SCR) is formed due to the difference in the electrochemical potentials of electrons in the two phases. as seen from Figure 2.4a. This leads to an upward BB ($\Delta\phi_{sc}$) and forms a Schottky-type junction at SCLJ.

$$\Delta\phi_{sc} = \phi_{F,SC} - \phi_{F,redox} \qquad \text{eq. (2.13)}$$

In Figure 2.2b, at a distance sufficiently away from the surface, the BB is completely diminished. This distance is known as space charge depletion width (W_{SC}). The equation for W_{SC} is derived using Poisson's equation and some necessary assumptions [50, 55] to get:

$$W_{SC} = \sqrt{\frac{2\varepsilon_o\varepsilon_{SC}}{qN_D}\left(\Delta\phi_{sc} - \frac{kT}{q}\right)} \qquad \text{eq. (2.14)}$$

where $\varepsilon_o\varepsilon_{SC}$ is the dielectric constant of a semiconductor and carrier concentration N_D.

The built-in field created by the BB is crucial to PEC for charge separation at the semiconductor/electrolyte interface. The extent of BB also depends on variations in externally applied bias ($\phi_{appl.}$). To derive the differential space-charge capacitance (C_{SC}) relation with doping and built-in potential, the Mott-Schottky expression is used:

$$C_{SC}^{-2} = \frac{1}{2\varepsilon_o\varepsilon_{SC}qN_DA^2}\left(\phi - \phi_{appl.} - \frac{kT}{q}\right) \qquad \text{eq. (2.15)}$$

A is the area of the semiconductor exposed to the electrolyte. When $\Delta\phi_{sc} = 0$, $\phi_{appl.}$ is equal to flat band potential (ϕ_{FB}). The ϕ_{FB} value is obtained by using the above Eqn. (2.15) and extrapolating the curve to C_{SC}^{-2} to zero. The ϕ_{FB} is defined as the externally applied potential for which there is no BB at the semiconductor surface. Therefore, from Eqn. (2.15) it is possible to determine ϕ_{FB} and N_D, which are very important to determine the charge separation in the semiconductor.

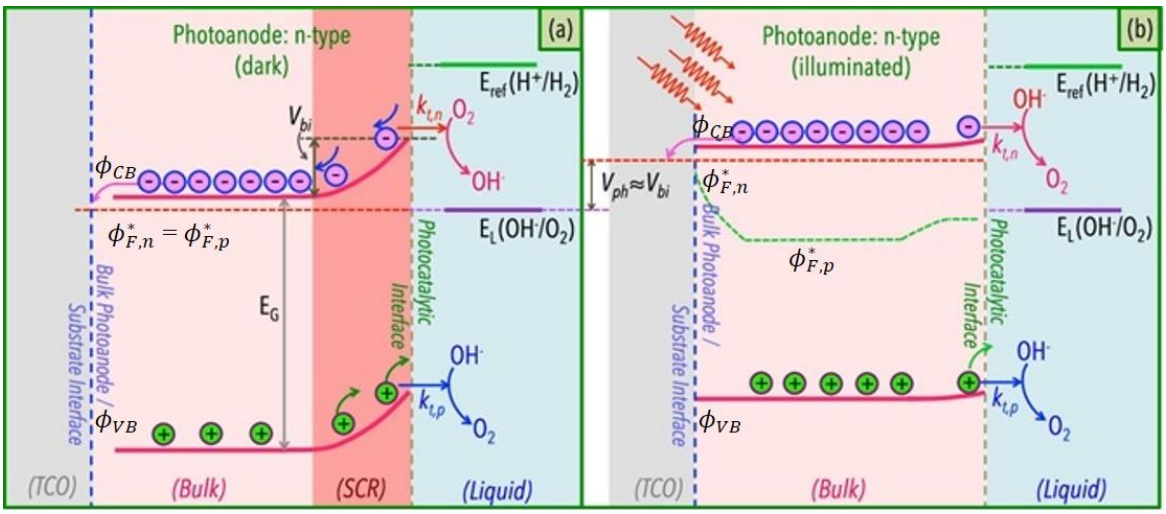

Figure 2.4. Schematic showing band-diagram of photoanode under (a) dark after equilibration and (b) illumination. Figure 2.4b shows the splitting of the Fermi level into quasi-Fermi levels with the generation of charges. This figure has been edited from the ref. [56] [56].

From Figure 2.4b, under illumination ($hv > E_g$), the *n*-type semiconductor immersed in the electrolyte produces many electron-hole pairs in the bulk and SCR. This leads to change in minority carrier concentration (holes) in the semiconductor and thereby splits the Fermi level into

quasi Fermi level for electron ($\phi^*_{F,n}$) and hole ($\phi^*_{F,p}$). The charge carrier concentrations are expressed as follows:

$$n = n_d + \Delta n = N_D(T)\, e^{-\frac{q}{kT}(\phi_{CB} - \phi^*_{F,n})} \quad \text{eq. (2.16)}$$

$$p = p_d + \Delta p = N_A(T)\, e^{-\frac{q}{kT}(\phi^*_{F,p} - \phi_{VB})} \quad \text{eq. (2.17)}$$

where n_d and p_d are electron and hole concentrations, respectively, under dark and Δn and Δp are additional photogenerated charges. The difference ($\phi^*_{F,n} - \phi^*_{F,p}$) between the quasi Fermi levels is known as the photovoltage (V_{ph}) for the SCLJ (shown in Figure 2.4b). The V_{ph} is influenced by bulk trap states and thereby impact the majority carrier transport properties.

2.3 Charge Transfer Kinetics

2.3.1 Butler-Volmer Equation and Tafel Slope Analysis

After photogeneration and charge separation of electron/hole pairs by the n-type semiconductor, it is essential to transfer the charges to catalytically active sites through SCLJ which is determined by the overpotential for OER and mass transport in the electrolyte. In this sub-section, the charge transfer across SCLJ is assumed as a simple electrochemical reaction where the reactant species is either going through oxidation or reduction. These transfers need to overcome the additional overpotential (concerning equilibrium potential of the electrode reaction) which is expressed as

$$\eta = \left|\phi_{appl} - \phi_{F,redox}\right| \quad \text{eq. (2.18)}$$

The change of current density *vs*. overpotential (J-η characteristic) obeys the Butler-Volmer model (not considering mass transfer effects) [57-59]:

$$J = J_o \left(e^{\left(\frac{-\alpha n F \eta}{RT}\right)} - e^{\left(\frac{(1-\alpha) n F \eta}{RT}\right)} \right) \quad \text{eq. (2.19)}$$

where α is the charge transfer coefficient (0<α<1), J is the current density under an overpotential. The first term in Eqn. (2.19) corresponds to the reduction reaction and the second term is the oxidation reaction [58]. J_o is exchange current density at the equilibrium potential of the electrode reaction which is given as [57]:

$$J_o = nFk_o C_O^{*(1-\alpha)} C_R^{*\alpha} \quad \text{eq. (2.20)}$$

where k_o is the rate constant of the electrode reaction; C_O^* and C_R^* are the bulk concentrations of the oxidized and reduced species. The Eqn. (2.19) implies that smaller the J_o value, more sluggish is the kinetics and therefore, it requires higher overpotential for driving the reaction to achieve desired net current.

As discussed in *Section 1.4.1*, overpotential ($\eta \gg \frac{nF}{RT}$) is required for both HER and OER. Thus, using the above condition, the second term in Eqn. (2.19) can be neglected for HER which gives

$$\frac{J}{J_o} = \left(e^{\left(\frac{(-\alpha_{HER})nF\eta}{RT}\right)} \right) \quad \text{eq. (2.21)}$$

Taking ln on both sides, rearranging the terms and then changing ln to log_{10}, we get

$$\eta = 2.303 \frac{RT}{\alpha_{HER} nF} log(J_o) - 2.303 \frac{RT}{\alpha_{HER} nF} log(J) \quad \text{eq. (2.22)}$$

Comparing Eqn. (2.22) to the standard Tafel slope: $\eta = a + b\ log(J)$ where a is a constant related to the magnitude of equilibrium current in forward and reverse direction; b is the Tafel slope (mV/dec)

$$|b_{HER}| = 2.303 \frac{RT}{\alpha_{HER} nF} \quad \text{eq. (2.23)}$$

Similar analysis gives the Tafel slope for OER after neglecting the first term in Eqn. (2.19) as

$$|b_{OER}| = 2.303 \frac{RT}{(1-\alpha_{OER)} nF} \quad \text{eq. (2.24)}$$

The HER or OER catalyst helps in reducing the overpotential and improving the charge transfer in SCLJ [60]. For better kinetic performance the Tafel slope value should be small [57, 61]. The Tafel plot is vital in determining the reaction mechanism by relating the electron transferred (n) and the charge transfer coefficient (α) and also understanding the rate determining step (RDS) in the reaction [61]. The best reported catalyst, in the literature so far, for HER is Pt [62] with an ideal $b_{HER} \approx 30\ mV/dec$ and a very low $\eta \approx 25\ mV$ at a high current density 20 mA/cm^2. Since, OER requires multiple electron transfer steps, it leads to lower J_o compared to HER. In Chapters-4 and 5, we will see the discussion on the use of Pt nanoparticles (NPs) cocatalyst with GaN nanowires (NW) protection layer on Si photocathode for high efficiency and ultrahigh stability H_2 production [63]. In an ideal case, from Eqn. (2.24), b_{OER} should be $15\ mV/dec$ at room temperature conditions. The best catalysts for OER are IrO_2 [64], RuO_2 [65] and NiFe LDH [66] with $b_{HER} \approx 40\ mV/dec$ and a relatively high $\eta \approx 300 - 340\ mV$. In Chapter-3, IrO_2 NPs are used as catalysts on the surface of InGaN NW photoanode [67] to improve reaction kinetics and thereby increase the efficiency.

2.3.2 Determination of Photocurrent Density

In this sub-section, the charge transfer from semiconductor to the electrolyte is illustrated by considering that all the photo-generated minority carriers can reach the interface and participate in a redox reaction. Gartner's model [68] derived *J-V* characteristics by neglecting the recombination and thermal generation of minority carriers and is not concerned with the SCLJ, as a transparent Ohmic metal contact is assumed at the surface of the interface. To derive the photocurrent, here we use the Reichman's model [59], where hole current density at the depletion edge is non-zero. In this chapter, we focused on *n*-type semiconductor photoanode, so we are interested in finding the total photocurrent density of holes which is given as,

$$J_G = J_{p,drift} + J_{p,diffusion} \qquad \text{eq. (2.25)}$$

An important assumption is that the solutions are time-independent ($\frac{dn}{dt}\ and\ \frac{dp}{dt} = 0$). The drift part of the Eqn. (2.25) is given as

$$J_{p,drift} = q\ \int_0^{W_{SC}} g(x)dx = qI_o(1\ -\ e^{-\alpha W_{SC}}) \qquad \text{eq. (2.26)}$$

where $g(x) =\ \alpha I_o e^{-\alpha x}$ which is the generation rate of holes at a depth x; I_o is the monochromatic photon flux; α is the absorption coefficient.

The diffusion part of current density (from Eqn. (2.25)) can be calculated for the minority carriers from bulk to SCR using the diffusion equation from $x =\ \infty$ to $x =\ W_{SC}$,

$$D\frac{d^2p}{dx^2} - \left(\frac{p - p_o}{\tau}\right) +\ g(x) = 0 \qquad \text{eq. (2.27)}$$

where D is hole diffusion coefficient, τ is hole carrier lifetime, $p_o = \frac{n_i^2}{N}$ is the equilibrium hole density and N is carrier density. The boundary conditions (BC) to solve Eqn. (2.27) are as follows:

$$p =\ p_o\ \ at\ x =\ \infty \qquad \text{eq. (2.28)}$$

$$p =\ p_{W_{SC}}\ \ at\ x =\ W_{SC} \qquad \text{eq. (2.29)}$$

After solving Eqn. (2.27) with BC and we get

$$J_{p,diffusion} =\ -J_{p,o}\ \left(\frac{p_{W_{SC}}}{p_o} - 1\right) + qI_o\alpha L\ \left(\frac{e^{-\alpha W_{SC}}}{1+\ \alpha L}\right) \qquad \text{eq. (2.30)}$$

$$J_{p,o} =\ \left(\frac{qp_oL}{\tau}\right) \qquad \text{eq. (2.31)}$$

where $J_{p,o}$ is saturated current density and L is the hole diffusion length ($L =\ \sqrt{\frac{kT}{q}\mu\tau}$); μ is the hole mobility.

By substituting Eqn. (2.26) and Eqn. (2.30) in Eqn. (2.25), we get

$$J_G =\ -J_{p,o}\ \left(\frac{p_{W_{SC}}}{p_o} - 1\right) +\ qI_o\ \left(1 -\ \frac{e^{-\alpha W_{SC}}}{1+\ \alpha L}\right) \qquad \text{eq. (2.32)}$$

In Gartner's model, $p_{W_{SC}} = 0$ which gives

$$J_G = J_{p,o} + qI_o \left(1 - \frac{e^{-\alpha W_{SC}}}{1+ \alpha L}\right) \quad \text{eq. (2.33)}$$

In general, Gartner's model has been used to analyze the photocurrents of the semiconductor-electrolyte barrier (Schottky junction) devices.

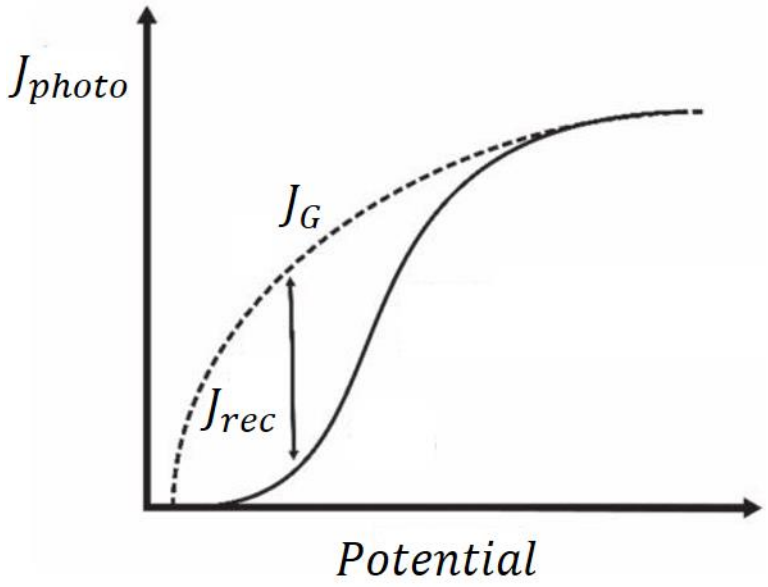

Figure 2.5. Photocurrent-voltage (*J*-*V*) relationship of a photoelectrode in an ideal situation (dotted curve) with no recombination and the one for a realistic system with surface recombination (solid curve). J_G is calculated from Eqn. (2.33). This graph has been edited from ref. [69] [69].

By using Eqn. (2.33), we can plot the *J*-*V* characteristics which give an ideal curve as shown in Figure 2.5. This approximation is inadequate in describing actual working systems. There is surface recombination due to slow interfacial hole transfer near SCLJ. Surface states are formed in the photoelectrode due to crystal defects, surface dangling bonds and chemisorbed species. The photogenerated holes trapped in these surface states are annihilated through recombination with electrons. Another reason for deviation from the ideal curve is due to recombination in SCR

through defects near the mid-band gap. The effect of recombination in the SCR on the *J-V* characteristics was further determined by using Sah's method [70].

2.4 Metrics of PEC water splitting

From *Section 1.8.2*, the most important metric of any PEC system is STH. Ideally, a given PEC device is required to be able to split water without any external electrical bias. As discussed in *Section 1.8.2*, the high STH devices for both photocathode and photoanode, reported so far in the literature, are a hybrid of PV+PEC. These devices have a high cost and are not stable for long durations. Therefore, appropriate diagnostic metrics need to be used to characterize different PEC systems and understand their inherent catalytically properties and performance which can be benchmarked for H_2 generation.

Solar-to-Hydrogen (STH) efficiency

In simple terms, STH is defined as of chemical energy produced during water splitting divided by total incident solar energy. From the definition, the system requires only energy from the solar irradiation AM1.5 G. So, there is no need for electrical power input. Therefore, STH is measured in a two-electrode configuration system.

$$STH\ (\%)\ =\ \left[\frac{|J_{SC}\ (mA.cm^{-2})| \times 1.23\ (V) \times \eta_F}{P_{tot}\ (mW.cm^{-2})}\right] \times 100 \qquad \text{eq. (2.34)}$$

where J_{SC} is the short circuit photocurrent density, P_{tot} is AM 1.5G one sun illumination (100 mW/cm^2); η_F is the Faradaic efficiency for H_2 production. The above Eqn. (2.34) is valid for $\eta_F = 100\%$ and absence of sacrificial donors or acceptors in the electrolyte.

Applied Bias Photon-to-Current Efficiency (ABPE)

Most of the single photoanode/photocathode are not capable of producing H_2 without external bias. In this context, ABPE is defined as the measure of H_2 generated under external bias

and incident light source. Therefore, ABPE is measured in a three-electrode configuration system with a working electrode (WE), a counter electrode (CE) and a reference electrode (RE).

For photoanode, the ABPE is given as

$$ABPE\ (\%) = \left[\frac{|J_{ph}\ (mA.cm^{-2})| \times (V_{o,anode} - V_{app})}{P_{tot}\ (mW.cm^{-2})}\right] \times 100 \qquad \text{eq. (2.35)}$$

For photocathode, the ABPE is given as

$$ABPE\ (\%) = \left[\frac{|J_{ph}\ (mA.cm^{-2})| \times (V_{app} - V_{o,cathode})}{P_{tot}\ (mW.cm^{-2})}\right] \times 100 \qquad \text{eq. (2.36)}$$

where $V_{o,anode} = 1.23\ V\ vs\ RHE$, $V_{o,cathode} = 0\ V\ vs\ RHE$, J_{ph} is photocurrent density measured under applied bias (V_{app}) *vs.* RHE.

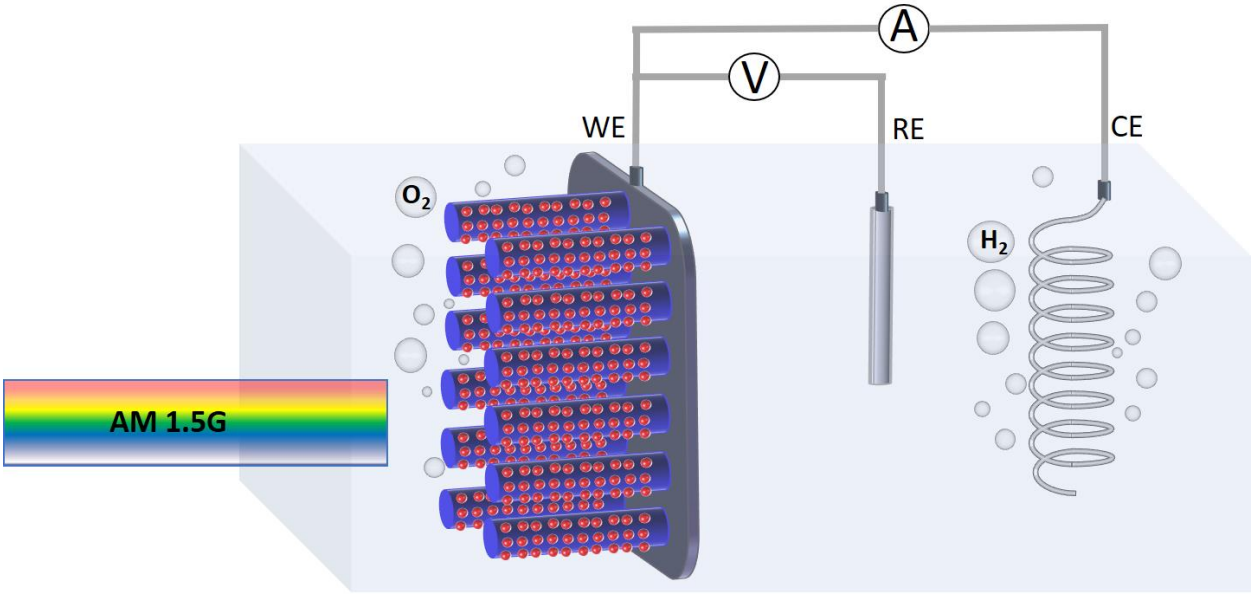

Figure 2.6. Schematic showing three-electrode configuration under AM1.5G illumination: nanowires photoanode as WE, Ag/AgCl as RE and Pt coil as CE [15].

ABPE is very important and most commonly used parameter for material characterization in the literature. As seen from Figure 2.6, the applied bias is versus RE, and this can be converted to an ideal CE by converting the measured bias to a bias *vs*. RHE or NHE using the below Eqn. (2.37)

$$E_{(RHE)} = E_{Ag/AgCl} + E^{o}_{Ag/AgCl} + 0.059 \times pH \qquad \text{eq. (2.37)}$$

where $E^{o}_{Ag/AgCl}$ is 0.197 V, and pH refers to that of the electrolyte. The ABPE *vs.* RHE values of state-of-art photoanodes and photocathodes are given in Tables 2.1 and 2.2.

Table 2.1. Summary of ABPE for state-of-art photocathodes

Materials	**Electrolyte**	**J_{sc} (mA/cm^2) at 0 V *vs.* RHE**	**ABPE (%)**	**Ref.**
TiO_2/Pt NPs/n^+np^+ Si	1M $HClO_4$	35	11.5	71
Pt NPs/TiO_2/n^+-p Si	1M $HClO_4$	35	10.8	72
Pt (2nm)/SiHJ	1M H_2SO_4	34	13.26	73
Pt/TiO_2/F:SnO_2/Ti/ n^+-p Si	KOH	35	10.9	74
Ru/TiO_2/p-InP	1M $HClO_4$	34	14	75
Pt/TiO_2/p-InP	1M $HClO_4$	30	11.6	76
Pt NPs /n^+-GaN nanowire/n^+-p Si	0.5M H_2SO_4	38	10.5	14

From Table 2.1, $ABPE > 10\,\%$ and much higher than the best photoanodes reported in Table 2.2. Chapter-4 provides more details about state-of-the-art photocathodes. As discussed earlier, OER is a sluggish reaction with high overpotentials compared to HER. Therefore, in recent times more research is focused on developing new OER catalysts and improving material quality for the photoanode.

Table 2.2. Summary of ABPE for state-of-art photoanodes

Materials	**Electrolyte**	**J_{ph} at 1.23 V *vs.* RHE**	**ABPE (%)**	**Ref.**
NiFe/SiO_x/*n*p^+-Si	1M KOH	30.7	3.3	77
NiO_x/CoO_x/SiO_x/*n*-Si	1M KOH	27.7	2.1	78
NiO_x/*n*p^+Si	1M KOH	30.9	2.1	79
CoO_x/Fe_2TiO_5-TiO_2	1M KOH	4.1	2.7	80
Ir, Co complex /$Ni(OH)_2$/Fh /TiO_x/Ta_3N_5	1M NaOH	12.1	2.5	81
IrO_2/InGaN	0.5M H_2SO_4	10.9	3.6	67

Incident Photon-to-Current Efficiency (IPCE)

IPCE is another critical parameter that is essential to find out the photo-response of the photoelectrode. It is obtained by measuring photocurrent density under monochromatic light at different wavelengths. Therefore, IPCE is the ratio of recorded photocurrent to the intensity of a calibrated monochromatic light source at different wavelengths.

$$IPCE\ (\%) = \left(\frac{\left|J_{ph}\ (mA.cm^{-2}\right| \times 1239.8\ (V \times nm)}{P_{mono}\ (mW.cm^{-2}) \times \lambda\ (nm)}\right) \times 100 \qquad \text{eq. (2.38)}$$

where P_{mono} is calibrated and monochromatic light source at wavelength (λ). The above Eqn. (2.38) represents the fraction of no. of electron-hole pairs generated per incident photon flux. Therefore, IPCE is the same as external quantum efficiency (EQE). By integrating IPCE with the standard solar spectrum AM 1.5G we can get the theoretical maximum photocurrent density for the photoelectrode. IPCE can be measured for both two and three-electrode configurations. In all the chapters, IPCE for different photoelectrodes are measured in either three- or two-electrode configurations in different electrolytes.

2.5 PEC Configurations and Efficiency Limitations

A PEC cell can be realized using a single photoelectrode either photocathode (*p*-type semiconductor) or photoanode (*n*-type) with a metal counter electrode. This configuration where a half-reaction occurs at the working electrode (either photocathode (HER) or photoanode (OER)) and other half-reaction at the counter electrode is known as S2. S2 stands for single band-gap which requires two photons (photocathode) to generate a molecule H_2. From Figure 2.7, the maximum STH efficiency is 11.2% for a band-gap of 2.26 eV.

As illustrated in *Section 1.8.2*, metal oxides (like $BiVO_4$ or α-Fe_2O_3) are ideal photoanode (S2 scheme) materials with the appropriate band-gap (2.1-2.4 eV) which can absorb the

wavelength of <560 nm of the solar spectrum (see Figure 2.8a) to achieve the high STH of ~ 12%. Unfortunately, these materials suffer from crystal defects [82], poor electrical conductivity [83, 84], short hole diffusion length [84], degradation via photo-corrosion [85] and short carrier lifetime [86]. Therefore, new materials such as III-nitrides are promising to achieve high efficiency. As shown in Table 2.2, as a first demonstration, Mi et al. [67] reported one of the highest efficiencies (ABPE) for InGaN photoanode with a band-gap of ~1.75 eV (this will be discussed in Chapter-3). Furthermore, Chowdhury et al. [87] demonstrated a high STH of 3.3% for InGaN nanosheets for PC water splitting. These demonstrations show the potential of band-gap engineered III-nitrides for developing high STH efficiency devices.

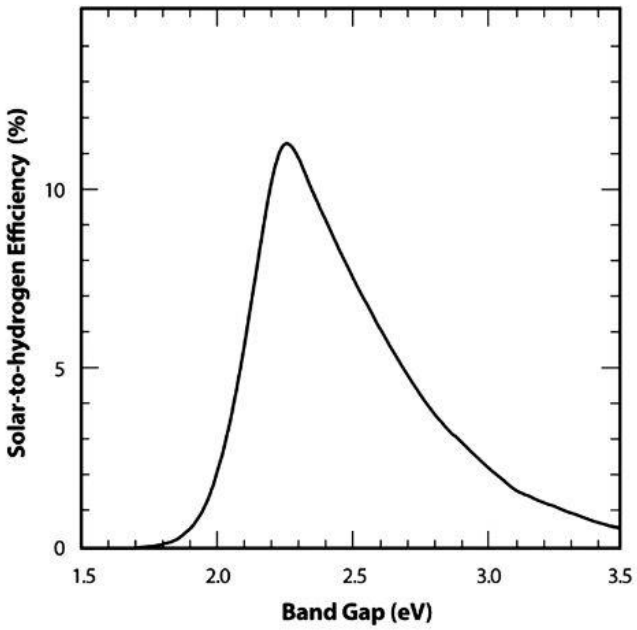

Figure 2.7. Maximum theoretical STH versus band-gap for a single photoelectrode [88].

The best materials for photocathode are Si and III-V semiconductors. These materials have favorable CBM which is much more negative than HER [89]. The STH efficiency of single band-gap photocathodes is poor due to the low photovoltage and poor reaction kinetics for two-electrode measurements. To overcome the efficiency bottleneck and reduce the cost, photovoltaic (PV) integration with a PEC system (PV + PEC) (already discussed in Section 1.4.2).

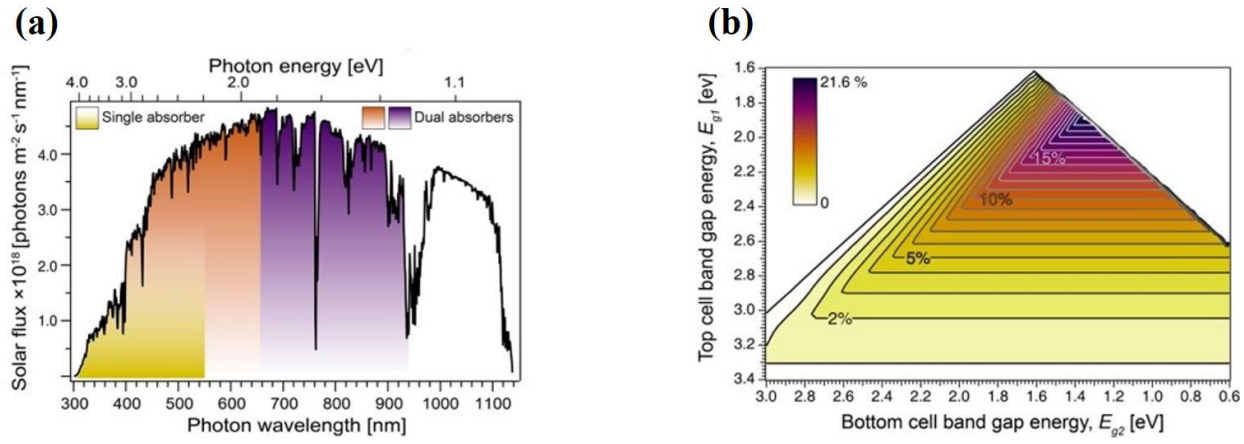

Figure 2.8. (a) Solar spectrum absorbed by a single photoelectrode (yellow shaded region) and an ideal high-efficiency tandem device (light brown-purple region). (b) Contour plot of the tandem device showing the maximum STH predicted under AM 1.5G illumination with E_{g1} as band-gap of top cell and E_{g2} as band-gap of bottom cell [38].

D4 scheme, which is analogous to *Z-scheme* of photosynthesis, is the use of two photoelectrodes which can absorb two photons each to give one molecule of H_2. This configuration is illustrated in the example shown in Figure 2.1. As shown in Figure 2.8b, a tandem device can achieve a maximum STH > 25% with $E_{g1} = 1.8\ eV$ and $E_{g2} = 1.15\ eV$. From Bolton's method [90], top photoelectrode absorbs photons with energy $hv > E_{g1}$ and transmits all photons with

energy $h\upsilon < E_{g1}$ to the bottom photoelectrode with E_{g2} without any reflection or scattering losses. The AM1.5 G incident photon flux absorption by the dual tandem device is shown in Figure 2.8a with top photoelectrode absorbing wavelengths 400-660 nm and bottom photoelectrode absorbing > 660 nm. Tandem device has advantages like low cost and simple design. For the bottom photoelectrode, the ideal candidate is Si with $E_g = 1.1\ eV$ and it is the most abundant material on the planet. There are very few candidates which can meet the top photoelectrode band-gap requirement. III-V semiconductors are promising candidates for this criterion. Fan et al. [23, 91] demonstrated MBE growth of high crystalline InGaN alloy with 50% In composition on Si substrate to achieve a $E_g = 1.75\ eV$ for high efficiency PEC devices tested in 1M HBr. Therefore, metal nitrides along with appropriate co-catalysts are promising materials to be explored for high efficiency PEC tandem devices.

Apart from material limitations on STH, several other experimental factors lead to parasitic losses in efficiency. The electrolyte itself acts as a spectral filter which can lead to a reduced number of photons (especially loss of IR photons) reaching the photoelectrode surface [92]. The catalysts on the surface of photoelectrode also absorb light which reduces the photocurrent. This problem can be mitigated by controlling the size of the catalyst by using NPs. The charge transfer from semiconductor to electrolyte from SCLJ gives rise to shunt resistances, effectively decreasing the efficiencies [93]. The high photocurrent required for high STH produces a huge amount of gas bubbles from the surface of the photoelectrode. The gas bubbles sticking on the photoelectrode leads to scattering and reduction in photon flux [94]. This bubbling effect can be partially reduced by either using a stirrer in the PEC chamber or a surfactant [95]. All these issues can be avoided by adequately designing the PEC experiments by optimizing electrode preparation, PEC reaction chamber, and co-catalyst synthesis.

2.6 Stability of Photoelectrode

A fundamental requirement for large-scale commercialization of PEC water splitting is the device durability against harsh electrolytes (with different pH) and under both dark and different illumination intensities. Most of the high-efficiency semiconductors for PEC like Si [96, 97], III-V [98] are easily prone to corrosion in the electrolyte. Si is readily oxidized to SiO_2 in aqueous solution (see Eqn. (2.39)) to form a passivation layer on Si surface which leads to a reduction in the stability [99].

$$Si + 2OH^- + 4H_2O \rightarrow Si(OH)_2^{2+} + 2H_2 + 4OH^- \quad \text{eq. (2.39)}$$

III-V compounds, like GaAs, also go through corrosion reaction (see Eqn. (2.40) due to either accumulation of a large amount of surface hole concentration in the dark or by light illumination which generates holes at the surface [100].

$$GaAs + 6h^+ + H_2O + aq \rightarrow Ga_{aq}^{3+} + 2AsO_2^- + 4H^+ \quad \text{eq. (2.40)}$$

Baker et al. reported that Ga terminated GaN has a photo-corrosion potential of $-0.66 \pm 0.07\ V\ vs.\ RHE$ in 0.5M H_2SO_4 ($pH = 1$) and under illumination GaN undergoes oxidation reaction shown in Eqn. (2.41) [101].

$$2GaN + 6h^+ \rightarrow 2Ga^{3+} + N_2 \quad \text{eq. (2.41)}$$

The major thermodynamic requirements for photoanode and photocathode to be stable are the: $\phi_{corr}^h < E_{anodic}$ (1.23 V *vs.* RHE) and $\phi_{corr}^e > E_{cathodic}$ (0 V *vs.* RHE), respectively; where ϕ_{corr}^e is energy level for cathodic corrosion reaction of semiconductor; ϕ_{corr}^h is energy level for anodic corrosion reaction of semiconductor. Figure 2.9 shows the cathodic corrosion potential (black) and anodic corrosion potential of all the semiconductor photoelectrodes. It can be concluded that almost all the high efficiency photocatalysts do not meet the thermodynamic requirements. Therefore, extra protection layers are required for these materials. Detailed

degradation mechanisms for some of the high efficiency photoelectrodes are discussed in Chapter-5.

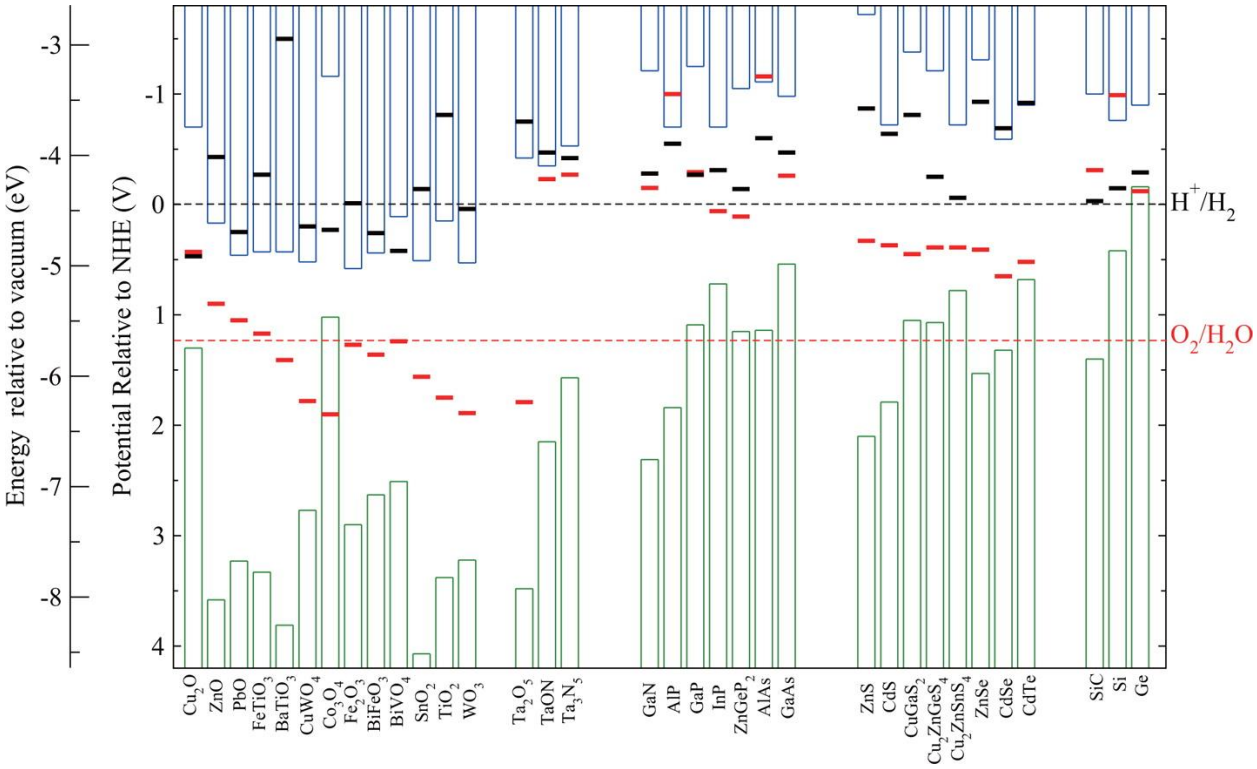

Figure. 2.9. Calculated oxidation potential (red bars) and reduction potential (black bars) relative to the NHE and vacuum level for a series of semiconductors in solution at pH = 0 [102].

In Chapters-4 and 5, we will see the advantages and comparisons of using GaN NW as a protection layer for Si photocathode over the state-of-art protection layers like TiO_2, MoS_2, etc. and report high stability > 100 h with a high ABPE ~ 12%. Also, in Chapter-6 we will discuss different catalysts and protection schemes for Si photoanodes and compare the results to our high efficiency (ABPE ~ 14%) $MoSe_2$ protected Si photoanode.

2.7 Conclusions

In this chapter, we discussed a brief history and the fundamentals of PEC water splitting. In *Sections 2.2 and 2.3*, the thermodynamic and kinetic factors affecting light absorption, charge separation and charge transfer from SCLJ to catalytically active sites, taking photoanode (*n*-type) as an example, have been derived and explained. Then, in *Section 2.4*, we discussed different metrics for PEC to benchmark different state-of-art photoelectrode materials. Lastly, in *Sections 2.5 and 2.6*, different PEC configurations and their efficiency limitations, and the importance of improving the stability of photoelectrodes have been discussed.

Chapter-3: Solar Water Oxidation by InGaN Nanowire Photoanode with a Bandgap of 1.7 eV

As discussed in *Section 1.7.2* and *Section 2.5*, OER is the rate determining step in the water splitting experiments and henceforth, much of the research is focused on addressing the issues related to OER reactions kinetics and mass transport. In *Section 2.3.2*, we described that IrO_2, one of the best co-catalysts for OER, can significantly reduce the overpotential and improve reaction kinetics. To achieve a high efficiency tandem photoelectrode (see *Section 2.5*), it is essential to develop a top light absorber with a bandgap ~ 1.75 eV. In this chapter*, we will discuss the implementation of InGaN nanowires, with energy bandgap of ~ 1.7 eV, for solar water oxidation under one-sun illumination. By coupling high crystalline MBE grown InGaN nanowires with IrO_2 co-catalyst, we achieved higher efficiency compared to other published reports under oxidation conditions.

---

* This chapter is from a published article: S. Cheng[1], **S. Vanka[1]**, Y. Wang, J. Gim, Y.J. Wang, Y.-Ho Ra, R. Hovden, H. Guo, I. Shih and Z. Mi, *ACS Energy Lett.*, 2018, 3, 307–314. [1]Authors contributed equally to this work.

3.1 Introduction

The availability of solar energy far exceeds global energy demands, but to date only provides a small fraction in the world energy market. A major hurdle to the widespread use of solar energy is the variability due to its intermittent and fluctuating nature, which requires a cost-effective energy storage for on-demand usage [103]. Photoelectrochemical (PEC) water splitting, which combines photovoltaics and electrolysis into a simple and fully integrated unit, is a promising approach to directly store solar energy in the form of energy-rich hydrogen fuel in a scalable and low-cost manner [104-106]. Among the proposed PEC cell configurations, the tandem device consisting of a *p*-type photocathode and an *n*-type photoanode with complementary bandgap absorption is advantageous for encompassing a substantial part of the solar spectrum while providing sufficient photovoltage to drive unassisted water splitting [38, 69, 107, 108]. In the PEC tandem cell, the maximum operating current density is the intersection of the overlapped current–potential curves of photocathode and photoanode. Compared to proton reduction on the photocathode, the water oxidation on the photoanode is more kinetically challenging due to the complicated four-electron transfer process. To date, the performance of PEC tandem devices has been largely limited by inefficient photoanodes, which are unable to offer high photocurrent density at low bias potential – for example, below 0.6 V versus reversible hydrogen electrode (RHE) to pair with high-performance photocathodes (e.g. Si) [109-112]. Si [113-115] (E_g ~1.1 eV), Fe_2O_3 [116, 117] (E_g ~2.0 eV) and Ta_3N_5 [118-120] (E_g ~2.1 eV)

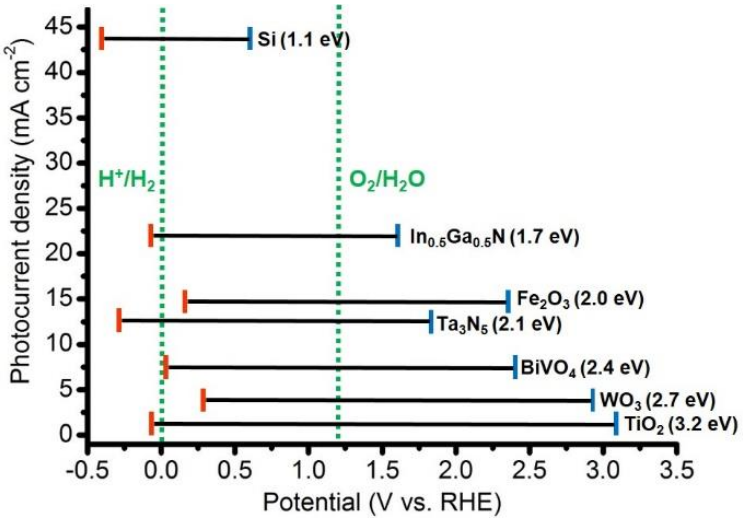

Figure 3.1. The maximum theoretical photocurrent densities of different photoanode materials under AM 1.5G 1-sun illumination. The conduction band (red bar) and valance band (blue bar) positions associated with the water redox potentials are also shown (pH = 0).

photoanodes promise high theoretical photocurrent densities (Figure 3.1), but their applications in PEC tandem cell have been largely limited by undesired high onset potentials, which were reported typically in the range of 0.9-1.1 V, 0.8-1.0 V and 0.6-0.8 V versus RHE, respectively. To date, $BiVO_4$ is the favorable photoanode material for PEC tandem cell due to its relatively high performance with negative onset potentials (0.2-0.3 V versus RHE) [121-126]. $BiVO_4$, however, is not ideal as the top light absorber in PEC tandem cell due to its wide bandgap of 2.4 eV that limits the efficient utilization of solar spectrum. Recent theoretical modeling studies, by considering current matching conditions and kinetic overpotentials for water splitting, have shown that the optimal top and bottom light absorbers in a tandem cell are with bandgaps of 1.6-1.8 eV and 0.9-1.2 eV, respectively, which can yield a potential solar-to-hydrogen efficiency over 25% [127-132]. Therefore,

it is highly desirable to develop photoanode material with a lower bandgap and high performance working at low applied potentials.

InGaN, a widely used semiconductor for solid-state lighting and power electronics, is a promising material as the top light absorber because of its tunable bandgap from 3.4 to 0.65 eV by increasing the indium content, as well as high absorption coefficient and large charge carrier mobility [11,133-135]. The conduction and valence band edges of InGaN straddle the water redox potentials for an indium composition up to ~50%, corresponding to an energy bandgap of ~1.7 eV with a theoretical photocurrent density of 22 mA cm^{-2} (Figure 3.1) [23, 136]. To date, however, previously reported InGaN photoanodes generally exhibit very poor performance for water oxidation (typically sub-mA cm^{-2} at 1.23 V versus RHE under simulated 1-sun illumination) [137, 138], which is largely limited by the inefficient light absorption due to low indium concentration, the presence of extensive recombination centers, and poor surface reaction kinetics for water oxidation. In the present study, we demonstrate highly efficient water oxidation using an In-rich InGaN nanowire photoanode with a bandgap of 1.7 eV. With the incorporation of an oxygen evolution co-catalyst, the InGaN nanowire photoanode produces a low onset potential of 0.1 V versus RHE and a high photocurrent density of 5.2 mA cm^{-2} at a potential as low as 0.6 V versus RHE. Moreover, a benchmarking half-cell solar energy conversion efficiency of 3.6% is achieved, which is the highest among single-photon photoanodes reported to date. In addition, using H_2O_2 or Na_2SO_3 as hole scavengers, the photocurrent density of InGaN nanowire photoanode reaches over 21 mA cm^{-2} at 1.23 V versus RHE, which approaches the theoretical limit for a 1.7 eV InGaN absorber.

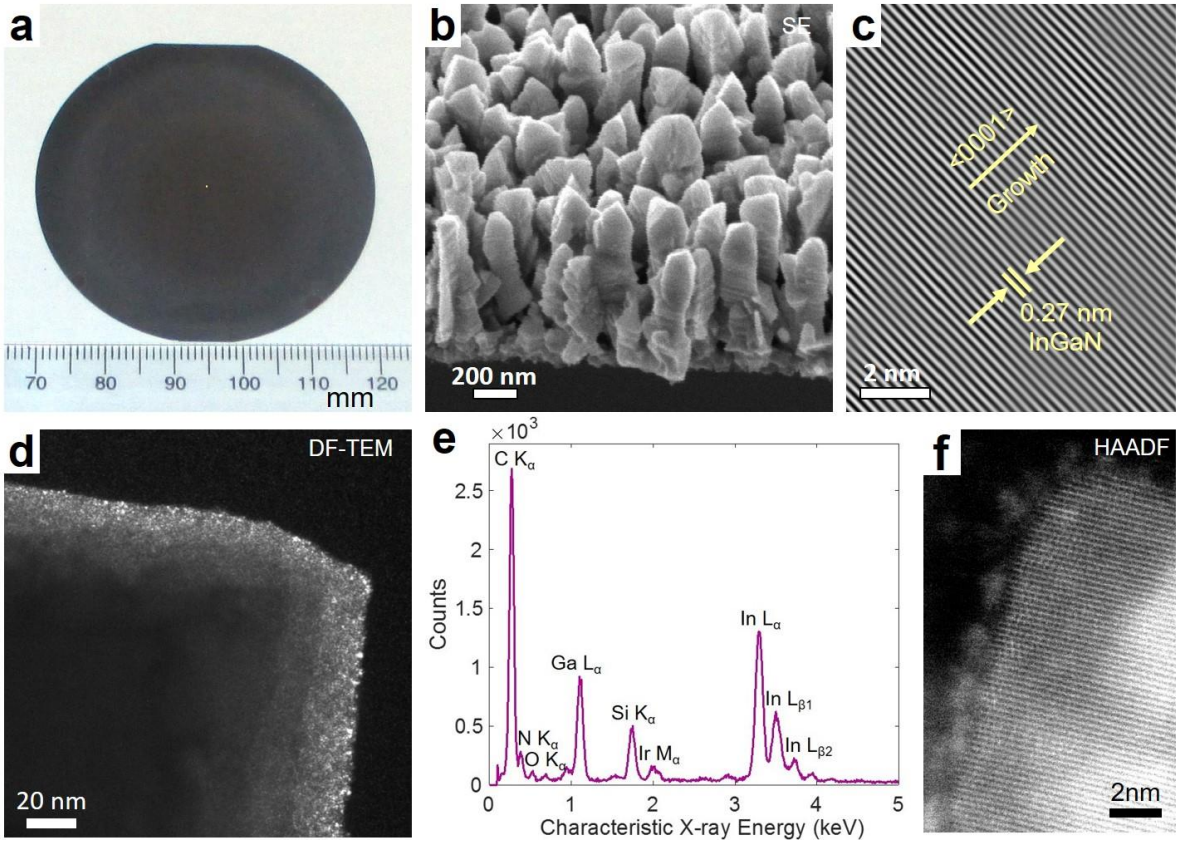

Figure 3.2. (a) Photograph, (b) 45°-tilted SEM, and (c) HRTEM images of InGaN nanowire sample. (d) Dark-field TEM image, (e) EDX and (f) HAADF-STEM image of IrO_2/InGaN sample.

3.2 Results and Discussions

InGaN nanowire arrays were grown on a large area Si substrate (Figure 3.2a, 2-inch wafer, diameter ~5 cm) by plasma-assisted molecular beam epitaxy (MBE) (see the Supporting Information). The cross-sectional electron microscopy of InGaN/Si reveals that the InGaN nanowires are vertically aligned to the Si substrate with an approximate diameter of ~200 nm (±40 nm) and height of ~700 nm (±50 nm)—shown by scanning electron microscopy (SEM) in Figure

2b and scanning transmission electron microscopy (STEM) in Appendix-1.1. The crystalline nanowires extend atop a polycrystalline growth layer of ~650 nm (±50 nm) where early growth of nanowires may have competed and coalesced. High-resolution transmission electron microscopy (HRTEM) image (Figure 3.2c) indicates uniform crystallinity near the termination of the nanowires where catalytic activity is expected to be highest. A lattice spacing of 0.27 nm uniquely corresponds to the (002) lattice plane of InGaN with the orientation that indicates preferred growth along <0001> direction (c-axis) (Figure 3.2c, Appendix-1.2). The <0001> orientation of InGaN nanowires is also confirmed by the presence of a predominant (002) diffraction peak in the X-ray diffraction (XRD) measurement (Appendix-1.3). The electron-diffraction pattern from the growth surface is consistent with the single-crystal observation of terminal nanowire segments (Appendix-1.3). Room temperature photoluminescence (PL) measurement shows a single optical emission peak at 720 nm (Appendix-1.4), corresponding to a bandgap of ~1.7 eV and indium composition of ~50% [23, 135]. The coexistence of Ga, N, and In was confirmed from electron energy-loss spectroscopy (EELS) taken on a cross-sectional InGaN nanowire (Appendix-1.5). The low substrate temperature (530 ^{o}C) and optimal N_2 flow rate (~0.5 sccm) used in the InGaN growth, together with the nanowire geometry allows for effective strain relaxation and reduces phase separation (for further details see *Section 1.5.2*) [91, 139, 140].

An IrO_2 co-catalyst, which is known as a highly active oxygen evolution catalyst with a low overpotential over a wide pH range [141], was loaded on InGaN nanowires by a simple photodeposition process (see the Appendix-1). As revealed by dark-field TEM (DF-TEM) (Figure 3.2d) and SEM (Appendix-1.6, Appendix-1.7a), IrO_2 nanoparticles are uniformly loaded on the InGaN nanowire surface. The atomic concentration of Ir compared to InGaN nanowire is only a few percent—estimated to be ~2% from EDX analysis (Figure 3.2e). Bright-field scanning-TEM

(BF-STEM) and high-angle annular dark field (HAADF-STEM) show IrO_2 nanoparticles with a size of 1-2 nm and density consistent with the heavier atomic weight of IrO_2 (Figure 3.2f, Appendix-1.7b-f). While some larger IrO_2 nanoparticles present partially crystallinity (Appendix-1.7b, Appendix-1.7d, *red arrows*), smaller particles often appear amorphous (Appendix-1.7b-f, *yellow arrows*). The X-ray photoemission spectroscopy (XPS) analysis indicates Ir^{4+} and is the expected valence for IrO_2 (Appendix-1.8). PEC performance of InGaN nanowire photoanode was investigated in 0.5 M H_2SO_4 under air mass 1.5 global (AM 1.5G) simulated 1-sun illumination in a conventional three-electrode cell (Figure 3.3a). Figure 3.3b shows the current-potential (J-V) curves of InGaN sample with and without IrO_2 deposition. In the dark, the electrodes show negligible current. Under AM 1.5G simulated 1-sun illumination, compared to the bare InGaN, IrO_2 modification produces ~500 mV cathodic shift in the onset potential and a large increase in the photocurrent, indicating enhanced charge separation and water oxidation reaction after IrO_2 loading. The substantially lower photocurrent density and larger overpotential of bare InGaN photoanode are ascribed mainly to the poor kinetics for water oxidation that leads to higher charge carrier recombination at the surface, which requires larger bias to achieve appreciable charge transfer across the semiconductor−electrolyte interface for the oxygen evolution reaction. In addition, the excessive accumulation of holes at the surface with bare InGaN may cause the self-oxidation of InGaN absorber, which is detrimental to the photoelectrode stability. The modification of InGaN with IrO_2 water oxidation co-catalyst enhances the reaction kinetic with reduced hole accumulation at the surface, which improves both the activity and photostability of the photoelectrode.

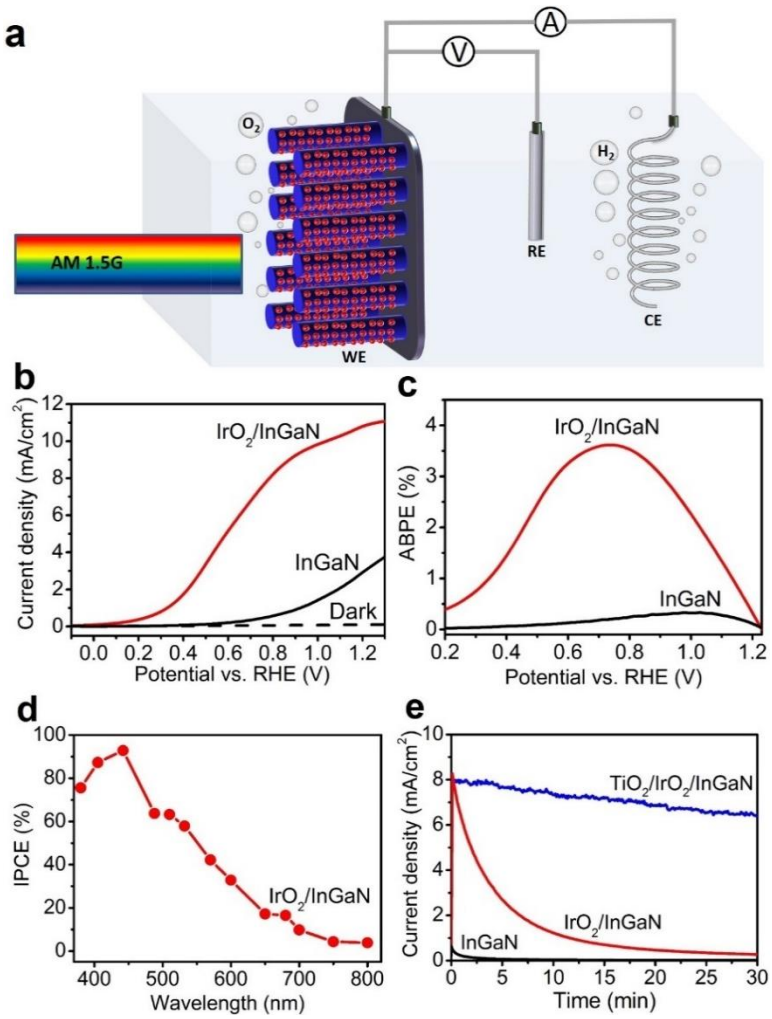

Figure 3.3. PEC water oxidation performance. (a) Schematic illustration of the three-electrode cell for PEC measurements. InGaN nanowire photoanode, Pt wire and Ag/AgCl were employed as working electrode (WE), counter electrode (CE) and reference electrode (RE), respectively. (b) J-V curves of InGaN and IrO_2/InGaN photoanodes in 0.5 M H_2SO_4 under AM 1.5G simulated 1-sun illumination. (c) ABPE of the photoanodes derived from the J-V curves. (d) IPCE of IrO_2/InGaN photoanode at 1.23 V versus RHE. (e) J-t curves of InGaN, IrO_2/InGaN and TiO_2/IrO_2/InGaN photoanodes in 0.5 M H_2SO_4 at 0.8 V versus RHE under AM 1.5G simulated 1-sun illumination.

A similar loading effect of IrO_2 co-catalyst was also observed for other photoanode materials [142-145]. The IrO_2/InGaN sample provides an onset potential of 0.1 V versus RHE (measured at 0.2 mA cm^{-2}), which is remarkable considering the small bandgap of InGaN (1.7 eV). The impressively low onset potential is largely attributed to the favorable conduction band position of InGaN that locates slightly above the water reduction potential, as determined by Mott−Schottky measurements (Appendix-1.9). Considering the bandgap energy of 1.7 eV, the valance band edge position of InGaN is estimated to be lower than the water oxidation potential (1.23 V versus RHE) by about 0.4 V. The conduction and valence band edges of InGaN that straddle the water redox potentials for an indium composition of ~50% is consistent with previous theoretical calculation [136].

In addition to the low onset potential, the photocurrent density of IrO_2/InGaN sample reaches 10.9 mA cm^{-2} at 1.23 V versus RHE, a 3.4-fold improvement compared to bare InGaN photoanode (Figure 3.3b). The maximum applied bias photon-to-current efficiency (ABPE) of IrO_2/InGaN photoanode calculated from the J-V curve is 3.6% (Figure 3.3c), which is the highest among those of previously reported photoanodes including 2.2-2.3% for $BiVO_4$-based materials [146-148], 2.5% for Ir, Co complex/$Ni(OH)_2$/Fh/TiOx/Ta_3N_5 [149], 2.7% for CoO_x/Fe_2TiO_5-TiO_2 [150] and 3.3% for NiFe/SiO_x/np^+-Si [151] (Appendix-1.21). Moreover, the PEC performance in the InGaN photoanode prepared here is much improved in comparison to the previously reported InGaN photoanodes [137, 138], and the underlying mechanisms are described. The main processes that affect the PEC performance are light absorption, charge carrier transfer, and surface redox reaction. (i) The small energy bandgap of 1.7 eV for the InGaN in this work results in much enhanced light absorption towards longer wavelength and thus higher achievable photocurrent density; (ii) The presented nanowires were grown by MBE using a self-catalytic growth process [152], *i.e.* without the

incorporation foreign metal catalysts, which together with the relatively low growth temperature, ultrahigh vacuum, and precisely controlled molecular beam flux allows for the synthesis of In-rich InGaN nanowires with drastically reduced defect densities and impurity incorporation [153], compared to the conventional chemical vapor deposition (CVD) growth processes [137, 138], thereby leading to significantly reduced charge recombination. The superior crystallinity of InGaN nanowires grown by MBE is further evidenced by the demonstration of high efficiency nanowire light emitting diodes and laser diodes [153-155]. (iii) During the MBE growth, the use of Ga seeding layer to initiate the nanowire nucleation, together with a N-rich growth condition, leads to the formation of InGaN nanowires with N-terminated surface, not only for their top faces but also for their side faces, which is different from the Ga-terminated top surface grown by CVD [26]. The N-terminated surfaces can help protect against photocorrosion, and provide polarization effect for efficient transport of photogenerated charge carriers. (iv) The surface reaction kinetics were further improved by coupling with efficient water oxidation co-catalyst (*i.e.* IrO_2 in this work), while no co-catalyst was applied in the previous reports [137, 138]. It is worth noting that although we have previously reported efficient two-electron Br^- oxidation with bare InGaN [11, 23, 91], the application of InGaN on more thermodynamically and kinetically challenging four-electron water oxidation has not been achieved prior to this work. This indicates the critical role of modification with efficient water oxidation catalyst to improve the surface kinetics.

Significantly, the photocurrent density produced by the IrO_2/InGaN photoanode in the low bias region is particularly outstanding. For example, a photocurrent density of 5.2 mA cm^{-2} is achieved at 0.6 V versus RHE, which is the highest among any single-photon photoanodes reported to date at such a low potential (Appendix-1.21). This characteristic promises a high operating point (zero bias) when paired with a high-performance photocathode for PEC tandem system (Appendix-

1.10). The 1.7 eV bandgap InGaN nanowire presented here is highly suited for the top light absorber of the PEC tandem device [127-132]. Compared to other reported photoanodes with bandgaps in the range of 1.6-1.8 eV, InGaN nanowire photoanode shows an efficiency at least one or two orders of magnitude higher and stands out as the best top absorber reported to date (Appendix-1.22). It is worth noting that the loading amount of IrO_2 plays a significant role on the photoanode performance. An optimum content of 2 at% IrO_2 on InGaN was found for the maximum activity of the photocurrent (Appendix-1.11). As shown by the SEM images in Appendix-1.12 in the Supporting Information, a lower loading amount produces less reactive sites for water oxidation, while excessive loading forms aggregated clusters, which may shield light absorption and act as recombination centers [156].

Figure 3.3d shows the wavelength dependence of the incident photon-to-current conversion efficiency (IPCE) for the IrO_2/InGaN photoanode at 1.23 V versus RHE. A maximum IPCE of 93% is achieved at 440 nm, and then gradually decreases to 63% at 500 nm, 33% at 600 nm and 10% at 700 nm. By integrating the IPCE spectrum with the standard solar spectrum of AM 1.5G, a photocurrent density of 10.3 mA cm^{-2} was obtained (Appendix-1.13), which is close to the measured value in Figure 3.3b. The photocurrent response of IrO_2/InGaN agrees well with the absorption edge of InGaN, indicating the photocurrent is originated from the bandgap transition of InGaN. This is further supported by control experiment showing that negligible photocurrent is produced by the IrO_2/Si photoanode in the absence of InGaN nanowires (Appendix-1.14).

The stability of photoanodes for water oxidation was evaluated by chronoamperometry (J-t) under continuous illumination at 0.8 V versus RHE (Figure 3.3e). For the bare InGaN, the photocurrent decayed rapidly to nil within 5 min. After modification of InGaN with IrO_2 co-catalyst, the stability was improved to some extent but obvious photocurrent decay was still

observed with the photocurrent decreased to a negligible level after 30 min. In contrast, significant improvement was achieved by coating the IrO_2/InGaN photoanode with 18 atomic layer deposition (ALD) cycles (total thickness ~1 nm) of TiO_2 (see the Appendix-1). ALD is a known technique for conformal coating with precise control over thickness [157-159]. XPS analysis confirmed the signal of Ti^{4+} from ALD TiO_2 (Appendix-1.15). The binding energy of 464.0 eV and 458.2 eV correspond to Ti $2p_{1/2}$ and Ti $2p_{3/2}$ orbitals of Ti^{4+} from TiO_2, respectively, consistent with previous reports.[160,161] A prolonged stability test of TiO_2/IrO_2/InGaN was also examined, showing that the photoanode remained active after 4 h continuous illumination (Appendix-1.16). The Faradaic efficiencies of H_2 and O_2 were measured to be about 96% and 88%, respectively (Appendix-1.17). It is seen that the TiO_2 protection layer plays a vital role in improving the PEC stability by preventing the underlying InGaN from direct contact with the electrolyte, while not compromising charge carrier transport or mass transport of reactant and product species related to the oxygen evolution reaction. Increasing the TiO_2 overlayer thickness beyond 2 nm resulted in diminished photocurrent (Appendix-1.18), which can be ascribed to the limited mass transport or large tunneling resistance to charge transport associated with thick TiO_2 layer [161, 163]. The holes can be transported by tunneling mechanism through the ultrathin TiO_2 layer to the electrolyte, while large resistance occurs on layers thicker than a few nm. In addition, we note that the loss of IrO_2 nanoparticles during the PEC operation was largely suppressed by adding the TiO_2 overlayer, evidenced by XPS analysis (Appendix-1.23). Therefore, TiO_2 overlayer may also serve as a "glue" to stabilize the IrO_2 nanoparticles adhered on InGaN nanowire surface to keep the high activity for water oxidation reaction. Despite the stability of InGaN photoanode is much improved with the protection of TiO_2 layer, the device performance does decrease during the test. SEM and TEM images of TiO_2/IrO_2/InGaN after the PEC stability test were examined, as shown in Figure 4. It

revealed some parts of the InGaN nanowire were photocorroded (morphology changes occur during stability testing under illumination) and etched away during the long-term stability testing, possibility caused by the oxidation of the electrode (via oxidation of N^{3-}) and eventual dissolution of InGaN [164, 165]. It is likely that the ultrathin 1 nm TiO_2 coating contains some pinholes that electrolyte can penetrate through to oxidize the underlying InGaN. This is in line with a recent study showing that a thick TiO_2 protection layer of at least 40 nm is required to acheive pinhole-free films [166]. Indeed, literature reports show that relatively thick layers (at least 40 nm) were applied for the protection of group III-V photoanodes to achieve long-term stability (in the range of hours to days, see Appendix-1.24), in which the holes are transported via electrically defective TiO_2 or band edge of p-type hole conducting materials [167-170]. However, compared to other III-V photoanodes, the InGaN presented here features an extremely low onset potential of 0.1 V versus RHE, which is advantageous to pair with a photocathode for unassisted solar water splitting. Ongoing work is to investigate the protection of InGaN with optimally designed TiO_2 layers (together with oxygen evolution catalysts) to achieve simultaneously high activity and stability for water oxidation.

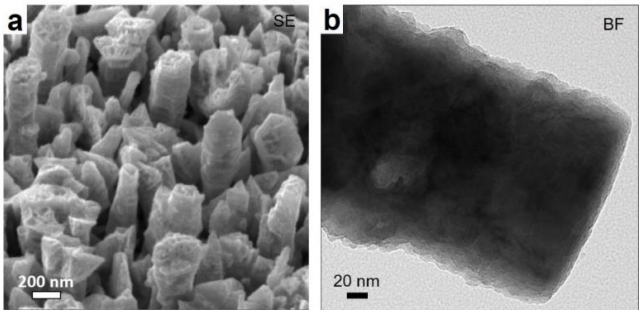

Figure 3.4. (a) 45°-tilted SEM and (b) TEM images of TiO_2/IrO_2/InGaN photoanode after PEC stability test for 4 h.

The maximum attainable photocurrent density for the InGaN with a 1.7 eV bandgap is ~22 mA/cm^2 under AM 1.5G solar irradiation. At 1.23 V versus RHE, our sample reaches half of this maximum. In order to gain more information about the photocurrent loss and rate-limiting factor, PEC performance of InGaN photoanode was also studied in the presence of H_2O_2 hole scavenger. As shown in Figure 3.5a, the photocurrent density of InGaN photoanode for H_2O_2 oxidation reaches as high as 21.2 mA/cm^2 at 1.23 V versus RHE, which exceeds 96% of the theoretical maximum for a 1.7 eV InGaN absorber. The attained near-theoretical photocurrent indicates the apparent quantum yield is nearly ideal over the wide wavelength range up to ~720 nm. This can be attributed to the enhanced light trapping due to the anti-reflection effects of nanowire geometry [171, 172], efficient charge carrier transport within low dimensional nanowires, improved charge separation efficiency due to the short radial diffusion distance in nanowire geometry for the minority carriers (holes) toward the electrolyte solution, and extremely fast surface reaction rate for H_2O_2 oxidation owing to its rapid oxidation kinetics (2-electron transfer) and favorable oxidation potential (+0.68 V versus RHE for the O_2/H_2O_2 couple, inset of Figure 5a) [173-174]. Notably, the photocurrent density of InGaN photoanode reached 20.4 mA/cm^2 at 0.6 V versus RHE, which is the highest for any photoanodes reported to date at such a low potential to our knowledge. The lower photocurrent for water oxidation compared to that for H_2O_2 oxidation is mainly ascribed to the sluggish surface reaction kinetics. The catalytic efficiency for water oxidation was calculated to be only ~50% at 1.23 V versus RHE and even lower at low bias region (Appendix-1.19). Moreover, the J-t test showed the InGaN photoanode exhibited excellent stability during 10 h operation in the presence of H_2O_2 (Figure 3.5b). In addition to H_2O_2, a high photocurrent density of 21.2 mA/cm^2 at 1.23 V versus RHE and excellent stability were also observed using Na_2SO_3 as a hole scavenger (Appendix-1.20). The studies in the presence of hole

scavengers imply the possibility of developing highly efficient and stable water oxidation system based on InGaN nanowires if coupled with suitable water oxidation co-catalyst with fast reaction kinetics. In addition, it is noted that the presence of phase separation may exist in highly disordered regions of the InGaN wafer, offering opportunities to further optimize the growth conditions. Further improvement of the quality of the nanowire wafer is expected to enhance the performance (e.g. photovoltage) for solar water oxidation.

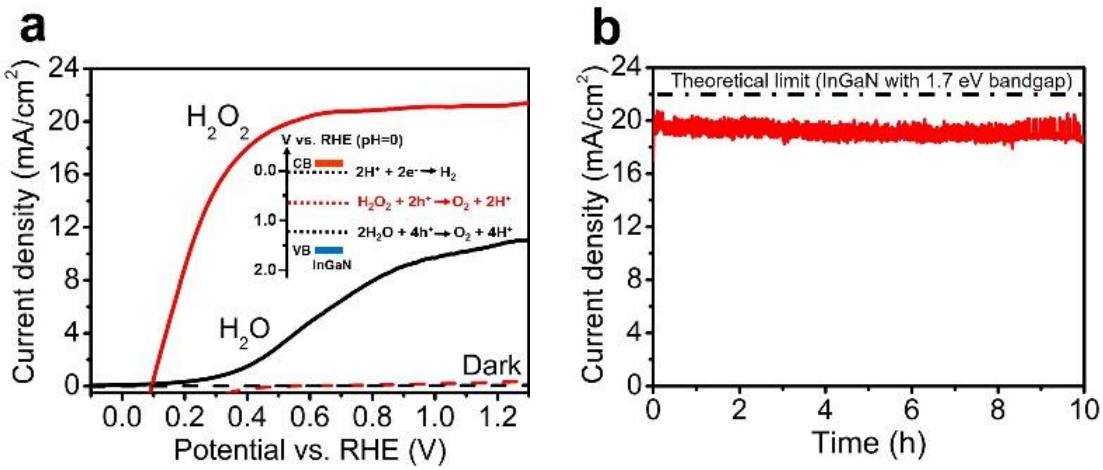

Figure 3.5. PEC performance in the presence of H_2O_2 hole scavenger. a) J-V curves of TiO_2/IrO_2/InGaN photoanode under AM 1.5G simulated 1-sun illumination in 0.5 M H_2SO_4 containing 0.5 M H_2O_2 hole scavenger. The data in 0.5 M H_2SO_4 without any scavengers is also shown for comparison. The inset illustrates the potentials of H_2O, and H_2O_2 oxidation, indicating H_2O_2 oxidation are more feasible from the view of both thermodynamic and kinetic. b) J-t curve of TiO_2/IrO_2/InGaN photoanode at 0.8 V versus RHE under AM 1.5G simulated 1-sun illumination in 0.5 M H_2SO_4 containing 0.5 M H_2O_2 hole scavenger. The fluctuation of photocurrent density was ascribed to the formation of O_2 bubbles on the photoanode surface.

3.3 Conclusions

In summary, we have demonstrated efficient solar water oxidation by InGaN nanowire photoanode with a bandgap of 1.7 eV. Owing to the low dimensional nanowire structure, appropriate band edge positions to straddle the redox potentials of water splitting, together with the effective coupling with an efficient water oxidation co-catalyst (*i.e.*, IrO_2), the InGaN photoanode produced a low onset potential of 0.1 V versus RHE and a record half-cell solar energy conversion efficiency of 3.6%. The InGaN nanowire can be leveraged with new high performing water oxidation co-catalysts as they become available, improving the performance towards the theoretical maximum for a 1.7 eV light absorber.

Chapter-4: High Efficiency Si Photocathode Protected by Multi-Functional GaN Nanostructures

In the previous chapter, we investigated the design and PEC performance of In-rich InGaN using IrO_2 co-catalyst photoanode for water splitting. These results showed the potential of III-nitrides for achieving favorable bandgap of ~1.7 eV for PEC water splitting, which can serve as a nearly ideal top light absorber in a tandem photoelectrode requirements. As discussed in *Section 1.7.3*, stability is an important requirement for large-scale PEC water splitting. Furthermore, we discussed in *Section 2.6* that to date all the reported high efficiency photoelectrodes require extra protection layers to achieve reasonable stability. In this chapter*, we investigated the use of GaN nanowires as a protection layer on Si photocathodes for PEC water splitting. We have shown that GaN nanowires help in charge carrier extraction and light absorption for Si photocathode. A high stability of > 100 h with high photocurrent density was achieved for Si photocathode with GaN protection under AM 1.5G one sun illumination.

---

* This chapter is from a published article: **S**. **Vanka**; E. Arca; S. Cheng; K. Sun; G. A. Botton; G. Teeter; Z. Mi, "High Efficiency Si Photocathode Protected by Multifunctional GaN Nanostructures", *Nano Lett.* **2018,** 18, (10), 6530-6537.

4.1 Introduction

Hydrogen (H_2) from solar water splitting is an excellent clean fuel which may potentially address the ever-increasing energy demand [2,69,88,159]. Photoelectrochemical (PEC) water splitting, which is clean, sustainable, and potentially economical [69, 88, 175], has emerged as one of the most promising methods to produce solar H_2 [88]. A key component of a PEC system is an efficient and stable photocathode [159, 104]. The semiconductor photocathode should ideally possess a conduction band minimum (CBM) that is more negative than that of the proton reduction potential [7, 176] and be stable against corrosion in the electrolyte [159]. Si has a favorable CBM [7] and absorbs a substantial portion of sunlight [177, 178] (energy bandgap ~1.1 eV), which renders it an excellent material for PEC H_2 generation. Other materials that meet the thermodynamic requirements for a photocathode include III-V semiconductors, such as GaAs, GaP, InP, and their alloys [43b,c, 179, 180-182]. Although high efficiency semiconductor photocathodes, including Si [73, 74], GaInP [43b, 180], and InP [75, 76] have been reported, they generally suffer from poor stability in aqueous solution [183]. In this regard, significant attention has been devoted to developing various surface protection schemes, e.g., the use of protection layers such as TiO_2 [71, 72, 74, 184, 185] , Ti [186-189], Al_2O_3 [183, 190, 191], $SrTiO_3$ [187] and $MoSe_2$ [192] to enhance the stability of semiconductor photoelectrodes. The use of extra protection layers, however, often compromises the charge carrier transport and limits the maximum achievable efficiency [69, 159, 193]. Consequently, long-term stability is only measured/achieved at efficiency levels far below those without surface protection [98, 184, 191, 192, 194]. Illustrated in Figure 4.1 is a summary, including the stability and maximum current density for some previously reported semiconductor photocathodes with applied-bias-photon-to-current efficiency (ABPE) >8%. While a Si photocathode can, in principle, deliver photocurrent density over 40 mA/cm^2 under AM1.5G one-sun illumination, there has been no demonstration of stability longer than 10

h when operated above 30 mA/cm^2. Long-term stability (up to ~60 days [96]) has been reported for semiconductor photoelectrodes but with significantly reduced ABPE [180, 185, 195].

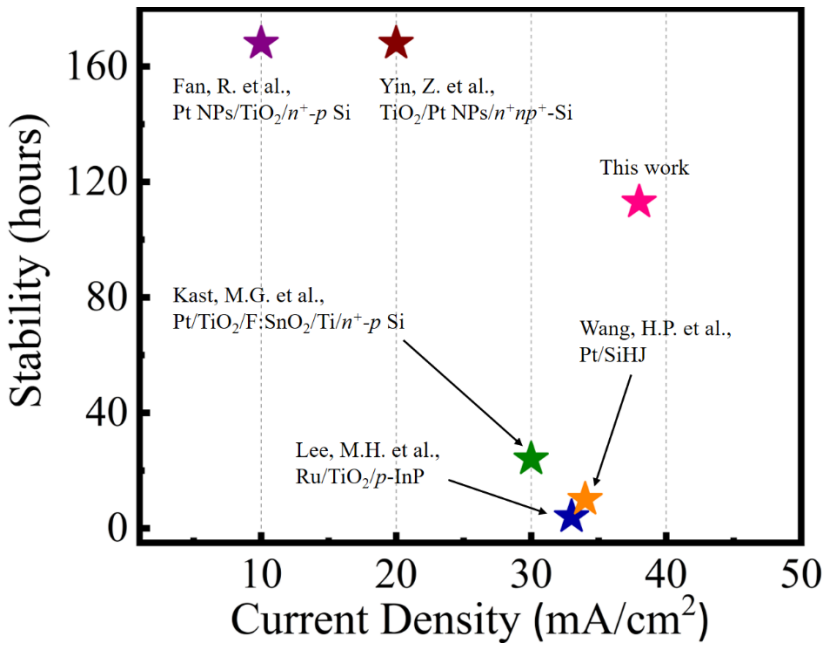

Figure 4.1. A summary, including stability and maximum current density for some previously reported semiconductor photocathodes with ABPE >8% [71-75] measured under AM 1.5G one sun illumination.

Important requirements of the surface protection layer include: i) stability in aqueous solution, ii) efficient charge carrier (electron) extraction, and iii) transparency to light illumination. It is also highly desired that the protection layer can effectively passivate the surface states and reduce surface recombination. In addition, the surface protection layer, together with the semiconductor photocathode, should ideally consist of materials already widely produced in industry to achieve controlled synthesis and scalable manufacturing. Si and gallium nitride (GaN), which have been

widely used in the electronic and photonic industries, are the two most produced semiconductor materials. Previous studies have shown that (In)GaN nanostructures can be used for photocatalytic (PC) water splitting [7, 87, 134, 196-199] and PEC water splitting [15, 200, 201]. GaN also exhibits many favorable properties to serve as the protection layer for PEC water splitting. The surfaces of GaN nanostructures can be tuned to be N-rich, not only for their top c-plane surfaces but also for their nonpolar lateral surfaces, which can effectively protect against corrosion [26]. GaN also exhibit a large energy bandgap (~3.4 eV) and is transparent in the visible and infrared wavelengths [7, 69].

In this work, we have investigated the use of GaN nanowire arrays as a multi-functional passivation layer for Si photocathodes, which not only offers robust protection against corrosion but also significantly improves the reaction kinetics and PEC efficiency. GaN nanowires are grown directly on Si wafer under N-rich conditions to promote the formation of N-terminated surfaces [26]. Detailed X-ray photoelectron spectroscopy (XPS) measurements reveal that the conduction band edges of GaN and Si are near-perfectly aligned, which enables efficient extraction of photo-generated electrons from the underlying Si wafer to GaN nanowires. Electrochemical impedance measurements further confirm that, due to the extremely large surface area of GaN nanowires, the charge carrier transfer resistance at the semiconductor/liquid junction is reduced by nearly two orders of magnitude compared to a planar Si photocathode. The GaN nanowire protected Si photocathodes exhibit excellent performance, including a saturated photocurrent density of ~38 mA/cm^2 with onset potential (V_{on}) ~0.5 V vs reversible hydrogen electrode (RHE) and a large ABPE of 10.5% in 0.5M H_2SO_4 under AM 1.5G one sun illumination. Chronoamperometry analysis for the photocathode shows a stable photocurrent density of ~38 mA/cm^2 for > 100 h, which, to our knowledge, is the best reported stability for a semiconductor photocathode at a photocurrent density of 35 mA/cm^2, or higher under one-sun illumination [43b, 71, 73, 75]. Our studies

offer a viable path in the quest for a high efficiency and highly stable semiconductor photoelectrode for solar water splitting.

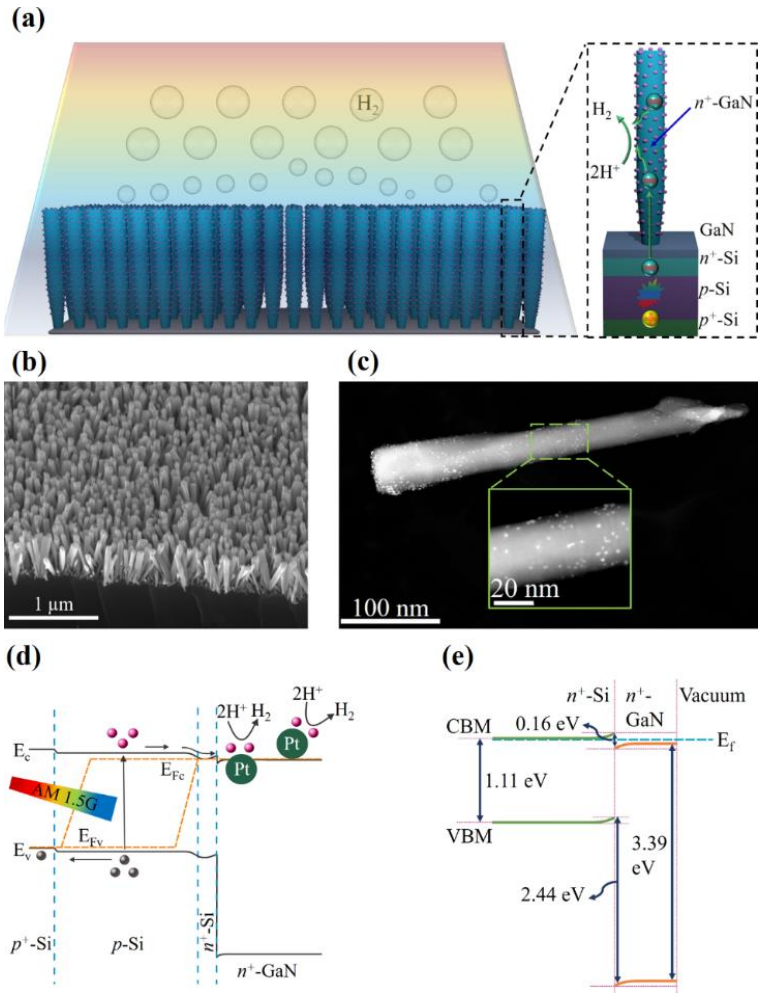

Figure 4.2. Design and structural characterization of n^+-GaN nanowires/n^+-p Si photocathode. (a) Schematic of n^+-GaN nanowires/n^+-p Si photocathode showing light absorption by the underlying Si wafer, electron transfer from Si wafer to GaN nanowires, and proton reduction on platinized GaN nanowires. (b) SEM image of GaN nanowire arrays on Si. (c) STEM HAADF image showing the uniform deposition of Pt nanoparticles on GaN nanowire arrays. Inset: magnified STEM HAADF image showing Pt NPs distributed on the highlighted (green dashed box) segment of n^+-GaN nanowire. (d) Schematic of the energy band diagram of Pt decorated n^+-GaN nanowires/n^+-p Si photocathode under light illumination. (e) Band diagram constructed for samples examined in XPS study for ~30 nm n^+-GaN/n^+-Si. The bulk E_f position in the n^+-Si wafer is positioned just below the CBM, and the extents of band bending in each layer at the interface are assumed to be approximately equal.

4.2 Results and Discussions

Schematically shown in Figure 4.2(a), the photocathode consists of planar n^+-p Si substrate and n^+-GaN nanowire arrays. The details for the fabrication and device performance of planar n^+-p Si substrate are described in Appendix-2.1. The n^+-p Si wafer serves as the light absorber, and photo-generated electrons are extracted by GaN nanowire arrays for proton reduction, shown in the inset of Figure 4.2(a). In this study, n^+-GaN nanowire arrays are grown on the n^+-p Si substrates using a Veeco GEN II radio frequency plasma-assisted molecular beam epitaxial (PA-MBE) growth system. Prior to loading into the MBE chamber, the n^+-p Si substrate is cleaned with acetone and methanol to remove any organic contaminants. Subsequently, Si substrate is immersed in 10% BHF (used in industrial cleaning of Si wafers) to remove native oxide. The nanowires are formed spontaneously under nitrogen-rich conditions without using any external metal catalyst on Si substrate [7, 11, 22, 87, 202]. The growth conditions included a substrate temperature range of 700-750 ^{o}C, a Ga beam equivalent pressure of 6×10^{-8} torr, nitrogen flow rate of 1 standard cubic centimeter per minute (sccm) and plasma forward power of 350 W. n^+-GaN nanowire arrays are grown for 1.5 h (see Appendix-2.4 for the growth optimization process). The scanning electron microscope (SEM) image in Figure 4.2(b) shows the vertically aligned nanowires without Pt nanoparticles (NPs) with a length of ~350 nm and diameter ~40 nm. Before the experiment, Pt NPs are deposited on the surfaces of nanowires. The photo-deposition of Pt NPs is described in Appendix-2.2. The structural properties were further characterized using scanning transmission electron microscopy (STEM). Illustrated in Figure 4.2(c), the photo-deposited Pt NPs are uniformly distributed on the entire GaN nanowire surface. The inset of Figure 4.2(c) reveals that the size of Pt NPs is ~2-3 nm. The electron energy loss spectroscopy (EELS) mapping for Pt NPs on the nanowires are clearly illustrated in our previous studies [22]. As seen from the band diagram shown in Figure 4.2(d),

photogenerated electrons from n^+-p Si substrate migrate towards Pt deposited n^+-GaN nanowires to participate in hydrogen evolution reaction (HER) and photoexcited holes travel to the counter electrode. The band alignment between n^+-Si and n^+-GaN interface is explained in the subsequent X-ray photoelectron spectroscopy (XPS) studies. It is to be noted that n^+-GaN acts as a hole blocking layer, due to the large valence band offset between GaN and Si, which facilitates charge carrier separation and thereby reduces the surface recombination of photo-generated charge carriers.

Critical for the operation of the monolithically integrated GaN/Si photocathode is the conduction band alignment between GaN and Si. To date, however, a direct measurement of the band alignment between Si and N-polar GaN was not available to our knowledge. In this study, XPS measurements were performed on GaN/Si samples in a Physical Electronics 5600 instrument using monochromatic Al-kα illumination (hυ = 1486.6 eV) at a pass energy of 11.75 eV. Samples tested for XPS are: bare n^+-Si(100), thin (~2-3 nm) n^+-GaN/Si(100), and relatively thick (~30 nm) n^+-GaN/Si(001). The samples were transferred under Ar and ultra-high vacuum (UHV) into the XPS system. XPS survey spectra and high-resolution core-level spectra revealed acceptably low levels of surface contamination, enabling subsequent band-offset measurements. Band diagram (Figure 4.2(e)) is constructed from the measured VBMs and the observed core-level shifts (see Appendix-2.10) between these samples. The Si wafer is heavily doped (>10^{19} cm^{-3}), so in the Appendix-2.3(a) the bulk Si E_f is placed just below the CBM. The measured position of the VBM (1.16±0.05 eV) on the bare Si surface indicates that, within uncertainty, E_F is pinned above the CBM (Appendix-2.3(a)). Deposition of 2-3 nm of GaN evidently passivates the Si surface and induces a small amount of upward band bending (Appendix-2.3(b)). Assuming the GaN band gap = 3.39 eV, for this surface E_f is ~0.1 eV above the GaN CBM, indicating that this thin layer is

degenerately doped *n*-type. Deposition of 30 nm of GaN (Figure 4.2(e)) shifts Ga and N core levels to lower band energies, relative to the thin GaN sample, by ~0.07 eV. The band diagram in Figure 4.2(e) assumes that there are roughly equal amounts of band bending in the Si wafer and in the GaN layer at the interface. But another possibility is that a majority of interfacial band bending occurs in the Si wafer, and that the 30 nm GaN epilayer is essentially in a flat-band condition. The interfacial valence-band offset calculated from measured VBMs and core-level shifts was 2.44±0.1 eV. This value, in combination with the individual band gaps of Si and GaN, leads to a conduction band offset of -0.16±0.1 eV, wherein the negative sign indicates that the CBM of GaN is lower than that of Si. Our measurements confirm for the first time that the CBM between N-polar GaN and Si is approximately aligned, thereby enabling efficient charge carrier (electron) transfer from Si to GaN.

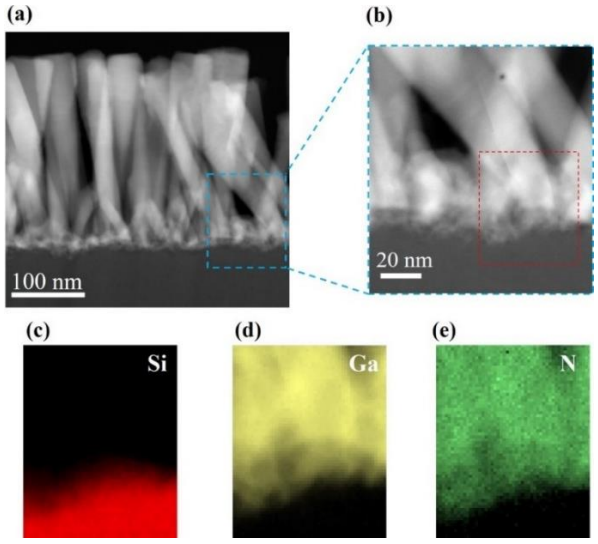

Figure 4.3. Structural characterization of n^+-GaN nanowires on Si substrate. (a) STEM image of the as-grown sample prepared by focused ion beam (FIB) lift-out method. (b) Magnified image of the highlighted (blue dashed box) portion of Figure 4.3(a). EELS elemental mapping results of: (c) Si K, (d) Ga $L_{2,3}$, and (e) N K edges for the region enclosed in the red dashed box of Figure 3(b). The surface of Si is covered by GaN layer.

Structural characterization of GaN/Si photocathode was further performed using STEM. Illustrated in Figure 4.3(a), the nanowires are mostly near-vertical with some of them oblique and connected at the bottom Si surface. It is also observed that a relatively thin (10-20 nm) GaN layer completely covers the Si surface, which was formed during the epitaxy of GaN nanowires. Such a GaN layer can effectively passivate the Si surface to protect against corrosion. The EELS elemental mapping shown in Figures 4.3(c)-(e) based on the STEM images (Figures 4.3(a)-(b)), further reveal the surface coverage of GaN on Si.

The PEC reaction was conducted in 0.5 M H_2SO_4 solution using n^+-GaN nanowires on n^+-p Si substrate with Pt co-catalyst, silver chloride electrode (Ag/AgCl), and Pt wire as the working, reference, and counter electrode, respectively. A solar simulator (Newport Oriel) with an AM1.5 G filter was used as the light source, and the light intensity was calibrated to be 100 mW/cm^2 for all subsequent experiments. The conversion of the Ag/AgCl reference potential to reversible hydrogen electrode (RHE) is calculated using the equation,

$$E_{(RHE)} = E_{Ag/AgCl} + E^{o}_{Ag/AgCl} + 0.059 \times pH \qquad \text{eq. (4.1)}$$

where $E^{o}_{Ag/AgCl}$ is 0.197 V, and pH of the electrolyte is nearly zero. Figure 4.4(a) shows the linear scan voltammogram (LSV) of platinized n^+-p Si photocathode (black curve) and platinized n^+-GaN nanowires/n^+-p Si photocathode (red curve) under AM 1.5G one sun illumination and dark condition (blue curve). The photocathode optimization in terms of MBE growth duration and Pt photo-deposition conditions are described in Appendix-2.4. The platinized n^+-p Si photocathode showed a poor V_{on} ~0.35 V *vs* RHE and low photocurrent density ~ 9 mA/cm^2 at 0 V *vs* RHE. The optimized Pt decorated (10 µl loading) n^+-GaN nanowires/n^+-p Si photocathode showed dramatic improvement in performance with V_{on} of ~0.5 V *vs* RHE and high photocurrent density of ~ 38 mA/cm^2 under AM 1.5G one illumination in 0.5 M H_2SO_4. The measured photocurrent onset

potentials are in reasonably good agreement with the flat-band potential derived from Mott-Schottky measurements (see Appendix-2.5).

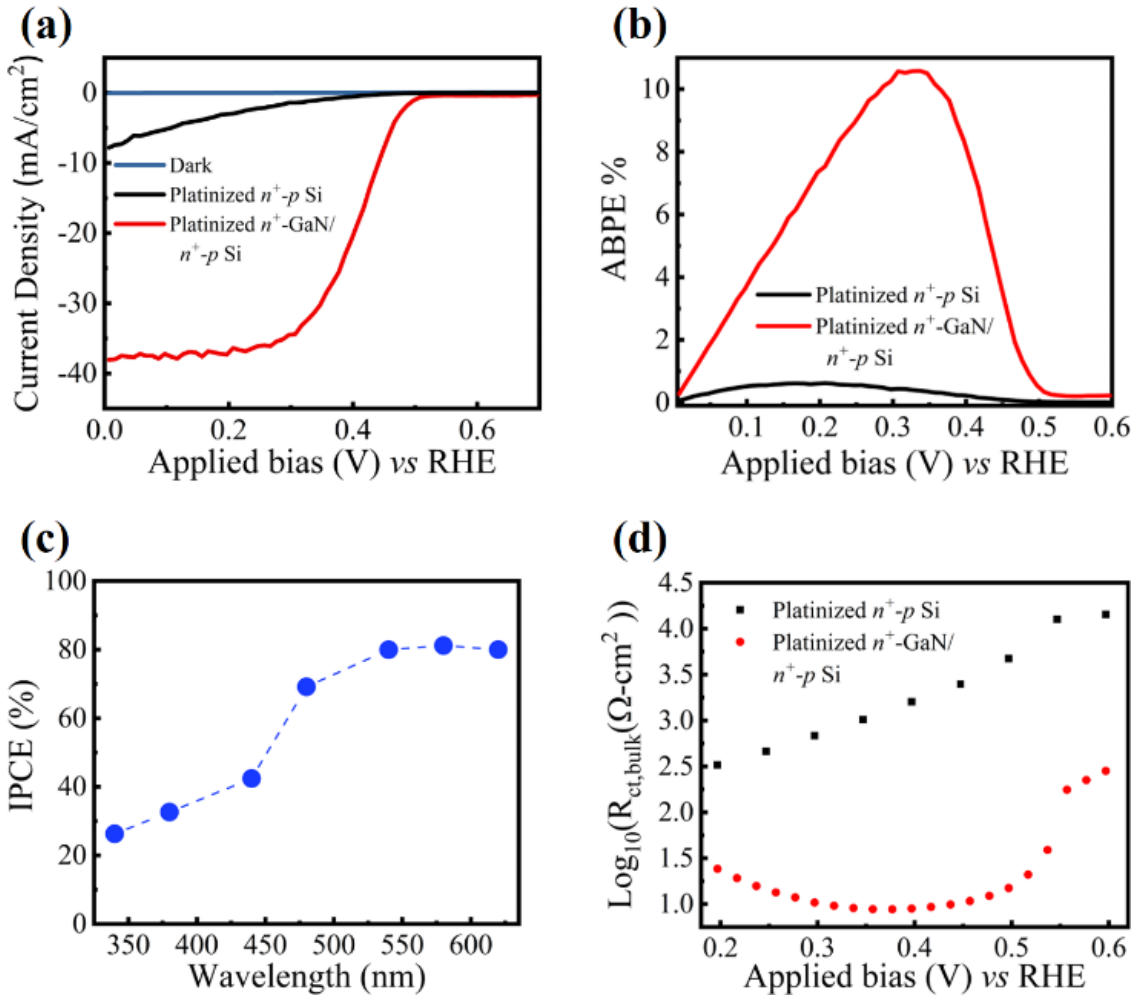

Figure 4.4. PEC performance and EIS characterization of n^+-GaN nanowires/n^+-p Si photocathode. (a) J-V curves of platinized n^+-GaN nanowires/n^+-p Si photocathode (red curve) and platinized n^+-p Si photocathode (black curve) in 0.5 M H_2SO_4 under AM 1.5G one sun illumination and dark condition (blue curve). The optimized Pt decorated n^+-GaN nanowires/n^+-p Si photocathode showed V_{on} of ~0.5 V *vs* RHE and high photocurrent density of ~ 38 mA/cm^2. (b) ABPE of the photocathodes under AM 1.5G one sun illumination. The maximum ABPE for platinized n^+-GaN nanowires/n^+-p Si photocathode (red curve) is 10.5% at 0.32 V *vs* RHE. (c) IPCE of platinized n^+-GaN nanowires/n^+-p Si photocathode at 0 V *vs* RHE. (d) Logrithimc values of charge transfer resistance ($R_{ct,bulk}$) at different applied biases *vs* RHE for platinized n^+-p Si photocathode and platinized n^+-GaN nanowires/n^+-p Si photocathode.

The ABPE of the photocathode was derived using the equation,

$$\eta(\%) = \frac{J(V_{RHE} - E^0_{rev})}{P_{in}} \times 100 \qquad \text{eq. (4.2)}$$

where J is the photocurrent density, E^0_{rev} = 0 V *vs* RHE, V_{RHE} is the applied bias *vs* RHE, and P_{in} is the power of the incident light (*i.e.* 100 mW/cm^2). Shown in Figure 4(b), the maximum ABPE for platinized n^+-GaN nanowires/n^+-p Si photocathode (red curve) is 10.5% at 0.32 V *vs* RHE under AM 1.5G one sun illumination. After iR compensation (see Appendix-2.6), the ABPE for this photocathode is ~13%. The measured (uncompensated) ABPE is one of the highest values for Si based photocathodes (see Appendix-2.12) when compared to 4.9% for Pt/Ti/$SrTiO_3$/p-Si [187], 8.9% for Pt/n^+-p Si [203], 1.9% for Ni-Mo-coated n^+-p Si [204] and 7% for Al_2O_3/n^+-p Si [190]. In contrast, the platinized n^+-p Si photocathode showed a poor ABPE (black curve) of less than 1% when compared to platinized n^+-GaN nanowires/n^+-p Si photocathode. The incident-photon-to-current-efficiency (IPCE) of platinized n^+-GaN nanowires/n^+-p Si photocathode was further measured. The measurement is conducted at 0 V *vs* RHE in 0.5M H_2SO_4 in a three-electrode system. The IPCE is calculated using the equation,

$$IPCE\ (\%) = {(1240 \times I)}\Big/{(\lambda \times P_{in})} \times 100 \qquad \text{eq. (4.3)}$$

where I is photocurrent density (mA/cm^2), λ is the incident light wavelength (nm) and P_{in} is the power density (mW/cm^2) of the incident illumination. The IPCE is ~80% at 620 nm as shown in Figure 4.4(c). It is worthwhile mentioning that the IPCE measurements were performed at very low level of light intensity, which is expected to give a lower IPCE than that under 1 sun illumination, due to the presence of traps and defects.

To further reveal the underlying mechanisms for the drastically improved performance of platinized n^+-GaN nanowires/n^+-p Si photocathode, we have performed detailed electrochemical

impedance spectroscopy (EIS) measurements in 0.5 M H_2SO_4 under AM 1.5G one sun illumination. AC perturbations of amplitude 10mV were superimposed with frequency in the range 0.1 Hz–2 MHz. Equivalent circuit modelling and curve fitting were done using EC lab software (BioLogic Science Instruments). EIS results in the form of Nyquist plots are shown in Appendix-2.11 for the two types of photocathodes, and the complete equivalent circuit model for Pt-decorated n^+-GaN nanowire/n^+-p Si photocathode is further illustrated in Appendix-2.7. The charge transfer resistance at the semiconductor/liquid junction, $R_{ct,bulk}$, is derived and plotted in logarithmic scale *vs.* applied bias (*vs.* RHE), shown in Figure 4.4(d). It is seen that $R_{ct,bulk}$ values are in the range of 10 Ω cm^2 for platinized n^+-GaN nanowire/n^+-p Si photocathode, which are nearly two orders of magnitude smaller compared to those (~1,000 Ω cm^2) of the platinized n^+-p Si photocathode. The sharp reduction of charge transfer resistance for n^+-GaN nanowire/n^+-p Si photocathode from 0.6 to 0.5 V *vs* RHE, illustrated in Figure 4.4(d), is a clear indication that the photocurrent onset potential (V_{on}) is ~0.5 V *vs* RHE (see Figure 4.4(a)). Further changes in the applied bias in the cathodic direction (from 0.4 to 0.2 V *vs* RHE), however, leads to a small increase in the charge transfer resistance, which is due to the increasing accumulation of H_2 gas at the electrode surface. The generation of H_2 gas also produces fluctuations in the photocurrent, which is evident in the red curve shown in Figure 4.4(a).

Our studies further provide unambiguous evidence that the charge (electron) transfer resistance at the Si/GaN heterointerface is negligibly small, which is consistent with the XPS measurements showing a very small conduction band offset between Si and GaN (Figure 4.2(e)). As such, photo-generated electrons of the underlying Si wafer can be readily extracted to the GaN nanowire arrays, which offer one to two orders of magnitude larger surface areas compared to a bare Si wafer. The exceedingly large surface area, together with the favorable conduction band edge position of GaN

for proton reduction, lead to extremely efficient charge carrier transfer from the semiconductor absorber to aqueous solution. It should be noted that Pt co-catalyst enhance charge carrier transfer to electrolyte for both photocathodes. In the case of n^+-p Si photocathode, however, the surface coverage of Pt co-catalyst NPs inevitably blocks any incident light and therefore reduces the photocurrent density [205-207]. Such an issue is effectively addressed in n^+-GaN nanowires/n^+-p Si photocathode, since the superior anti-reflectance of nanowires enhances the light absorption of the underlying Si wafer. Moreover, due to the absence of surface dangling bonds and minimal impurity incorporation, the Pt/GaN interface is expected to have significantly reduced resistance, compared to the Pt/Si interface, which is reflected by the better photocurrent onset potential with the incorporation of GaN nanowires (see Figure 4.4(a)). The surface recombination of Si is also reduced by the presence of a thin GaN passivation layer, which is explained next.

We have further evaluated the Faraday efficiency by analyzing the H_2 generation from platinized n^+-GaN nanowire/n^+-p Si photocathode. The Faraday efficiency ($\eta_{(Faraday)}$) for the measurements was calculated using the equation below,

$$\eta_{(Faraday)}(\%) = \frac{2 \times n_{H_2}\,(t=T_0)[mol] \times F}{\int_0^{T_0} I\,[A]\,.dt\,[s]} \times 100 \qquad \text{eq. (4.4)}$$

where I is measured current, F is Faradaic constant (96485 C/mol) and n_{H_2} is the total amount of H_2 produced for a time duration T_0. H_2 was detected by gas chromatograph (GC, Shimadzu GC-8A) equipped with a thermal conducting detector (TCD). Shown in Figure 4.5(a), the photocurrent and H_2 evolution are simultaneously measured at 0.02 V *vs* RHE for a duration of 2.5 h in 0.5 M H_2SO_4 under AM 1.5G one sun illumination. The Faraday efficiency ($\eta_{Faraday}$) is calculated using Eqn. 4.4 by correlating average experimental (red dots) and calculated (black dotted line) H_2 production. The Faraday efficiency is nearly 100%, considering that there is an error bar ~10% of H_2 sampling.

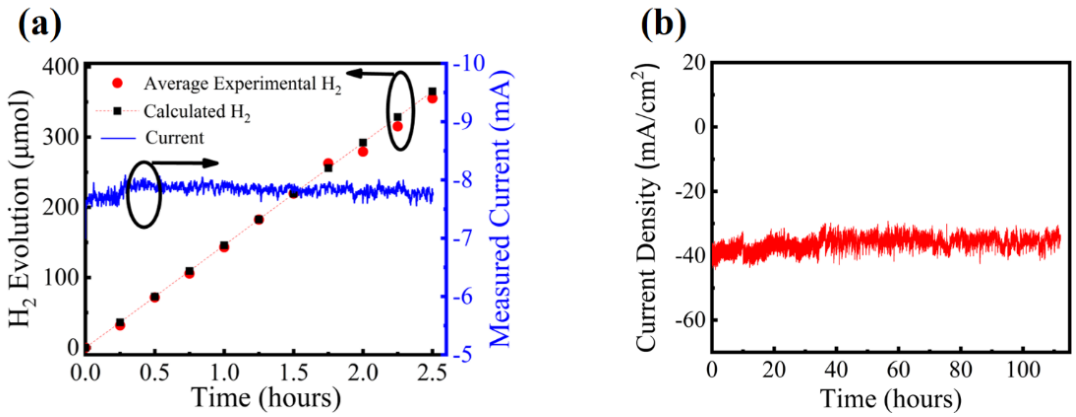

Figure 4.5. Faraday efficiency and stability of platinized n^+-GaN nanowires/n^+-p Si. (a) H_2 generation for platinized n^+-GaN nanowires/n^+-p Si photocathode at 0.02 V *vs* RHE under AM 1.5G one sun illumination in 0.5 M H_2SO_4 for 2.5 h. Blue curve represents the photocurrent, red dots represent the average amount of H_2 generated at various times and black dotted line is the theoretical amount of H_2 produced against time based on photocurrent. The Faraday efficiency is nearly 100%. The electrode area for the sample is 0.2 cm^2, which corresponds to a photocurrent density of ~ 39 mA/cm^2. (b) PEC long term stability measurement for platinized n^+-GaN nanowires/n^+-p Si photocathode at 0 V *vs* RHE in 0.5 M H_2SO_4 under AM 1.5G one sun illumination. The photocurrent density of photocathode showed no degradation for >100 h duration (113 h).

We subsequently conducted a long duration stability test for platinized n^+-GaN nanowire/n^+-p Si photocathode at 0 V *vs* RHE in 0.5 M H_2SO_4 under AM 1.5G one sun illumination. Illustrated in Figure 4.5(b), the photocurrent density showed no degradation for a duration of 113 h. The observed fluctuation in current is due to the accumulation and release of H_2 bubbles from the sample surface. To maintain the same experimental conditions, the electrolyte was changed after every 24 h. To our knowledge, this high stability measured at ~38 mA/cm^2 is the best for any semiconductor photocathodes tested at a photocurrent density of 30 mA/cm^2, or higher, when

compared with 10 h for Pt (2nm)/SiHJ [73], 24 h for Pt/TiO_2/F:SnO_2/Ti/ n^+-p Si [74] and 4 h for Ru/TiO_2/p-InP [75] (see Appendix-2.13). The photocurrent density of platinized n^+-GaN nanowire/n^+-p Si photocathode reduced to ~35 mA/cm^2 and the fill factor became worse after 113 h of stability test (see Appendix-2.8). We conducted detailed structural characterization of these samples after 50 h stability test using SEM and TEM. Appendix-2.9(a)-(b) show that the nanowire dimensions (length ~350 nm and diameter ~40 nm) remained virtually the same compared to those before the experiments (Figure 4.2(c)), suggesting that the nanowires were not etched during the long-term stability experiments. It is noticed, however, that the surface coverage of Pt NPs, shown in the inset of Appendix-2.9(b), was significantly reduced compared to that prior to the experiments (see Figure 4.2(c)), which explains the degraded performance. The SEM image of the n^+-GaN nanowire/n^+-p Si photocathode after 113 h stability test is shown in Appendix-2.9(c).

The underlying mechanisms for the long-term stability of GaN/Si photocathode are further discussed. Compared to conventional III-V semiconductors, III-nitrides have strong ionic bonds, which leads to the bunching of surface states near the band-edge, rather than the forbidden bandgaps [27, 134]. Therefore, the surface states of III-nitrides do not serve as nonradiative recombination centers, which is instrumental for achieving long-term stability against corrosion. Moreover, the nanowires grown by MBE have nearly perfect single-crystal wurtzite structure and are free of dislocations. Recent theoretical and experimental studies of the actual atomic structure of GaN nanowires grown by MBE further revealed that they exhibited a unique N-termination, not only for the $(000\bar{1})$ top faces but also for their nonpolar side faces [26, 27]. Such N-terminated surfaces can further protect against corrosion when compared to Ga-terminated surfaces which readily get oxidized to Ga_2O_3 and dissolve during harsh PEC conditions [26]. Moreover, the

underlying Si surface is also protected by the presence of a thin GaN layer (see EELS mapping results in Figures 4.3(c)-(e)).

Finally, we describe the unique advantages of using GaN nanostructures compared to other schemes for protecting Si photocathodes in water splitting reaction reported previously. The use of transition metal dichalcogenides protection layers such as MoS_2 requires additional conductive buffer layers between Si and MoS_2 to enhance stability and prevent inter-diffusion [191, 208]. Recent studies by Jaramillo and co-workers [96, 98] reported a stability of ~ 60 days at an average photocurrent density of ~ 11 mA/cm^2 [96] using three interlayers between MoS_2 and planar n^+-p Si with a total thickness of ~14 nm. These photocathode designs are limited by the fabrication complexities and, more importantly, by the loss of photogenerated carriers at MoS_2/Si interfaces. It was reported that $MoSe_2$ with a relatively thick layer (~60 nm) on textured n^+-p Si could have a stability of ~120 h, but with a low ABPE ~ 3.8% [192]. Chorkendorff and co-workers reported that thick TiO_2 protection layers (~100 nm with 5 nm Ti) on planar n^+-p Si could achieve relatively high stability (~15 days) at a photocurrent density ~ 22 mA/cm^2 [209] under the red part of AM 1.5G solar spectrum (λ >635 nm) illumination. The major concern using thick TiO_2 layers is poor charge carrier transport kinetics due to many recombination sites [159, 210]. Fan et al. reported the use of thinner TiO_2 protection layers (10-20 nm) together with native interlayer of SiO_2 on textured n^+-p Si for long term stability (168 h) at a photocurrent density of ~10 mA/cm^2 [72]. It is evident that, compared to previously reported protection schemes, the integration of GaN nanostructures to protect Si photocathodes can sustain unprecedentedly large photocurrent densities and high ABPE (see Figure 4.1), which is attributed to i) the near-perfect band alignment between the conduction band edge of Si and GaN for efficient extraction of photo-generated electrons, ii) the N-terminated GaN surfaces to protect against corrosion, and iii) the large surface area of GaN nanostructures to

significantly enhance charge carrier extraction and light absorption. With the use of industrial standard epitaxial process, the fabrication of GaN nanostructures is also highly controllable, reproducible, and scalable.

4.3 Conclusions

In summary, we have demonstrated that GaN-based nanostructures, due to their unique structural, electronic, surface, and electrochemical properties, can serve as a multi-functional protection layer for an otherwise unstable, low performance semiconductor photocathode. The direct integration of GaN nanowire arrays on n^+-p Si substrates not only protects the underlying Si surface from corrosion, but also significantly enhances the reaction kinetics by reducing the charge carrier transfer resistance at the semiconductor/liquid junction, leading to unprecedentedly long-term stability (>100 h) at a large current density (>35 mA/cm^2). This is in direct contrast to the conventional approaches, wherein the incorporation of an extra surface protection layer often compromises the charge carrier extraction and limits the maximum achievable efficiency. The measured ABPE of 10.5% (~13% with iR correction) is also among the highest values ever reported for a Si-based photocathode. Significantly, both Si and GaN have already been widely produced in the electronics and photonics industries, thereby providing a scalable platform for future solar fuel devices and systems.

Chapter-5: Ultrahigh Stable Si Photocathode Using GaN Protection for High-Efficiency Solar Water Splitting

In Chapter-4, we have successfully demonstrated GaN as an exceptional multi-functional protection layer on Si photocathode to achieve high efficiency and long-term stability for PEC water splitting. The reason for performance degradation in the devices was found out to be Pt nanoparticles falling-off from the nanowires. In this chapter*, we built on the GaN/Si photocathode platform to achieve ultrahigh stability using catalyst regeneration process under AM 1.5G one-sun illumination. We have shown through structural analysis that there was no degradation in the nanowires and PEC performance for 3,000 h.

---

* This chapter is based on a manuscript under preparation: **S. Vanka** *et al.* (Except for primary authors: S. Vanka and Z. Mi, other co-authors and their orders are to be determined). K. Sun contributed to the TEM measurements.

5.1 Introduction

One of the significant challenges for the coming few decades is providing affordable, reliable and environmentally sustainable energy to the world's population [69, 211, 212]. Photoelectrochemical (PEC) solar water splitting is one of the clean and sustainable ways to convert the two most abundant natural resources on earth, i.e., sunlight and water, into high calorific value, storable and clean chemical fuel such as hydrogen (H_2) [102. 212-216]. It is essential to develop high efficiency (~ 15%), durable (>20,000 h) and cost-effective (< \$2 (kg H_2)$^{-1}$) photocathode materials using industry-ready semiconductors for large-scale implementation of PEC devices [69, 216, 217]. Only a few semiconductors like Si [14, 73, 96, 102, 209, 217] and III-V compound semiconductors with their alloys [75, 98, 195, 218, 219] have favorable conduction band minimum (CBM) which is more negative than hydrogen evolution reaction (HER) (i.e., -4.44 eV *vs.* vacuum level in solutions having pH=0). Although these materials can achieve high efficiency [43c,d, 71, 73, 75, 95], most of them have mediocre stability performance (< 200 h) because of the chemical as well as photochemical corrosion. Due to the intermittency of solar radiation and light absorber in direct contact with the electrolyte, the degradation of PEC devices is more accelerated compared to photovoltaic electrolyzer (PV-EL) devices [220] and thus reduce the semiconductor's lifetime. Photo-corrosion mechanisms of semiconductors are influenced by many factors such as intensity of light illumination, biasing conditions, semiconductor/electrolyte as well as catalyst/electrolyte interfaces, catalyst, and surface passivation contaminations, semiconductor electronic band structure and electrolyte composition [102, 193, 221]. These factors are fundamentally categorized into thermodynamic and kinetic protection requirements.

Gerischer's model [222] describes the thermodynamic considerations for photo-corrosion of a photoelectrode. To avoid competition between cathodic and anodic photo-corrosion of

photoelectrode with HER and oxygen evolution reaction (OER) respectively, it is vital that the photoelectrode satisfy the criteria: $\phi_{corr}^{h} < E_{anodic}$ (1.23 V *vs.* RHE) and $\phi_{corr}^{e} > E_{cathodic}$ (0 V *vs.* RHE); where ϕ_{corr}^{e} is energy level for cathodic corrosion reaction of semiconductor; ϕ_{corr}^{h} is energy level for anodic corrosion reaction of semiconductor. From previous reports [167, 223], it is hard to find an ideal semiconductor material which can satisfy the both thermodynamic requirements simultaneously. In theory, Si is easily oxidized under anodic conditions but it is expected to be thermodynamically stable under cathodic conditions [223]. As shown in other reports, Si can get oxidized into an insulating oxide even under cathodic conditions [193, 224] and forms a passivation layer on Si surface which leads to its stability reduction. III-V compounds, like GaAs, go through chemical corrosion reaction due to accumulation of large amount of surface hole concentration in dark and light which generates holes at the surface [225]. It was observed that N-terminated III-nitrides show almost no chemical or photoelectrochemical corrosion when in contact with different electrolytes [11, 14, 24, 26]. Recently, Baker et al. reported that Ga terminated GaN had a photocorrosion potential of -0.66 ± 0.07 V *vs.* RHE in 0.5M H_2SO_4 (pH=1) [226]. It is to be noted that only under a bias and light illumination GaN undergoes oxidation reaction under anodic conditions. Thus, III-nitrides are stable against chemical corrosion and N-terminated metal nitrides are stable even against photo-corrosion [26]. Therefore, to achieve long-term stability for high efficiency Si and III-arsenide/phosphide materials, it is quintessential to use chemically stable coating layers which can passivate these semiconductor surfaces [193].

Over the years, various protection schemes have been employed to enhance the stability of photoelectrodes by overcoming both thermodynamic and kinetic requirements. Kinetic protection for a given photoelectrode is possible by using a synergetic combination of the stable surface protection layer and highly active co-catalyst [193, 221]. The first generation of protection layers

consists of photoelectrode coupled with a highly active catalyst (see Figure 5.1(a)) which can simultaneously improve the stability with excellent reaction kinetics by extracting the photogenerated charge carriers more efficiently. Since oxygen evolution reaction (OER) is sluggish, this approach is more suited for photoanodes to avoid further device losses. As seen in Appendix-3.10, Si photoanode with $NiCrO_x/TiO_2$ protection [227] showed long-term stability of ~ 2200 h, but the photocurrent density is very low, and the applied bias is higher than 1.23 V *vs.* RHE. It is to be noted that hematite (α-Fe_2O_3) and bismuth vanadate ($BiVO_4$) report high stability with efficiencies reaching their theoretical maximum values [228, 229]. The longest stability for nanostructured $BiVO_4$ photoanode is >1000 h by using *in-situ* on-demand NiFe catalyst regeneration [228]. In the case of HER, catalysts like Pt [230-233], MoS_2 [96, 98, 219, 234, 235] and NiMo [204, 236] can act as both protection layer and co-catalyst. As shown in Supp. Info. Table 1, Jaramillo et al. [96] reported stability of >1500 h by using MoS_2 for Si photocathode. However, the photocurrent density of this device is relatively low due to the interfacial charge carrier losses at MoS_2/Si interfaces, and its degradation in stability is due to Mo oxidation.

The second generation approach, as shown in Figure 5.1(b), for achieving long-term stability is to use relatively thick metal oxides, such as TiO_2 [72, 97, 167, 237], Al_2O_3 [190], IrO_x [115], as passivation layers for photocathode and photoanode along with a suitable co-catalyst [78, 115, 167, 238]. Although the stability of these devices has improved substantially, the major issue with these thick protection layers is the loss of photocurrent due to poor charge transfer and light absorption by the protection layers [221, 239, 240]. From Appendix-3.10, the best photocathode stability was reported by Bae et al. [220] using Pt co-catalyst and thick TiO_2 for MOS Si photocathode for ~ 82 days with a relatively low photocurrent density ($\leq$ 23 mA/cm^2). The degradation mechanism for this photocathode is the contamination of TiO_2 with carbonaceous species dissolved in the electrolyte.

Therefore, it is essential to develop a robust protection layer which can simultaneously protect the semiconductor without any performance degradation.

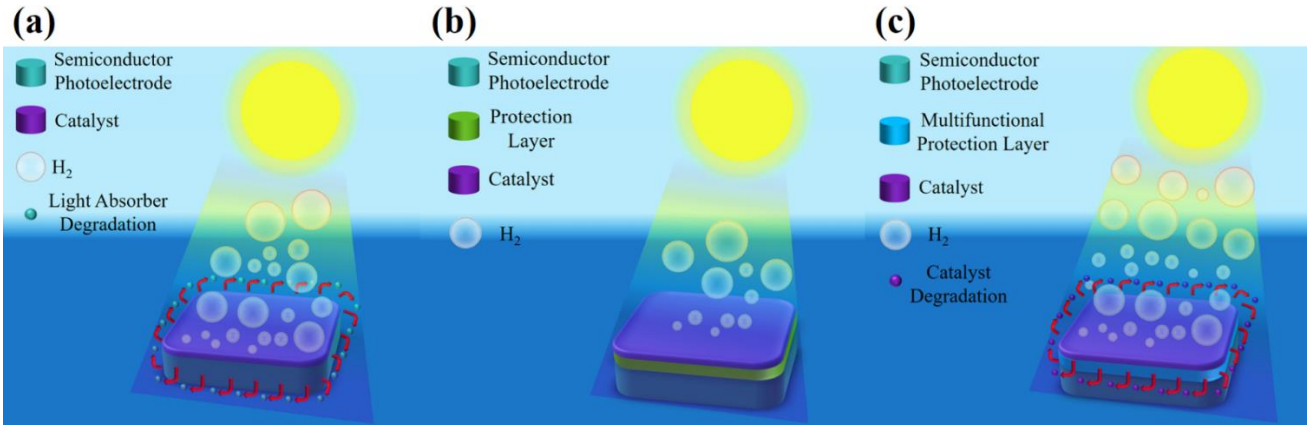

Figure 5.1. Schemes of PEC photoelectrode degradation and evolution of protection layers. (a) The first generation of protection schema consists of semiconductor photoelectrode and catalyst on top. The degradation mechanism is due to corrosion of the light absorber as shown by the red arrows. (b) The second generation of protection schema consists of semiconductor photoelectrode, the conventional protection layer, and catalyst. The protection layer is not robust which gives rise to lower H_2 production (grey bubbles). (c) The third generation of protection schema consists of semiconductor photoelectrode, the multi-functional protection layer, and catalyst. The protection layer is inherently stable in the electrolyte which gives long-term stability without degradation in performance. The long-term stability for this system is limited by catalyst loss over long durations of experiments (as shown by the red arrows).

Figure 5.1(c) gives a blueprint for developing the third generation of multi-functional protection layer along with a catalyst for long-term stability devices. In such a design, the catalyst

degradation will be the bottleneck in achieving long-term stability as the protection layer is chemically inert to the electrolyte and it can protect the light absorber against photo-corrosion. As mentioned earlier, the co-catalyst and electrolyte degradations impact the PEC stability performance by reducing charge carrier transfer kinetics of the photoelectrode [221]. Out of the two, deterioration in the co-catalysts on semiconductor surface has a more severe effect on the device performance. These co-catalysts act as the first line of defense on the surface of semiconductor photoelectrode materials against photo-corrosion [221, 228]. This degradation leads to an accelerated semiconductor photo-corrosion. Such degradations are mainly due to morphology changes on the surface of photoelectrodes and agitations/dissolutions in the electrolytes. To avoid these degradations, implementation of thicker co-catalysts layers can help in surface passivation. However, thicker co-catalyst layers have the same disadvantage of interfacial losses like the traditional thicker surface passivation layers. Nanoparticles (NPs) co-catalysts help in reducing device complexity and improves device performance which thereby eliminates the use of thick co-catalyst protection layers. The major issue with this approach is that NPs can easily get detached from the photoelectrode surface and dissolve in the electrolyte as the stability test continues, which again leads to degradation in performance [241]. Therefore, in summary, to achieve stability for more than tens of hundreds of hours, it is essential to develop the third generation of use chemically inert surface protection (as shown in Figure 5.1(c)) with co-catalyst regeneration on the surface of a PEC photoelectrode to satisfy the thermodynamic and kinetic protection requirements [228].

GaN and Si are the two most widely produced semiconductor materials in the world. It was shown that N-terminated surfaces (both top and non-polar side faces) of GaN nanostructures are resilient to harsh PEC conditions and thereby protect against corrosion [26, 242, 243]. Previous publication clearly illustrated the unique advantages of using GaN nanowires (NWs) compared to

other protection schemes used for Si photocathodes [14]. In this work, we use the established Pt-decorated n^+-GaN NWs/n^+-p Si platform [14] combined with catalyst regeneration process to attain unprecedented ultrahigh stability of 3000 h with a stable photocurrent density ~ 38 mA/cm^2. To the best of our knowledge, the reported stability is the longest stability for any photoelectrode materials in a half-cell configuration for H_2 production. The long-term stability experiments are carried out in more than 100 regeneration cycles with each cycle consisting of a 24 h continuous AM 1.5G one-sun illumination experiment followed by Pt catalyst regeneration (see Scheme1). Structural characterizations are done at different stages of the long-term stability experiments to confirm that GaN NWs remained unchanged during the experiments. The best performing platinized n^+-GaN NWs/n^+-p Si photocathode also showed excellent onset potential (V_{on}) ~0.56 V *vs.* RHE with high photocurrent density of ~37 mA/cm^2 and a high applied bias photon-to-current efficiency (ABPE) of 11.9% under AM 1.5G one-sun illumination in 0.5M H_2SO_4. This work shows the advent of the third-generation protection scheme by using high efficiency and ultrahigh stable photocathode using GaN as a protection layer for economic and industrial viable solar water splitting.

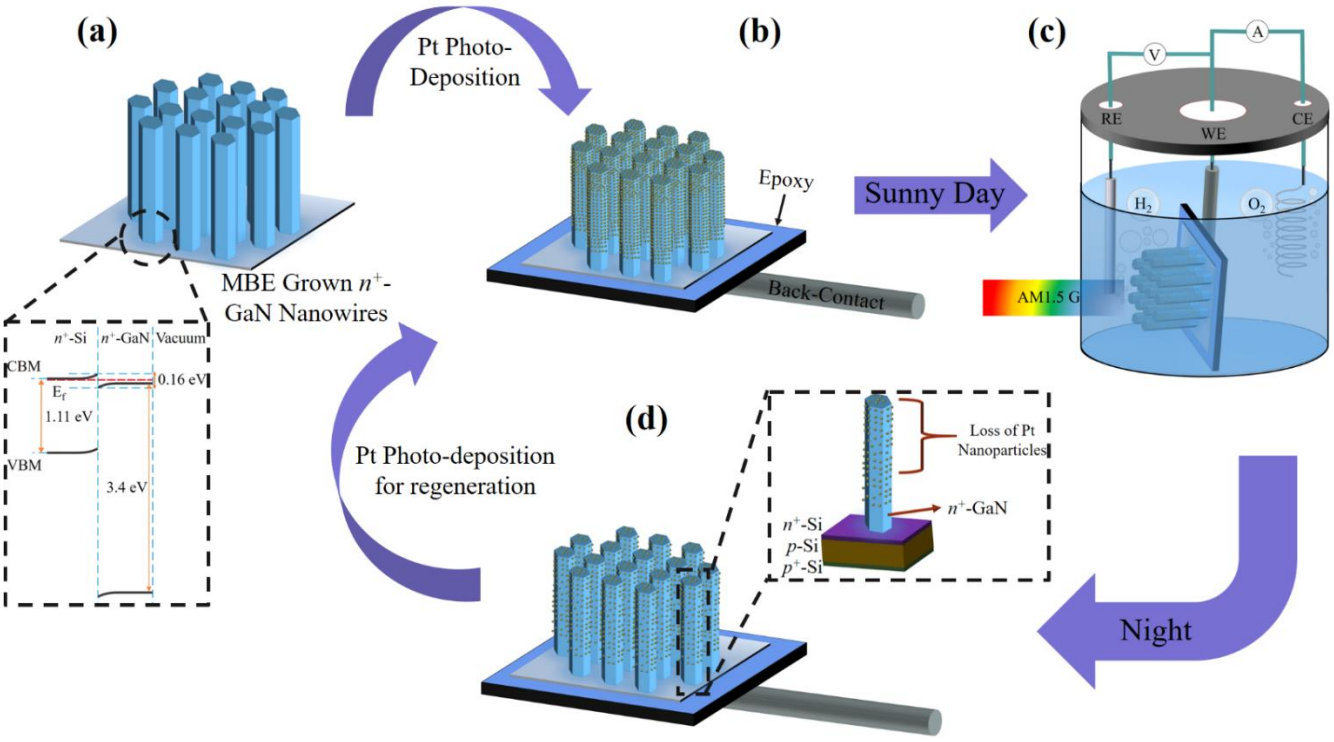

Scheme 5.1. Pt catalyst regeneration process during stability experiment using (a) MBE grown n^+-GaN nanowires on n^+-p Si photocathode. The band-diagram at the bottom shows the unique advantage of small conduction band offset between n^+-GaN and n^+-Si which allows efficient charge carrier extraction [10]. This photocathode first undergoes (b) Pt photo-deposition after electrode preparation, then followed by (c) The start of three-electrode stability experiment inside the glass chamber during a sunny day (AM 1.5G one-sun illumination). (d) After this run, the loss of Pt nanoparticles can be replenished, during night time, to Scheme 5.1(b) by doing Pt photo-deposition on the photocathode. Then the next cycle starts as shown in Scheme 5.1(c). This cycle consisting of stability run for 24 h, and subsequent Pt catalyst regeneration has been repeated more than 100 times throughout 3000 h.

5.2 Results and Discussions

For this study, n^+-GaN NWs are grown on the n^+-p Si substrates using a Veeco GEN II radio-frequency plasma-assisted molecular beam epitaxial growth (MBE) system. Fabrication of n^+-p Si substrate is discussed elsewhere [10]. The n^+-p Si substrate is first cleaned with acetone, methanol, and water to remove any organic contaminants. After drying the wafer with N_2 gun, it is immersed in BHF to remove native oxide. This pre-treatment of Si wafers is done before loading the wafer into the MBE system. The nanowires are formed spontaneously under nitrogen-rich conditions without using any external metal catalyst on Si substrate. The growth conditions included a substrate temperature range of 730 ^{o}C, a Ga BEP of 6×10^{-8} torr, nitrogen flow rate of 1 standard cubic centimeter per minute, forward plasma power of 420 W and growth duration of 2 h. The Pt regeneration cycle process is shown in Scheme 5.1. Scheme 5.1(a) shows as-grown n^+-GaN nanowires (NWs) on the n^+-p Si substrates using MBE, and at the bottom, the band-diagram is shown for the n^+-Si/n^+-GaN interface. In this band-diagram, the conduction band minimum (CBM) for n^+-GaN nearly aligns with n^+-Si CBM with a relatively small conduction band offset of 0.16 eV [14]. Detailed XPS measurements on GaN/Si interface are mentioned elsewhere [14]. Due to this small band-offset, the photo-generated electrons from n^+-p Si substrate are extracted by GaN NWs and provide surface passivation for Si by reducing interfacial recombination. The unique property of nearly aligned CBM between Si and GaN highlights the advantage of using GaN as an excellent protection layer on Si without compromising on PEC performance unlike other traditional protection layers [14, 72, 96, 244]. The scanning electron microscope (SEM) image in Figure 5.2(a) shows the nanowires without Pt NPs are vertically aligned to the Si substrate. Shown in the Scheme 1(b), after the MBE growth of n^+-GaN NWs on n^+-p Si substrate, the photo-electrodes are prepared, and Pt nanoparticles (NPs) are photo-deposited on these electrodes. The

structural characterizations after Pt photo-deposition for the samples are discussed using scanning transmission electron microscopy (STEM). Shown in Figure 5.2(b), the photo-deposited Pt NPs are uniformly distributed from middle to the bottom of the nanowire. Shown in Scheme 5.1(c), after Pt deposition, the stability test is started in a three-electrode configuration in 0.5M H_2SO_4 under AM1.5G one sun illumination. For this study, each stability test is carried out for ~ 24 h run experiment. Previously, it has been confirmed that loss of Pt NPs during stability experiments lead to worsening of *J-V* characteristics for the sample [14, 241]. Therefore, Pt catalyst regeneration is an efficient way to curtail the performance degradation and restore the *J-V* characteristics precisely the same as the initial measurements before the start of the stability test. Scheme 5.1(d) shows the loss of Pt NPs can be replenished, during "night" time, by doing an *ex-situ* regeneration using photo-deposition method. After restoring the Pt NPs on the electrode, the stability experiment continues as shown in Schemes 5.1(b) and 5.1(c). In this work, we have demonstrated that by repeated cycles of 24 h stability runs and subsequent catalyst regenerations, GaN/Si photocathode can achieve ultrahigh stability >3000 h with a high photocurrent density of ~38 mA/cm^2 under standard one-sun illumination.

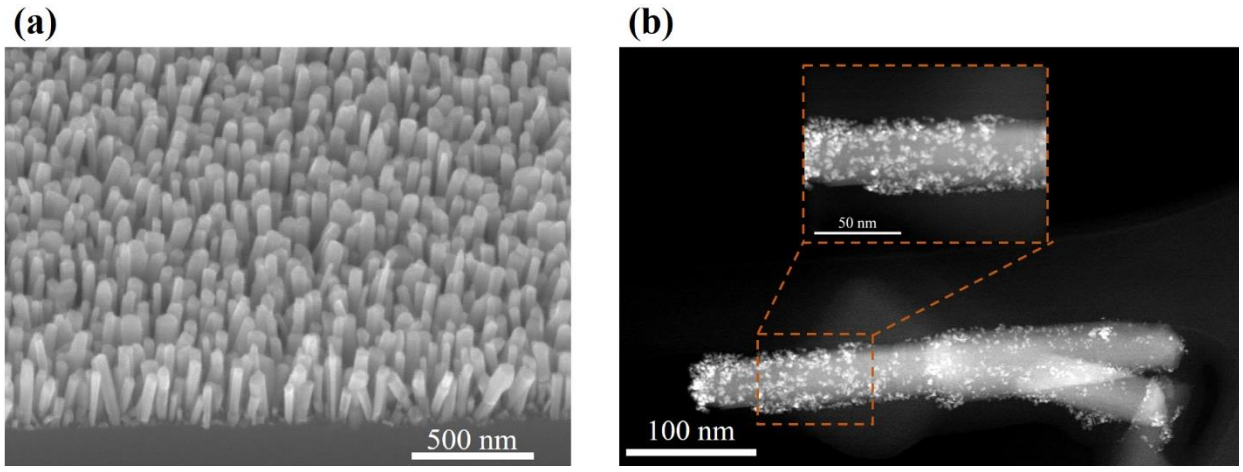

Figure 5.2. Structural characterization of n^+-GaN NWs on n^+-p Si substrate. (a) 45^o tilt SEM image of n^+-GaN nanowires on Si and (b) TEM image (HDAAF) of Pt nanoparticles decorated n^+-GaN nanowire. Inset is the magnified HDAAF image of the highlighted box region (brown color) showing the distribution of Pt nanoparticles on the nanowire.

All the PEC experiments, like *J-V* characterization and stability experiments, are conducted in 0.5 M H_2SO_4 solution in three-electrode configuration using n^+-GaN nanowires on n^+-p Si substrate with Pt co-catalyst, silver chloride electrode (Ag/AgCl), and Pt wire as the working (WE), reference (RE), and counter electrode (CE), respectively (see Scheme 5.1(c)). A solar simulator (Newport Oriel) with an AM1.5 G filter was used as the light source, and the light intensity was calibrated to be 100 mW/cm^2 for all the experiments. Considering the duration of the long-term stability experiments, it is essential to regularly calibrate the intensity of solar simulator, which was done by using Newport-Power-818-ST-UV power meter. The conversion of the Ag/AgCl reference potential to a reversible hydrogen electrode (RHE) is calculated using Eqn. 5.1,

$$E_{(RHE)} = E_{Ag/AgCl} + E^{o}_{Ag/AgCl} + 0.059 \times pH \quad \text{eq (5.1)}$$

where $E^{o}_{Ag/AgCl}$ is 0.197 V, and pH of the electrolyte is nearly zero. Figure 5.3(a) shows the linear scan voltammogram (LSV) of Pt deposited n^+-GaN NWs on n^+-p Si photocathode under AM 1.5G one sun illumination (red curve) and dark (black curve) conditions. The Pt NPs/n^+-GaN NWs/n^+-p Si photocathode showed an excellent performance with onset potential (V_{on}) of ~0.56 V *vs* RHE (at $|J|$ ~ 0.5 mA/cm^2 with dark current < 0.1 mA/cm^2) and high photocurrent density of ~ 37 mA/cm^2 under AM 1.5G one-sun illumination in 0.5M H_2SO_4. The applied bias photon-current efficiency (ABPE) of the photocathode was derived using Eqn. 5.2,

$$\eta(\%) = \frac{J(V_{RHE} - E^{0}_{rev})}{P_{in}} \times 100 \quad \text{eq (5.2)}$$

where J is the photocurrent density, E^{0}_{rev} = 0 V *vs.* RHE, V_{RHE} is the applied bias *vs.* RHE, and P_{in} is the power of the incident light (i.e., 100 mW/cm^2). In Figure 5.3(b), the maximum ABPE for Pt/n^+-GaN NWs/n^+-p Si photocathode (red curve) is 11.88% at 0.38 V *vs.* RHE under AM 1.5G one sun illumination in 0.5M H_2SO_4. This ABPE is one of the best reported for Si photocathodes in the literature [14, 71-73]. For the stability tests (both under dark and light), we have chosen only those samples with ABPE ≥ 10% and J at 0 V *vs.* RHE ~ 38 mA/cm^2.

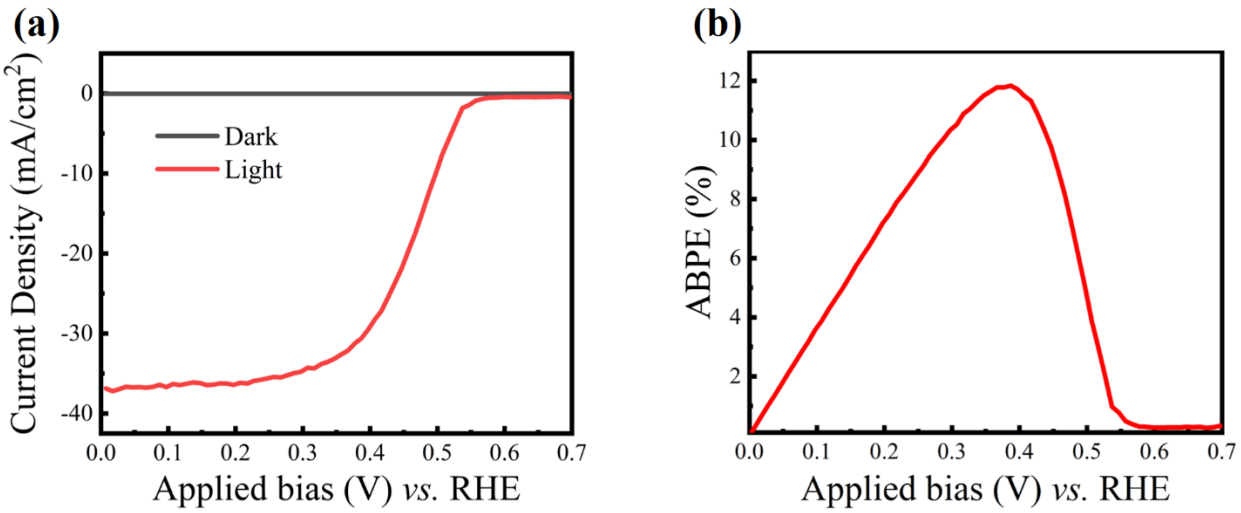

Figure 5.3. PEC characterization of n^+-GaN nanowires/n^+-*p* Si photocathode. (a) *J-V* curves of platinized n^+-GaN nanowires/n^+-*p* Si photocathode under AM 1.5G one-sun illumination (red curve) and dark (black curve) in 0.5M H_2SO_4. The Pt-decorated n^+-GaN nanowires/n^+-*p* Si photocathode showed V_{on} of ~0.56 V *vs.* RHE and high photocurrent density of ~ 37 mA/cm^2. (b) ABPE of n^+-GaN nanowires/n^+-*p* Si photocathode under AM 1.5G one sun illumination. The maximum ABPE for platinized n^+-GaN nanowires/n^+-*p* Si photocathode is 11.88% at 0.38 V *vs.* RHE.

Before starting the stability experiments, the electrode is thoroughly rinsed with distilled water and dried with N_2 gun. As discussed in Scheme 5.1(c), the photo-deposited electrode is then placed in 0.5M H_2SO_4 inside the PEC chamber, and the stability experiment is started at a constant applied potential of 0 V *vs.* RHE under AM1.5G one-sun illumination for a 24 h run experiment. Thus, after 24 h experiment, the electrode is taken out, and catalyst regeneration is initiated. Before starting the next cycle, the *J-V* characteristics are measured under both dark and AM 1.5G one-sun illumination to make sure there is no degradation in performance compared to 0^{th} h *J-V*

characteristics. After the *ex-situ* catalyst regeneration and LSV measurements, the experiment is resumed for the next cycle of stability test and catalyst regeneration. It is important to mention here that after every 24 h experiment (either dark or light condition), the electrolyte is replaced with a fresh solution to maintain a constant pH ~ 0 for all the runs and to reduce possible carbonaceous contaminations from epoxy [220]. After each regeneration cycle, the LSV curves (not shown here) deviate from the 0^{th} h *J-V* curve (J_0) under AM1.5 G one-sun illumination, which is due to the loss of Pt NPs as discussed in previous report [14]. If the Pt catalyst regeneration is delayed beyond a certain amount of time (>100 h), it may lead to further worsening in *J-V* characteristics and thereby cause irreversible degradation in photocurrent density [14]. Therefore, it is imperative to regenerate the Pt NPs promptly and avoid degradation in PEC performance.

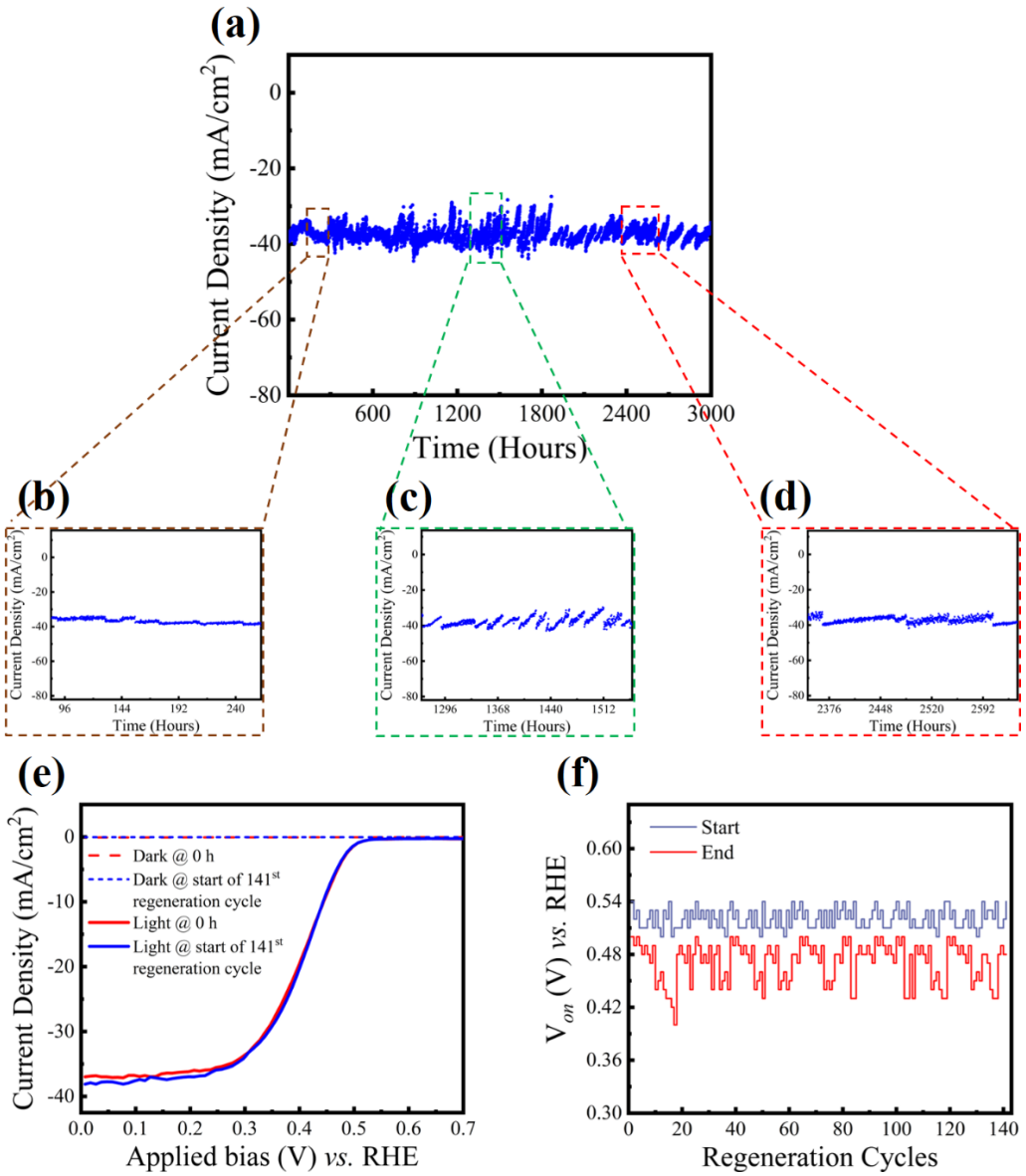

Figure 5.4. Long term stability of platinized n^+-GaN/n^+-p Si photocathode. (a) Chronoamperometry long term stability measurements for platinized n^+-GaN nanowires/n^+-p Si photocathode at 0 V *vs.* RHE in 0.5M H_2SO_4 under AM 1.5G one sun illumination. The photocurrent density of photocathode remained constant at ~38 mA/cm^2 for 3000 h duration with 140 catalyst regeneration cycles. (b) Stability results of the highlighted (brown dashed box) for 80-264 h runs (4th-12th regeneration cycles). (c) Stability results of the highlighted (green dashed box) for 1270-1539 h runs (59th-73rd regeneration cycles). (d) Stability results of the highlighted (red dashed box) for 2350-2640 h runs (113th-125th regeneration cycles). (e) LSV comparison between 0 h (red curves) and the start of the 141st regeneration cycle (blue curves) under dark (dotted) and AM 1.5G one-sun illumination (solid) in 0.5M H_2SO_4. (f) V_{on} (versus RHE) variations at the start (purple) and end (red) of each regeneration cycle during the ultrahigh long-term stability.

Figure 5.4(a) shows the photocurrent density variation over the entire duration of 3000 h for Pt NPs/n^+-GaN NWs/n^+-p Si photocathode under AM 1.5G one-sun illumination at 0 V *vs.* RHE in 0.5M H_2SO_4. As shown in Figure 5.4(b), for 80-264 h runs, i.e., between 4th and 12th regeneration cycles, the J varied between 36-40 mA/cm^2 which is within ± 10% of the J_0 at 0 V *vs.* RHE. Figure 5.4(c) shows that the variations in J increased to ~ ± 20-25% of the J_0 at 0 V *vs.* RHE for 1270-1539 h runs, i.e., from 59 to 73 regeneration cycles. These variations are mainly due to the unexpected epoxy meltdown, malfunctioning of potentiostat (due to electrical fluctuations in the building) and bad backside contact. Due to these unforeseen problems, we had to stop the experiments and troubleshoot these issues, which lead to an increase in the number of regeneration cycles. The experimental problems have been addressed during the subsequent runs by frequently redoing the backside contact after every 100-120 h runs and carefully monitoring the potentiostat during the cycles. Figure 5.4(c) shows the J variations for 2350-2640 h runs (between 113th and 125th regeneration cycles) is within ± 10% of the J_0. It is to be noted that despite J variations during the entire runs, the *J-V* characteristics at the start of 141st regeneration cycle, i.e., after 3008 h run with Pt redeposition, are the same as J_0 curve (see Figure 5.4(d)) which implies that GaN nanowires remain intact on Si surface. Furthermore, Figure 5.4(e) shows the variation of V_{on} for each regeneration cycle at the start (purple curve) and end (red curve) of each cycle. It is clear, from Figure 5.4(e), that due to the Pt NPs falling-off the charge transfer resistance increases which lead to a reduction in V_{on}. The catalyst regeneration, at the start of each cycle, helps in immediately recovering the V_{on} for the LSV curves. The structural analysis after 3000 h experiments was further confirmed by doing STEM and SEM studies. SEM image in Figure 5.5(a) shows that nanowires are still covering the Si substrate with no apparent reduction in dimensions compared to Figure 5.2(a). As shown in Figure 5.5(b), STEM image shows that the nanowire length is ~400 nm and

the diameter is ~ 40 nm which is the same as Figure 5.2(b). The inset in Figure 5.5(b) shows the reduction of Pt NPs over the nanowire compared to Figure 5.2(b). Due to the Pt NPs falling-off, the *J-V* curve immediately at the end of the 140th regeneration cycle has degraded compared to J_0 curve. By doing Pt regeneration at the start 141st regeneration cycle, the *J-V* characteristics have been restored to 0th h curves, which clearly shows that GaN NWs are still protecting the Si photocathode and the GaN-protected Si photocathode can last significantly longer than 3,000 h.

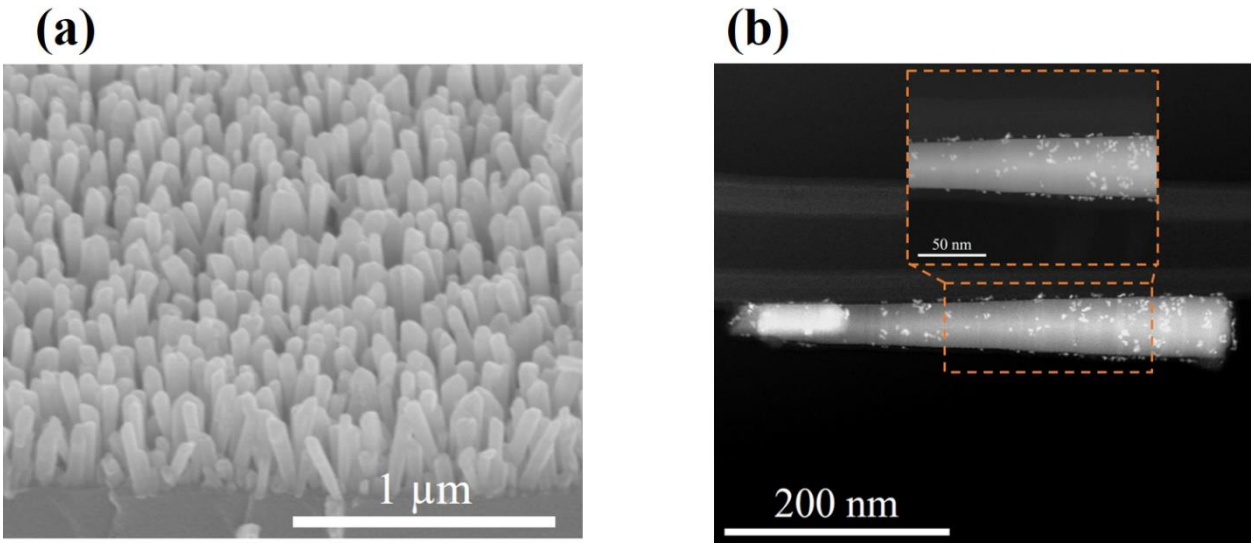

Figure 5.5. Structural characterizations of platinized n^+-GaN/n^+-*p* Si photocathode. (a) 45^o tilt SEM and (b) TEM of Pt-decorated n^+-GaN nanowire/n^+-*p* Si photocathode after 3000 h stability experiment. The inset in Figure 4(b) shows the HR-STEM image showing fewer Pt NPs non-uniformly distributed on the highlighted (brown dashed box) segment of the n^+-GaN nanowire.

We also evaluated the Faraday efficiency by analyzing the H_2 generation from Pt/n^+-GaN NWs/n^+-*p* Si photocathode between 0-2 h and 3000-3002 h. As shown in Figure 5.6(a), the photocurrent and H_2 evolution are simultaneously measured for the sample between 0-2 h at 0 V

vs. RHE for a duration of 2 h in 0.5M H_2SO_4 under AM 1.5G one sun illumination. Similarly, H_2 evolution experiment was carried out for the sample between 3000-3002 h (shown in Figure 5.6(b)) under the same conditions. The Faraday efficiency ($\eta_{(Faraday)}$) for these measurements were calculated by using Eqn. 5.3, which is basically the ratio of average experimental (red dots) and theoretically calculated (black dots) H_2 production.

$$\eta_{(Faraday)}(\%) = \frac{2 \times n_{H_2}\,(t=T_0)[mol] \times F}{\int_0^{T_0} I\,[A]\,.dt\,[s]} \times 100 \qquad \text{eq. (5.3)}$$

where *I* is the measured photocurrent, *F* is Faradaic constant (96485 C/mol) and n_{H_2} is the total amount of H_2 produced for a time duration T_0. H_2 was detected by gas chromatograph (GC, Shimadzu GC-8A) equipped with a thermal conducting detector (TCD). In both cases, the Faraday efficiency is nearly 100%, considering that there is an error bar ~10% of H_2 sampling. Given the nearly identical LSV curves measured at 0 h and 3000 h, it is reasonably concluded that the GaN/Si photocathode can drive solar water splitting for >3,000 h.

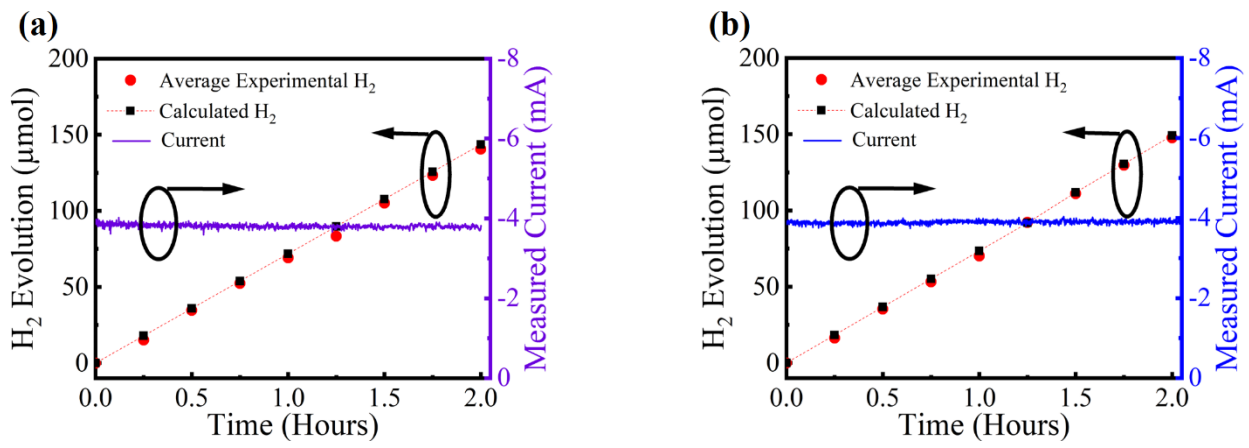

Figure 5.6. Faraday Efficiency of platinized n^+-GaN nanowires/n^+-p Si. H_2 generation for platinized n^+-GaN nanowires/n^+-p Si photocathode at 0 V *vs.* RHE under AM 1.5G one-sun illumination in 0.5M H_2SO_4 for (a) 0 h- 2 h and (b) 3000 h – 3002 h after Pt catalyst regeneration. Figures 4 (a) and (b) pink and blue curves are the measured photocurrents respectively. Red dots represent the average amount of H_2 generated at various times, and the black dotted line is the theoretical amount of H_2 produced against time based on photocurrent. The Faraday efficiency is nearly 100% in both experiments. The sample area is 0.12 cm^2 which corresponds to a photocurrent density of ~ 38 mA/cm^2.

The unprecedentedly ultrahigh stability of GaN protected Si photocathode can be attributed to two primary reasons. Firstly, the MBE grown GaN NWs are dislocations-free, and near-perfect single-crystal wurtzite nanostructures are having strong ionic bonds and absence of non-radiative recombination surface states [26, 245]. Also, these MBE grown NWs on Si substrate under N_2-rich conditions have the unique N-termination in both longitudinal and lateral directions which can improve the stability [26, 243]. Due to the relatively small conduction band offset between Si and GaN, there is no loss in charge carrier extraction [14]. These unique properties clearly show that GaN NWs

can protect the underlying Si surface against photo-corrosion with enhanced charge carrier extraction kinetics and better light absorption. As shown previously, there is a thin GaN layer beneath the NWs which protects the Si from the formation of insulating oxide and passivate the surface states to prevent charge carrier recombination [14]. Secondly, the Pt/GaN interface further enhances the charge carrier extraction compared to Pt/Si [14, 244] and thereby improve the overall stability of the photocathode. Thus, degradation of the Pt catalyst NPs will accelerate the whole photocathode degradation mechanism. As discussed earlier, through Pt catalyst regeneration process it is possible to replenish the fallen-off NPs on the GaN NWs and thereby prevent photocathode degradation to maintain the same level of performance for more than a thousand hours.

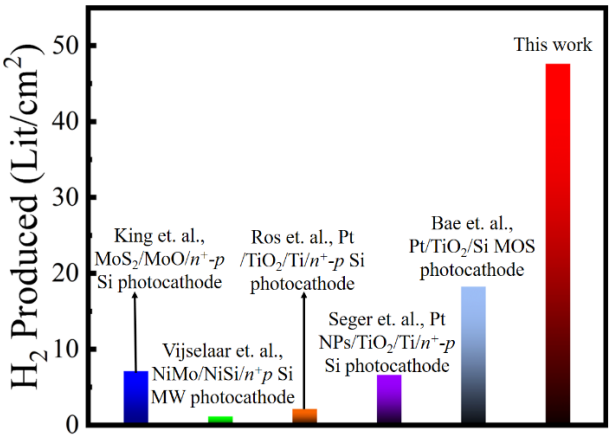

Figure 5.7. H_2 production for the best long-term stability photocathodes. Total H_2 production in Lit/cm^2 at STP for the best photocathodes [96, 97, 209, 220, 246]. Pt/n^+-GaN NWs/n^+-p Si photocathode gives the highest H_2 production of ~48 Lit/cm^2.

The total charge passed during 3000 h light experiment for Pt/n^+-GaN NWs/n^+-p Si photocathode is 410400 C/cm^2 by considering an average saturation photocurrent density of ~38 mA/cm^2 for 3000 h. The reported operation of the platinized n^+-GaN NWs/n^+-p Si photocathode for 3000 h contained the same amount of charge passed during >1.5 years of outdoor operation under AM 1.5G one-sun conditions with a solar capacity of 20% [216]. As the projected operation is a lower limit on the actual stability of Pt/n^+-GaN NWs/n^+-p Si, it is required to do accelerated long-term stability tests with temperature and light intensity variations to precisely identify the degradation/corrosion mechanisms. Furthermore, Figure 5.7 shows the amount of H_2 production (in Lit/cm^2) at STP conditions between the best reported long-term stability photocathodes [96, 97, 209, 220, 246] over the entire duration of the stability experiments. Compared to these photocathodes, the platinized n^+-GaN NWs/n^+-p Si photocathode has the highest H_2 production of > 45 Lit/cm^2. These results combined with the fact that GaN and Si are industry established materials clearly shows the scalability and economic viability of this photocathode system for large-scale implementation of PEC water splitting. Recent studies show that the PEC characteristics for n^+-GaN NWs/n^+-p Si photocathode are further improved by using controllable Pt loading amounts through PEC photo-deposition [244]. For future studies, we will focus on *in-situ* catalyst regeneration by using controllable Pt loading amounts, which can further reduce the H_2 production cost, to achieve ultrahigh stability and high efficiency.

5.3 Conclusions

In conclusion, we have demonstrated that Pt/n^+-GaN NWs/n^+-p Si photocathode can achieve high photocurrent density of ~ 38 mA/cm^2 with ultrahigh stability of 3000 h (>500 days) with no apparent degradation. The unique and robust combination of N-terminated GaN NWs along with Pt catalyst regeneration can protect the Si surface for 3000 h without any loss in *J-V* characteristics and ABPE. The Pt/GaN protects the underlying Si from photo-corrosion with enhancement in the charge carrier extraction, and through *ex-situ* catalyst regeneration it is possible to recover the fallen-off Pt NPs during the stability test. TEM and SEM analysis revealed that GaN NWs remained unchanged throughout the stability runs. The maximum achieved ABPE of 11.88% is also one of the highest values ever reported for a Si-based photocathode. This platform lays the foundation for developing high efficiency and long-term stable double junction InGaN/Si photocathode for unassisted water splitting. Moreover, we believe that the GaN protection layer will be of great interest in developing low cost, high efficiency, and ultrahigh stable photoelectrodes for solar hydrogen production.

Chapter 6: A High Efficiency Si Photoanode Protected by Few-Layer $MoSe_2$

In Chapter-5, we achieved high efficiency and ultrahigh stabile GaN/Si photocathodes using Pt nanoparticles for PEC water splitting. To reduce the H_2 production cost, it is essential to develop earth abundant passivation layers and co-catalysts. As discussed in Chapter-5, a passivation layer needs to be robust, i.e., it should simultaneously protect the semiconductor photocatalyst without any loss in PEC activity. Over the years, it has been established that transition metal dichalcogenides are catalytically active and low-cost materials for PEC water splitting. However, the growth of these materials over large-area wafers has not been fully developed. In this chapter*, we demonstrate, for the first time, the MBE growth of few monolayers $MoSe_2$ as a protection layer on Si photoanodes. Initially testing revealed that $MoSe_2$ protected Si photoanodes showed high photocurrent density and efficiency in 1M HBr solution.

---

* This chapter is from a published article: **S. Vanka**, Y. Wang, P. Ghamari, S. Chu, A. Pandey, P. Bhattacharya, I. Shih and Z. Mi, "A High Efficiency Si Photoanode Protected by Few-Layer $MoSe_2$", *Solar RRL*, 2, 1800113 (2018).

6.1 Introduction

The ever-increasing demand for energy has inspired intensive research on the development of sustainable and renewable energy sources to diminish our dependence on fossil fuels [247]. PEC water splitting is one of the most promising methods to convert solar energy into storable chemical energy in the form of H_2 production [248], which is a clean and eco-friendly alternative fuel that can be stored, distributed and consumed on demand [249]. A PEC device generally consists of a semiconductor photocathode and photoanode, which collect photo-generated electrons and holes to drive H_2 and O_2 evolution reaction, respectively [250]. For practical application, it is essential that the semiconductor photoelectrodes can efficiently harvest sunlight, are of low cost, and possess a high level of stability in aqueous solution. To date, however, it has remained challenging, especially for semiconductor photoanodes, to simultaneously meet these demands. Recently, Fe_2O_3 [251], $BiVO_4$ [252], Ta_3N_5 [253], GaP [254], GaN/InGaN [23, 202] and Si [255] have been intensively studied as photoanodes. Among these materials, Si is a low cost and abundantly available photoabsorber material, with an energy band-gap of 1.12 eV, which has advantages such as high carrier mobility and absorption of a substantial portion of sunlight [250, 178]. Si, however, is highly prone to photocorrosion [255a, 256]. Various surface protection schemes, including the use of TiO_2 and NiO_x, have been developed to improve the stability of Si-based photoanodes [254 257]. The use of wide bandgap and/or thick protection layers, however, severely limits the extraction of photoexcited holes, leading to very low photocurrent density and extremely poor applied bias photon-to-current efficiency (ABPE) in the range of 1-2% [254, 255a, 256b, 257b,d]. Recently, by using NiFe-LDH catalyst with Ni/NiO_x as a protection layer, an ABPE of ~4.3% has been demonstrated for Si photoanodes [258], which however, still lags significantly behind those (~10-15%) for Si-based photocathodes [72, 255c].

Studies have shown that earth-abundant two-dimensional (2D) transition metal dichalcogenides (TMDC), including MoS_2 [259], WSe_2 [260], $MoSe_2$ [260b, 261] and WS_2 [262a], possess remarkable properties for PEC application. The edge states of monolayer TMDC can provide catalytic sites for H_2 evolution reaction (HER) [262], and TMDCs have also been employed as photoanodes for oxidation reaction [259, 260b,d, 261, 263]. Recent first principles calculations have further revealed that perfect 2D TMDCs are chemically inert [264], and their excellent stability in acidic electrolyte has also been reported [96]. Due to the van der Waals bonds, high quality interface can be formed when 2D TMDC is deposited on Si surface, which can offer an effective means to passivate the Si surface and minimize surface recombination [265]. To date, however, there have been no reports on the use of 2D TMDCs as a surface protection layer for semiconductor photoanodes. This has been limited, to a large extent, by the lack of controllable synthesis process of 2D TMDCs. The commonly used exfoliation process is not suited to produce uniform TMDCs with controlled thickness and high-quality interface on a large area wafer [266a, b]. Alternatively, the growth/synthesis of 2D TMDCs using bottom-up approaches such as chemical vapor deposition (CVD) and molecular beam epitaxy (MBE) have been intensively studied [266]. The latter method, which utilizes ultrahigh vacuum (UHV) environment, is highly promising to produce high purity and controllable film thickness [266a, b, 267].

Herein, we have investigated the MBE growth of large area $MoSe_2$ film on p^+-n Si substrate and have further studied the PEC performance of Si photoanode with $MoSe_2$ protection layers of varying thicknesses. It is observed that the incorporation an ultrathin (~3 nm) epitaxial $MoSe_2$ can significantly enhance the performance and stability of p^+-n Si photoanode. The $MoSe_2$/p^+-n Si photoanode produces a nearly light-limited current density of ~30 mA/cm^2 in 1M HBr under AM 1.5G one sun illumination, with a current-onset potential of 0.3 V *vs* RHE. The ABPE reaches up

to 13.8%, compared to the negligible ABPE values (< 0.1%) of bare Si photoanode. Moreover, nearly 100% hole injection efficiency is achieved under a relatively low voltage of < 0.6 V *vs* RHE. The chronovoltammetry analysis for the photoanode shows a stable voltage of ~0.38 V *vs* RHE for ~14 hrs at ~2 mA/cm^2. The effect of $MoSe_2$ layer thickness on the PEC performance is also investigated. This work shows the extraordinary potential of 2D TMDC in PEC application and promises a viable approach for achieving high efficiency Si-based photoanodes.

6.2 Results and Discussions

Schematically shown in Figure 6.1a, $MoSe_2$ films were grown on p^+-n Si substrate using a Veeco GENxplor MBE system. The fabrication of p^+-n Si wafer is described in Appendix-3.1. As described in Experimental Section, the MBE growth of $MoSe_2$ thin film results in 2H structure [266b], which is schematically shown in Figure 6.1a. The energy band diagram of the $MoSe_2$/p^+-n Si photoelectrode is illustrated in Figure 6.1b. Photoexcited holes can tunnel through the thin $MoSe_2$ protection layer to participate in oxidation reaction, while photoexcited electrons from Si migrate towards the counter electrode to participate in H_2 evolution reaction. The $MoSe_2$ layer also suppresses surface recombination [265b]. It is seen that the thickness of $MoSe_2$ is critical: it needs to be optimally designed and synthesized to protect the Si surface against photocorrosion and oxidation without compromising the hole transport and extraction.

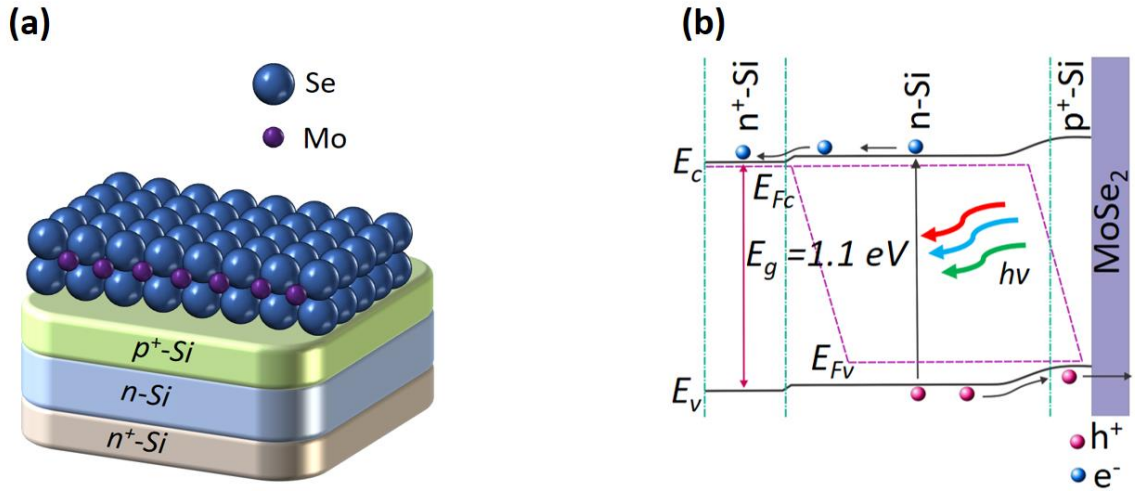

Figure 6.1. (a) Schematic illustration of p^+-*n* Si photoanode protected by few-layer 2H $MoSe_2$. Dark blue and purple colored atoms denote Se, and Mo, respectively. (b) Schematic of the energy band diagram of $MoSe_2$ /p^+-*n* Si photoanode under AM1.5G light illumination.

Properties of $MoSe_2$ grown on Si wafer by MBE are characterized using X-ray photoelectron spectroscopy (XPS), atomic force microscopy (AFM), and micro-Raman spectroscopy. We have first analyzed the composition of $MoSe_2$ layers by using XPS measurement (Thermo Scientific K-Alpha XPS system with a monochromatic Al Kα source (hν=1486.6 eV)). The binding energy of carbon (284.58 eV) was used as a reference peak position for the measurements.

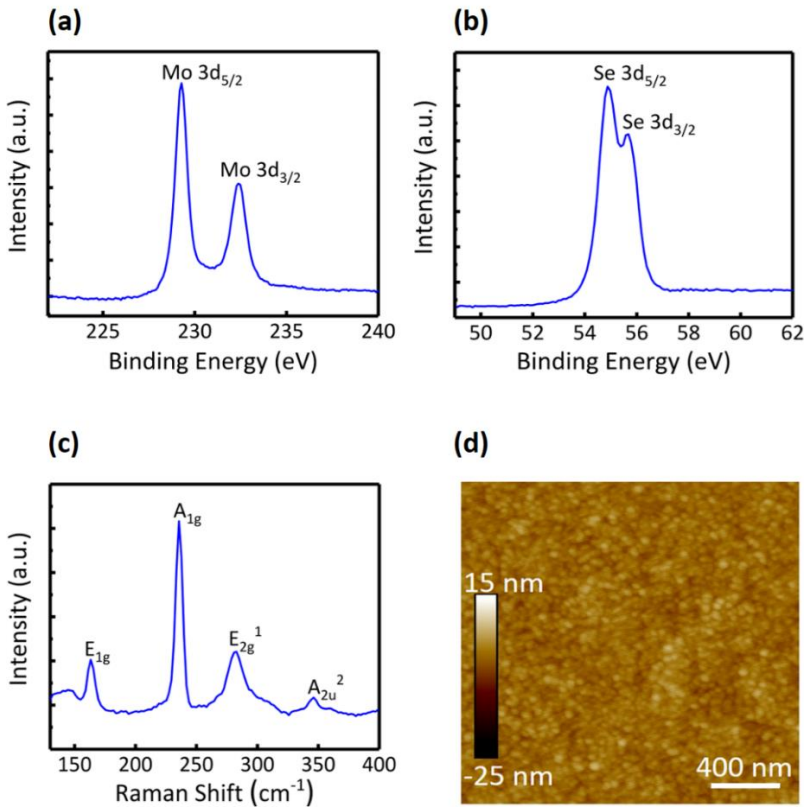

Figure 6.2. Structural characterization of few-layer $MoSe_2$ grown on Si substrate. XPS measurements show (a) two peaks at 229.2 and 232.4 eV corresponding to Mo^{4+} and (b) doublet of 54.9 and 55.6 eV corresponding to Se^{2-} for $MoSe_2$ film. (c) Raman spectra for $MoSe_2$ film showing E_{1g}, A_{1g}, $E_{2g}{}^1$ and $A_{2u}{}^2$ modes at 163.02, 235.67, 281.89 and 346.18 cm^{-1}, respectively. (d) AFM image of $MoSe_2$ surface on Si wafer; scale bar 400 nm. The thickness of $MoSe_2$ layer is ~ 3nm.

Figure 6.2a shows two peaks located at 229.2 and 232.4 eV which originated from Mo $3d_{5/2}$ and Mo $3d_{3/2}$ orbitals, respectively, confirming the existence of Mo^{4+} [268]. Shown in Figure 6.2b, a single doublet of Se $3d_{5/2}$ at 54.9 eV and Se $3d_{3/2}$ at 55.6 eV can be observed, corresponding to the oxidation state of -2 for Se [266b, e, 268]. These results confirm the formation of $MoSe_2$ on the Si wafer.

Micro-Raman spectroscopy was carried out using a 514 nm argon ion laser as the excitation source. Illustrated in Figure 6.2c, emission peaks at 163.02, 235.67, 281.89 and 346.18 cm^{-1} have been identified, which correspond to E_{1g}, A_{1g}, $E_{2g}{}^1$ and $A_{2u}{}^2$ modes, respectively. The most prominent peaks are A_{1g} and $E_{2g}{}^1$ modes, which are related to the out-of-plane vibration and in-plane vibration, respectively. These Raman modes, unique to 2H-$MoSe_2$, have been observed in previous reports and suggest the formation of 2H-phase $MoSe_2$ on Si wafer [269]. Shown in is the AFM image of $MoSe_2$ film (~3 nm thick) grown on Si (also see Appendix-3.3).

We have subsequently investigated the PEC performance of $MoSe_2/p^+$-*n* Si photoanode. As a first demonstration, we have conducted the PEC experiments in HBr electrolyte. The OER on the photoanode is a sluggish process which requires four holes and due to the slow kinetics, the H_2 formation is hindered on the counter electrode. It is known that Br evolution reaction (BrER) is thermodynamically favored over OER and therefore, BrER compliments H_2 production. Due to the minimal overpotential for BrER, most of the materials are limited by photocurrent rather than photovoltage and thereby shows HBr electrolyte is well suited to test the quality of the PEC material and produce H_2 for large-scale commercial usage. The linear scan voltammogram (LSV) of $MoSe_2/p^+$-*n* Si photoanodes with various $MoSe_2$ thicknesses is shown in Figure 6.3a under both dark and illumination conditions. Further details of the LSV for p^+-*n* Si photoanode with and without any $MoSe_2$ coverage are shown in Appendix-3.4. It is observed that the p^+-*n* Si photoanode exhibit negligible photocurrent, which is directly related to the rapid surface oxidation of unprotected Si surface [270]. Superior performance was achieved for $MoSe_2/p^+$-*n* Si photoanodes with ~3 nm $MoSe_2$. Shown in Figure 6.3a, the current-onset potential is ~0.3 V *vs* RHE, with a nearly light-limited current density ~30 mA/cm^2 measured at ~0.8 V *vs* RHE (Appendix-3.5). The measurement of light-limited current density also suggests that the thin $MoSe_2$ layer can effectively

passivate the Si surface to minimize surface recombination. The achievement of high photocurrent density for a photoanode under relatively low bias voltage is essentially required to realize unassisted solar H_2 generation when paired with a high-performance photocathode for PEC tandem system. With increasing $MoSe_2$ thickness to ~5 nm, the photocurrent density is reduced to ~27 mA/cm^2, due to the less efficient tunneling of photo-excited holes from Si to electrolyte. It is worth mentioning that the reduction of photocurrent density may be partly related to the increased absorption of $MoSe_2$ protection layer due to the slightly larger thickness. Previous studies have shown that the hole tunneling through the protection layer is extremely sensitive to the layer thickness [254b].

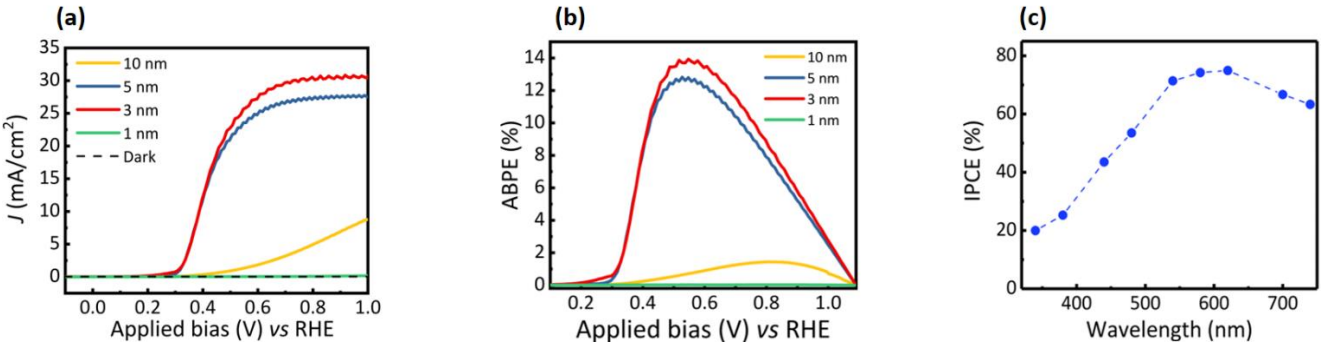

Figure 6.3. PEC performance characterization of $MoSe_2/p^+$-*n* Si photoanode. (a) *J-V* characteristics of $MoSe_2/p^+$-*n* Si photoanode with $MoSe_2$ thicknesses of 1nm (green curve), 3 nm (red curve), 5 nm (blue curve) and 10 nm (yellow curve) under AM1.5G one sun illumination (100 mW/cm^2) and dark condition (black dashed curve) in 1M HBr. (b) ABPE measurement for $MoSe_2/p^+$-*n* Si photoanode with different $MoSe_2$ thicknesses. The highest ABPE of 13.8% was measured for Si photoanode with 3 nm $MoSe_2$ protection layer at ~0.5 V *vs* RHE. (c) IPCE of $MoSe_2/p^+$-*n* Si photoanode under AM1.5G one sun illumination (100 mW/cm^2) in 1 M HBr. The peak value is ~75% at 620 nm.

In this study, since the surface roughness is relatively large (~ 1-2 nm) for $MoSe_2$ layers, we observed a relatively small difference in the photocurrent density by increasing the thicknesses from 3 nm to 5 nm. Also for these reasons, it is observed that decreasing the $MoSe_2$ thickness to ~1 nm leads to negligible photocurrent density, due to the uneven surface coverage and the resulting oxidation of the Si surface. With further increasing the $MoSe_2$ thickness to ~10 nm, both the photocurrent density and current-onset potential become significantly worse, due to the suppressed tunneling for photo-generated holes. In these studies, the underlying Si wafers are identical and are contacted from the backside. Therefore, the drastically different PEC characteristics are directly related to the thicknesses of $MoSe_2$ protection layer, which provides unambiguous evidence that an optimum thickness of epitaxial $MoSe_2$ can protect the semiconductor photoanode without compromising the extraction of photo-generated holes. Through detailed studies on the $MoSe_2$ growth temperature and *in situ* annealing conditions (see Appendix-3.2), it was identified that the best performing $MoSe_2/p^+$-*n* Si photoanodes could be achieved for $MoSe_2$ thickness ~3 nm and growth temperature in the range of 200 to 400 °C.

The ABPE of the photoanode was derived using the Equation (6.1),

$$\eta(\%) = \frac{J(E^0_{rev} - V_{RHE})}{P_{in}} \times 100 \qquad \text{eq. (6.1)}$$

where J is the photocurrent density, E^0_{rev} is the standard electrode oxidation potential for Br^-, V_{RHE} is the applied bias *vs* RHE, and P_{in} is the power of the incident light (*i.e.* 100 mW/cm^2). Variations of the ABPE *vs* applied bias are shown in Figure 6.3b for $MoSe_2/p^+$-*n* Si photoanodes with $MoSe_2$ thicknesses varying from 1 to 10 nm. It is seen that a maximum ABPE of 13.8% is achieved at ~0.5 V *vs* RHE for $MoSe_2/p^+$-*n* Si photoanodes with $MoSe_2$ thickness ~3 nm. The maximum ABPE decreases to ~12% and 2% with increasing $MoSe_2$ thickness to 5 and 10 nm, respectively, and to negligible values for $MoSe_2$ thicknesses of 1 nm or less. The reported ABPE of 13.8% is

significantly higher than previously reported TMDC-based photoanode in polyhalide-based redox systems and hole scavenger solutions [260b-d, 261, 271]. However, the cost of using HBr for solar-to-hydrogen production needs to be analyzed, compared to water splitting [272]. The incident-photon-to-current-efficiency (IPCE) of $MoSe_2/p^+$-*n* Si photoanode with $MoSe_2$ thickness ~3 nm was further measured. The measurement was conducted at 1 V *vs* RHE in 1M HBr in a three-electrode system. The IPCE was calculated using the Equation (6.2),

$$IPCE\ (\%) = {}^{(1240\ \times I)}\Big/_{(\lambda\ \times P_{in})} \times 100 \qquad \text{eq. (6.2)}$$

where I is photocurrent density (mA/cm^2), λ is the incident light wavelength (nm) and P_{in} is the power density (mW/cm^2) of the incident illumination. Shown in Figure 6.3c, the maximum IPCE is above 70%.

We have further studied the open circuit potential (OCP) of $MoSe_2/p^+$-*n* Si photoanodes, which was measured *vs* RHE under chopped light illumination. A negative shift of the OCP was measured under light illumination, which is characteristic of photoanodes. The OCP (E_{ocp} *vs* RHE) of p^+-*n* Si and $MoSe_2/p^+$-*n* Si with $MoSe_2$ thickness ~3 nm is shown in Figure 6.4a. The p^+-*n* Si photoanode (dotted blue curve) exhibits a dark potential ~0.3 V and an illuminated potential ~0 V, with a change in OCP ~0.3 V. The change in OCP under dark and illumination conditions is less than the photovoltage ~0.53 V for a typical p^+-*n* Si junction, which is due to the change of potential drop across the Helmholtz layer at the Si/electrolyte interface. E_{ocp} of the $MoSe_2/p^+$-*n* Si photoanode (solid red curve) is ~0.3 V and 0.8 V *vs* RHE under illumination and dark conditions, respectively. The potential difference under light and dark conditions is ~0.5 V, which is nearly identical to the flat-band potential (V_{fb}) derived from the Mott-Schottky measurements (Appendix-3.6). Moreover, the light-induced OCP shift (~0.5 V) for $MoSe_2/p^+$-*n* Si photoanode is reasonably close to the open circuit voltage expected from the p^+-*n* Si junction. The negligible voltage loss

further confirms that the thin (~3 nm) $MoSe_2$ layer can effectively protect the Si surface from oxidation in acidic solution and that photoexcited holes can tunnel efficiently through the $MoSe_2$ layer. Chronovoltammetry experiments were further performed to test the stability of $MoSe_2/p^+$-*n* Si photoanode at photocurrent density of ~2 mA/cm^2 under AM 1.5G one sun illumination. Shown in Figure 6.4b, the voltage stays nearly constant at ~0.38 V vs RHE, and there is no any apparent degradation under continuous illumination for ~14 h. The chronoamperometry experiment (see Appendix-3.7) also showed stable photocurrent density of ~26 mA/cm^2 for 1 h at 0.6 V vs RHE and subsequent XPS measurements on that sample showed Mo:Se ratio of 1:2.

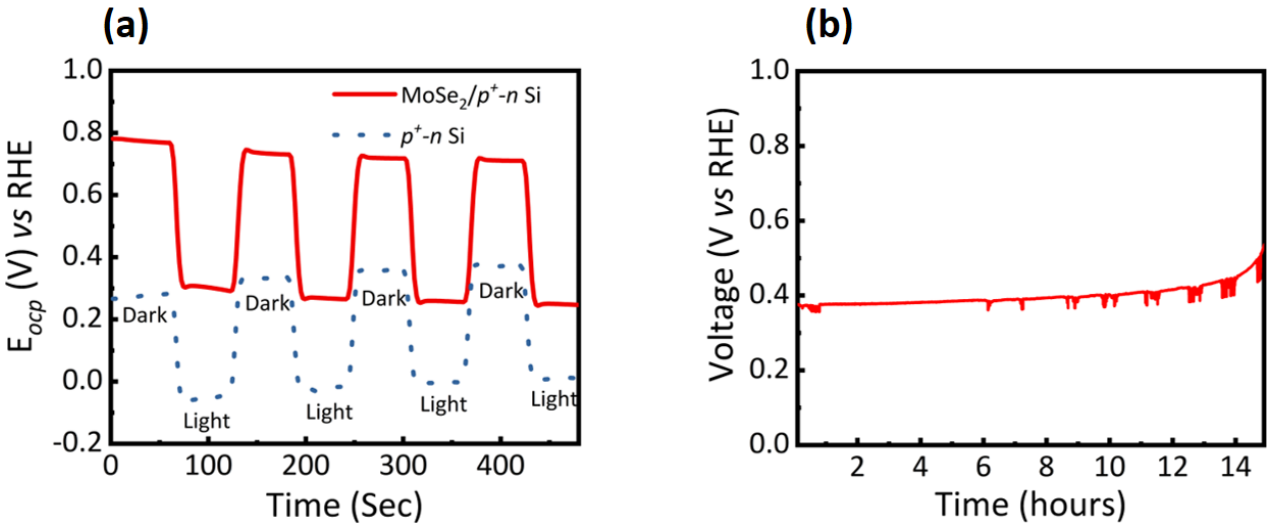

Figure 6.4. OCP and Stability measurements of $MoSe_2/p^+$-*n* Si photoanode. (a) OCP *vs* RHE under chopped light illumination. Red curve shows OCP for $MoSe_2/p^+$-*n* Si photoanode, and dotted blue curve is OCP for p^+-*n* Si without $MoSe_2$. (b) Stability of $MoSe_2/p^+$-*n* Si photoanode. Chronopotentiometry graph shows stable voltage (*vs* RHE) ~0.38 V for ~14 hrs at ~2 mA/cm^2 under AM 1.5G one sun illumination in 1 M HBr.

The underlying mechanisms for the dramatically improved performance of Si-based photoanodes are described. The use of a $MoSe_2$ protection layer allows for the efficient tunneling of photoexcited holes from p^+-n Si to electrolyte through the $MoSe_2$ barrier, compared to the previously reported wide bandgap, e.g. TiO_2 protection layer [254, 273]. This is evidenced by the very large hole injection efficiency (>80%) even at a relatively low potential (~0.5 V *vs* RHE) (see Appendix-3.8). As seen from Appendix-3.8, at relatively low bias ~0.5-0.6 V *vs* RHE the hole injection efficiency is ≥ 80% for $MoSe_2$ thicknesses of 3 nm and 5 nm. The shaded region in Appendix-3.8 indicates hole injection efficiency >80%. The achievement of very high hole injection efficiency at a relatively low biasing voltage suggests the efficient tunneling of photogenerated holes from Si to solution through the $MoSe_2$ protection layer. Therefore, thin $MoSe_2$ layer (~3 nm) is sufficient to allow for most of the incident light to pass through, thereby leading to a nearly light-limited current density. For a perfect $MoSe_2$ sheet, there are no dangling bonds and surface states, since the lone pair of electrons on chalcogen (Se) atom terminate on the surface [265a].

Recent first principles calculations have further shown that a perfect $MoSe_2$ sheet is intrinsically chemically inert and can effectively protect against oxidation [264, 265a] and photocorrosion [265a], which explains the dramatically improved performance and stability, compared to a bare Si photoanode. It is also worthwhile mentioning that the enhanced performance is not likely due to the catalytic property of $MoSe_2$, since the $MoSe_2$ layer showed no activity under dark condition (see Appendix-3.4 and Figure 6.3a) and the 1 nm thickness sample (in Figure 6.3a) showed very poor light scan. To further improve the device stability, it is essential to eliminate, or minimize the presence of Se vacancy and related defects, which are known to significantly enhance the oxidation effect [264, 274].

6.3 Conclusions

In conclusion, we have demonstrated that the integration of few-layer $MoSe_2$ can protect the surface of an otherwise unstable Si photoelectrode in corrosive environment, while allowing for efficient electron/hole tunneling between Si photoanode and solution. The $MoSe_2/p^+$-*n* Si photoanode exhibit remarkable PEC performance, including an excellent current-onset potential of 0.3 V *vs* RHE, a light-limited current photocurrent density of ~30 mA/cm^2 under AM1.5G one sun illumination, an ABPE of 13.8%, and relatively high stability in acidic solution. For future work, it would be important to investigate and optimize the $MoSe_2$/Si heterointerface, to engineer the surface properties of $MoSe_2$, and to couple with suitable water oxidation co-catalysts, which will further improve the current-onset potential and enhance the photoanode performance and stability in PEC water splitting. These studies will contribute to the development of low cost, high efficiency, and highly stable Si-based photoelectrodes for solar H_2 production.

Chapter-7: High Efficiency and High Stability InGaN/Si Double Junction Photocathode for Solar Water Splitting

In Chapters-4 and 5, we demonstrated the extraordinary potential of N-terminated GaN nanowires for achieving unprecedented levels of stability without any degradation in PEC performance. These studies lay a solid foundation for developing tandem device structure which can produce high efficiency and long-term stability for unassisted PEC water splitting. As described in *Section 2.5 and Section 1.7.2*, tandem photoelectrodes are essentially required to achieve high efficiency but the current III-V based photoelectrodes are unstable. In this work*, we present a framework for the tandem design of p^+-InGaN nanowires monolithically integrated on Si solar cell via a customized tunnel junction. From the PEC experiments, we observed that this photocathode can generate an open circuit potential of ~ 2 V which is sufficient to split water under unbiased conditions.

---

* This chapter is based on a manuscript under preparation: **S. Vanka** *et al.* (Except for primary authors: S. Vanka and Z. Mi, other co-authors and their orders are to be determined). B. Zhou and N. Pant contributed to some of the photoelectrochemical experiments.

7.1 Introduction

Solar hydrogen (H_2) fuel is one of the best sustainable and clean alternatives to address the current global energy needs by using the two most abundant natural resources on earth, i.e., water and sunlight [69, 211, 275]. Photoelectrochemical (PEC) water splitting is one of the most promising approaches to solar water splitting [69, 276, 277] and for this approach to be competitive, it is pertinent to achieve solar-to-hydrogen (STH) efficiency > 10%, lifetime stability > 10 years and low H_2 production costs [38, 88, 211]. PEC devices using tandem configurations, with top light absorber bandgap ~ 1.8 eV and bottom light absorber bandgap ~ 1.1 eV, have the potential to reach a maximum theoretical STH efficiency ~ 27% [43c, 69, 38, 130]. Apart from bandgap requirements, a tandem device must have an active tunnel junction (TJ) which are optically transparent and electrically conducting and possess a low level of structural defects and dislocations. Since the first III-V tandem structure demonstration by Khaselev et al. [43b], there have been significant improvements in the STH values of III-V materials. The state-of-the-art STH and stability for all photoelectrodes, over the last two decades, is summarised in Figure 7.1. The highest STH reported for III-V photoelectrodes is 19.3% [43d], and the range of efficiencies for the III-V photoelectrodes are generally reported between ~ 10-19% [43, 218]. The significant disadvantages for the high-efficiency III-V semiconductors are: 1) the inherent spontaneous photo-corrosion in acidic or alkaline electrolytes which leads to the deterioration in materials properties [221, 278]; and 2) the high costs required for fabrication of high-quality single-crystalline materials [88]. There have been efforts to improve the stability of III-V compound semiconductors, at the expense of reduced STH and higher fabrication cost, by adding TiO_2 protection layer [43f] and using bifacial electrode design with thick metal layers for GaAs photoelectrodes [218]. As shown in Figure 7.1, the stability for III-V compound semiconductors, with the protection schemes, under two-electrode measurement

conditions, is still low (<40 h). On the other hand, as seen in Figure 7.1, the non-III-V photoelectrodes, i.e., metal oxides like $BiVO_4$ and Fe_2O_3 [279-282]; and Si [283], are plagued by low STH efficiencies (< 9%), due to the poor material quality which leads to inefficient bulk transport of charge carriers and instability in different electrolytes [23, 229, 284]. Therefore, there is a need to develop alternative low cost, high efficiency and high stability photoelectrodes for unassisted water splitting.

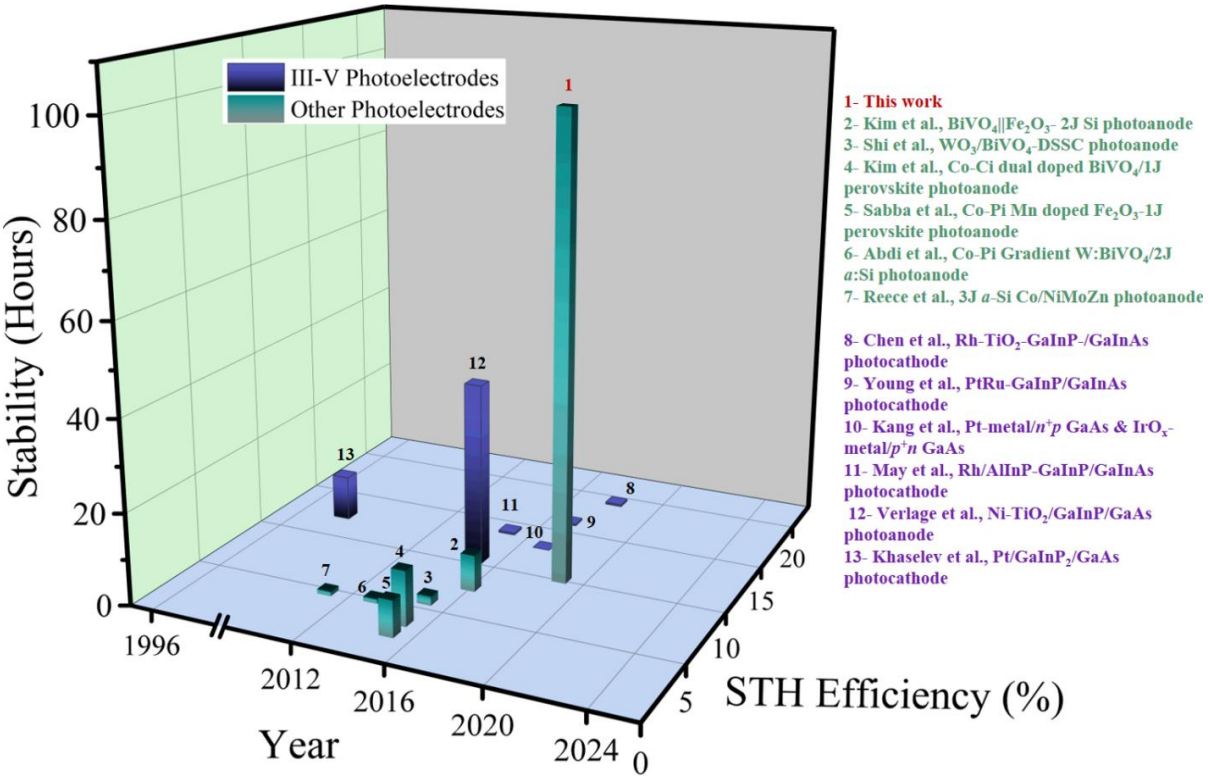

Figure 7.1. State-of-the-art comparison between different photoelectrodes. Graphical representation of stability and solar-to-hydrogen (STH) efficiency for previously reported semiconductor photoelectrodes measured under AM 1.5G one sun illumination [43, 218, 279-283, 292-294]

.

N-terminated III-nitride compound semiconductors have tunable bandgap from 0.65 eV to 3.4 eV by varying the indium incorporation [7], large carrier mobility [134], and high light absorption [285] and are stable in different electrolytes [14, 242, 243]. Over the years, many research groups focused on using III-nitride nanostructures as photocatalysts for water splitting [11, 13, 14, 24, 134, 286] to achieve high efficiency and long-term stability. Molecular beam epitaxy (MBE) grown III-nitrides under nitrogen-rich conditions produce stable N-terminated (In)GaN nanostructures compared to Ga-terminated structures grown via chemical vapor deposition (CVD) or metal organic chemical vapor deposition techniques (MOCVD) [26, 243]. It has been demonstrated that InGaN or Al TJ can be incorporated inside the III-nitride nanowires (NWs), grown either on Si and other substrates, to achieve high performing LED [40, 41, 287, 288] and photocathodes for H_2 production in different electrolytes [22, 289]. Since InGaN and Si are the two most widely used semiconductors in electronics and optoelectronic industries, a tandem device consisting of these two light absorbers will be an excellent alternative in achieving high STH and high stability with reasonably low fabrication cost for solar water splitting.

In this work, we investigate and demonstrate the use of surface modified InGaN/Si double-junction photocathode to achieve high STH efficiency > 10 % and stability of 100 h for unassisted water splitting. This double-junction consists of a top p^+-InGaN cell, with an energy bandgap ~ 2.3 eV, connected to n^+-p Si wafer using a unique TJ design within the nanowire arrays. The MBE grown p^+-InGaN/TJ/n^+-InGaN NWs on Si wafers have N-terminated surfaces which protect against photo-corrosion [26]. The nanowire surface is modified using the Pt nanoparticles (NPs) and the subsequently deposited Al_2O_3 thin film using atomic layer deposition (ALD) method. ALD provides a uniform and homogenous surface passivation layer for the NWs. The best performing surface modified p^+-InGaN/TJ/n^+-InGaN NWs/n^+-p Si photocathode shows an excellent onset

potential (V_{on}) ~2.3 V *vs.* RHE with high photocurrent density of ~16 mA/cm^2 at 0 V *vs.* RHE and a high applied bias photon-to-current efficiency (ABPE) of 9.6% under AM 1.5G one-sun illumination in 0.5M H_2SO_4. The PEC performance in the two-electrode configuration of Al_2O_3/Pt/p^+-InGaN/TJ/n^+-InGaN NWs n^+-p Si photocathode shows photocurrent density ~ 8.2 mA/cm^2 at 0 V *vs.* IrO_x and the corresponding STH is ~ 10.1% under same experimental conditions. Further impedance studies reveal the charge transfer mechanism in the double-junction device. Chronoamperometry analysis for the photocathode shows a stable photocurrent density of ~8.2 mA/cm^2 for 100 h at 0 V vs. IrO_x under AM 1.5G one-sun illumination in 0.5M H_2SO_4. This work provides a new perspective in developing high efficiency and high stability devices from industry-ready materials for large-scale solar water splitting.

7.2 Results and Discussions

Design of photocathode and structural characterization. As shown in Figure 7.2a, the double junction photocathode consists of p^+-InGaN top light absorber, p^{++}-InGaN/n^{++}-InGaN tunnel junction, and n^+-p Si bottom light absorber. The n^+-p Si wafers are prepared using thermal diffusion, and the details were described elsewhere [14]. The scanning electron microscope (SEM) image, illustrated in Figure 7.2b, shows the NWs are vertically aligned on n^+-p Si wafer with a height of ~800 nm and diameter of ~100 nm. The photoluminescence emission spectrum (see Figure 7.2c) shows a sharp peak wavelength at ~540 nm, corresponding to an average indium composition of ~27% and an energy bandgap of ~2.3 eV [197, 289]. In principle, the photoexcited electrons from p^+-InGaN can reduce protons without any external bias [87, 197]. As shown in Figure 7.2d, the downward band bending of p^+-InGaN can promote the extraction of photo-generated electrons to the electrolyte. The photo-generated electrons from n^+-p Si wafer are extracted by n^+-InGaN nanowire arrays as shown in the inset of Figure 7.2a. The bottom n^+-InGaN acts as an

active hole blocking layer for n^+-p Si. These photo-generated electrons from the bottom Si cell then recombine with the photo-generated holes from the top p^+-InGaN layer in the TJ (as shown in Figures 7.2a and 7.2d). Before PEC testing, p^+-InGaN/TJ NWs/n^+-p Si photocathode undergoes surface modifications as shown in Figure 7.2a. First, Pt NPs are deposited on p^+-InGaN/TJ NWs/n^+-p Si using photo-deposition. Then, as shown in the inset of Figure 7.2a, the Pt NPs/ p^+-InGaN/TJ NWs/n^+-p Si is covered by a thin layer (~2 nm) of Al_2O_3.

Photoelectrochemical measurements. Figure 7.3a shows the three-electrode linear scan voltammogram (LSV) comparison between the Al_2O_3/Pt/p^+-InGaN/TJ/n^+-InGaN NWs n^+-p Si photocathode (red curve) and platinized n^+-InGaN NWs/n^+-p Si photocathode (blue curve) under AM 1.5G one-sun illumination and dark condition (green curve) in 0.5M H_2SO_4. The Pt/n^+-InGaN NWs/n^+-p Si photocathode has V_{on} of ~ 0.5 V *vs.* RHE, whereas Al_2O_3/Pt/p^+-InGaN/TJ/n^+-InGaN NWs n^+-p Si has V_{on} of ~ 2.3 V *vs.* RHE. This improvement is due to voltage add up between p^+-InGaN (~1.8 V *vs.* RHE) and Si (~0.5 V *vs.* RHE). Assuming that the HER overpotential is low [290], the V_{on} will be close to flat-band potential (V_{fb}), suggesting that V_{fb} is ~ 2.34 V *vs.* RHE.

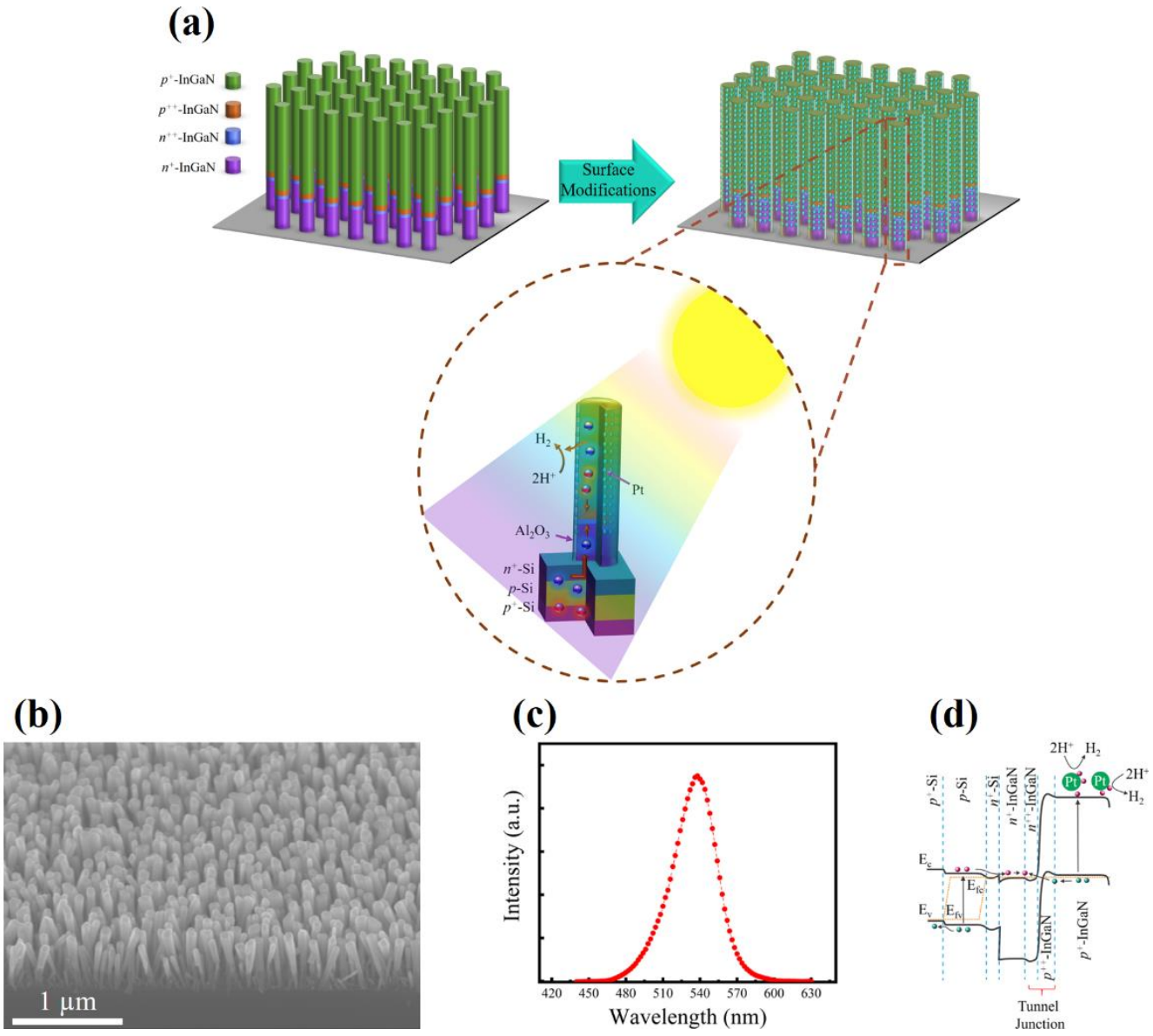

Figure 7.2. Structural and optical properties of InGaN nanowires. (a) Top schematic shows InGaN nanowire arrays on Si substrate before and after surface modifications. The bottom schematic is the cross-sectional view of nanowire and Si substrate showing light absorption by the p^+-InGaN and Si, subsequent electron transfer from Si wafer to n^+-InGaN, charge recombination in the tunnel junction and proton reduction on Al_2O_3/Pt covered p^+-InGaN nanowires. (b) 45° tilt SEM image of as-grown p^+-InGaN nanowires with tunnel junction on Si wafer. (c) Room-temperature photoluminescence spectrum from as-grown p^+-InGaN nanowires. (d) Band-diagram of the Pt/p^+-InGaN/TJ/n^+-InGaN NWs n^+-p Si photocathode showing charge carrier generation in Si and p^+-InGaN, and charge extraction from Pt/p^+-InGaN.

As shown in Figure 7.3a, the maximum photocurrent density for Al_2O_3/Pt/p^+-InGaN/TJ/n^+-InGaN NWs n^+-p Si photocathode is ~ 16 mA/cm^2 at 0 V *vs.* RHE. Compared to the Pt/n^+-InGaN NWs/n^+-p Si, the photocurrent density for Al_2O_3/Pt/p^+-InGaN/TJ/n^+-InGaN NWs n^+-p Si photocathode are lower at 0 V vs. RHE. This is because the device is limited by the top p^+-InGaN segment (with a band gap ~ 2.3 eV) which can give a theoretical maximum of ~ 9- 11 mA/cm^2 [291], whereas for the other photocathodes, without this segment, Si is the primary light absorber, and it can achieve a maximum photocurrent density ~ 44 mA/cm^2. The reason for higher photocurrent density for the double-junction (~ 16 mA/cm^2) compared to the theoretical maximum is due to the additional current coming from the bottom n^+-InGaN/n^+-p Si cell. Since Pt photo-deposition is uniformly distributed throughout the nanowire [14, 22], the Pt NPs/n^+-InGaN segment will extract photo-generated electrons from the bottom Si cell to participate in proton reduction [22]. Therefore, at lower biases (< 0 V *vs.* RHE), the bottom Si cell provides additional photocurrent density along with top p^+-InGaN segment which thereby increases the overall photocurrent density of the photocathode. The applied bias photon-to-current efficiency (ABPE) of this photocathode is ~ 9.6% at 1.3 V *vs.* RHE (see Figure 7.3b). The reported ABPE is one of the highest for Si-based photocathodes [187, 190, 192, 203].

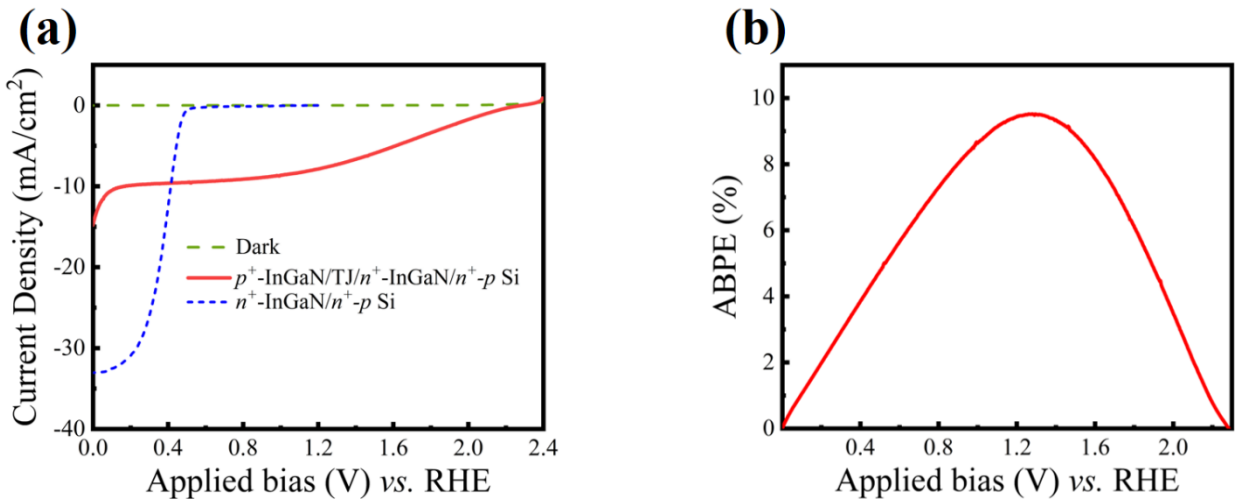

Figure 7.3. Photoelectrochemical performance of surface modified InGaN/Si double-junction photocathode. (a) Three-electrode linear scan voltammogram (LSV) of p^+-InGaN/tunnel junction (TJ)/n^+-InGaN nanowires/n^+-p Si photocathode (red curve) and platinized n^+-InGaN nanowires/n^+-p Si photocathode (blue curve) in 0.5 M H_2SO_4 under AM 1.5G one sun illumination and dark condition (green curve). (b) Applied bias photon-to-current efficiency (ABPE) of p^+-InGaN/tunnel junction (TJ)/n^+-InGaN nanowires/n^+-p Si photocathode under AM 1.5G one sun illumination.

The maximum photocurrent density for the optimized Al_2O_3/Pt/p^+-InGaN/TJ/n^+-InGaN NWs n^+-p Si photocathode, at 0 V *vs.* IrO_x, is ~ 8.2 mA/cm^2 (see Figure 7.5b) under AM 1.5G one-sun illumination in 0.5M H_2SO_4. The effect of Al_2O_3 on the double junction in terms of improving charge transfer characteristics is further discussed in the subsequent section. The STH, as calculated using Eqn. 7.3, for Al_2O_3/Pt/p^+-InGaN/TJ/n^+-InGaN NWs n^+-p Si photocathode is ~ 10.1% under AM 1.5G one-sun illumination. As shown in Figure 7.1, to the best of our knowledge, this is the highest STH for Si and non-III-V based photocathodes [279-283, 292, 293].

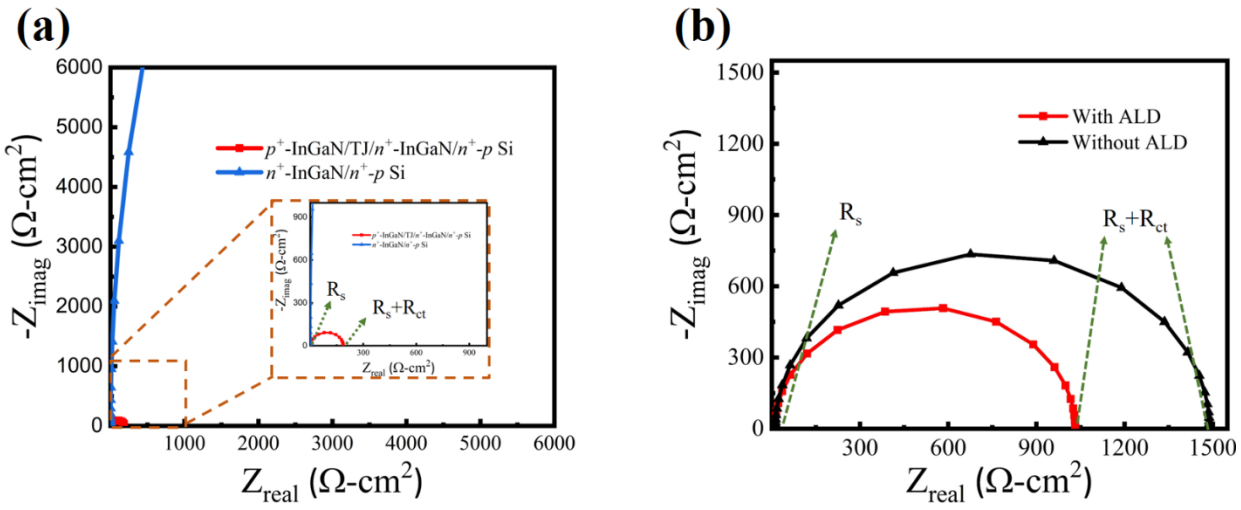

Figure 7.4. Impedance spectroscopy of surface modified InGaN/Si double-junction photocathode. (a) Nyquist plots of p^+-InGaN/tunnel junction (TJ)/n^+-InGaN nanowires/n^+-p Si photocathode (red curve) and platinized n^+-InGaN nanowires/n^+-p Si photocathode (blue curve) at 1.2 V vs. RHE in 0.5 M H_2SO_4 under AM 1.5G one sun illumination. Impedance values represented by dots on each curve correspond to frequencies from 10^6 to 0.1 Hz (in the clockwise direction along the semicircle arc). R_{ct} is the charge resistance at the catalyst/liquid junction interface and R_s is the charge transfer resistance at the semiconductor/catalyst interface. Inset: Magnified Nyquist plots for the two photocathodes. (b) Nyquist plots of p^+-InGaN/tunnel junction (TJ)/n^+-InGaN nanowires/n^+-p Si photocathode with (red curve) and without (black curve) ALD Al_2O_3 in 0.5 M H_2SO_4 under AM 1.5G one sun illumination.

Impedance measurements. Further detailed electrochemical impedance spectroscopy (EIS) measurements are done in 0.5 M H_2SO_4 under AM 1.5G one sun illumination for both two- and three-electrode configurations for different samples to understand the charge transfer characteristics. Figure 7.4a shows the Nyquist plots between Al_2O_3/Pt/p^+-InGaN/TJ/n^+-InGaN

NWs n^+-p Si and Pt/n^+-InGaN/n^+-p photocathodes. The R_{ct} is calculated using the equivalent circuit models derived from these plots [14]. It is to be noted that double-junction photocathode has the lowest R_{ct} (< 150 Ω cm^2) at an applied bias 1.2 V *vs.* RHE compared to Pt/n^+-InGaN/n^+-p photocathode (> 10,000 Ω cm^2). This result shows that the top p^+-InGaN under illumination gives out photo-generated electrons, which are efficiently transferred to the electrolyte through the surface modification layers (i.e., Pt NPs and Al_2O_3) and the photo-generated holes recombine with the electrons from bottom Si without any losses in the TJ.

As discussed previously, the Al_2O_3 passivation layer helps in improving the LSV characteristics for the double junction device. Figure 7.4b shows the two-electrode EIS measurements at 0 V *vs.* IrO_x for double-junction photocathode with and without Al_2O_3. The semicircle arc in the lower frequency range (especially R_{ct}) for the double-junction photocathode with Al_2O_3 has a smaller diameter compared to the one without Al_2O_3 which is due to the reduction in charge carrier recombination, especially in p^+-InGaN segment. Since the NWs are coated with relatively thin (~ 2 nm) ALD Al_2O_3 films, the photo-generated electrons from Pt NPs/p^+-InGaN segment can easily tunnel through Al_2O_3 and participate in HER. Thus, Al_2O_3 thin-film further helps in reducing HER overpotential which has been previously observed in Si-based photocathodes [183, 190]. This Al_2O_3 film also acts as a protection layer [183 , 190, 191] for the NWs and assist in improving the stability of the double-junction photocathode.

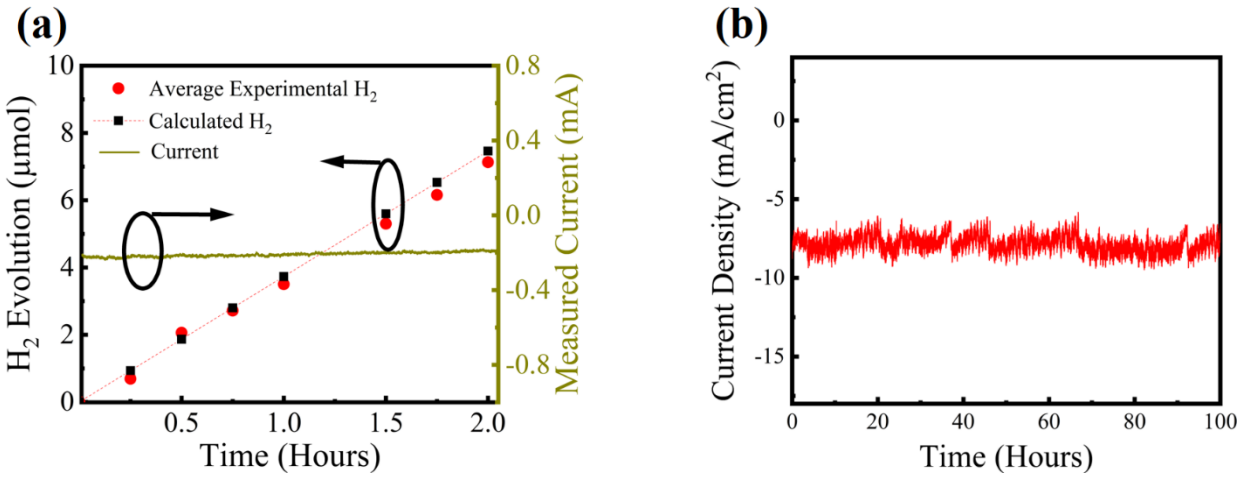

Figure 7.5. Hydrogen evolution and stability measurements of surface modified InGaN/Si double-junction photocathode. (a) H_2 generation for p^+-InGaN/tunnel junction (TJ)/n^+-InGaN nanowires/n^+-p Si photocathode at 0 V *vs.* IrO_x under AM 1.5G one-sun illumination in 0.5 M H_2SO_4 for 2 h. (b) Long-term stability measurement for p^+-InGaN/tunnel junction (TJ)/n^+-InGaN nanowires/n^+-p Si photocathode at 0 V *vs.* IrO_x in 0.5 M H_2SO_4 under AM 1.5G one-sun illumination.

Faraday efficiency and Stability measurements. We have evaluated the Faraday efficiency by analyzing the H_2 generation from Al_2O_3/Pt/p^+-InGaN/TJ/n^+-InGaN NWs n^+-p Si photocathode. In Figure 7.5a, the photocurrent, and H_2 evolution are simultaneously measured at 0 V *vs.* IrO_x for a duration of 2 h in 0.5M H_2SO_4 under AM 1.5G one-sun illumination. The Faraday efficiency ($\eta_{Faraday}$) is calculated using Eqn. 7.5 and it is in the range of 95-100%. We further conducted a long duration stability test for Al_2O_3/Pt/p^+-InGaN/TJ/n^+-InGaN NWs n^+-p Si photocathode at 0 V *vs.* IrO_x in 0.5M H_2SO_4 with 1 mM Triton X-100 surfactant under AM 1.5G one-sun illumination. As shown in Figure 7.5b, the photocurrent density showed no degradation for a duration of 100 h. To maintain the same experimental conditions throughout the stability test,

the electrolyte was changed after every 24 h experiments. The J varied within 10-20% of the average photocurrent density ~ 8.2 mA/cm^2 which corresponds to STH variation ~ 9 ± 1.5% throughout the stability experiments. The observed fluctuations in photocurrent are due to the changes in the potential of the counter electrode at 0 V *vs.* IrO_x. This high stability at STH ~ 10%, as shown in Fig. 1, is the longest stability reported for any photoelectrodes including III-V photoelectrodes in two-electrode configuration [43, 218, 279-283, 292-294].

The underlying mechanisms for the high efficiency and long-term stability of Al_2O_3/Pt/p^+-InGaN/TJ/n^+-InGaN NWs n^+-p Si photocathode are further discussed. The high STH value of ~10% is due to the MBE grown N-terminated NWs which have nearly perfect single wurtzite structure with no defects or dislocations [26]. Previous studies show that the conduction band edges of GaN and Si are nearly perfectly aligned with an offset of ~ 0.16 eV [14]. These unique characteristics combined with the nanowire morphology help achieve high efficiency by significantly improving the charge carrier extraction at the InGaN/Si interface and light absorption for the underlying Si, which was also observed in the EIS measurements. Due to the unique polarization induced TJ incorporated in the NWs [287, 288, 295], the charge carriers from the top p^+-InGaN cell (photo-generated holes) can easily tunnel and recombine with charge carriers from bottom Si cell (photo-generated electrons) in the TJ. It is to be noted that the TJ also serves as an excellent electron blocking layer to enhance electron extraction from the p^+-InGaN segment. One of the critical limitations for this structural design is the surface recombination at the top p^+-InGaN segment. As shown in Figure 7.4b, there are some significant surface recombination sites at Pt/p^+-InGaN interface which gives rise to lower J, poor fill factor and higher R_{ct} values. Depositing a thin Al_2O_3 layer on the nanowire surface helps in reducing the surface recombination, which acts as an efficient tunneling layer for electrons from Pt/p^+-InGaN to the electrolyte and further protects

the nanowire against corrosion. Due to the efficient InGaN/Si photocathode design and Al_2O_3 protection layer, the device is capable of performing unassisted water splitting [134]. Therefore, it can be concluded that Al_2O_3/Pt/p^+-InGaN/TJ/n^+-InGaN NWs n^+-p Si photocathode can achieve high STH values and further In-rich InGaN (with bandgap ~ 1.8 eV) growth optimization will help in achieving STH > 15%.

Although Al_2O_3 is amphoteric, studies have shown that Al_2O_3 can be stable in PEC long-term stability experiments [183, 190, 191]. The high stability for Al_2O_3/Pt/p^+-InGaN/TJ/n^+-InGaN NWs n^+-p Si photocathode of 100 h is also attributed to the stability of III-nitride NWs. It is known that III-nitrides have strong ionic bonds compared to other III-V semiconductors, with surface states bunched near the band edges, which make them resistant against corrosion in different electrolytes [10, 26, 296]. Recent theoretical studies show that MBE grown III-nitrides have unique N-termination not only on their top c-plane but also along the nonpolar sidewalls [26]. Such N-terminated NWs experimentally demonstrated high stability of > 500 h under photocatalytic water splitting conditions with no additional protection layers [242] and > 100 h under PEC water splitting conditions under three-electrode measurements [14]. Previous studies show that N-terminated InGaN NWs on non-planar Si wafers, without any additional protection layer, can achieve high stability ~ 30 h with high J ~12 mA/cm^2 at 0 V *vs.* RHE in 0.5M H_2SO_4 under AM 1.5G one-sun illumination [289]. Therefore, p^+-InGaN NWs are stable in acidic solution and protect the underlying Si wafer against photo-corrosion which makes this double-junction photocathode a viable option for large-scale implementation of high-efficiency PEC water splitting.

7.3 Conclusions

In conclusion, we have demonstrated the fabrication of monolithically integrated MBE grown p^+-InGaN/TJ/n^+-InGaN NWs on n^+-p Si wafer which can achieve a high STH > 10% with long-term stability of 100 h for PEC water splitting. The MBE grown InGaN TJ NWs on Si have high-crystalline quality, large surface area, and N-termination on both polar and non-polar side faces which provides stability against photo-corrosion for the entire structure without compromising the PEC performance. Impedance studies showed the importance of top p^+-InGaN segment, TJ and surface modifications to improve electron extraction and reduce the surface recombination. The Al_2O_3/Pt/p^+-InGaN/TJ/n^+-InGaN NWs n^+-p Si photocathode exhibits a photocurrent density of ~ 8.2 mA/cm^2 at 0 V *vs.* IrO_x under AM 1.5G one-sun illumination in 0.5M H_2SO_4. There was no performance degradation observed during 100 h stability experiment for unassisted solar water splitting, which can be attributed to two reasons: the formation of N-terminated surfaces of MBE grown InGaN NWs to protect against photo-corrosion and surface passivation by Al_2O_3 thin-films. Our studies provide a via platform for developing industry-ready materials to achieve highly efficient and stable unassisted solar water splitting for low-cost H_2 production.

Chapter-8: Conclusion and Future Work

8.1 Summary of the Completed Work

III-nitrides are one of the most widely produced compound semiconductors for solid-state lighting, blue/green laser diodes, and high-power electronic devices. Compared to conventional oxide-based photoelectrodes, III-nitride nanowires offer distinct advantages, including a tunable energy bandgap (0.65-3.4 eV) across nearly the entire solar spectrum, conduction and valence band edges that can straddle water redox and carbon dioxide (CO_2) reduction potentials under deep visible and possibly near-infrared light irradiation, and efficient charge carrier separation and extraction. It was observed that III-nitrides with unique N-termination are robust against attack by air/aqueous electrolytes and lead to exceptional stability in harsh water splitting and CO_2 reduction conditions. Therefore, III-nitrides are excellent photocatalyst materials for PEC/PC solar water splitting and CO_2 reduction. Over the years, tremendous progress has been made in developing III-nitride films and nanostructures for solar-to-chemical fuel conversion applications, using only sunlight and H_2O/CO_2 as inputs. Molecular beam epitaxy (MBE) grown III-nitrides, under nitrogen-rich conditions, on commercially available Si wafers provides high quality, single-crystalline, and N-terminated custom-designed nanostructures which can meet kinetic and thermodynamic requirements for PEC water splitting.

In this work, we have first investigated the design and implementation of In-rich InGaN nanowires on Si as a photoanode with IrO_2 co-catalysts for high-efficiency solar water oxidation. By engineering the InGaN nanowires with a bandgap of ~ 1.7 eV, we achieved a half-cell conversion efficiency (ABPE) of ~ 3.6% and an excellent onset potential of 0.1 V *vs.* RHE. These studies show the potential of developing a tandem device using InGaN nanowires as the top light absorber to achieve STH >25%.

We further investigated the use of GaN nanostructures as a multi-functional protection layer for Si photocathode. By doing X-ray photo spectroscopy measurements (see Chapter-4), we observed that the conduction band offset between N-terminated GaN and Si is relatively small ~ 0.16 eV. These observations along with impedance spectroscopy results for charge transfer resistance helped in understanding the unique advantages of GaN as a protection layer over current protection layers. From these pioneering studies, we showed that GaN protection layer on Si photocathode could achieve ultrahigh stability of 3,000 h (over 500 days, considering 5.5 h of available sunlight during a day) at a large photocurrent density (> 35 mA/cm^2) in 0.5M H_2SO_4 under AM 1.5G one-sun illumination with catalyst regeneration. The reported half-cell conversion efficiency (ABPE) of 11.88% is among the highest values ever reported for Si-based photocathodes for PEC water splitting.

We also investigated the use of earth-abundant transition metal dichalcogenides (TMDC) as protection layers for PEC water splitting. Large area $MoSe_2$ film was grown on p^+-n Si substrates using MBE. Structural properties and photoelectrochemical measurements were conducted in 1M HBr under AM 1.5G one-sun illumination. We report nearly 100%-hole injection efficiency is achieved under a relatively low voltage of < 0.6 V *vs.* RHE. The half-cell conversion efficiency (ABPE) is 13.8%, and the photoanode further produced a stable voltage for ~14 h under AM 1.5G one-sun illumination. These results show the potential of 2-D TMDC for development of low cost, high efficiency, and highly stable Si-based photoelectrodes for solar H_2 production.

In the end, we demonstrated the growth and implementation of InGaN/Si double-junction photocathode for unassisted PEC water splitting. As discussed in *Section 2.5*, PV+PEC devices can achieve high STH values of > 25% with top and bottom light absorber bandgaps of ~ 1.75 eV and 1.1 eV respectively. In this study, p^+-InGaN nanowires, with energy bandgap ~ 2.3 eV, are

monolithically integrated on n^+-p Si solar cell with the use of polarization induced TJ incorporated in the nanowires. This N-terminated p^+-InGaN/tunnel junction/n^+-InGaN nanowires on Si solar cell, with surface modifications, achieved one of the highest solar-to-hydrogen (STH) efficiency values of ~ 10.1% along with unprecedented long-term stability of 100 h in the two-electrode configuration for unbiased photoelectrochemical water splitting in 0.5M H_2SO_4 under AM 1.5G one-sun illumination. These pathbreaking results provide an attractive platform for building large scale high efficiency and stable PEC water splitting systems.

In conclusion, this thesis mainly focuses on the extraordinary potential of MBE grown N-terminated III-nitride compound semiconductors on large area Si wafers, as a low-cost and viable platform, for developing high efficiency (STH > 10%) and ultrahigh stability (> 500 days) for solar hydrogen production.

8.2 Future Work

8.2.1 CO_2 Reduction using III-Nitrides

CO_2 is a major greenhouse gas that is negatively impacting the earth's environment. PC CO_2 reduction is a widely researched topic, and it is different from the conventional approaches which require high pressure and temperature. In PC CO_2 reduction, solar energy is directly converted into storable hydrocarbon fuels and help mitigate greenhouse emissions into the atmosphere. CH_3OH is an essential chemical product from PC CO_2 reduction. Unlike the two-electron process for CO_2 to CO, CH_3OH requires multiple proton-coupled electron process. The following Eqns. (8.1) - (8.8) show the electrochemical potential versus RHE to convert CO_2 into different reduction compounds along with redox potentials for splitting water at pH=7. The photocatalytic methane-forming reaction requires eight electrons and eight protons compared to

the carbon monoxide, which needs only two electrons and two protons. All the products from these reduction reactions are useful feedstock for many industrial purposes.

$$CO_2 + 2H^+ + 2e^- \rightarrow HCOOH \qquad E^o = -0.61\,V \qquad \text{eq. (8.1)}$$

$$CO_2 + 2H^+ + 2e^- \rightarrow CO + H_2O \qquad E^o = -0.53\,V \qquad \text{eq. (8.2)}$$

$$CO_2 + 4H^+ + 4e^- \rightarrow HCHO + H_2O \qquad E^o = -0.48\,V \qquad \text{eq. (8.3)}$$

$$CO_2 + 6H^+ + 6e^- \rightarrow CH_3OH + H_2O \qquad E^o = -0.38\,V \qquad \text{eq. (8.4)}$$

$$CO_2 + 8H^+ + 8e^- \rightarrow CH_4 + H_2O \qquad E^o = -0.23\,V \qquad \text{eq. (8.5)}$$

$$2H^+ + 2e^- \rightarrow H_2 \qquad E^o = -0.41\,V \qquad \text{eq. (8.6)}$$

$$2H_2O + 4h^+ \rightarrow O_2 + 4H^+ \qquad E^o = 0.82\,V \qquad \text{eq. (8.7)}$$

$$H_2O + h^+ \rightarrow {}^*OH + H^+ \qquad E^o = 2.32\,V \qquad \text{eq. (8.8)}$$

Many semiconductors have been directly used as photocatalysts to reduce CO_2 to other fuel products. The thermodynamic requirements for a photocatalyst/photoelectrode are: 1) CBM must be more negative than the redox potentials of CO_2 reduction as shown in Eqs. (8.1) - (8.8) and VBM must be more positive than water oxidation potential; 2) Bandgap should cover majority of the solar spectrum. Since CO_2 is a very stable molecule, the catalytic conversion efficiencies into valuable hydrocarbons using photocatalysts are low. The key issue for CO_2 reduction is to tune the selectivity towards valuable fuel. There have been studies on many co-catalyst metal particles on the surface of the photocatalyst to help in improving the solar-to-fuel conversion efficiency and selectivity. However, it remains a major challenge to develop an efficient and stable PC/PEC catalytic system that can activate the stable CO_2 molecule at relatively low overpotential or even spontaneously, and selectively produce solar-fuels on a large-scale.

Our preliminary research studies showed a high degree of selectivity of co-catalysts nanoparticles such as Rh/Cr_2O_3 core-shells and Pt. Since Pt is an expensive catalyst, we also tried

with copper oxide (CuO_x) as a co-catalyst using the multi-band InGaN/GaN nanowires photocatalyst. From Figure 8.1a, the maximum CH_3OH gas production with CuO_x is ~ 3 mmole/g_{cat}/hr. As seen in Figure 8.1b, the average rate of CH_3OH gas production is ~ 1mmole/g_{cat}/hr under the full spectrum of a Xe lamp with an AM1.5G filter which is two times better than Pt-decorated InGaN/GaN nanowires (~0.5 mmoles/g_{cat}/hr) [297]. This proves the potential of using earth abundant CuO_x as an active co-catalyst which complements the activity of the photocatalyst. Further studies are required to investigate the visible light irradiation (>400 nm) using CuO_x co-catalyst on multi-band *p*-InGaN/GaN nanowires.

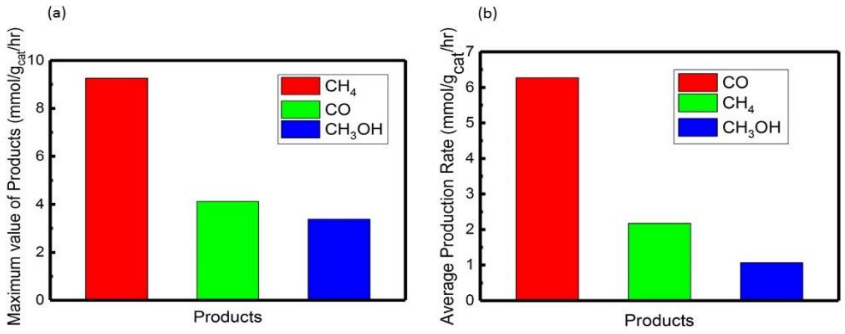

Figure 8.1. (a) Maximum value and (b) average production rates of CO, CH_4, and CH_3OH evolution rates on CuO_x-decorated *p*-InGaN/GaN nanowire photocatalysts under the full spectrum of a Xe lamp with an AM1.5G filter.

We have also demonstrated an efficient and stable PEC CO_2 reduction system for syngas production with controlled composition, by employing a metal/oxide interface. These nanostructured III-nitride photocatalysts provide a new pathway for artificial photosynthesis, thereby opening new avenues for solar chemical fuels production using renewable energy sources. Future work will focus on developing III-nitride photocatalysts with appropriate co-catalysts such

as Sn, Pd, and Fe for selectively producing liquid HCOOH and CH_3OH products with high solar-to-fuel conversion efficiency and stability. Apart from the co-catalyst optimization, the InGaN/Si double-junction, as discussed in Chapter-7, can be used for developing high efficiency and stability PEC CO_2 reduction photocathodes under AM 1.5G one-sun illumination.

8.2.2 Double-Junction Photocathode for STH> 15% and Stability > 1000 h

From Chapter-7, InGaN/Si double-junction with surface modifications provides a new avenue for achieving a solar-to-hydrogen conversion efficiency of over 15% and stability over 1,000 hours. To improve the current performance of the double-junction, for reaching the goals mentioned above, it is important to address three main important factors. Firstly, the yield and uniformity of the Si solar cell need to be improved with further optimization of doping concentration, annealing temperature, texturing the planar Si surface into non-planar micro-pyramid structures and using different dopant sources. In the current device, the open circuit potential contribution of Si is limited to ~0.5 V, whereas a good n^+-p Si solar cell with an anti-reflection coating can give a maximum open circuit potential of ~ 0.75 V [298, 299]. The second factor for improvement is to further reduce the bandgap of InGaN to ~ 1.75 eV which can absorb solar spectrum up to 700 nm wavelength and thereby increase the photocurrent density for the top cell to ~ 20 mA/cm^2 [15, 23]. Finally, the charge carrier resistance at the InGaN/Si interface can be further reduced by increasing the diameter of the nanowires. The diameter of the nanowire can be controlled by optimizing the MBE growth conditions such as Ga flux, In flux, growth temperature, doping concentrations and N_2 flow. The efficiency and stability for these optimized double-junction devices should be thoroughly investigated, which may lead to a solar-to-hydrogen conversion efficiency of more than 25%.

8.2.3 GaN Protection for Ultrahigh Efficiency Devices

In Chapters-4 and 5, we discussed GaN multifunctional protection on Si for achieving ultrahigh stability. This protection can be further used for protecting ultrahigh efficiencies (STH> 15%) devices like GaAs/Ge solar cell substrate, tandem III-V semiconductor devices and triple junction Si solar cells. It is important to investigate the performance and stability of these ultrahigh efficiencies GaN protected devices under accelerated long-term stability tests (to be discussed in the next section) to precisely identify the degradation/corrosion mechanisms. With the unique advantages of N-terminated GaN protection layer (as discussed in Chapter-4) on ultrahigh efficiency devices, it is possible to achieve ultrahigh efficiency (STH > 15%) with ultrahigh stability (> 3000 h) for PEC water splitting and thereby achieve desired goals for large-scale implementation of PEC water splitting.

8.2.4 Temperature and Pressure Influence on Solar Water Splitting

In Chapter-5, ultrahigh stability of GaN protection on Si has been discussed and an important aspect to further investigate for this device is the degradation mechanism. A detailed analysis on degradation mechanism needs to be done under accelerated testing protocols. These studies need to be coupled with the effects of temperature, pressure and day/night cycling to establish the ultimate limit on the stability of the GaN protected PEC devices.

Previous studies with co-catalyst deposited multi-band InGaN/GaN nanowires showed long-term stability of 580 h for photocatalytic water splitting. It was observed during these experiments that the level of vacuum and temperature variance inside the reaction chamber significantly affected the H_2 production and thereby accelerated the degradation of the photocatalyst. Future studies can focus on the effect of temperature and pressure on III-nitride photocatalysts to identify the degradation mechanisms. Passivation layers such as Al_2O_3 can be

employed to improve stability without any loss in H_2 generation to achieve long-term stability for photocatalytic water splitting.

8.2.5 Large-Scale Implementation of Solar Water Splitting Systems

The large-scale practical deployment of PEC/PC water splitting systems is limited by the manufacturing costs and scalability of the high-efficiency photocatalysts. As discussed earlier, (In)GaN and Si are the most widely produced industry-ready semiconductors, and the combination of these two light absorbers will be an excellent choice in achieving high STH and high stability with reasonably low fabrication cost for solar water splitting. The existing technologies offer scalability of high single-crystalline and defect-free epitaxial growth of III-nitrides on different sizes of Si wafers ranging from 2" to 6" diameters. The InGaN/Si double-junction, mentioned in Chapter-7, serves as a prototype for developing simple wired PEC system which can spontaneously split water under AM 1.5G one-sun illumination. Shown in Figure 8.2 is the experimental setup of a wired InGaN/Si double-junction with IrO_x counter electrode. This configuration spontaneously generates H_2 on the semiconductor surface in 0.5M H_2SO_4 solution under one-sun illumination. Although this setup is simple and elegant, the major challenges are the cost issues related to expensive co-catalyst (Pt) and special PEC chamber designs to separate the mixture of H_2 and O_2. Therefore, it is essential to develop earth-abundant catalysts along with high-efficiency In-rich InGaN nanowires (as discussed in *Section 8.2.2*) for reducing the cost. From Figure 7.5(b), the number of H_2 moles produced by the InGaN/Si double-junction for 100 h stability test is 0.015 mol/cm^2. Since the nanowires are grown on 2" wafer, the volume of H_2 produced at STP is ~ 7 Lit under one-sun illumination.

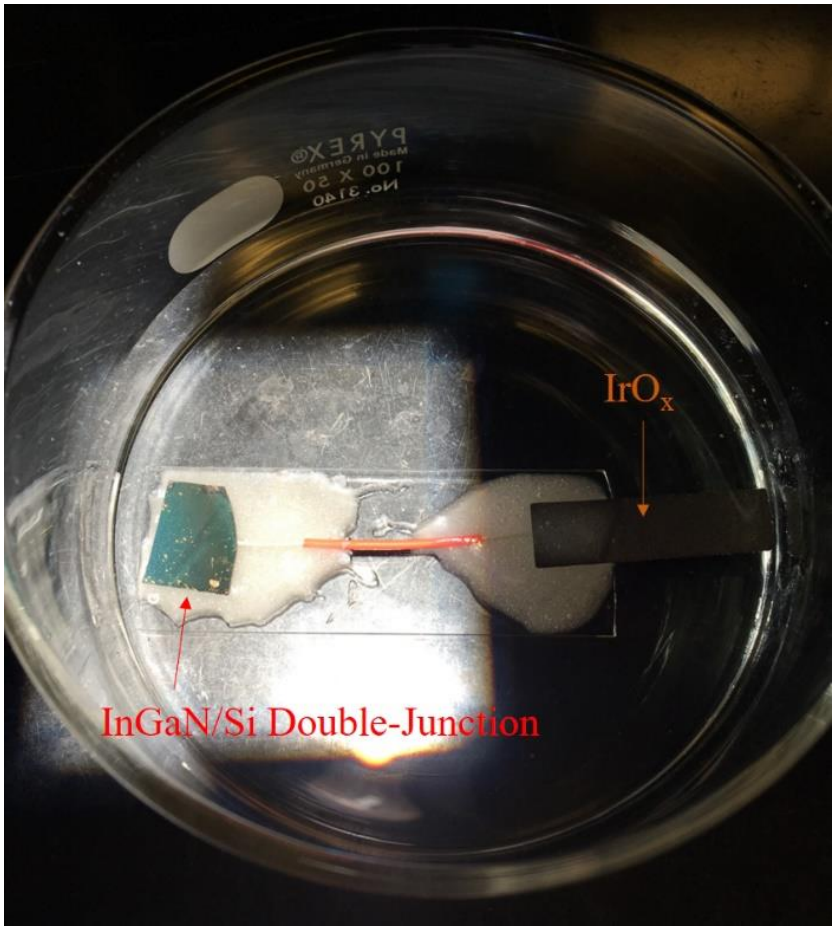

Figure 8.2. Experimental setup is showing the wired configuration of InGaN/Si double-junction with IrO_x. H_2 bubbles emerge from the surface of InGaN under illumination without any additional bias.

Therefore, it is evident that further growth optimization of double-junction along with earth abundant co-catalysts will enable high H_2 production at a relatively lower cost under one-sun and concentrated sunlight. For the future work, it is essential to understand and resolve the issues arising from the effects of light intensity and other factors (discussed in *Section 8.2.4*) for the InGaN/Si double-junction devices.

References

1. U. S. Energy Information Administration, International Energy Outlook **2016**. https://www.eia.gov/outlooks/ieo/pdf/0484(2016).pdf
2. (a) IPCC, Summary for Policymakers. In Climate Change **2013**: The Physical Science Basis. Contribution of Working Group I to the Fifth Assessment Report of the Intergovernmental Panel on Climate Change, Stocker, T. F.; Qin, D.; Plattner, G.-K.; Tignor, M.; Allen, S. K.; Boschung, J.; Nauels, A.; Xia, Y.; Bex, V.; Midgley, P. M., Eds. Cambridge University Press: Cambridge, United Kingdom, and New York, NY, USA, **2013**; pp 1–30. (b) Paris Agreement, United Nations Framework Convention on Climate Change **2015**: https://unfccc.int/sites/default/files/english_paris_agreement.pdf.
3. Cook, T. R.; Dogutan, D. K.; Reece, S. Y.; Surendranath, Y.; Teets, T. S.; Nocera, D. G. *Chem. Rev.* **2010**, 110, (11), 6474-6502.
4. (a) Armaroli, N.; Balzani, V. *ChemSusChem* **2011**, 4, (1), 21-36. (b) Gandía, L. M.; Arzamendi, G.; Diéguez, P. M. *Renewable Hydrogen Technologies: Chapter-1*, **2013**, 1-17. (c) Dincer, I. *Int. J. Hyd. Energy.* **2012**, 37, (2), 1954-1971.
5. (a) Vos, A. D. *Journal of Physics D: Applied Physics* **1980**, 13, (5), 839. (b) Jia, J.; Seitz, L. C.; Benck, J. D.; Huo, Y.; Chen, Y.; Ng, J. W.; Bilir, T.; Harris, J. S.; Jaramillo, T. F. Nat Commun **2016**, 7, 13237.
6. Purchase, R. L.; de Groot, H. J. *Interface Focus* **2015**, 5, (3), 20150014.
7. Kibria, M. G.; Mi, Z. *J. Mater. Chem. A* **2016**, 4, (8), 2801-2820
8. Arafin, S.; Liu, X.; Mi, Z. *J. Nanophotonics*, **2013**, 7, (1), 074599.
9. Bhuiyan, A. G.; Hashimoto, A.; Yamamoto, A. *J. Appl. Phys.* **2003**, 94, (5), 2779-2808.
10. Moustakas, T. D. *Phys Status Solidi A* **2013**, 210, (1), 169-174.

11. AlOtaibi, B.; Nguyen, H. P.; Zhao, S.; Kibria, M. G.; Fan, S.; Mi, Z. *Nano Lett.* **2013**, 13, (9), 4356-61.

12. Jung, H. S.; Hong, Y. J.; Li, Y.; Cho, J.; Kim, Y.-J.; Yi, G.-C. *ACS Nano* **2008**, 2, (4), 637-642.

13. AlOtaibi, B.; Harati, M.; Fan, S.; Zhao, S.; Nguyen, H. P.; Kibria, M. G.; Mi, Z. *Nanotechnology* **2013**, 24, (17), 175401.

14. Vanka, S.; Arca, E.; Cheng, S.; Sun, K.; Botton, G. A.; Teeter, G.; Mi, Z. *Nano Lett.* **2018**, 18, (10), 6530-6537.

15. Chu, S.; Vanka, S.; Wang, Y.; Gim, J.; Wang, Y.; Ra, Y.-H.; Hovden, R.; Guo, H.; Shih, I.; Mi, Z. *ACS Energ. Lett.* **2018**, 3, (2), 307-314.

16. Osterloh, F. E. *Chem. Soc. Rev.* **2013**, 42, (6), 2294-320.

17. Hwang, Y. J.; Wu, C. H.; Hahn, C.; Jeong, H. E.; Yang, P. *Nano Lett.* **2012**, 12, (3), 1678-82.

18. Kocha, S. S.; Peterson, M. W.; Arent, D. J.; Redwing, J. M.; Tischler, M. A.; Turner, J. A. *J. Electrochem. Soc.* **1995**, 142, (12), L238-L240.

19. Beach, J. D.; Collins, R. T.; Turner, J. A. *J. Electrochem. Soc.* **2003**, 150, (7), A899.

20. Fujii, K.; Ohkawa, K. *Physica Status Solidi* (c) **2006**, 3, (6), 2270-2273.

21. Katsushi, F.; Takeshi, K.; Kazuhiro, O. *Jpn. J. Appl. Phys.* **2005**, 44, (4L), L543.

22. Fan, S.; AlOtaibi, B.; Woo, S. Y.; Wang, Y.; Botton, G. A.; Mi, Z. *Nano Lett.* **2015**, 15, (4), 2721-6.

23. Fan, S.; Shih, I.; Mi, Z. *Adv. Energ. Mater.* **2016**, 1600952.

24. Varadhan, P.; Fu, H. C.; Priante, D.; Retamal, J. R.; Zhao, C.; Ebaid, M.; Ng, T. K.; Ajia, I.; Mitra, S.; Roqan, I. S.; Ooi, B. S.; He, J. H. *Nano Lett.* **2017**, 17, 3, 1520-1528.

25. Butson, J.; Narangari, P. R.; Karuturi, S. K.; Yew, R.; Lysevych, M.; Tan, H. H.; Jagadish, C. *Nanotechnology* **2018**, 29, (4), 045403.

26. Kibria, M. G.; Qiao, R.; Yang, W.; Boukahil, I.; Kong, X.; Chowdhury, F. A.; Trudeau, M. L.; Ji, W.; Guo, H.; Himpsel, F. J.; Vayssieres, L.; Mi, Z. *Adv. Mater*. **2016**, 28, (38), 8388-8397.

27. Foresi, J. S., Moustakas, T. D. *Appl. Phys. Lett.*, **1993**, 62(22): 2859.

28. Sanchez-Garcia, M. A.; Calleja, E.; Monroy, E.; Sanchez, F. J.; Calle, F.; Muñoz, E.; Beresford, R. *J. Cryst. Growth* **1998**, 183, (1), 23-30.

29. Masaki, Y.; Akihiko, K.; Masashi, M.; Nobuhiko, F.; Katsumi, K. *Jpn. J. Appl. Phys.* **1997**, 36, (4B), L459.

30. Schuster, F.; Furtmayr, F.; Zamani, R.; Magen, C.; Morante, J. R.; Arbiol, J.; Garrido, J. A.; Stutzmann, M. *Nano Lett.* **2012**, 12, (5), 2199-204.

31. Fernandez-Garrido, S.; Kong, X.; Gotschke, T.; Calarco, R.; Geelhaar, L.; Trampert, A.; Brandt, O. *Nano Lett.* **2012**, 12, (12), 6119-25.

32. (a) Lorenzo, M. Silicon Based Thin Film Solar Cells, *Bentham Science*, **2013**, 81-107. (b) Wagner, R. S.; Ellis, W. C. *Appl. Phys. Lett.* **1964**, 4, (5), 89-90.

33. D. Dheeraj, H. Zhou, A. Moses, T. Hoang, A. Van Helvoort, B. Fimland, et al., *Nanowires, InTech*, **2010**.

34. J. Ristić, E. Calleja, S. Fernández-Garrido, L. Cerutti, A. Trampert, U. Jahn, *et al.*, "On the mechanisms of spontaneous growth of III-nitride nanocolumns by plasma-assisted molecular beam epitaxy," *Journal of Crystal Growth*, vol. 310, pp. 4035-4045, **2008**.

35. Bertness, K. A.; Roshko, A.; Mansfield, L. M.; Harvey, T. E.; Sanford, N. A. Journal of Crystal Growth **2008**, 310, (13), 3154-3158.

36. Debnath, R. K.; Meijers, R.; Richter, T.; Stoica, T.; Calarco, R.; Lüth, H. Appl. Phys. Lett. **2007**, 90, (12), 123117.

37. Fernández-Garrido, S.; Grandal, J.; Calleja, E.; Sánchez-García, M. A.; López-Romero, D. *J. Appl. Phys.* **2009**, 106, (12), 126102.

38. Prévot, M. S.; Sivula, K. *J. Phys. Chem. C* **2013**, 117, (35), 17879-17893.

39. Krishnamoorthy, S. *et al.* Polarization-engineered GaN/InGaN/GaN tunnel diodes. *Appl. Phys. Lett.* **97**, 203502 (**2010**).

40. Sadaf, S. M., Ra, Y. H., Szkopek, T. & Mi, Z. *Nano Lett.* **2016**, 16, 1076-108).

41. Sadaf, S. M., Ra, Y. H., Nguyen, H. P., Djavid, M. & Mi, Z.. *Nano Lett.* **2015** 15, 6696-6701.

43. (a) Fujishima, A.; Honda, K. *Nature* **1972**, 238, (5358), 37. (b) Khaselev, O.; Turner, J. A. *Science* **1998**, 280, (5362), 425-427. (c) Young, J. L.; Steiner, M. A.; Döscher, H.; France, R. M.; Turner, J. A.; Deutsch, Todd G. *Nat. Energ.* **2017**, 2, 17028. (d) Cheng, W.-H. *et al. ACS Energ. Lett.* **2018**, 3, 1795-1800. (e) Kim, J. H.; Jang, J. W.; Jo, Y. H.; Abdi, F. F.; Lee, Y. H.; van de Krol, R.; Lee, J. S. *Nat Commun.* **2016**, 7, 13380. (f) Verlage, E. *et al. Energ. Environ. Sci.* **2015**, 8, 3166-3172.

44. Parkinson, B. *J. Chem. Education* **1983,** 60, (4), 338.

45. Hellman, A. CHAPTER 10. Photoelectrochemical Water Splitting: A First Principles Approach. **2013**, 266-288.

46. Boddy, P. J. *J. Electrochem. Soci.* **1968,** 115, (2), 199-203.

47. Fujishima, A.; Honda, K. *Nature* **1972,** 238, (5358), 37.

48. Kibria, M. G.; Mi, Z. *J. Mater. Chem. A* **2016,** 4, (8), 2801-2820.

49. Seeger, K., Energy Band Structure. In *Semiconductor Physics: An Introduction*, Springer Berlin Heidelberg: Berlin, Heidelberg, **1999**, 10-33.

50. Yang, X.; Wang, D. Photophysics and Photochemistry at the Semiconductor/Electrolyte Interface for Solar Water Splitting. **2017,** 97, 47-80.

51. Gerischer, H. *Surface Science* **1969,** 18, (1), 97-122.

52. Memming, R. Electron Transfer Theories. *Semiconductor Electrochem.*, Wiley-VCH, **2001**, 112-151.

53. Memming, R. Charge Transfer Processes at the Semiconductor-Liquid Interface. *Semiconductor Electrochem.,* Wiley-VCH, **2001**, 152-242.

54. Srinivasan, S., Electrode/electrolyte interfaces: structure and kinetics of charge transfer. *Fuel Cells: From Fundamentals to Applications*, Springer US: Boston, MA, **2006**; pp 27-92.

55. Rajeshwar, K., Fundamentals of Semiconductor Electrochemistry and Photoelectrochemistry. *Encyclopedia of Electrochem*., A. J. Bard (Ed.), **2007**, 1-59.

56. Iqbal, A.; Yuan, S.; Wang, Z.; Bevan, K. H. *J. Phys. Chem. C* **2018,** 122, (42), 23878-23889.

57. Jiao, Y.; Zheng, Y.; Jaroniec, M.; Qiao, S. Z. *Chem. Soc. Rev.* **2015,** 44, (8), 2060-86.

58. Bard, A. J.; Faulkner, L. R., *Electrochemical methods : fundamentals and applications*. 2nd ed.; Wiley: New York, **2001**, 833.

59. Reichman, J. *Appl. Phys. Lett.* **1980,** 36, (7), 574-577.

60. Yang, X.; Du, C.; Liu, R.; Xie, J.; Wang, D. *J. Catal.* **2013,** 304, 86-91.

61. Doyle, R. L.; Lyons, M. E. G., The Oxygen Evolution Reaction: Mechanistic Concepts and Catalyst Design. *Photoelectrochemical Solar Fuel Production: From Basic Principles to*

Advanced Devices, Giménez, S.; Bisquert, J., Eds. Springer International Publishing: Cham, **2016**; pp 41-104.

62. Popczun, E. J.; Read, C. G.; Roske, C. W.; Lewis, N. S.; Schaak, R. E. *Angew. Chem. Int. Ed. Engl.* **2014,** 53, (21), 5427-30.

63. Vanka, S.; Arca, E.; Cheng, S.; Sun, K.; Botton, G. A.; Teeter, G.; Mi, Z. *Nano Lett.* **2018,** 18, (10), 6530-6537.

64. Ouattara, L.; Fierro, S.; Frey, O.; Koudelka, M.; Comninellis, C. *J. Appl. Electrochem.* **2009,** 39, (8), 1361-1367.

65. Tsuji, E.; Imanishi, A.; Fukui, K.-i.; Nakato, Y. *Electrochimica Acta* **2011,** 56, (5), 2009-2016.

66. Song, F.; Hu, X. *Nat. Commun.* **2014,** 5, 4477.

67. Chu, S.; Vanka, S.; Wang, Y.; Gim, J.; Wang, Y.; Ra, Y.-H.; Hovden, R.; Guo, H.; Shih, I.; Mi, Z. *ACS Energ. Lett.* **2018,** 3, (2), 307-314.

68. Gärtner, W. W. *Phys. Rev.* **1959,** 116, (1), 84-87.

69. Chu, S.; Li, W.; Yan, Y.; Hamann, T.; Shih, I.; Wang, D.; Mi, Z. *Nano Futures* **2017,** 1, (2), 022001.

70. Sah, C.; Noyce, R. N.; Shockley, W. *Proceedings of the IRE* **1957,** 45, (9), 1228-1243.

71. Yin, Z.; Fan, R.; Huang, G.; Shen, M. *Chem. Commun. (Camb)* **2018,** 54, (5), 543-546.

72. Fan, R.; Dong, W.; Fang, L.; Zheng, F.; Shen, M. *J. Mater. Chem. A* **2017**, 5, 18744-18751.

73. Wang, H. P.; Sun, K.; Noh, S. Y.; Kargar, A.; Tsai, M. L.; Huang, M. Y.; Wang, D. L.; He, J. H. *Nano Lett.* **2015,** 15, (5), 2817-2824.

74. Kast, M. G.; Enman, L. J.; Gurnon, N. J.; Nadarajah, A.; Boettcher, S. W. *ACS Appl. Mater. Interfaces* **2014,** 6, (24), 22830-7.

75. Lee, M. H.; Takei, K.; Zhang, J.; Kapadia, R.; Zheng, M.; Chen, Y. Z.; Nah, J.; Matthews, T. S.; Chueh, Y. L.; Ager, J. W.; Javey, A. *Angew. Chem. Int. Ed. Engl.* **2012,** 51, (43), 10760-4.

76. Hettick, M.; Zheng, M.; Lin, Y.; Sutter-Fella, C. M.; Ager, J. W.; Javey, A. *J. Phys. Chem. Lett.* **2015,** 6, (12), 2177-82.

77. Yu, X.; Yang, P.; Chen, S.; Zhang, M.; Shi, G. *Adv. Energ. Mater.* **2017,** 7, (6), 1601805.

78. Zhou, X. H.; Liu, R.; Sun, K.; Friedrich, D.; McDowell, M. T.; Yang, F.; Omelchenko, S. T.; Saadi, F. H.; Nielander, A. C.; Yalamanchili, S.; Papadantonakis, K. M.; Brunschwig, B. S.; Lewis, N. S. *Energ. Environ. Sci.* **2015,** 8, (9), 2644-2649.

79. Sun, K.; McDowell, M. T.; Nielander, A. C.; Hu, S.; Shaner, M. R.; Yang, F.; Brunschwig, B. S.; Lewis, N. S. *J. Phys. Chem. Lett.* **2015,** 6, (4), 592-8.

80. Liu, Q.; He, J.; Yao, T.; Sun, Z.; Cheng, W.; He, S.; Xie, Y.; Peng, Y.; Cheng, H.; Sun, Y.; Jiang, Y.; Hu, F.; Xie, Z.; Yan, W.; Pan, Z.; Wu, Z.; Wei, S. *Nat. Commun.* **2014,** 5, 5122.

81. Liu, G.; Ye, S.; Yan, P.; Xiong, F.; Fu, P.; Wang, Z.; Chen, Z.; Shi, J.; Li, C. *Energ. Environ. Sci.* **2016,** 9, (4), 1327-1334.

82. Sharp, I. D.; Cooper, J. K.; Toma, F. M.; Buonsanti, R. *ACS Energ. Lett.* **2017,** 2, (1), 139-150.

83. Morin, F. J. *Phys. Rev.* **1951,** 83, (5), 1005-1010.

84. Rettie, A. J. E.; Chemelewski, W. D.; Emin, D.; Mullins, C. B. *J. Phys. Chem. Lett.* **2016,** 7, (3), 471-479.

85. Dare-Edwards, M. P.; Goodenough, J. B.; Hamnett, A.; Trevellick, P. R. *Journal of the Chemical Society, Faraday Transactions 1: Physical Chemistry in Condensed Phases* **1983,** 79, (9), 2027-2041.

86. Barroso, M.; Pendlebury, S. R.; Cowan, A. J.; Durrant, J. R. *Chem. Sci.* **2013,** 4, (7), 2724-2734.

87. Chowdhury, F. A.; Trudeau, M. L.; Guo, H.; Mi, Z. *Nat. Commun.* **2018,** 9, (1), 1707.

88. Pinaud, B. A.; Benck, J. D.; Seitz, L. C.; Forman, A. J.; Chen, Z. B.; Deutsch, T. G.; James, B. D.; Baum, K. N.; Baum, G. N.; Ardo, S.; Wang, H. L.; Miller, E.; Jaramillo, T. F. *Energ. Environ. Sci.* **2013,** 6, (7), 1983-2002.

89. Kitano, M.; Hara, M. *J. Mater. Chem.* **2010,** 20, (4), 627-641.

90. Bolton, J. R.; Strickler, S. J.; Connolly, J. S. *Nature* **1985,** 316, 495.

91. Fan, S.; Woo, S. Y.; Vanka, S.; Botton, G. A.; Mi, Z. *APL Mater.* **2016,** 4, (7).

92. Parkinson, B. *Accounts of Chem. Res.* **1984,** 17, (12), 431-437.

93. Seitz, L. C.; Chen, Z.; Forman, A. J.; Pinaud, B. A.; Benck, J. D.; Jaramillo, T. F. *ChemSusChem* **2014,** 7, (5), 1372-85.

94. Hernández, S.; Barbero, G.; Saracco, G.; Alexe-Ionescu, A. L. *J. Phys. Chem. C* **2015,** 119, (18), 9916-9925.

95. Young, J. L.; Steirer, K. X.; Dzara, M. J.; Turner, J. A.; Deutsch, T. G. *J. Mater. Chem. A* **2016,** 4, (8), 2831-2836.

96. King, L. A.; Hellstern, T. R.; Park, J.; Sinclair, R.; Jaramillo, T. F. *ACS Appl. Mater. Interfaces* **2017,** 9, (42), 36792-36798.

97. Ros, C.; Andreu, T.; Hernandez-Alonso, M. D.; Penelas-Perez, G.; Arbiol, J.; Morante, J. R. *ACS Appl. Mater. Interfaces* **2017**.

98. Britto, R. J.; Benck, J. D.; Young, J. L.; Hahn, C.; Deutsch, T. G.; Jaramillo, T. F. *J. Phys. Chem. Lett.* **2016,** 7, (11), 2044-2049.

99. Kainthla, R. C.; Zelenay, B.; Bockris, J. O. M. *J. Electrochem. Soc.* **1986,** 133, (2), 248-253.

100. Lewerenz, H. J. *J. Electrochem. Soc.* **2014,** 161, (13), H3117-H3129.

101. Baker, D. R.; Lundgren, C. A. *J. Mater. Chem. A* **2017,** 5, (39), 20978-20984.

102. Fan, R.; Mi, Z.; Shen, M. *Optics Express* **2019,** 27, (4), A51.

103. Lewis, N. S.; Nocera, D. G. *Proc. Natl. Acad. Sci. U. S. A.* **2006**, 103, 15729−15735.

104. Walter, M. G.; Warren, E. L.; Mckone, J. R.; Boettcher, S. W.; Mi, Q. X.; Santori, E. A.; Lewis, N. S. *Chem. Rev.* **2010**, 110, 6446-6473.

105. Li, Z.; Luo, W., Zhang, M.; Feng, J.; Zou, Z. *Energy Environ. Sci.* **2013**, 6, 347-370.

106. Sivula, K.; Van De Krol, R. *Nature Rev. Mater.* **2016**, 1, 15010.

107. Nozik, A. J. *Appl. Phys. Lett.* **1976**, 29, 150-153.

108. Bolton, J. R.; Strickler, S. J.; Connolly, J. S. *Nature* **1985**, 316, 495-500.

109. Wang, H. L.; Deutsch, T.; Turner, J. A. *J. Electrochem. Soc.* **2008**, 155, F91-F96.

110. Liu, C.; Tang, J. Y.; Chen, H. M.; Liu, B.; Yang, P. D. *Nano Lett.* **2013**, 13, 2989-2992.

111. Jang, J. W.; Du, C.; Ye, Y. F.; Lin, Y. J.; Yao, X. H.; Thorne, J.; Liu, E.; Mcmahon, G.; Zhu, J. F.; Javey, A. *Nat. Commun.* **2015**, 6, 7447.

112. Lai, Y. H.; Palm, D. W.; Reisner, E. *Adv. Energy Mater.* **2015**, 5, 1501668.

113. Zhou, X.; Liu, R.; Sun, K.; Papadantonakis, K. M.; Brunschwig, B. S.; Lewis, N. S. *Energy Environ. Sci.* **2016**, 9, 892-897.

114. Yang, J.; Cooper, J. K.; Toma, F. M.; Walczak, K. A.; Favaro, M.; Beeman, J. W.; Hess, L. H.; Wang, C.; Zhu, C.; Gul, S.; et al. *Nat. Mater.* **2017**, 16, 335-341

115. Mei, B.; Seger, B.; Pedersen, T.; Malizia, M.; Hansen, O.; Chorkendorff, I.; Vesborg, P. C. K. *J. Phys. Chem. Lett.* **2014**, 5, 1948-1952.

116. Sivula, K.; Le Formal, F.; Gratzel, M. *Chemsuschem* **2011**, 4, 432-49.

117. Shen, S.; Lindley, S. A.; Chen, X.; Zhang, J. Z. *Energy Environ. Sci.* **2016**, 9, 2744-2775.

118. Li, M. X.; Luo, W. J.; Cao, D. P.; Zhao, X.; Li, Z. S.; Yu, T.; Zou, Z. G. *Angew. Chem. Int. Ed.* **2013**, 52, 11016-11020.

119. He, Y.; Thorne, James E.; Wu, Cheng H.; Ma, P.; Du, C.; Dong, Q.; Guo, J.; Wang, D. *Chem* **2016**, 1, 640-655.

120. Zhong, M.; Hisatomi, T.; Sasaki, Y.; Suzuki, S.; Teshima, K.; Nakabayashi, M.; Shibata, N.; Nishiyama, H.; Katayama, M.; Yamada, T.; et al. *Angew. Chem. Int. Ed.* **2017**, 56, 4739-4743.

121. Park, Y.; Mcdonald, K. J.; Choi, K.-S. *Chem. Soc. Rev.* **2013**, 42, 2321−2337.

122. Sharp, I. D.; Cooper, J. K.; Toma, F. M.; Buonsanti, R. *ACS Energy Lett.* **2017**, 2, 139-150.

123. Bornoz, P.; Abdi, F. F.; Tilley, S. D.; Dam, B.; Van De Krol, R.; Graetzel, M.; Sivula, K. *J. Phys. Chem. C* **2014**, 118, 16959-16966.

124. Xu, P.; Feng, J.; Fang, T.; Zhao, X.; Li, Z.; Zou, Z. *RSC Adv.* **2016**, 6, 9905.

125. Zhao, J.; Guo, Y.; Cai, L.; Li, H.; Wang, K. X.; Cho, I. S.; Lee, C. H.; Fan, S.; Zheng, X. *ACS Energy Lett.* **2016**, 1, 68-75.

126. Chakthranont, P.; Hellstern, T. R.; Mcenaney, J. M.; Jaramillo, T. F. *Adv. Energy Mater.* **2017**, 7, 1701515.

127. Hu, S.; Xiang, C. X.; Haussener, S.; Berger, A. D.; Lewis, N. S *Energy Environ. Sci.* **2013**, 6, 2984-2993.

128. Doscher, H.; Geisz, J. F.; Deutsch, T. G.; Turner, J. A., *Energy Environ. Sci.* **2014**, 7, 2951-2956.

129. Seitz, L. C.; Chen, Z.; Forman, A. J.; Pinaud, B. A.; Benck, J. D.; Jaramillo, T. F. *Chemsuschem* **2014**, 7, 1372-1385.

130. Fountaine, K. T.; Lewerenz, H. J.; Atwater, H. *Nat. Commun.* **2016**, 7, 13706.

131. Seger, B.; Hansen, O.; Vesborg, P. C. K. *Solar RRL* **2017**, 1, E201600013;

132. Montoya, J. H.; Seitz, L. C.; Chakthranont, P.; Vojvodic, A.; Jaramillo, T. F.; Norskov, J. K. *Nat. Mater.* **2017**, 16, 70-81.

133. Luo, W. J.; Liu, B.; Li, Z. S.; Xie, Z. L.; Chen, D. J.; Zou, Z. G.; Zhang, R. *Appl. Phys. Lett.* **2008**, 92, 262110.

134. Kibria, M. G.; Chowdhury, F. A.; Zhao, S.; Alotaibi, B.; Trudeau, M. L.; Guo, H.; Mi, Z. *Nat. Commun.* **2015**, 6, 6797.

135. Wu, J.; Walukiewicz, W.; Yu, K. M.; Ager, J. W.; Haller, E. E.; Lu, H.; Schaff, W. J. *Appl. Phys. Lett.* **2002**, 80, 4741-4743.

136. Moses, P. G.; Van De Walle, C. G. *Appl. Phys. Lett.* **2010**, 96, 021908;

137. Hwang, Y. J.; Wu, C. H.; Hahn, C.; Jeong, H. E.; Yang, P. D. *Nano Lett.* **2012**, 12, 1678-1682.

138. Caccamo, L.; Hartmann, J.; Fabrega, C.; Estrade, S.; Lilienkamp, G.; Prades, J. D.; Hoffmann, M. W. G.; Ledig, J.; Wagner, A.; Wang, X. *ACS Appl. Mater. Inter.* **2014**, 6, 2235-2340.

139. Kuykendall, T.; Ulrich, P.; Aloni, S.; Yang, P *Nat. Mater.* **2007**, 6, 951-956.

140. Pendyala, C.; Jasinski, J. B.; Kim, J. H.; Vendra, V. K.; Lisenkov, S.; Menon, M.; Sunkara, M. K. *Nanoscale* **2012**, 4, 6269-6975.

141. Mccrory, C. C. L.; Jung, S. H.; Peters, J. C.; Jaramillo, T. F. *J. Am. Chem. Soc.* **2013**, 135, 16977-16987.

142. Tilley, S. D.; Cornuz, M.; Sivula, K.; Gratzel, M. *Angew. Chem., Int. Ed.* **2010**, 49, 6405-6408.

143. Abe, R.; Higashi, M.; Domen, K. *J. Am. Chem. Soc.* **2010**, 132, 11828-11829.

144. Bledowski, M.; Wang, L. D.; Neubert, S.; Mitoraj, D.; Beranek, R. *J. Phys. Chem. C* **2014**, 118, 18951-18961.

145. Li, W.; He, D.; Sheehan, S. W.; He, Y.; Thorne, J. E.; Yao, X.; Brudvig, G. W.; Wang, D. *Energy Environ. Sci.* **2016**, 9, 1794-1802.

146. Kim, T. W.; Ping, Y.; Galli, G. A.; Choi, K. S. *Nat. Commun.* **2015**, 6, 8769.

147. Kuang, Y. B.; Jia, Q. X.; Nishiyama, H.; Yamada, T.; Kudo, A.; Domen, K. *Adv. Energy Mater.* **2016**, 6, 1501645.

148. Ye, K.-H.; Wang, Z.; Gu, J.; Xiao, S.; Yuan, Y.; Zhu, Y.; Zhang, Y.; Mai, W.; Yang, S. *Energy Environ. Sci.* **2017**, 10, 772-779.

149. Liu, G. J.; Ye, S.; Yan, P. L.; Xiong, F. Q.; Fu, P.; Wang, Z. L.; Chen, Z.; Shi, J. Y.; Li, C. *Energy Environ. Sci.* **2016**, 9, 1327-1334.

150. Liu, Q. H.; He, J. F.; Yao, T.; Sun, Z. H.; Cheng, W. R.; He, S.; Xie, Y.; Peng, Y. H.; Cheng, H.; Sun, Y. F. *Nat. Commun.* **2014**, 5, 5122.

151. Yu, X.; Yang, P.; Chen, S.; Zhang, M.; Shi, G. *Adv. Energy Mater.* **2016**, 6, 1601805.

152. Chang, Y. L.; Li, F.; Fatehi, A.; Mi, Z. *Nanotechnology* **2009**, 20, 345203.

153. Zhao, S.; Nguyen, H. P. T.; Kibria, M. G.; Mi, Z. *Prog. Quant. Electron.* **2015**, 44, 14-68.

154. Nguyen, H. P. T.; Zhang, S.; Cui, K.; Han, X.; Fathololoumi, S.; Couillard, M.; Botton, G. A.; Mi, Z. *Nano Lett.* **2011**, 11, 1919-1924.

155. Ra, Y.; Wang, R., Woo, S. Y.; Djavid, M.; Sadaf, S. M.; Lee, J.; Gianluigi A. Botton, G. A.; Mi, Z. *Nano Lett.* **2016**, 16, 4608-4615.

156. Ran, J. R.; Zhang, J.; Yu, J. G.; Jaroniec, M.; Qiao, S. Z. *Chem. Soc. Rev.* **2014**, 43, 7787-7812.

157. Hu, S.; Lewis, N. S.; Ager, J. W.; Yang, J. H.; Mckone, J. R.; Strandwitz, N. C. *J. Phys. Chem. C* **2015**, 119, 24201-24228

158. Scheuermann, A. G.; Mcintyre, P. C. *J. Phys. Chem. Lett.* **2016**, 7, 2867-2878.

159. Bae, D.; Seger, B.; Vesborg, P. C. K.; Hansen, O.; Chorkendorff, I. *Chem. Soc. Rev.* **2017**, 46, 1933-1954.

160. Zhang, P.; Wang, T.; Gong, J. L. *Chem. Commun.* **2016**, 52, 8806-8809.

161. Mcdowell, M. T.; Lichterman, M. F.; Spurgeon, J. M.; Hu, S.; Sharp, I. D.; Brunschwig, B. S.; Lewis, N. S *J. Phys. Chem. C* **2014**, 118, 19618-19624.

162. Chen, Y. W.; Prange, J. D.; Duhnen, S.; Park, Y.; Gunji, M.; Chidsey, C. E. D.; Mcintyre, P. C. *Nat. Mater.* **2011**, 10, 539-544.

163. Kim, H. J.; Kearney, K. L.; Le, L. H.; Haber, Z. J.; Rockett, A. A.; Rose, M. J. *J. Phys. Chem. C* **2016**, 120, 25697-25708.

164. Kamimura, J.; Bogdanoff, P.; Lahnemann, J.; Hauswald, C.; Geelhaar, L.; Fiechter, S.; Riechert, H. *J. Am. Chem. Soc.* **2013**, 135, 10242-10245.

165. Caccamo, L.; Cocco, G.; Martin, G.; Zhou, H.; Fundling, S.; Gad, A.; Mohajerani, M. S.; Abdelfatah, M.; Estrade, S.; Peiro, F. *ACS Appl. Mater. Inter.* **2016**, 8, 8232-8238.

166. Moehl T.; Suh J.; Severy L.; Wick-Joliat R.; Tilley S. D. *ACS Appl. Mater. Inter.* **2017**, 9, 43614-43622.

167. Hu, S.; Shaner, M. R.; Beardslee, J. A.; Lichterman, M.; Brunschwig, B. S.; Lewis, N. S., *Science* **2014**, 344, 1005-1009.

168. Verlage, E.; Hu, S.; Liu, R.; Jones, R. J. R.; Sun, K.; Xiang, C. X.; Lewis, N. S.; Atwater, H. A., *Energy Environ. Sci.* **2015**, 8, 3166-3172.

169. Sun, K.; Kuang, Y. J.; Verlage, E.; Brunschwig, B. S.; Tu, C. W.; Lewis, N. S., *Adv. Energy Mater.* **2015**, 5, 1402276.

170. Chen, L.; Yang, J. H.; Klaus, S.; Lee, L. J.; Woods-Robinson, R.; Ma, J.; Lum, Y.; Cooper, J. K.; Toma, F. M.; Wang, L. W.; et al. *J. Am. Chem. Soc.* **2015**, 137, 9595-9603.

171. Liu, C.; Dasgupta, N. P.; Yang, P. D. *Chem. Mater.* **2014**, 26, 415-422.

172. Mozharov, A. M.; Bolshakov, A. D.; Kudryashov, D. A.; Kryzhanovskaya, N. V.; Cirlin, G. E.; Mukhin, I. S.; Harmand, J. C.; Tchernysheva, M. *J. Phys. Conf. Ser.* **2015**, 643, 012115.

173. Dotan, H.; Sivula, K.; Gratzel, M.; Rothschild, A.; Warren, S. C. *Energy Environ. Sci.* **2011**, 4, 958-964.

174. Abdi, F. F.; Van De Krol, R. *J. Phys. Chem. C* **2012**, 116, 9398-9404.

175. Yilmaz, F.; Balta, M. T.; Selbas, R. *Renew. Sust. Energ. Rev.* **2016,** 56, 171-178.

176. Kitano, M.; Hara, M. *J. Mater. Chem.* **2010,** 20, (4), 627-641.

177. Hu, S.; Xiang, C. X.; Haussener, S.; Berger, A. D.; Lewis, N. S. *Energ. Environ. Sci.* **2013,** 6, (10), 2984-2993.

178. Sun, K.; Shen, S. H.; Liang, Y. Q.; Burrows, P. E.; Mao, S. S.; Wang, D. L. *Chem. Rev.* **2014,** 114, (17), 8662-8719.

179. May, M. M.; Lewerenz, H. J.; Lackner, D.; Dimroth, F.; Hannappel, T. *Nat. Commun.* **2015,** 6, 8286.

180. Gu, J.; Aguiar, J. A.; Ferrere, S.; Steirer, K. X.; Yan, Y.; Xiao, C.; Young, James L.; Al-Jassim, M.; Neale, N. R.; Turner, J. A. *Nat. Energ.* **2017,** 2, 16192.

181. Garner, L. E.; Steirer, K. X.; Young, J. L.; Anderson, N. C.; Miller, E. M.; Tinkham, J. S.; Deutsch, T. G.; Sellinger, A.; Turner, J. A.; Neale, N. R. *ChemSusChem* **2017,** 10, (4), 767-773.

182. Standing, A.; Assali, S.; Gao, L.; Verheijen, M. A.; van Dam, D.; Cui, Y.; Notten, P. H.; Haverkort, J. E.; Bakkers, E. P. *Nat. Commun.* **2015,** 6, 7824.

183. Choi, M. J.; Jung, J. Y.; Park, M. J.; Song, J. W.; Lee, J. H.; Bang, J. H. *J. Mater. Chem. A* **2014,** 2, (9), 2928-2933.

184. Andoshe, D. M.; Choi, S.; Shim, Y.-S.; Lee, S. H.; Kim, Y.; Moon, C. W.; Kim, D. H.; Lee, S. Y.; Kim, T.; Park, H. K.; Lee, M. G.; Jeon, J.-M.; Nam, K. T.; Kim, M.; Kim, J. K.; Oh, J.; Jang, H. W. *J. Mater. Chem. A* **2016,** 4, (24), 9477-9485.

185. Ros, C.; Andreu, T.; Hernandez-Alonso, M. D.; Penelas-Perez, G.; Arbiol, J.; Morante, J. R. *ACS Appl. Mater. Interfaces* **2017**, 9, (21), 17932-17941.

186. Chen, F.; Zhu, Q.; Wang, Y.; Cui, W.; Su, X.; Li, Y. *ACS Appl. Mater. Interfaces* **2016,** 8, (45), 31025-31031.

187. Ji, L.; McDaniel, M. D.; Wang, S. J.; Posadas, A. B.; Li, X. H.; Huang, H. Y.; Lee, J. C.; Demkov, A. A.; Bard, A. J.; Ekerdt, J. G.; Yu, E. T. *Nat. Nanotechnol.* **2015,** 10, (1), 84-90.

188. Zhang, Q.; Li, T.; Luo, J.; Liu, B.; Liang, J.; Wang, N.; Kong, X.; Li, B.; Wei, C.; Zhao, Y.; Zhang, X. *J. Mater. Chem. A* **2018,** 6, (3), 811-816.

189. Feng, J.; Gong, M.; Kenney, M. J.; Wu, J. Z.; Zhang, B.; Li, Y.; Dai, H. *Nano Res.* **2015,** 8, (5), 1577-1583.

190. Fan, R.; Dong, W.; Fang, L.; Zheng, F.; Su, X.; Zou, S.; Huang, J.; Wang, X.; Shen, M. *Appl. Phys. Lett.* **2015,** 106, (1), 013902.

191. Fan, R.; Mao, J.; Yin, Z.; Jie, J.; Dong, W.; Fang, L.; Zheng, F.; Shen, M. *ACS Appl. Mater. Interfaces* **2017,** 9, (7), 6123-6129.

192. Huang, G.; Mao, J.; Fan, R.; Yin, Z.; Wu, X.; Jie, J.; Kang, Z.; Shen, M. *Appl. Phys. Lett.* **2018,** 112, (1), 013902.

193. Kaneko, H.; Minegishi, T.; Domen, K. *Chemistry* **2018,** 24, (22), 5697-5706.

194. Li, Q.; Zheng, M.; Zhong, M.; Ma, L.; Wang, F.; Ma, L.; Shen, W. *Sci Rep* **2016,** 6, 29738.

195. Gu, J.; Yan, Y.; Young, J. L.; Steirer, K. X.; Neale, N. R.; Turner, J. A. *Nat. Mater.* **2016,** 15, (4), 456-60.

196. Kibria, M. G.; Zhao, S.; Chowdhury, F. A.; Wang, Q.; Nguyen, H. P.; Trudeau, M. L.; Guo, H.; Mi, Z. *Nat. Commun.* **2014,** 5, 3825.

197. Kibria, M. G.; Nguyen, H. P. T.; Cui, K.; Zhao, S. R.; Liu, D. P.; Guo, H.; Trudeau, M. L.; Paradis, S.; Hakima, A. R.; Mi, Z. T. *ACS Nano* **2013,** 7, (9), 7886-7893.

198. Wang, D.; Pierre, A.; Kibria, M. G.; Cui, K.; Han, X.; Bevan, K. H.; Guo, H.; Paradis, S.; Hakima, A. R.; Mi, Z. *Nano Lett.* **2011,** 11, (6), 2353-7.

199. Ebaid, M.; Priante, D.; Liu, G.; Zhao, C.; Sharizal Alias, M.; Buttner, U.; Khee Ng, T.; Taylor Isimjan, T.; Idriss, H.; Ooi, B. S. *Nano Energ.* **2017,** 37, 158-167.

200. Butson, J.; Narangari, P. R.; Karuturi, S. K.; Yew, R.; Lysevych, M.; Tan, H. H.; Jagadish, C. *Nanotechnol.* **2018,** 29, (4), 045403.

201. Varadhan, P.; Fu, H. C.; Priante, D.; Retamal, J. R.; Zhao, C.; Ebaid, M.; Ng, T. K.; Ajia, I.; Mitra, S.; Roqan, I. S.; Ooi, B. S.; He, J. H. *Nano Lett.* **2017**, 17, (3), 1520-1528.

202. AlOtaibi, B.; Fan, S.; Vanka, S.; Kibria, M. G.; Mi, Z. *Nano Lett.* **2015,** 15, (10), 6821-8.

203. Fan, R.; Tang, C.; Xin, Y.; Su, X.; Wang, X.; Shen, M. *Appl. Phys. Lett.* **2016,** 109, (23), 233901.

204. Warren, E. L.; McKone, J. R.; Atwater, H. A.; Gray, H. B.; Lewis, N. S. *Energ. Environ. Sci.* **2012,** 5, (11), 9653-9661.

205. Jung, J.-Y.; Park, M.-J.; Li, X.; Kim, J.-H.; Wehrspohn, R. B.; Lee, J.-H. *J. Mater. Chem. A* **2015,** 3, (18), 9456-9460.

206. Jung, J.-Y.; Choi, M. J.; Zhou, K.; Li, X.; Jee, S.-W.; Um, H.-D.; Park, M.-J.; Park, K.-T.; Bang, J. H.; Lee, J.-H. *J. Mater. Chem. A* **2014,** 2, (3), 833-842.

207. Oh, I.; Kye, J.; Hwang, S. *Nano Lett.* **2012,** 12, (1), 298-302.

208. Seger, B.; Laursen, A. B.; Vesborg, P. C.; Pedersen, T.; Hansen, O.; Dahl, S.; Chorkendorff, I. *Angew. Chem. Int. Ed. Engl.* **2012,** 51, (36), 9128-31.

209. Seger, B.; Tilley, D. S.; Pedersen, T.; Vesborg, P. C. K.; Hansen, O.; Grätzel, M.; Chorkendorff, I. *RSC Adv.* **2013,** 3, (48), 25902.

210. Chen, X.; Mao, S. S. *Chem. Rev.* **2007,** 107, (7), 2891-2959.

211. Tuller, H. L *Mater. Renew. Sustain. Energ.* **2017,** 6, (1), 3.

212. Lopes, T.; Dias, P.; Andrade, L.; Mendes, A. *Solar Energ. Mater. and Solar Cells* **2014,** 128, 399-410.

213. He, Y.; Hamann, T.; Wang, D. *Chem. Soc. Rev.* **2019**, DOI: 10.1039/C8CS00868J.

214. Lewis, N. S. *Science* **2016,** 351, (6271), aad1920.

215. Dumortier, M.; Tembhurne, S.; Haussener, S. *Energ. Environ. Science* **2015,** 8, (12), 3614-3628.

216. Shaner, M. R.; Atwater, H. A.; Lewis, N. S.; McFarland, E. W. *Energ. Environ. Science* **2016,** 9, (7), 2354-2371.

217. Benck, J. D.; Lee, S. C.; Fong, K. D.; Kibsgaard, J.; Sinclair, R.; Jaramillo, T. F. *Adv. Energ. Mater.* **2014,** 4, (18), 1400739.

218. Kang, D.; Young, J. L.; Lim, H.; Klein, W. E.; Chen, H.; Xi, Y.; Gai, B.; Deutsch, T. G.; Yoon, J. *Nat. Energ.* **2017,** 2, 17043.

219. Li, Q.; Zheng, M.; Zhong, M.; Ma, L.; Wang, F.; Ma, L.; Shen, W. *Sci. Rep.* **2016,** 6, 29738.

220. Bae, D.; Seger, B.; Hansen, O.; Vesborg, P. C. K.; Chorkendorff, I. *ChemElectroChem* **2019,** 6, (1), 106-109.

221. Nandjou, F.; Haussener, S. *J. Phys. D: Appl. Phys.* **2017,** 50, (12), 124002.

222. Gerischer, H. *J. Electroanalytical Chem. and Interfacial Electrochemistry* **1975,** 58, (1), 263-274.

223. Chen, S.; Wang, L.-W.. *Chem. Mater.* **2012,** 24, (18), 3659-3666.

224. Boettcher, S. W.; Warren, E. L.; Putnam, M. C.; Santori, E. A.; Turner-Evans, D.; Kelzenberg, M. D.; Walter, M. G.; McKone, J. R.; Brunschwig, B. S.; Atwater, H. A.; Lewis, N. S. *J. Am. Chem. Soc.* **2011,** 133, (5), 1216-9.

225. Lewerenz, H. J. *J. Electrochemical Soc.* **2014,** 161, (13), H3117-H3129.

226. Baker, D. R.; Lundgren, C. A. *J. Mater. Chem. A* **2017,** 5, (39), 20978-20984.

227. Shaner, M. R.; Hu, S.; Sun, K.; Lewis, N. S. *Energ. Environ. Sci.* **2015,** 8, (1), 203-207.

228. Kuang, Y.; Jia, Q.; Ma, G.; Hisatomi, T.; Minegishi, T.; Nishiyama, H.; Nakabayashi, M.; Shibata, N.; Yamada, T.; Kudo, A.; Domen, K. *Nat. Energ.* **2016,** 2, (1), 16191.

229. Dias, P.; Vilanova, A.; Lopes, T.; Andrade, L.; Mendes, A. *Nano Energ.* **2016,** 23, 70-79.

230. Dasgupta, N. P.; Liu, C.; Andrews, S.; Prinz, F. B.; Yang, P. *J. Am. Chem. Soc.* **2013,** 135, (35), 12932-5.

231. Fabre, B.; Li, G.; Gouttefangeas, F.; Joanny, L.; Loget, G. *Langmuir* **2016,** 32, (45), 11728-11735.

232. Kemppainen, E.; Bodin, A.; Sebok, B.; Pedersen, T.; Seger, B.; Mei, B.; Bae, D.; Vesborg, P. C. K.; Halme, J.; Hansen, O.; Lund, P. D.; Chorkendorff, I. *Energ. Environ. Sci.* **2015,** 8, (10), 2991-2999.

233. Maier, C. U.; Specht, M.; Bilger, G. *Int. J. Hydrogen Energ.* **1996,** 21, (10), 859-864.

234. Zhou, B.; Kong, X.; Vanka, S.; Chu, S.; Ghamari, P.; Wang, Y.; Pant, N.; Shih, I.; Guo, H.; Mi, Z. *Nat. Commun.* **2018,** 9, (1), 3856.

235. Andoshe, D. M.; Jin, G.; Lee, C.-S.; Kim, C.; Kwon, K. C.; Choi, S.; Sohn, W.; Moon, C. W.; Lee, S. H.; Suh, J. M.; Kang, S.; Park, J.; Heo, H.; Kim, J. K.; Han, S.; Jo, M.-H.; Jang, H. W. *Adv. Sus. Sys.* **2018,** 2, (3), 1700142.

236. Fan, R.; Cheng, S.; Huang, G.; Wang, Y.; Zhang, Y.; Vanka, S.; Botton, G. A.; Mi, Z.; Shen, M. *J. Mater. Chem. A* **2019,** 7, (5), 2200-2209.

237. McDowell, M. T.; Lichterman, M. F.; Carim, A. I.; Liu, R.; Hu, S.; Brunschwig, B. S.; Lewis, N. S. *ACS Appl. Mater. Interfaces* **2015,** 7, (28), 15189-99.

238. Seger, B.; Pedersen, T.; Laursen, A. B.; Vesborg, P. C.; Hansen, O.; Chorkendorff, I. *J. Am. Chem. Soc.* **2013,** 135, (3), 1057-64.

239. Guo, L.-J.; Luo, J.-W.; He, T.; Wei, S.-H.; Li, S.-S. *Phys. Rev. Appl.* **2018,** 10, (6), 064059.

240. Chen, X.; Mao, S. S. *Chem. Rev.* **2007,** 107, (7), 2891-2959.

241. Peng, K.-Q.; Wang, X.; Wu, X.-L.; Lee, S.-T. *Nano Lett.* **2009,** 9, (11), 3704-3709.

242. Guan, X.; Chowdhury, F. A.; Wang, Y.; Pant, N.; Vanka, S.; Trudeau, M. L.; Guo, L.; Vayssieres, L.; Mi, Z. *ACS Energ. Lett.* **2018**, 3, 2230−2231.

243. Su, J.; Wei, Y.; Vayssieres, L. *J. Phys. Chem. Lett.* **2017,** 8, (20), 5228-5238.

244. He, Y.; Vanka, S.; Gao, T.; He, D.; Espano, J.; Zhao, Y.; Dong, Q.; Lang, C.; Wang, Y.; Hamann, T. W.; Mi, Z.; Wang, D. *Nano Res.* **2019**, DOI: 10.1007/s12274-019-2346-3.

245. Moustakas, T. D. *Phys. Status Solidi A* **2013,** 210, (1), 169-174.

246. Vijselaar, W.; Tiggelaar, R. M.; Gardeniers, H.; Huskens, J. *ACS Energ. Lett.* **2018,** 3, (5), 1086-1092.

247. Chu, S.; Majumdar, A. *Nature* **2012,** 488, (7411), 294-303.

248. a) Walter, M. G.; Warren, E. L.; McKone, J. R.; S. W. Boettcher; Q. X. Mi; E. A. Santori, N. S. Lewis, *Chem. Rev.* **2010,** 110, (11), 6446-6473; b) Y. Hou,; X. Zhuang,; X. Feng, *Small Methods* **2017,** 1, (6), 170009.

249. a) J. A. Turner, *Science* **2004,** 305, (5686), 972-974; b) N. S. Lewis,; D. G. Nocera, *Proc. Natl. Acad. Sci. U S A* **2006,** 103, (43), 15729-35.

250. S. Hu,; C. X. Xiang,; S. Haussener,; A. D. Berger,; N. S. Lewis, *Energ. Environ. Sci.* **2013,** 6, (10), 2984-2993.

251. a) K. Sivula,; F. Le Formal,; M. Gratzel, *ChemSusChem* **2011,** 4, (4), 432-49; b) S. Shen,; S. A. Lindley,; X. Chen,; J. Z. Zhang, *Energ. Environ. Sci.* **2016,** 9, (9), 2744-2775.

252. a) Y. Park,; K. J. McDonald,; K.-S. Choi, *Chem. Soc. Rev.* **2013,** 42, (6), 2321-2337; b) I. D. Sharp, J. K. Cooper, F. M. Toma, R. Buonsanti, *ACS Energ. Lett.* **2017,** 2, (1), 139-150.

253. a) M. Li,; W. Luo,; D. Cao,; X. Zhao,; Z. Li,; T. Yu,; Z. Zou, *Angew. Chem. Int. Ed.* **2013,** 52, (42), 11016-11020; b) M. Zhong,; T. Hisatomi,; Y. Sasaki,; S. Suzuki,; K. Teshima,; M. Nakabayashi,; N. Shibata,; H. Nishiyama,; M. Katayama,; T. Yamada,; K. Domen, *Angew. Chem. Int. Ed.* **2017,** 56, (17), 4739-4743.

254. a) S. Hu, M. R. Shaner, J. A. Beardslee, M. Lichterman, B. S. Brunschwig, N. S. Lewis, *Science* **2014,** 344, (6187), 1005-1009; b) M. T. McDowell, M. F. Lichterman, A. I. Carim, R. Liu, S. Hu, B. S. Brunschwig, N. S. Lewis, *ACS Appl. Mater. Interfaces* **2015**, 7, (28), 15189-99.

255. a) B. Mei, B. Seger, T. Pedersen, M. Malizia, O. Hansen, I. Chorkendorff, P. C. K. Vesborg, *J. Phys. Chem. Lett.* **2014,** 5, (11), 1948-1952; b) X. H. Zhou, R. Liu, K. Sun, K. M. Papadantonakis, B. S. Brunschwig, N. S. Lewis, *Energ. Environ. Sci.* **2016,** 9, (3), 892-897; c) H. P. Wang, K. Sun, S. Y. Noh, A. Kargar, M. L. Tsai, M. Y. Huang, D. L. Wang, J. H. He, *Nano Lett.* **2015,** 15, (5), 2817-2824.

256. a) H. Gerischer, *Faraday Discussions of the Chemical Society* **1980,** 70, (0), 137-151; b) M. J. Kenney, M. Gong, Y. Li, J. Z. Wu, J. Feng, M. Lanza, H. Dai, *Science* **2013,** 342, (6160), 836-840.

257. a) Y. W. Chen, J. D. Prange, S. Duhnen, Y. Park, M. Gunji, C. E. D. Chidsey, P. C. McIntyre, *Nat. Mater.* **2011,** 10, (7), 539-544; b) X. H. Zhou, R. Liu, K. Sun, D. Friedrich, M. T. McDowell, F. Yang, S. T. Omelchenko, F. H. Saadi, A. C. Nielander, S. Yalamanchili, K. M. Papadantonakis, B. S. Brunschwig, N. S. Lewis, *Energ. Environ. Sci.* **2015,** 8, (9), 2644-2649; c) G. Xu, Z. Xu, Z. Shi, L. Pei, S. Yan, Z. Gu, Z. Zou, *ChemSusChem* **2017,** 10, (14), 2897-2903; d) K. Sun, M. T. McDowell, A. C. Nielander, S. Hu, M. R. Shaner, F. Yang, B. S. Brunschwig, N. S. Lewis, *J. Phys. Chem. Lett.* **2015,** 6, (4), 592-8.

258. B. Guo, A. Batool, G. Xie, R. Boddula, L. Tian, S. U. Jan, J. R. Gong, *Nano Lett.*, **2018**, 18, (2), 1516-1521.

259. a) X. Xu, G. Zhou, X. Dong, J. Hu, *ACS Sustain. Chem. Eng.* **2017,** 5, (5), 3829-3836; b) F. M. Pesci, M. S. Sokolikova, C. Grotta, P. C. Sherrell, F. Reale, K. Sharda, N. Ni, P. Palczynski, C. Mattevi, *ACS Catal.* **2017,** 7, (8), 4990-4998.

260. a) J. R. McKone, A. P. Pieterick, H. B. Gray, N. S. Lewis, *J. Am. Chem. Soc.* **2013,** 135, (1), 223-31; b) G. Kline, K. Kam, D. Canfield, B. A. Parkinson, *Sol. Energ. Mater.* **1981,** 4, (3), 301-308; c) H. J. Lewerenz, A. Heller, F. J. DiSalvo, *J. Am. Chem. Soc.* **1980,** 102, (6), 1877-1880; d) R. Tenne, A. Wold, *Appl. Phys. Lett.* **1985,** 47, (7), 707-709.

261. L. P. Bicelli, G. Razzini, *Surface Technology* **1982,** 16, (1), 37-47.

262. a) X. Yu, M. S. Prevot, N. Guijarro, K. Sivula, *Nat. Commun.* **2015,** 6, 7596; b) Y. Ouyang, C. Ling, Q. Chen, Z. Wang, L. Shi, J. Wang, *Chem. Mater.* **2016,** 28, (12), 4390-4396; c) A. K. Singh, K. Mathew, H. L. Zhuang, R. G. Hennig, *J. Phys. Chem. Lett.* **2015,** 6, (6), 1087-98;

263. R. Bourezg, G. Couturier, J. Salardenne, F. Lévy, *Phys. Rev. B* **1992,** 46, (23), 15404-15410.

264. H. Liu, N. Han, J. Zhao, *RSC Adv.* **2015,** 5, (23), 17572-17581.

265. a) M. Chhowalla, H. S. Shin, G. Eda, L. J. Li, K. P. Loh, H. Zhang, *Nat. Chem.* **2013,** 5, (4), 263-75; b) N. Balis, E. Stratakis, E. Kymakis, *Mater. Today* **2016,** 19, (10), 580-594.

266. a) E. Xenogiannopoulou, P. Tsipas, K. E. Aretouli, D. Tsoutsou, S. A. Giamini, C. Bazioti, G. P. Dimitrakopulos, P. Komninou, S. Brems, C. Huyghebaert, I. P. Radu, A. Dimoulas, *Nanoscale* **2015,** 7, (17), 7896-905; b) Y. H. Choi, D. H. Lim, J. H. Jeong, D. Park, K. S. Jeong, M. Kim, A. Song, H. S. Chung, K. B. Chung, Y. Yi, M. H. Cho, *ACS Appl. Mater. Interfaces* **2017**; c) Y.-H. Chang, W. Zhang, Y. Zhu, Y. Han, J. Pu, J.-K. Chang, W.-T. Hsu, J.-K. Huang, C.-L. Hsu, M.-H. Chiu, T. Takenobu, H. Li, C.-I. Wu, W.-H. Chang, A. T. S. Wee, L.-J. Li, *ACS Nano* **2014,** 8, (8), 8582-8590; d) X. Lu, M. I. Utama, J. Lin, X. Gong, J. Zhang, Y. Zhao, S. T. Pantelides, J. Wang, Z. Dong, Z. Liu, W. Zhou, Q. Xiong, *Nano Lett.* **2014,** 14, (5), 2419-25; e) F. S. Ohuchi, B. A. Parkinson, K. Ueno, A. Koma, *J. Appl. Phys.* **1990,** 68, (5), 2168-2175.

267. D. Tsoutsou, K. E. Aretouli, P. Tsipas, J. Marquez-Velasco, E. Xenogiannopoulou, N. Kelaidis, S. Aminalragia Giamini, A. Dimoulas, *ACS Appl. Mater. Interfaces* **2016,** 8, (3), 1836-41.

268. Y. Zhao, H. Lee, W. Choi, W. Fei, C. J. Lee, *RSC Adv.* **2017,** 7, (45), 27969-27973.

269. a) C. Jung, S. M. Kim, H. Moon, G. Han, J. Kwon, Y. K. Hong, I. Omkaram, Y. Yoon, S. Kim, J. Park, *Sci. Rep.* **2015,** 5, 15313; b) M. I. Utama, X. Lu, D. Zhan, S. T. Ha, Y. Yuan, Z. Shen, Q. Xiong, *Nanoscale* **2014,** 6, (21), 12376-82; c) D. Nam, J. U. Lee, H. Cheong, *Sci. Rep.* **2015,** 5, 17113; d) P. Soubelet, A. E. Bruchhausen, A. Fainstein, K. Nogajewski, C. Faugeras, *Phys. Rev. B* **2016,** 93, (15).

270. A. Q. Contractor, J. O. M. Bockris, *Electrochim. Acta* **1984,** 29, (10), 1427-1434.

271. a) J. R. McKone, R. A. Potash, F. J. DiSalvo, H. D. Abruna, *Phys. Chem. Chem. Phys.* **2015,** 17, (21), 13984-91; b) L. A. King, W. Zhao, M. Chhowalla, D. J. Riley, G. Eda, *J. Mater. Chem. A* **2013,** 1, (31), 8935.

272. B. Mei, G. Mul, B. Seger, *Adv. Sus. Sys.* **2017**, 1, (1-2), 1600035.

273. A. G. Scheuermann, J. P. Lawrence, K. W. Kemp, T. Ito, A. Walsh, C. E. Chidsey, P. K. Hurley, P. C. McIntyre, *Nat. Mater.* **2016,** 15, (1), 99-105.

274. J. Gao, B. Li, J. Tan, P. Chow, T. M. Lu, N. Koratkar, *ACS Nano* **2016,** 10, (2), 2628-35.

275. Shaner, M. R., Atwater, H. A., Lewis, N. S. & McFarland, E. W. *Energ. Environ. Sci.* **2016**, 9, 2354-2371.

276. Lopes, T., Dias, P., Andrade, L. & Mendes, A. *Sol. Energ. Mat. Sol. C* **128**, 399-410 (2014).

277. Lewis, N. S. *Science* **351**, aad1920, (2016).

278. Ostermayer, F. W.; Kohl, P. A. *Appl. Phys. Lett.* **1981**, 39, 76-78.

279. Abdi, F. F.; Han, L.; Smets, A. H.; Zeman, M.; Dam, B.,; Van de Krol, R. *Nat. Commun.* **2013**, 4, 2195.

280. Kim, J. H.; Jo, Y.; Kim, J. H.; Jang, J. W.; Kang, H. J.; Lee, Y. H.; Kim, D. S.; Jun, Y.; Lee, J. S. *ACS Nano* **2015**, 9, 11820-11829.

281. Shi, X.; Zhang, K.; Shin, K.; Ma, M.; Kwon, J.; Choi, I. T.; Kim, J. K.; Kim, H. K.; Wang, D. H.; Park, J. H. *Nano Energ.* **2015**, 13, 182-191.

282. Kim, J. H.; Jang, J. W.; Jo, Y. H.; Abdi, F. F.; Lee, Y. H.; van de Krol, R.; Lee, J. S. *Nat. Commun.* **2016**, 7, 13380.

283. Reece, S. Y.; Hamel, J. A.; Sung, K.; Jarvi, T. D.; Esswein, A. J.; Pijpers, J. J. H.; Nocera, D. G. *Science* **2011**, 334, 645-648.

284. Steier, L.; Herraiz-Cardona, I.; Gimenez, S.; Fabregat-Santiago, F.; Bisquert, J.; Tilley, S. D.; Grätzel, M. *Adv. Funct. Mater.* **2014**, 24, 7681-7688.

285. Luo, W.; Liu, B.; Li, Z.; Xie, Z.; Chen, D.; Zou, Z.; Zhang, R. *Appl. Phys. Lett.* **2008**, 92, 262110.

286. ElAfandy, R. T.; Ebaid, M.; Min, J. W.; Zhao, C.; Ng, T. K.; Ooi, B. S. *Opt. Express* **2018**, 26, A640-A650.

287. Krishnamoorthy, S.; Nath, D. N.; Akyol, F.; Park, P. S.; Esposto, M.; Rajan, S. *Appl. Phys. Lett.* **2010**, 97, 203502.

288. Grundmann, M. J.; Mishra, U. K. *Phys. Status Solidi C* **2007**, 4, 2830-2833.

289. Wang, Y.; Vanka, S.; Gim, J.; Wu, Y.; Fan, R.; Zhang, Y.; Shi, J.; Shen, M.; Hovden, R.; Mi, Z. *Nano Energ.* **2019**, 57, 405-413.

290. Lv, C.; Chen, Z.; Chen, Z.; Zhang, B.; Qin, Y.; Huang, Z.; Zhang, C. *J. Mater. Chem. A* **2015**, 3, 17669-17675.

291. Chen, Z.; Jaramillo, T. F.; Deutsch, T. G.; Kleiman-Shwarsctein, A.; Forman, A. J.; Gaillard, N.; Garland, R.; Takanabe, K.; Heske, C.; Sunkara, M.; McFarland, E. W.; Domen, K.; Miller, E. L.; Turner, J. A.; Dinh, H. N. *J. Mater. Res.* **2011**, 25, 3-16.

292. Gurudayal; Sabba, D.; Kumar, M. H.; Wong, L. H.; Barber, J.; Gratzel, M.; Mathews, N. *Nano Lett.* **2015**, 15, 3833-3839.

293. Licht, S.; Wang, B.; Mukerji, S.; Soga, T.; Umeno, M.; Tributsch, H. *J. Phys. Chem. B* **2000**, 104, 8920-8924.

294. May, M. M.; Lewerenz, H. J.; Lackner, D.; Dimroth, F.; Hannappel, T. *Nat. Commun.* **2015**, 6, 8286 (2015).

295. Bernardini, F.; Fiorentini, V.; Vanderbilt, D. *Phys. Rev. B* **1997**, 56, R10024-R10027.

296. Li, J.; Lin, J. Y.; Jiang, H. X. *Appl. Phys. Lett.* **2008**, 93, 162107.

297. AlOtaibi, B.; Kong, X.; Vanka, S.; Woo, S. Y.; Pofelski, A.; Oudjedi, F.; Fan, S.; Kibria, M. G.; Botton, G. A.; Ji, W.; Guo, H.; Mi, Z. *ACS Energ. Lett.* **2016,** 1, (1), 246-252.

298. Yu, Z.; Raman, A.; Fan, S. *Proc. Natl. Acad. Sci. U S A* **2010,** 107, (41), 17491-6.

299. Taguchi, M.; Yano, A.; Tohoda, S.; Matsuyama, K.; Nakamura, Y.; Nishiwaki, T.; Fujita, K.; Maruyama, E. *IEEE J. Photovoltaics* **2014,** 4, (1), 96-99.

Appendix-1

Experimental Section

InGaN nanowire growth: InGaN nanowires were grown on a 2-inch n-Si(100) wafer by plasma-assisted molecular beam epitaxy under nitrogen-rich conditions without any foreign catalysts.[1,2] The InGaN growth conditions are as follows: a growth temperature of 530 ºC for 7 h, a Ga beam equivalent pressure of ~2×10^{-8} Torr, an In beam equivalent pressure of ~8×10^{-8} Torr, a nitrogen flow rate of 0.5 standard cubic centimeter per minute (sccm), and a plasma power of 350 W. The Si substrate was thoroughly cleaned with acetone and methanol solvent to remove any organic contaminants and subsequently with 10% hydrofluoric acid to remove native oxide, prior to loading into the growth chamber.

IrO_2 deposition: IrO_2 was photodeposited on the InGaN nanowires in a sealed Pyrex chamber with a quartz lid. 60 mL deionized water, 15 mL methanol, and 2 mL of IrO_2 colloid were added in the chamber. The chamber was then evacuated and irradiated for 30 min using 300 W Xe lamp (Excelitas Technologies) for the photodeposition of IrO_2 nanoparticles. The IrO_2 colloid was prepared according to the reported procedure.[3,4] 80 mg Na_2IrCl_6 (99.9%, Sigma Aldrich) was added to a 100 mL deionized water, and the pH value of the solution was adjusted to 12 by adding aqueous NaOH solution followed by a heat treatment at 80 ºC for 30 min. Then, the solution was cooled in an ice-water bath and the pH value was adjusted to 9 with HNO_3. Finally, the solution was heated to 80 ºC for 1 h to form a deep blue solution containing colloidal IrO_2 nanoparticles.

TiO_2 deposition: TiO_2 film was deposited using a Gemstar Arradiance 8 ALD tool. Tetrakis (dimethylamido)-titanium (TDMAT, Sigma-Aldrich) and deionized water were used as the titanium precursor and the reactant, respectively. The substrate temperature in the deposition chamber was 225 °C. In an ALD cycle, a 0.7 s pulse of TDMAT was followed by a 23 s purge of

N_2 at 10 sccm, followed by a 0.022 s pulse of H_2O before another 23 s purge with N_2. This process was repeated for 18 cycles to provide films of ~1 nm in thickness. The thickness of TiO_2 layer can be precisely controlled by setting different ALD cycles.

Characterization: SEM images were recorded with a secondary electron (SE) detector using an Inspect F-50 FE-SEM system (5 keV) and a Tescan MIRA3 GMU system (15 keV). TEM images were obtained on FEI Tecnai G2 F20 microscope operated at 200 keV. HAADF-STEM images were collected using a JEOL 3100R05 microscope with double Cs aberration corrected STEM (300 keV, 29 mrad), with EDX. EELS data was acquired on Nion UltraSTEM 100 (100 kV, 26 mrad) with a Gatan Quantum Energy Filter, at 0.5 eV per channel to capture the Ga, In, N, and O edges simultaneously. Samples for STEM and EELS measurements were prepared in cross-section by mechanical wedge polishing. Samples for TEM measurements were scratched off from the Si substrate onto a TEM grid. XRD patterns were acquired on a Bruker D8 Discovery X-ray diffractometer using Cu Kα source. PL spectra were measured using a micro-PL system at room temperature with a 405 nm laser as the excitation source. XPS measurements were performed in a Thermo Scientific K-Alpha XPS system with a monochromatic Al Kα source (hv=1486.6 eV). Charging effects were compensated by using a flood gun, and binding energies were calibrated with respect to the residual C (1s) peak at 284.8 eV. Mott–Schottky plots were collected in 0.5 M H_2SO_4 under dark conditions using a potentiostat (Gamry Instruments, Interface 1000). An AC amplitude of 10 mV was applied at frequencies of 1 and 2 kHz.

PEC measurements: PEC performances were evaluated in a typical undivided three-electrode configuration using a potentiostat (Gamry Instruments, Interface 1000). A Pt wire and Ag/AgCl (bought from Pine Research Instrumentation) were employed as the counter electrode and the reference electrode, respectively. An AM 1.5G solar simulator (Newport Oriel) was used as the

light source, and the illumination intensity was calibrated to be 100 mW cm^{-2}. The scan rate of J-V curves was 20 mV/s. The recorded potentials versus Ag/AgCl were converted to versus RHE by the following equation: E(versus RHE) = E(versus Ag/AgCl) + (0.0591× pH) + 0.1976, where 0.1976 is a conversion factor from the Ag/AgCl electrode to RHE at 25 ºC. The working electrode (0.1-0.2 cm^2) was prepared as follows: a Ga-In eutectic (99.99%, Sigma-Aldrich) was rubbed on the backside of the Si substrate to form Ohmic contact, which was subsequently attached to a copper wire using conductive silver paint (Ted Pella). After the drying of paint, the entire sample except the front nanowire side was then sealed with epoxy (PC-Clear).

The ABPE was calculated using the following equation:

$$\mathrm{ABPE}(\%)=\left[\frac{J(\mathrm{mA\ cm^{-2}})\times(1.23-V_{bias})(V)}{P_{in}(\mathrm{mW\ cm^{-2}})}\right]\times\ 100\%$$

where J is the photocurrent density, V_{bias} is the applied bias, and P_{in} is the incident illumination power density (AM 1.5G, 100 mW cm^{-2}).

The wavelength dependence of IPCE was measured under monochromatic irradiation from a 300 W Xe lamp (Excelitas Technologies) equipped with different bandpass filters. IPCE was calculated using the following equation:

$$\mathrm{IPCE}(\%)=\left[\frac{J(\mathrm{mA\ cm^{-2}})\times 1240}{\lambda\times P_{in}(\mathrm{mW\ cm^{-2}})}\right]\times\ 100\%$$

where J is the photocurrent density, λ is the wavelength of incident light, and P_{in} is the incident illumination power density at the specific wavelength of λ.

Products of solar water splitting (H_2 and O_2) were detected by a gas chromatograph (GC, Shimadzu GC-8A) equipped with a thermal conducting detector (TCD), using high purity Ar as carrier gas. Prior to the measurements, the reaction system was purged with Ar for 30 min and evacuated using a pump to remove any residual air.

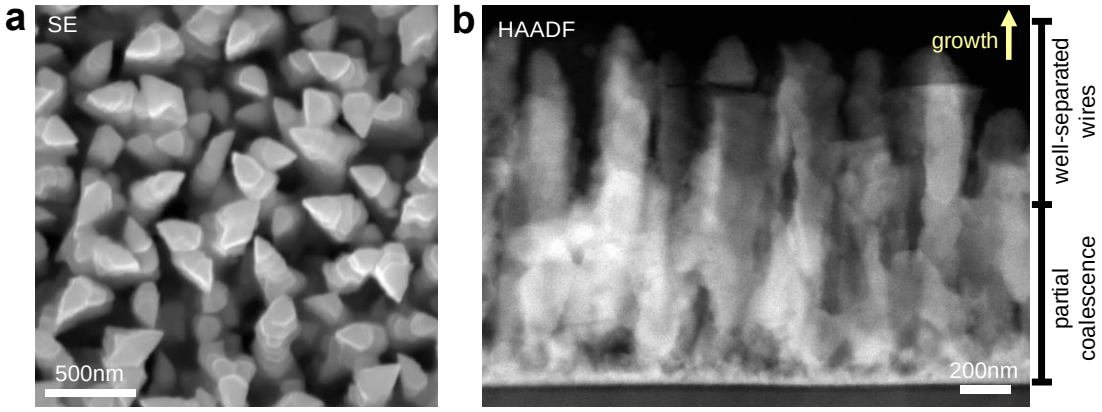

Appendix-1.1. Top-view SEM image and cross-sectional HAADF-STEM image of InGaN sample. (a) Well-separated nanowires observed in top-view. (b) Well separated crystalline nanowires grow atop a partially coalesced polycrystalline growth. The image of (b) was acquired at an accelerating voltage of 300 kV with a convergence angle of 22 mrad.

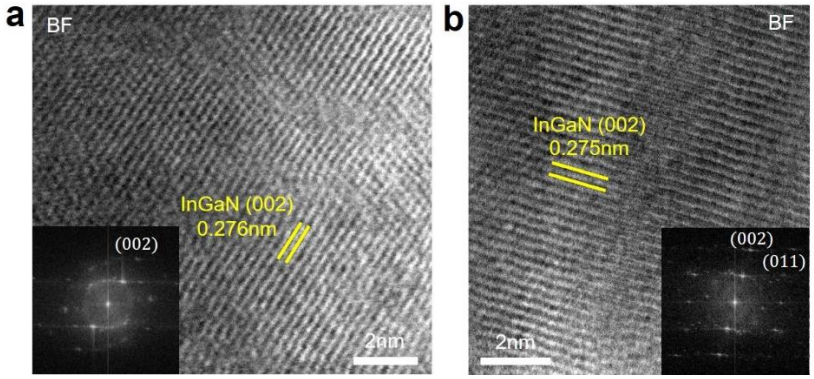

Appendix-1.2. Bright-field scanning-TEM (BF-STEM) images of IrO_2/InGaN sample. Lattice spacings of 0.276 nm in (a) and 0.275 nm in (b) correspond to the InGaN (002) plane. Insets are corresponding Fast Fourier Transform (FFT) images.

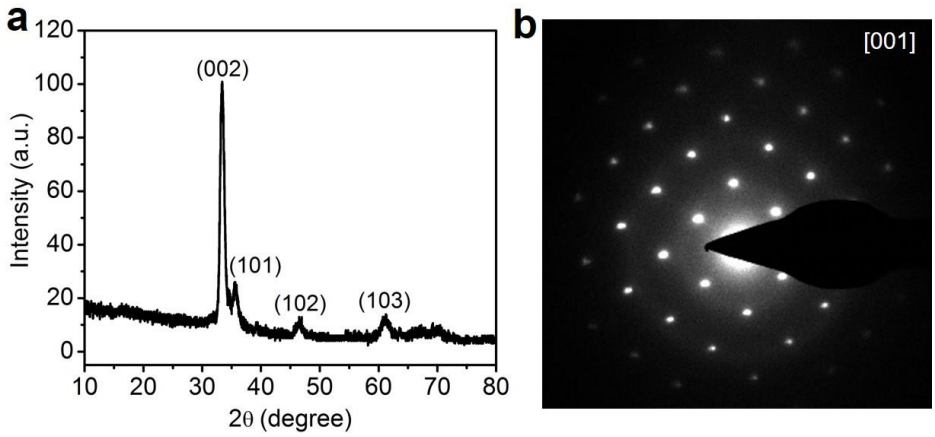

Appendix-1.3. Crystallographic analysis of InGaN nanowires. (a) The XRD pattern shows a strong (002) peak indicating preferential nanowire growth along the c-axis <0001> direction. The presence of a single set of peaks with (002) peak at ~33.2° is consistent with crystalline InGaN.[5,6] (b) Electron-diffraction pattern taken from a InGaN nanowire region shows a single crystal domain using a selected-area aperture with a diameter of 270 nm.

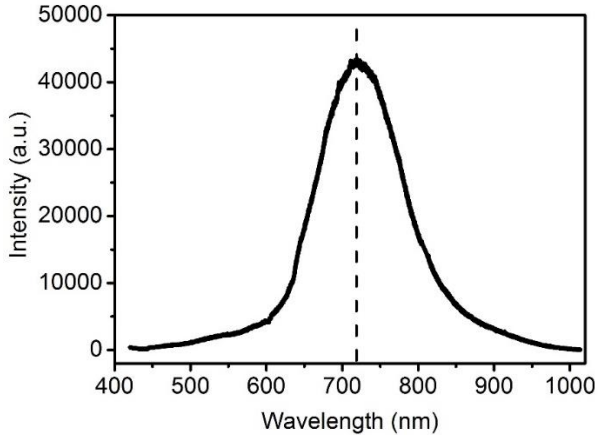

Appendix-1.4. Room-temperature PL spectrum of InGaN nanowire sample.

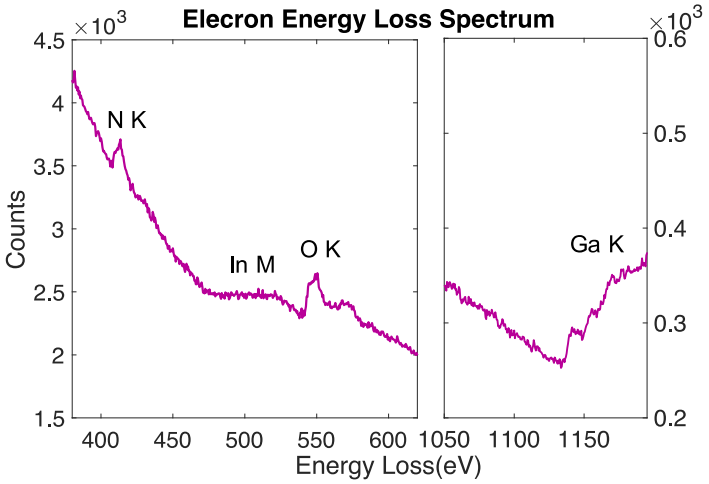

Appendix-1.5. STEM EELS spectrum taken from one of the IrO_2/InGaN nanowires. N-K, In-M, O-K and Ga-L electron energy loss spectra were measured. EELS spectrum was acquired at an accelerating voltage of 100 keV.

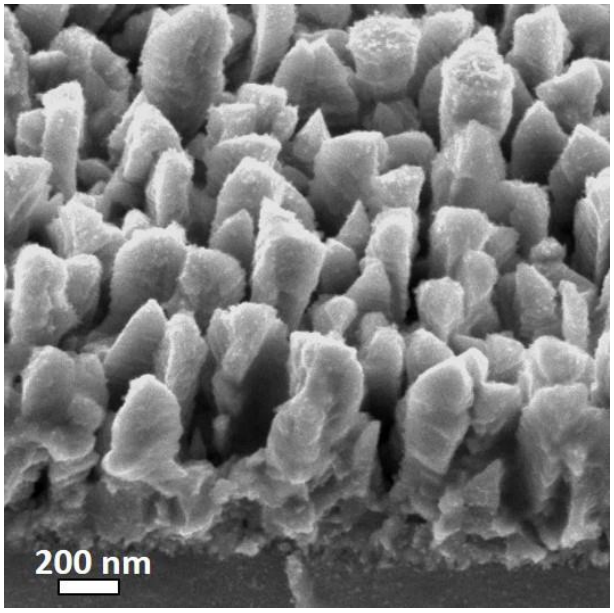

Appendix-1.6. 45°-Tilted SEM image of IrO_2/InGaN sample. The image was acquired at an accelerating voltage of 5 kV with a SE detector.

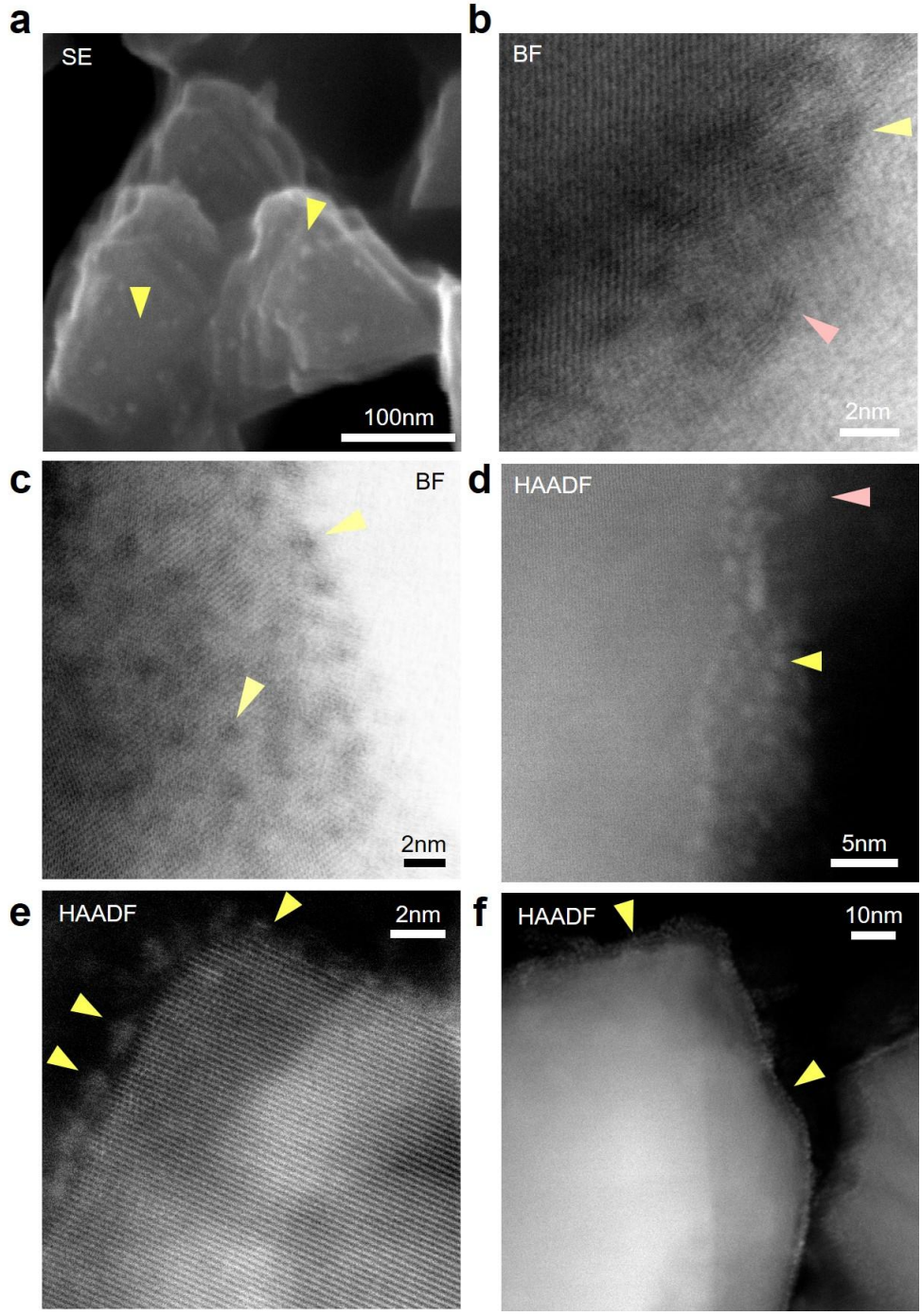

Appendix-1.7. Electron microscopy analysis of IrO_2/InGaN sample. (a) Top-view SEM, (b, c) BF-STEM and (d-f) HAADF-STEM images of IrO_2/InGaN sample. IrO_2 nanoparticles (arrows) are visible atop InGaN nanowire surface in the SEM image. The IrO_2 nanoparticles are partially

crystalline and mostly amorphous (arrows) with a width c.a. 1-2 nm. The images of (b-f) were acquired at an accelerating voltage of 300 kV with a convergence angle of 22 mrad.

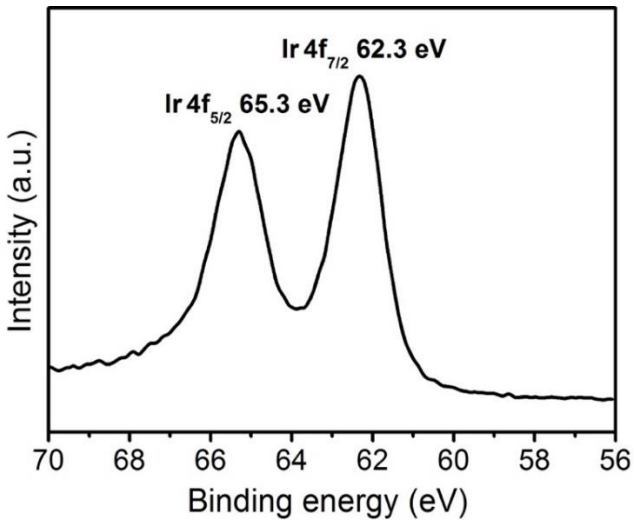

Appendix-1.8. XPS of Ir 4f for IrO_2/InGaN sample. The binding energy of 62.3 and 65.3 eV can be attributed to the Ir $4f_{7/2}$ and Ir $4f_{5/2}$ components of Ir^{4+} from IrO_2.[7,8]

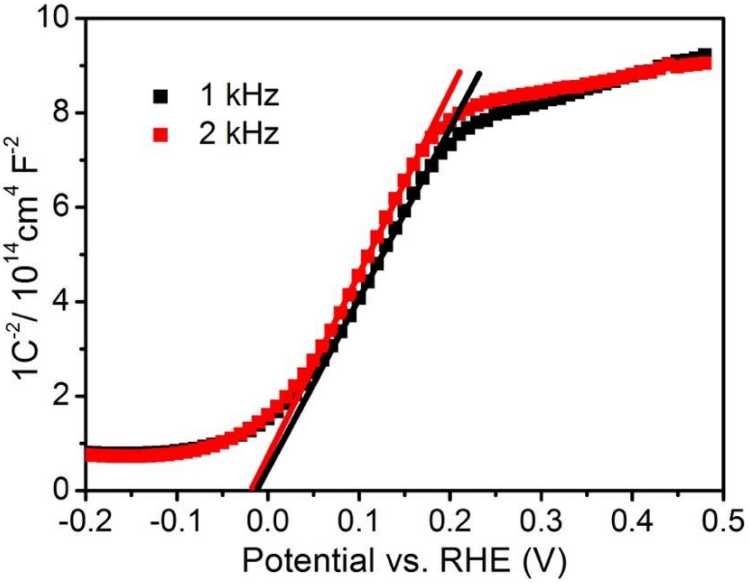

Appendix-1.9. Mott−Schottky plots of InGaN nanowire sample measured at two different frequencies, 1 kHz and 2 kHz. The positive slope of the plot indicates the InGaN nanowires are n-type. From the x-axis intercept, the flat-band potential of InGaN is determined to be 0.02 V versus

RHE. It is known that the conduction band edge of an n-type semiconductor is close to the flat-band potential.[9] Therefore, the position of the conduction band edge of InGaN is estimated to be slightly above the water reduction potential.

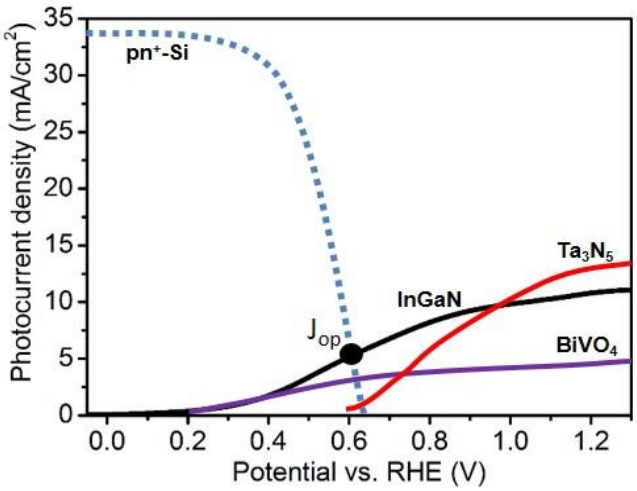

Appendix-1.10. A comparison of J-V curves of three different photoanodes with a state-of-the-art Si photocathode[10] to construct a PEC tandem device. The data of $BiVO_4$ and Ta_3N_5 are obtained from references 11 and 12, respectively. It is seen that the InGaN photoanode from this work gives the highest operating current density (J_{OP}) when paired with the Si photocathode, although its photocurrent density at 1.23 V versus RHE is lower than that of Ta_3N_5. This indicates the importance of acquiring high photocurrent density at the low bias region to construct efficient tandem devices.

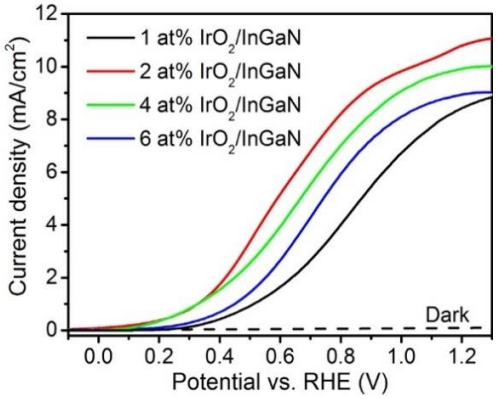

Appendix-1.11. J-V curves of IrO_2/InGaN photoanodes with different IrO_2 loading amount in 0.5 M H_2SO_4 under AM 1.5G simulated 1-sun illumination. The IrO_2 content was controlled by varying the amount of precursor solution in the photodeposition process. It was found that 2 at% IrO_2-loaded sample showed the highest PEC performance.

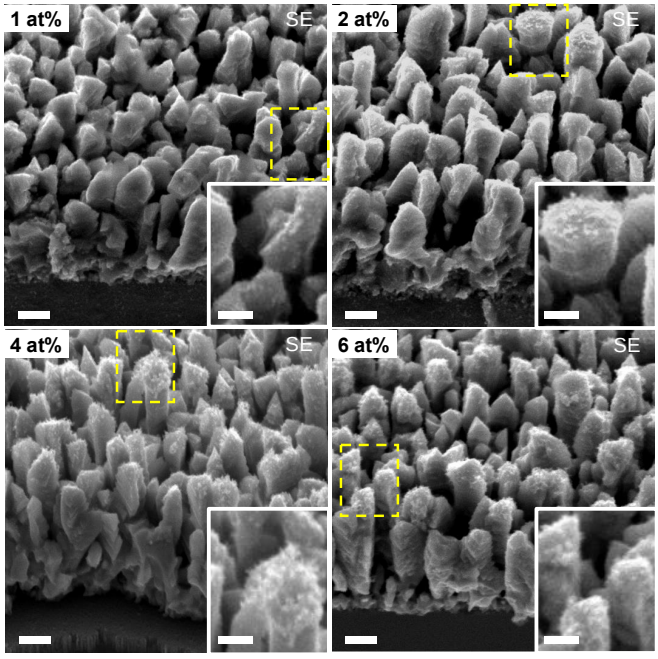

Appendix-1.12. 45°-tilted SEM images of IrO_2/InGaN sample with different nominal amounts of Ir precursor (1%, 2%, 4%, and 6% corresponding to 1, 2, 4, and 6 ml IrO_2 colloidal solutions,

respectively). The images were acquired at an accelerating voltage of 5 kV with a SE detector. Scale bars, 200 nm. Scale bars of magnified insets, 100 nm.

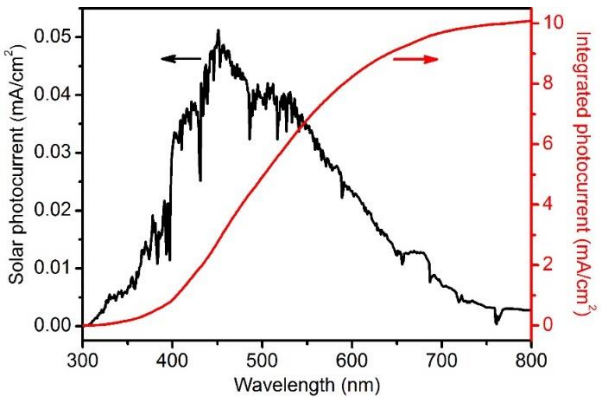

Appendix-1.13. Integrated solar photocurrent of IrO_2/InGaN photoanode at 1.23 V versus RHE by integrating the IPCE data in Figure 3.3d with the standard solar spectrum of AM 1.5G (ASTM G173-03). An integrated photocurrent density of 10.3 mA cm^{-2} (red curve) was estimated, which is close to the value (10.9 mA cm^{-2}) measured in Figure 3.3b.

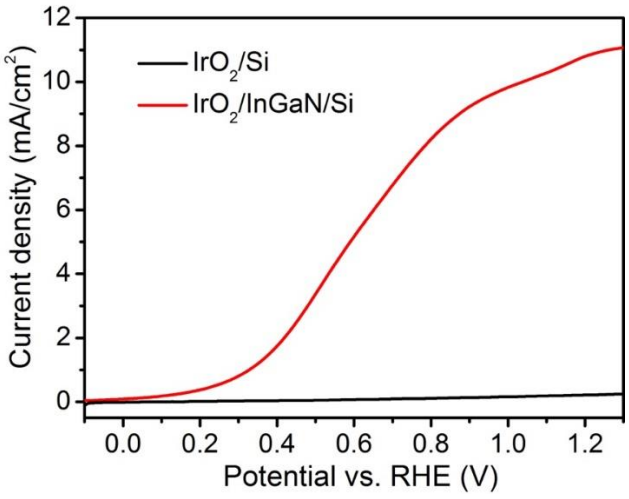

Appendix-1.14. J-V curves of photoanodes with or without InGaN nanowire in 0.5 M H_2SO_4 under AM 1.5G simulated 1-sun illumination. IrO_2/Si was prepared by IrO_2 photodeposition on Si substrate using the same protocol as IrO_2/InGaN/Si sample.

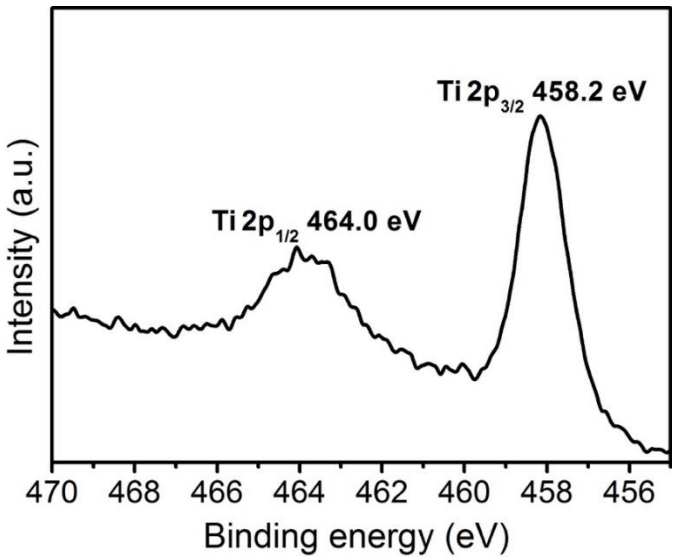

Appendix-1.15. XPS of Ti 2p for $TiO_2/IrO_2/InGaN$ sample.

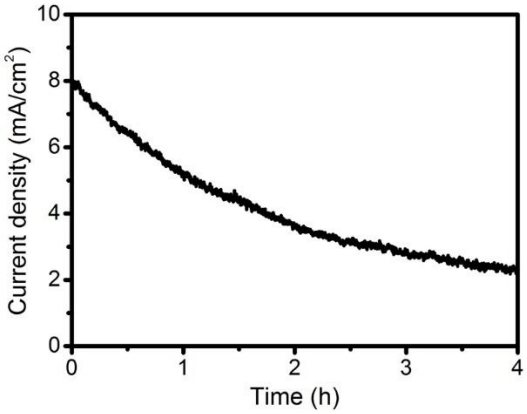

Appendix-1.16. J-t curve of $TiO_2/IrO_2/InGaN$ photoanode in 0.5 M H_2SO_4 at 0.8 V versus RHE under AM 1.5G simulated 1-sun illumination for 4 h. The decrease of photocurrent during the test was largely caused by the existence of pinholes within the ultrathin 1 nm TiO_2 protection layer and the exfoliation of TiO_2 layer, which is evidenced by XPS analysis showing the decrease of Ti atomic content from 4.5% to 2.8% after the PEC stability test. Without the protection of TiO_2 layer, InGaN was easily photocorroded and deactivated, as shown in Figure 3.2e.

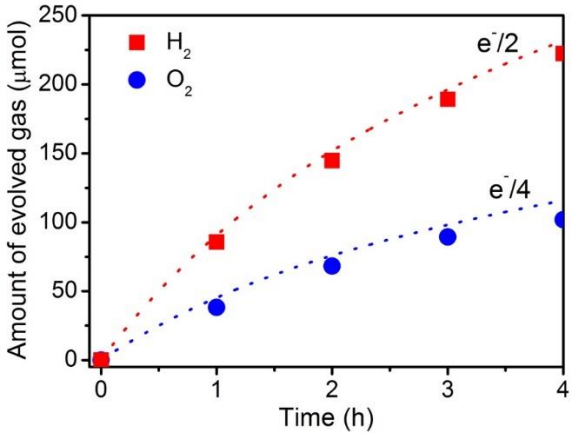

Appendix-1.17. Time courses of H_2 and O_2 evolution of $TiO_2/IrO_2/InGaN$ photoanode in 0.5 M H_2SO_4 under AM 1.5G simulated 1-sun illumination using a two-electrode cell. The bias was 0.8 V versus Pt counter electrode. The dotted lines represent the calculated amount of H_2 and O_2 evolution assuming 100% Faraday efficiency.

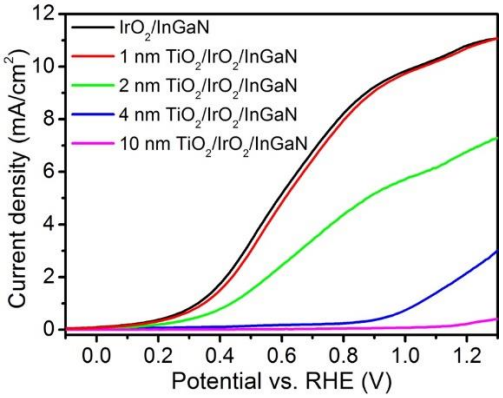

Appendix-1.18. J-V curves of $TiO_2/IrO_2/InGaN$ photoanodes with different TiO_2 thicknesses in 0.5 M H_2SO_4 under AM 1.5G simulated 1-sun illumination. The thickness of TiO_2 was controlled by varying the cycles in the ALD process.

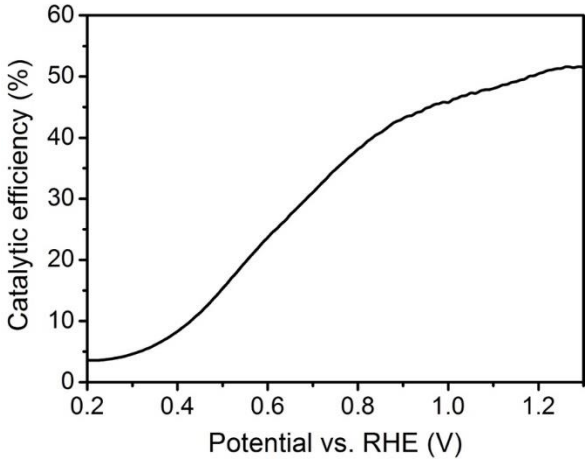

Appendix-1.19. Catalytic efficiency for water oxidation of TiO_2/IrO_2/InGaN photoanode as a function of applied bias. Assuming the catalytic efficiency for H_2O_2 oxidation is ~100% considering its extremely fast oxidation kinetics, the catalytic efficiency for water oxidation ($\eta_{catalysis}$) is calculated using the following equation according to the literature[13-14]:

$$\eta_{catalysis} = J_{H2O}/J_{H2O2}$$

where J_{H2O} and J_{H2O2} are the photocurrent density measured for oxidation of H_2O and H_2O_2, respectively.

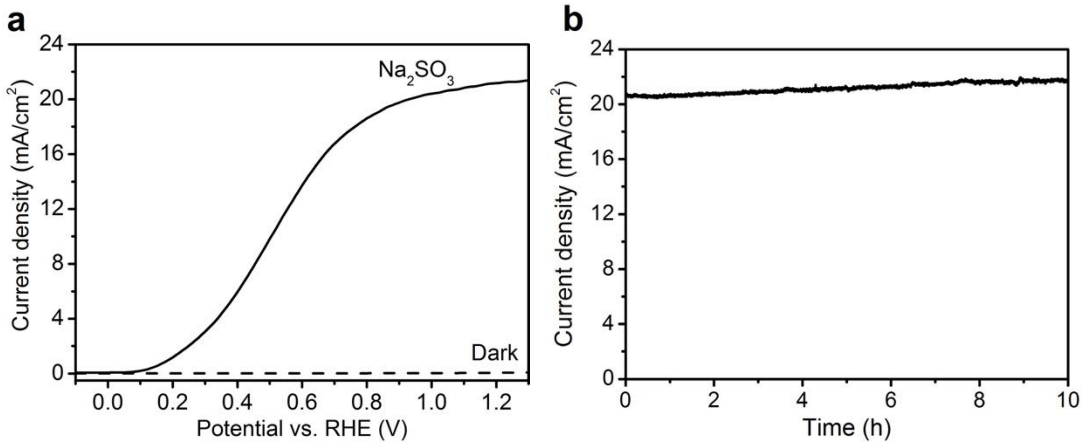

Appendix-1.20. (a) J-V curves of TiO_2/IrO_2/InGaN photoanode under AM 1.5G simulated 1-sun illumination in 0.5 M Na_2SO_4 containing 0.5 M Na_2SO_3 hole scavenger (pH = 10.2). (b) J-t curve of TiO_2/IrO_2/InGaN photoanode at 1.23 V versus RHE under AM 1.5G simulated 1-sun

illumination in 0.5 M Na_2SO_4 containing 0.5 M Na_2SO_3 hole scavenger.

Appendix-1.21. Performance comparison between the presented InGaN nanowire photoanode and state-of-the-art photoanodes for water oxidation under AM 1.5G simulated 1-sun illumination.

Photoanode	E_g (eV)	V_{onset} (V vs. RHE)	$J_{0.6\ V\ vs.\ RHE}$ (mA cm^{-2})	$J_{1.23\ V\ vs.\ RHE}$ (mA cm^{-2})	ABPE	Electrolyte	Ref
NiOOH/FeOOH/ $BiVO_4$	2.5	0.2	2.8	4.2	1.75%	0.5 M KPi (pH 7)	[15]
Co_4O_4 cubane/ $BiVO_4$	2.45	0.2	2.5	5.1	1.84%	0.5 M KBi (pH 9.3)	[16]
NiOOH/FeOOH/ N-doped $BiVO_4$	2.27	0.24	3.47	5.0	2.2%	0.5 M KPi (pH 7.2)	[11]
$NiFeO_x$-B_i/$BiVO_4$	2.4	~0.2	3.5	4.8	2.25%	1 M KBi (pH 9.3)	[17]
NiOOH/FeOOH/ CQD/$BiVO_4$	2.28	0.25	3.9	6.0	2.29%	KPi (pH 7)	[18]
Co-Pi/Ba-Ta_3N_5	2.1	0.65	0	6.7	1.5%	0.5 M KPi +KOH (pH 13)	[19]
Ir, Co complex /$Ni(OH)_2$/Fh /TiO_x/Ta_3N_5	2.1	0.45	~0.5	12.1	2.5%	1 M NaOH	[12]
Co_{ox}/Fe_2TiO_5-TiO_2	2.2	0.18	3.5	4.1	2.7%	1 M KOH	[20]

Photoanode	E_g (eV)	V_{onset} (V vs. RHE)	$J_{0.6\ V\ vs.\ RHE}$ (mA cm^{-2})	$J_{1.23\ V\ vs.\ RHE}$ (mA cm^{-2})	ABPE	Electrolyte	Ref
NiO_x/np^+Si	1.1	1.03	0	30.9	2.1%	1 M KOH	[21]
$NiO_x/CoO_x/SiO_x$/ n-Si	1.1	0.99	0	27.7	2.1%	1 M KOH	[22]
$NiFe/SiO_x/np^+$-Si	1.1	0.89	0	30.7	3.3%	1 M KOH	[23]
IrO_2/InGaN	1.7	0.1	5.2	10.9	3.6%	0.5 M H_2SO_4	This work

Appendix-1.22. Performance comparison of photoanodes with bandgaps of 1.6-1.8 eV as potential top light absorber for water oxidation under AM 1.5G simulated 1-sun illumination.

Photoanode	E_g (eV)	V_{onset} (V vs. RHE)	$J_{0.6\ V\ vs.\ RHE}$ (mA cm^{-2})	$J_{1.23\ V\ vs.\ RHE}$ (mA cm^{-2})	IPCE at 1.23 V vs. RHE	Electrolyte	Ref
$SrNbO_2N$	1.8	~0.5	~0.05	1.5	-	0.2 M NaP_i /NaOH (pH 13)	[24]
CoO_x-FeO_x /$BaNbO_2N$	~1.7	~0.8	0	0.85	6.1% at 480 nm, 1.6% at 660 nm	0.5 M KB_i (pH 13)	[25]
Co_3O_4-$Ba_2Bi_{1.4}Nb_{0.6}O_6$	1.64	0.875	-	0.4	-	1 M KOH	[26]
$Cu_3V_2O_8$	1.8	0.9	0	0.06	3% at 360 nm	B_i/NaOH (pH 9.2)	[27]

Photoanode	E_g (eV)	V_{onset} (V vs. RHE)	$J_{0.6\ V\ vs.\ RHE}$ (mA cm^{-2})	$J_{1.23\ V\ vs.\ RHE}$ (mA cm^{-2})	IPCE at 1.23 V vs. RHE	Electrolyte	Ref
$SnWO_4$	1.78	-0.1	0.03	0.08	2.8% at 350 nm	0.5 M KP_i (pH 7)	[28]
Fe_2WO_6	1.7	1.0	0	0.07	2% at 350 nm	0.1 M KOH	[29]
Sb_2S_3	1.72	0.25	0.12	0.6	-	0.1 M Na_2SO_4 (pH 5.5)	[30]
IrO_2/InGaN	1.7	0.1	5.2	10.9	93% at 440 nm, 63% at 500 nm, 33% at 600 nm	0.5 M H_2SO_4	This work

Appendix-1.23. Ir content of IrO_2/InGaN and TiO_2/IrO_2/InGaN photoanodes before and after PEC stability test, as determined by XPS measurements. All compositions are expressed as atomic concentration.

Sample	PEC conditions	% Ir before the PEC test	% Ir after the PEC test
IrO_2/InGaN	0.8 V versus RHE for 0.5 h	10.01	0.70
TiO_2/IrO_2/InGaN	0.8 V versus RHE for 4 h	3.48	2.43

Appendix-1.24. Stability and performance comparison between the presented InGaN nanowire photoanode and other related group III-V photoanodes for water oxidation under AM 1.5G simulated 1-sun illumination.

Photoanode structure	Protection layer and thickness	Stability	V_{onset} (V vs. RHE)	$J_{1.23\ V\ vs.\ RHE}$ (mA cm^{-2})	Hole transport mechanism	Ref
Ni/TiO_2/GaAs	TiO_2, 118 nm	> 25 h	0.65	~14	Defect band conduction	[31]
Ni/TiO_2/GaP	TiO_2, 118 nm	> 5 h	1.0	~2	Defect band conduction	[31]
Ni/TiO_2/InGaP-GaAs[a]	TiO_2, 62.5 nm	80 h	-	-	Defect band conduction	[32]
NiO_x/InP	NiO_x, 70 nm	> 48 h	0.86	17.5	Defect band conduction	[33]
$NiCo_2O_4$/InP	$NiCo_2O_4$, 40 nm	4 h	1.55	-	Valence band transport	[34]
TiO_2/IrO_2/InGaN	TiO_2, 1 nm	0.5 h	0.1	10.9	Tunneling	This work

[a] A tandem junction device.

Reference:

(1) Fan, S.; Woo, S. Y.; Vanka, S.; Botton, G. A.; Mi, Z. An $In_{0.5}Ga_{0.5}N$ Nanowire Photoanode for Harvesting Deep Visible Light Photons. *APL Mater.* **2016**, *4*, 076106.

(2) Fan, S.; Shih, I.; Mi, Z. A Monolithically Integrated InGaN Nanowire/Si Tandem Photoanode Approaching the Ideal Bandgap Configuration of 1.75/1.13 eV. *Adv. Energy Mater*. **2017**, *7*, 1600952.

(3) Abe, R.; Higashi, M.; Domen, K. Facile Fabrication of an Efficient Oxynitride TaON Photoanode for Overall Water Splitting into H_2 and O_2 under Visible Light Irradiation. *J. Am. Chem. Soc.* **2010**, *132*, 11828-11829.

(4) Bledowski, M.; Wang, L. D.; Neubert, S.; Mitoraj, D.; Beranek, R. Improving the Performance of Hybrid Photoanodes for Water Splitting by Photodeposition of Iridium Oxide Nanoparticles. *J. Phys. Chem. C* **2014**, *118*, 18951-18961.

(5) De, A.; Shivaprasad, S. M. Epitaxy, Phase Separation and Band-Edge Emission of Spontaneously Formed InGaN Nanorods. *J. Phys. D Appl. Phys.* **2016**, *49*, 355304.

(6) Pendyala, C.; Jasinski, J. B.; Kim, J. H.; Vendra, V. K.; Lisenkov, S.; Menon, M.; Sunkara, M. K. Nanowires as Semi-Rigid Substrates for Growth of Thick, $In_xGa_{1-x}N$ ($x > 0.4$) Epi-Layers without Phase Segregation for Photoelectrochemical Water Splitting. *Nanoscale* **2012**, *4*, 6269-6275.

(7) Li, W.; Sheehan, S. W.; He, D.; He, Y. M.; Yao, X. H.; Grimm, R. L.; Brudvig, G. W.; Wang, D. W. Hematite-Based Solar Water Splitting in Acidic Solutions: Functionalization by Mono- and Multilayers of Iridium Oxygen-Evolution Catalysts. *Angew. Chem. Int. Ed.* **2015**, *54*, 11428-11432.

(8) Minguzzi, A.; Locatelli, C.; Lugaresi, O.; Achilli, E.; Cappelletti, G.; Scavini, M.; Coduri, M.;

Masala, P.; Sacchi, B.; Vertova, A.; Ghigna, P.; Rondinini, S. Easy Accommodation of Different Oxidation States in Iridium Oxide Nanoparticles with Different Hydration Degree as Water Oxidation Electrocatalysts. *ACS Catal.* **2015**, *5*, 5104-5115.

(9) Beranek, R. (Photo)electrochemical Methods for the Determination of the Band Edge Positions of TiO_2-Based Nanomaterials. *Adv. Phys. Chem.* **2011**, *2011*, 1-20.

(10) Wang, H. P.; Sun, K.; Noh, S. Y.; Kargar, A.; Tsai, M. L.; Huang, M. Y.; Wang D. L.; He, J. H. High-Performance a-Si/c-Si Heterojunction Photoelectrodes for Photoelectrochemical Oxygen and HydrogenEvolution. *Nano Lett.* **2015**, *15*, 2817-2824.

(11) Kim, T. W.; Ping, Y.; Galli, G. A.; Choi, K. S. Simultaneous Enhancements in Photon Absorption and Charge Transport of Bismuth Vanadate Photoanodes for Solar Water Splitting. *Nat. Commun.* **2015**, *6*, 8769.

(12) Liu, G. J.; Ye, S.; Yan, P. L.; Xiong, F. Q.; Fu, P.; Wang, Z. L.; Chen, Z.; Shi, J. Y.; Li, C. Enabling an Integrated Tantalum Nitride Photoanode to Approach the Theoretical Photocurrent Limit for Solar Water Splitting. *Energy Environ. Sci.* **2016**, *9*, 1327-1334.

(13) Dotan, H.; Sivula, K.; Gratzel, M.; Rothschild, A.; Warren, S. C. Probing the Photoelectrochemical Properties of Hematite (α-Fe_2O_3) Electrodes Using Hydrogen Peroxide as a Hole Scavenger. *Energy Environ. Sci.* **2011**, *4*, 958-964.

(14) Abdi, F. F.; Van De Krol, R. Nature and Light Dependence of Bulk Recombination in Co-Pi-Catalyzed $BiVO_4$ Photoanodes. *J. Phys. Chem. C* **2012**, *116*, 9398-9404.

(15) Kim, T. W.; Choi, K. S. Nanoporous $BiVO_4$ Photoanodes with Dual-Layer Oxygen Evolution Catalysts for Solar Water Splitting. *Science* **2014**, *343*, 990-994.

(16) Wang, Y.; Li, F.; Zhou, X.; Yu, F.; Du, J.; Bai, L.; Sun, L. Highly Efficient Photoelectrochemical Water Splitting with an Immobilized Molecular Co_4O_4 Cubane Catalyst.

Angew. Chem. Int. Edit. **2017**, *56***,** 6911-6915.

(17) Kuang, Y. B.; Jia, Q. X.; Nishiyama, H.; Yamada, T.; Kudo, A.; Domen, K. A Front-Illuminated Nanostructured Transparent $BiVO_4$ Photoanode for > 2% Efficient Water Splitting. *Adv. Energy Mater.* **2016**, *6*, 1501645.

(18) Ye, K.-H.; Wang, Z.; Gu, J.; Xiao, S.; Yuan, Y.; Zhu, Y.; Zhang, Y.; Mai, W.; Yang, S. Carbon Quantum Dots as a Visible Light Sensitizer to Significantly Increase the Solar Water Splitting Performance of Bismuth Vanadate Photoanodes. *Energy Environ. Sci.* **2017**, *10*, 772.

(19) Li, Y. B.; Zhang, L.; Torres-Pardo, A.; Gonzalez-Calbet, J. M.; Ma, Y. H.; Oleynikov, P.; Terasaki, O.; Asahina, S.; Shima, M.; Cha, D.; et al. Cobalt Phosphate-Modified Barium-Doped Tantalum Nitride Nanorod Photoanode with 1.5% Solar Energy Conversion Efficiency. *Nat. Commun.* **2013**, *4***,** 2566.

(20) Liu, Q. H.; He, J. F.; Yao, T.; Sun, Z. H.; Cheng, W. R.; He, S.; Xie, Y.; Peng, Y. H.; Cheng, H.; Sun, Y. F.; et al. Aligned Fe_2TiO_5-Containing Nanotube Arrays with Low Onset Potential for Visible-Light Water Oxidation. *Nat. Commun.* **2014**, *5***,** 5122.

(21) Sun, K.; McDowell, M. T.; Nielander, A. C.; Hu, S.; Shaner, M. R.; Yang, F.; Brunschwig B. S.; Lewis, N. S. Stable Solar-Driven Water Oxidation to O_2 by Ni-Oxide-Coated Silicon Photoanodes. *J. Phys. Chem. Lett.* **2015**, *6*, 592-598.

(22) Zhou, X. H.; Liu, R.; Sun, K.; Friedrich, D.; McDowell, M. T.; Yang, F.; Omelchenko, S. T.; Saadi, F. H.; Nielander, A. C.; Yalamanchili, S. K.; et al. Interface Engineering of the Photoelectrochemical Performance of Ni-Oxide-Coated n-Si Photoanodes by Atomic-Layer Deposition of Ultrathin Films of Cobalt Oxide. *Energy Environ. Sci.* **2015**, *8*, 2644-2649.

(23) Yu, X.; Yang, P.; Chen, S.; Zhang, M.; Shi, G. NiFe Alloy Protected Silicon Photoanode for Efficient Water Splitting. *Adv. Energy Mater.* **2016**, *6*, 1601805.

(24) Kodera, M.; Urabe, H.; Katayama, M.; Hisatomi, T.; Minegishi, T.; Domen, K., Effects of Flux Synthesis on $SrNbO_2N$ Particles for Photoelectrochemical Water Splitting. *J. Mater. Chem. A* **2016**, 4, 7658-7664.

(25) Seo, J.; Moriya, Y.; Kodera, M.; Hisatomi, T.; Minegishi, T.; Katayama, M.; Domen, K., Photoelectrochemical Water Splitting on Particulate $ANbO_2N$ (A = Ba, Sr) Photoanodes Prepared from Perovskite-Type $ANbO_3$. *Chem. Mater.* **2016**, *28*, 6869-6876.

(26) Weng, B.; Xiao, Z.; Meng, W.; Grice, C. R.; Poudel, T.; Deng, X.; Yan, Y. Bandgap Engineering of Barium Bismuth Niobate Double Perovskite for Photoelectrochemical Water Oxidation. *Adv. Energy Mater.* **2016**, *6*, 1602260.

(27) Jiang, C.-M.; Farmand, M.; Wu, C. H.; Liu, Y.-S.; Guo, J.; Drisdell, W. S.; Cooper, J. K.; Sharp, I. D. Electronic Structure, Optoelectronic Properties, and Photoelectrochemical Characteristics of γ-$Cu_3V_2O_8$ Thin Films. *Chem. Mater.* **2017**, *29*, 3334-3345.

(28) Zhu, Z. H.; Sarker, P.; Zhao, C. Q.; Zhou, L. T.; Grimm, R. L.; Huda, M. N.; Rao, P. M. Photoelectrochemical Properties and Behavior of α-$SnWO_4$ Photoanodes Synthesized by Hydrothermal Conversion of WO_3 Films. *ACS Appl. Mater. Inter.* **2017**, *9*, 1459-1470.

(29) Abdi, F. F.; Chemseddine, A.; Berglund, S. P.; van de Krol, R. Assessing the Suitability of Iron Tungstate (Fe_2WO_6) as a Photoelectrode Material for Water Oxidation. *J. Phys. Chem. C* **2017**, *121*, 153-160.

(30) DeAngelis, A. D.; Kemp, K. C.; Gaillard, N.; Kim, K. S., Antimony(III) Sulfide Thin Films as a Photoanode Material in Photocatalytic Water Splitting. *ACS Appl. Mater. Inter.* **2016**, *8*, 8445-8451.

(31) Hu, S.; Shaner, M. R.; Beardslee, J. A.; Lichterman, M.; Brunschwig, B. S.; Lewis, N. S., Amorphous TiO_2 Coatings Stabilize Si, GaAs, and GaP Photoanodes for Efficient Water

Oxidation. *Science* **2014,** *344*, 1005-1009.

(32) Verlage, E.; Hu, S.; Liu, R.; Jones, R. J. R.; Sun, K.; Xiang, C. X.; Lewis, N. S.; Atwater, H. A., A Monolithically Integrated, Intrinsically Safe, 10% Efficient, Solar-Driven Water-Splitting System Based on Active, Stable Earth-Abundant Electrocatalysts in Conjunction with Tandem III-V Light Absorbers Protected by Amorphous TiO_2 Films. *Energy Environ. Sci.* **2015,** *8*, 3166-3172.

(33) Sun, K.; Kuang, Y. J.; Verlage, E.; Brunschwig, B. S.; Tu, C. W.; Lewis, N. S., Sputtered NiO_x Films for Stabilization of p^+n-InP Photoanodes for Solar-Driven Water Oxidation. *Adv. Energy Mater*. **2015,** *5*, 1402276.

(34) Chen, L.; Yang, J. H.; Klaus, S.; Lee, L. J.; Woods-Robinson, R.; Ma, J.; Lum, Y.; Cooper, J. K.; Toma, F. M.; Wang, L. W.; et al. p-Type Transparent Conducting Oxide/n-Type Semiconductor Heterojunctions for Efficient and Stable Solar Water Oxidation. *J. Am. Chem. Soc.* **2015,** *137*, 9595-9603.

Appendix-2

Appendix-2.1: Fabrication of n^+-p Si substrates

Double side polished p-type Si(100) wafers (WRS Materials, thickness: 254 – 304 µm; resistivity: 1 - 10 Ω·cm) are spin-coated with liquid phosphorous dopant precursor (Futurrex, Inc.) on one side to form the n^+-Si emitter and liquid boron dopant precursor (Futurrex, Inc.) on the other side to form the p^+-Si back field layer. Subsequently, the thermal diffusion process is conducted at 950 ^oC for 240 min under argon gas flow in a furnace. The residue of the precursor is removed in buffered oxide etch (BHF) solution. To measure the efficiency of the solar cells, metal contacts are made on n-side and p-side by depositing Ti/Au and Ni/Au using e-beam evaporator, respectively.

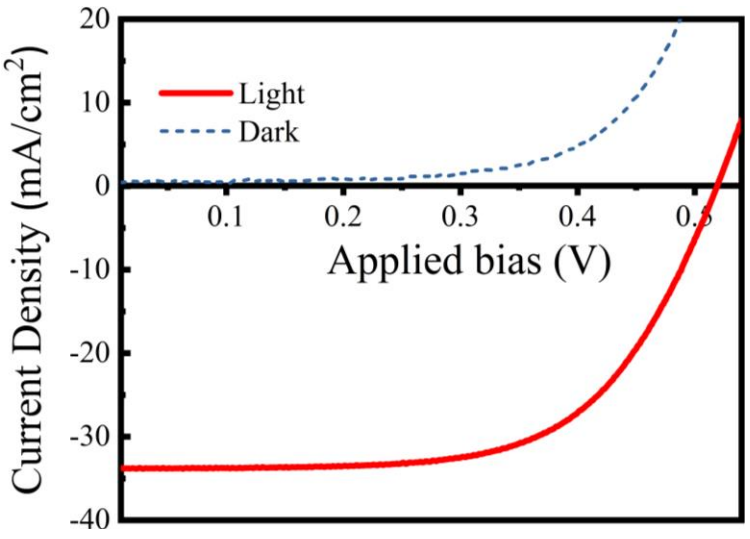

Figure 1. J-V characteristics of n^+-p Si under AM1.5G one sun illumination 100 mW/cm^2 (red curve) and dark condition (blue dashed curve). Shown in Supp. Info. Figure S1, J_{sc} of n^+-p Si device is ~33 mA/cm^2, V_{oc} is ~0.52 V and energy conversion efficiency is ~11%.

Appendix-2.2: **Methods**

Pt NPs photodeposition. The photocathode (either n^+-GaN nanowire/n^+-p Si or n^+-p Si) is put on a Teflon holder and placed in the bottom of a Pyrex chamber with a quartz window. Next, 10 μL of 0.2 M Chloroplatinic acid hydrate (99.9%, Sigma Aldrich) is used as Pt precursor, and 10 mL of CH_3OH (i.e., a hole scavenger) and 50 mL of Milli-Q (~18 MΩ) water are poured into the Pyrex chamber. The chamber is evacuated using a vacuum pump for 10 min. Then the sample is irradiated using a 300 W xenon lamp (PerkinElmer, PE300BF) for 30 min (optimized deposition conditions, see Appendix-2.4).

SEM and STEM Characterization. SEM images are taken using MIRA3 TESCAN at an accelerating voltage of 10 kV. High angle annular dark field (HAADF)-STEM images (Figure 2(c) and Figure S8(b)) are collected using a JEOL 2100F microscope with STEM aberration corrector operated at 200 kV. The nanowires are scratched off from the Si substrate onto a TEM copper grid. The scanning transmission electron microscopy high angle annular dark field (STEM-HAADF) images (Figure 3) are taken by a FEI Titan TEM operated at 200kV. One of the typical features for HAADF images is the Z contrast: the heavier atom has brighter contrast. The HAADF images are acquired with a convergence semi-angle of 19 mrad.

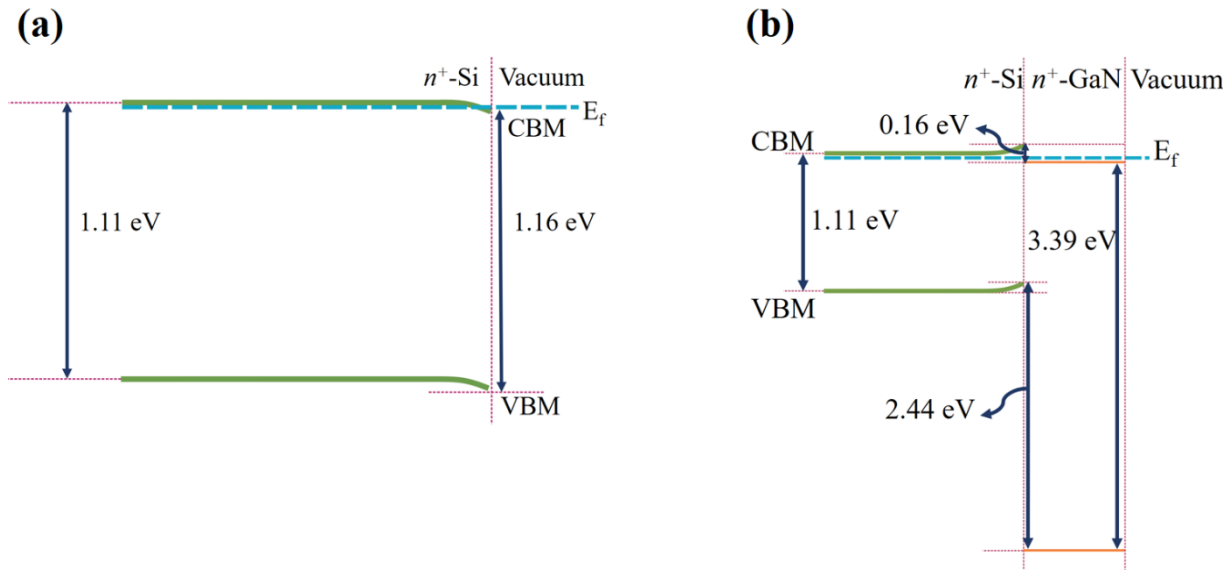

Appendix-2.3. Band diagrams constructed for samples examined in XPS study: (a) bare n^+-Si; (b) 2-3 nm n^+-GaN/n^+-Si. The bulk E_f position in the n^+-Si wafer is placed near the CBM.

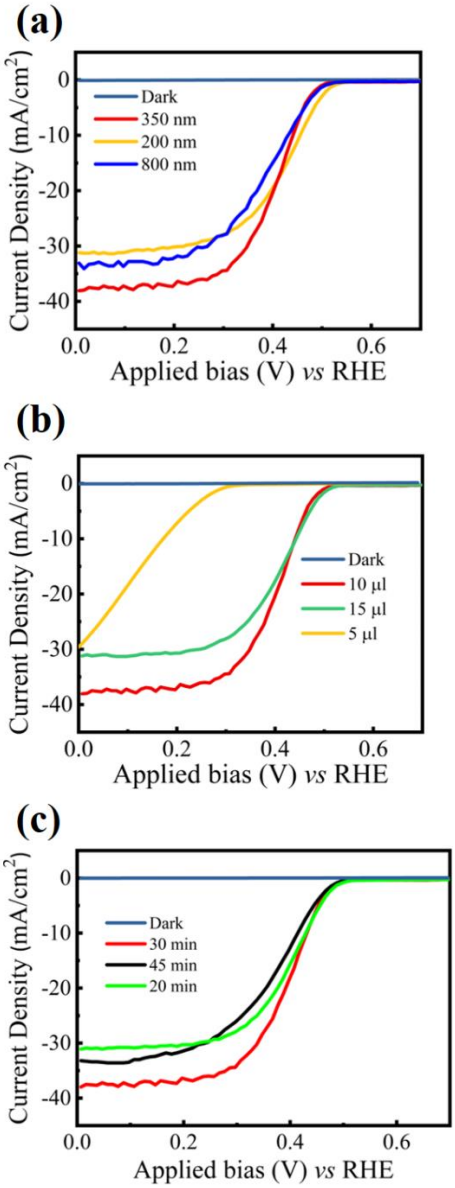

Appendix-2.4. MBE growth and Pt NPs photo-deposition optimization: J-V characteristics of n^+-GaN/n^+-*p* Si photocathode in 0.5M H_2SO_4 under AM1.5G one sun illumination for (a) different nanowire lengths: 200 nm, 350 nm and 800 nm; (b) different Pt loading amounts: 5 µl, 10 µl and 15 µl; (c) different photo-deposition durations: 20 min, 30 min and 45 min. Based on these measurements the best optimized condition for the photocathode consists of 350 nm n^+-GaN nanowires with 10 µl Pt precursor and irradiation for 30 min.

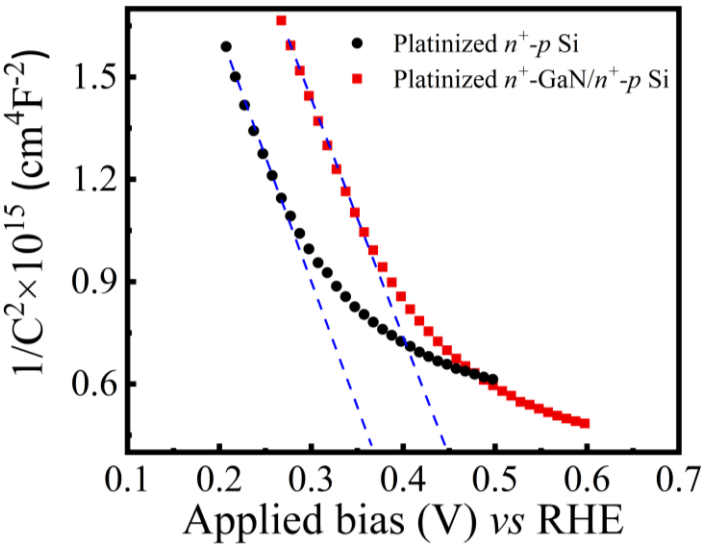

Appendix-2.5. Mott-Schottky curves for platinized n^+-GaN nanowires/n^+-p Si photocathode (red curve) and platinized n^+-p Si photocathode (black curve) in 0.5 M H_2SO_4. The extrapolations for these curves are given by the blue dashed lines. Mott−Schottky measurements were done at 2 kHz by sweeping the applied bias *vs* RHE from 0.2 V to 0.6 V with the above-mentioned AC perturbation amplitude.

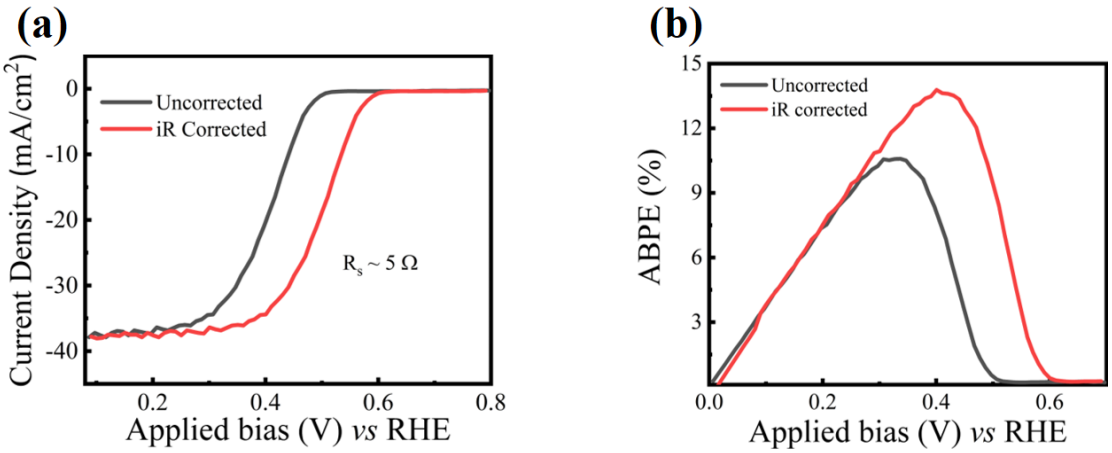

Appendix-2.6. (a) J-V and (b) ABPE curves of platinized n^+-GaN/n^+-p Si photocathode with (red curve) and without (black curve) iR compensation.

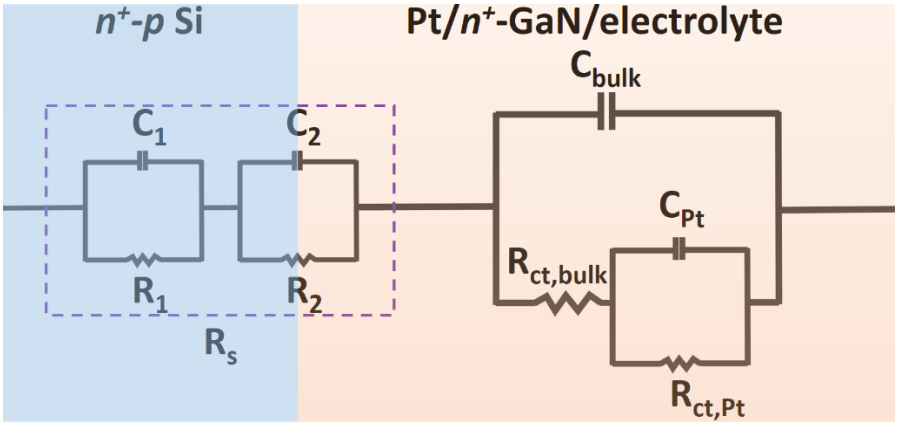

Appendix-2.7. The complete equivalent circuit used to fit the Nyquist plots for platinized n^+-GaN/n^+-*p* Si photocathode measured in 0.5M H_2SO_4 under AM1.5G one sun illumination. C_1 and R_1 represent the band-bending (BB) within n^+-*p* Si; C_2 and R_2 is for BB between n^+-Si and n^+-GaN. The two electrical components R_1 and R_2 combinedly give the series resistance R_s, by assuming the BB between n^+-Si and n^+-GaN and within n^+-*p* Si junction to be negligible. The equivalent circuit elements include a constant phase element (CPE) for the bulk semiconductor (Si or GaN) with the electrolyte, C_{bulk}; a charge transfer resistance from semiconductor conduction band which determines electron transfer kinetics at the electrode/electrolyte interface, $R_{ct,bulk}$; a series resistance, R_S; a charge transfer resistance of electrons from Pt cocatalysts on the surface of the semiconductor (Si or GaN) to solution $R_{ct,Pt}$; a CPE for Pt, C_{Pt}.

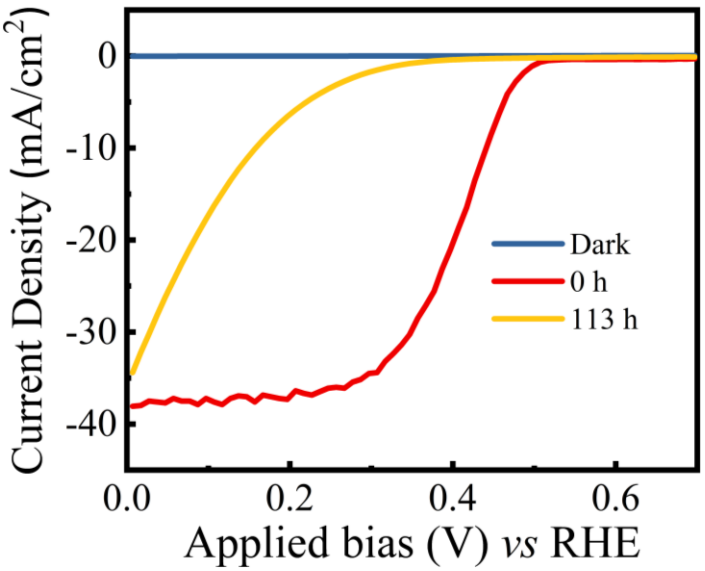

Appendix-2.8. J-V characteristics of platinized n^+-GaN/n^+-*p* Si photocathode in 0.5M H_2SO_4 under AM1.5G one sun illumination for 0 h (red curve) and 113 h (orange curve) and dark condition (blue curve). This indicates that the n^+-GaN nanowires/n^+-*p* Si photocathode after long-term experiment for 113 h showed a significant increase in V_{on} (~0.3 V *vs* RHE) compared to the V_{on} (~0.5 V *vs* RHE) before the experiment. The poor fill-factor could be due to the lack of Pt NPs coverage as observed in previous report [1].

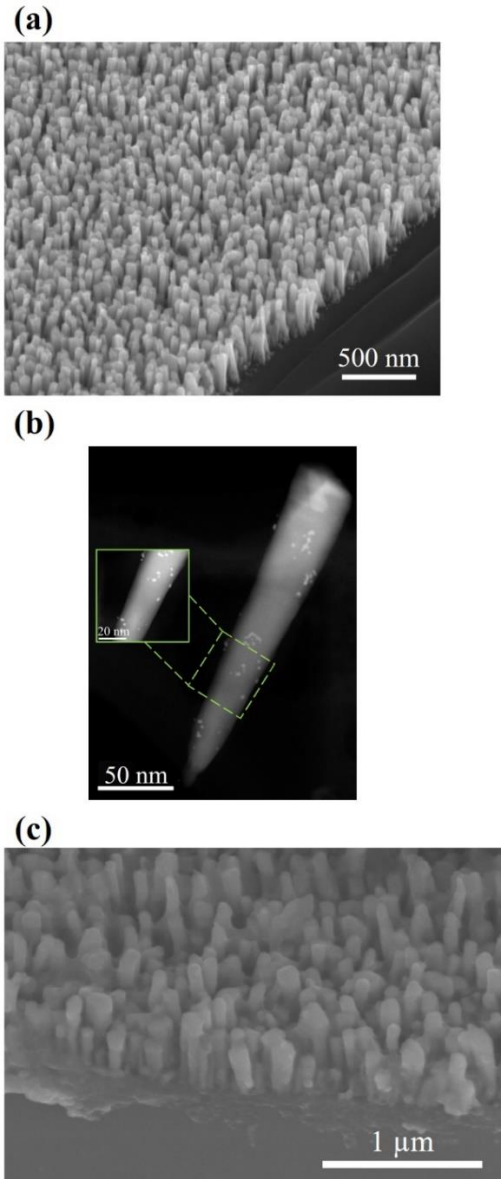

Appendix-2.9. (a) SEM and (b) TEM of Pt decorated n^+-GaN nanowire/n^+-*p* Si photocathode after 50 h stability experiment. Inset in Figure S8(b): HR-STEM image showing fewer Pt NPs non-uniformly distributed on the highlighted (green dashed box) segment of n^+-GaN nanowire. (c) SEM of n^+-GaN nanowire/n^+-*p* Si photocathode after 113 h stability experiment. The loss of Pt NP catalyst over prolonged periods of testing may induce corrosion in the nanowires.

Appendix-2.10: **XPS measurements**

Valence-band measurements on the three samples are represented in Figure 10(a). From these measurements, individual valence-band maxima (VBMs) were extracted for the bare Si and thick GaN samples, which revealed VBM_{Si} = 1.16±0.05 eV and VBM_{GaN} = 3.42±0.05 eV, Interestingly, in both cases these values exceed the materials' band gaps (nominally 1.11 eV and 3.39 eV, respectively), indicating that the surface Fermi levels (E_f) are located very near or within the conduction bands, consistent with strong or even degenerate *n*-type doping.

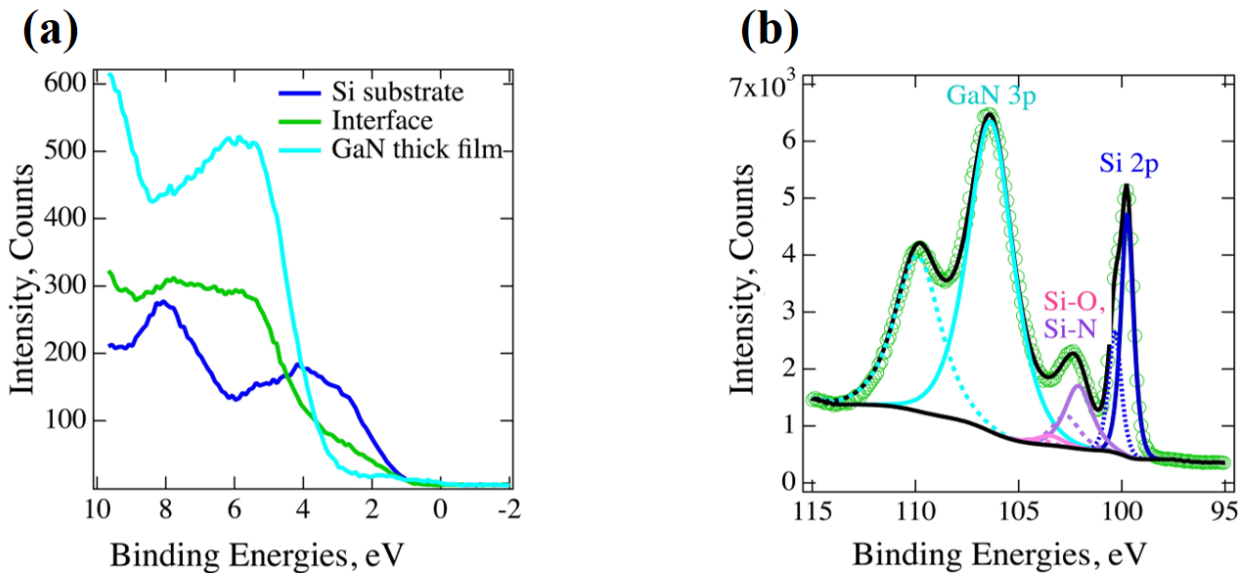

Appendix-2.10. (a) X-ray excited valence-band spectra acquired from the Si wafer substrate (blue curve), thin (~2-3 nm) epilayer (epi) n^+-GaN/n^+-Si for understanding interface (green curve), and thick (~ 30 nm) epi n^+-GaN/n^+-Si (light blue curve). (b) Ga 3p and Si 2p core levels acquired from the thin epi n^+-GaN/n^+-Si samples.

Figure 10(b) shows Ga 3p and Si 2p core-level spectra from the intermediate thickness (~2-3 nm) GaN/Si sample. Band-bending in the Si wafer and GaN layers was assessed by tracking core-level shifts (not shown) between values extracted the interfacial spectrum and those from the bare Si and thick epi-GaN samples. Figure S9(b) also reveals the existence of Si-O and Si-N features associated with the interfacial region. The interfacial valence-band offset calculated from measured VBMs and core-level shifts was 2.44±0.1 eV.

Appendix-2.11: **Impedance study**

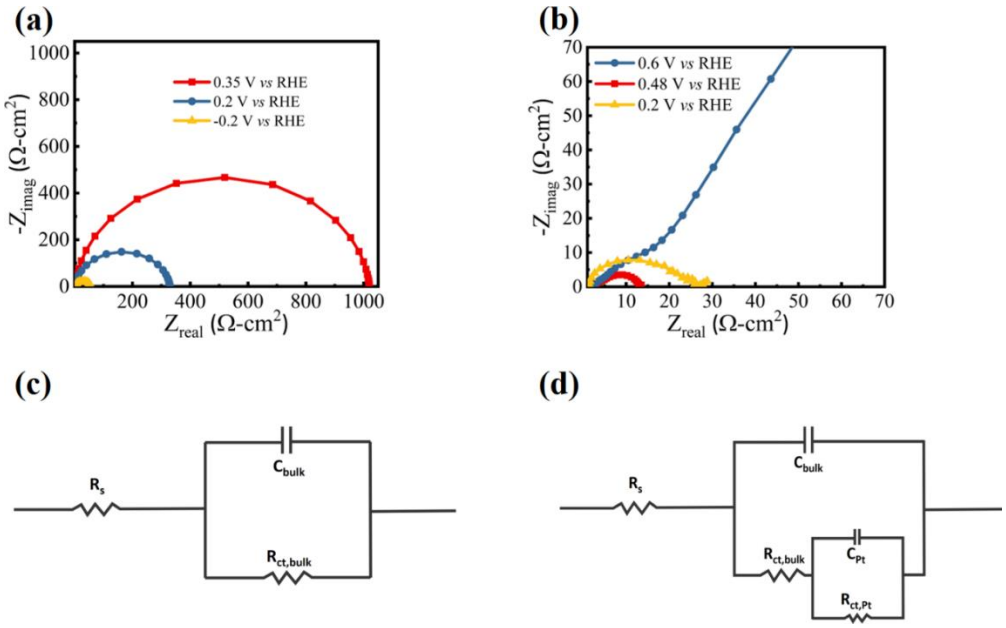

Figure 11. Nyquist plots for (a) platinized n^+-p Si photocathode and (b) platinized n^+-GaN nanowires/n^+-p Si photocathode at different biases in 0.5 M H_2SO_4 under AM 1.5G one sun illumination. Imepdance values represented by dots on each curve correspond to frequencies from 10^6 to 0.1 Hz (in the clockwise direction along the semicircle arc). Equivalent circuit models used for interpretation of Nyquit plots: (c) Nyquist plots that show 1 semicircle and (d) Nyquist plots that show 2 semicircles.

For the Figures 11(a)-(b), we assume that the direct electron transfer through semiconductor (Si or GaN) to electrolyte is negligible and the photoexcited electrons reach the electrolyte via semiconductor (Si or GaN)/Pt NPs interface. As seen from Figure 11(a), at different biases the EIS plots have a single semicircle which can be interpreted using the EC shown in Figure 11(c). On the other hand, for the interpretation of Figure 11(b), which consists of two semicircles, we use the EC shown in Figure 11(d) as previously reported examples of semiconductor/catalyst systems [2, 3]. It is observed from Figure 11(b) that as the photocurrent density approaches the saturation level, there is an additional resistance due to the accumulation of H_2 gas at the surface of the electrode which fluctuates the photocurrent as seen in Figure 4.4(a) and thereby slightly increases the $R_{ct,bulk}$ at 0.2 V *vs* RHE (yellow color curve in Figure 11(b)).

Appendix-2.12: Performance comparison between the presented n^+-GaN nanowire/n^+-p Si photocathode and previously reported Si-based photocathodes under AM 1.5G one sun illumination in the literature.

Materials	**Electrolyte**	**V_{on} (V vs RHE)**	**J_{sc} (mA/cm^2)**	**ABPE (%)**	**Stability**	**Ref.**
NiP_2/Ti/pn^+-Si	0.5M H_2SO_4	0.41	12	NA	6 h (at 5 mA/cm^2)	4
Pt-decorated (1–2.5 nm diameter) TiO_2 nanorods/p-Si	0.5M H_2SO_4	0.44	40	NA	40 h (at 0 V *vs* RHE)	5
p-Si/$NiCoSe_x$ core/shell nanopillar array	0.5M H_2SO_4	0.25	37.5	NA	2 h (at 0.1 V *vs* RHE)	6
Pt/Ti/$SrTiO_3$/p-Si	0.5M H_2SO_4	0.4	15	4.9	35 h (at 0.2 V *vs* RHE)	7
MoS_2/n^+-p Si	0.5M H_2SO_4	0.3	17	<3%	100 h (at 0 V *vs* RHE)	8

Ni-Mo-coated n^+-*p* Si microwire	KHP adjusted using KOH	0.46	9.1	1.9	<2h (at 0 V *vs* RHE)	9
nano-MoS_2 layer on Al_2O_3/n^+-*p* Si	1M $HClO_4$	0.4	35.6	NA	120 h (at 0 V *vs* RHE)	10
$TiO_2/Pt_2/n^+$-*p* Si	1M $HClO_4$	0.55	35	10.8	168 h (at 10 mA/cm^2)	11
Pt (2nm)/SiHJ	1M H_2SO_4	0.64	34	13.26	10 h (at 0 V *vs* RHE)	12
Pt-Al_2O_3-Nanoporous-*p* Si	0.5M H_2SO_4	0	NA	NA	12 h (at -0.9 V *vs* RHE)	13
$MoSe_2/n^+$-*p* Si	1M $HClO_4$	0.4	29.3	3.8	120 h (0 V *vs* RHE)	14
Pt/n^+-*p* Si	K_2SO_4 and H_2SO_4	0.41	28	8.9	2.5 h (at 0 V *vs* RHE)	15
Al_2O_3/n^+-*p* Si	K_2SO_4 and H_2SO_4	0.5	30	7	120 h (at -0.8 V *vs* RHE)	16
Ag@Si/MoS_2	0.5M H_2SO_4	0.1	2	NA	12 h (at 0 V *vs* RHE)	17
Co-S/Ti/a-Si	1M KOH	1.78	7	6	10 h (at 0 V *vs* RHE)	18
Ni/Ti/*p*-Si	1M KOH	0.3	17	NA	12 h (at 10 mA/cm^2)	19
NiFe/Ti/*p*-Si	1M KOH	0.3	7	NA	24 h (at -0.186 V vs RHE)	20
Pt/TiO_2/Si nanowire	0.5M H_2SO_4	0	0	NA	2h (at -0.78 V *vs* RHE)	21
$MoS_2/TiO_2/n^+$-*p* Si nanowire	0.5M H_2SO_4	0.2	15	NA	1.25 h (at -0.33 V *vs* RHE)	22

3D $MoS_2/TiO_2/p$-Si	0.5 M H_2SO_4	0.3	30	1.8	108 h (at -0.05 V *vs* RHE)	23
TiO_2/Pt NPs/n^+np^+ Si	1M $HClO_4$	0.5	35	11.5	168 h (at 0.4 V *vs* RHE)	24
Pt NPs /n^+-GaN nanowire/n^+-p Si	0.5M H_2SO_4	0.5	38	10.5	113 h (at 0 V *vs* RHE)	This work

Appendix-2.13: Performance comparison between the presented n^+-GaN nanowire/n^+-p Si photocathode and state-of-the-art single junction photocathodes having ABPE>10% under AM 1.5G one sun illumination.

Materials	**Electrolyte**	**V_{on} (V *vs* RHE)**	**J_{sc} (mA/cm^2)**	**ABPE (%)**	**Stability**	**pH**	**Ref**
TiO_2/Pt NPs/n^+np^+ Si	1M $HClO_4$	0.5	35	11.5	168 h (at 0.4 V *vs* RHE)	0	24
Pt NPs/TiO_2/n^+-p Si	1M $HClO_4$	0.55	35	10.8	168 h (at 10 mA/cm^2)	0	11
Pt (2nm)/SiHJ	1M H_2SO_4	0.64	34	13.26	10 h (at 0 V *vs* RHE)	0.4	12
Pt/TiO_2/F:SnO_2/Ti/ n^+-p Si	KOH	0.5	35	10.9	24 h (at 0.3 V *vs* RHE)	14	25

Ru/TiO_2/*p*-InP	1M $HClO_4$	0.73	34	14	4 h (at 0.23 V *vs* NHE)	0	26
Pt/TiO_2/*p*-InP	1M $HClO_4$	0.63	30	11.6	NA	0	27
Pt NPs /n^+-GaN nanowire/n^+-*p* Si	0.5M H_2SO_4	0.5	38	10.5	113 h (at 0 V *vs* RHE)	0	This work

References

1. Peng, K.-Q.; Wang, X.; Wu, X.-L.; Lee, S.-T. *Nano Lett.* **2009,** 9, (11), 3704-3709.

2. Klahr, B.; Gimenez, S.; Fabregat-Santiago, F.; Bisquert, J.; Hamann, T. W. *J. Am. Chem. Soc.* **2012,** 134, (40), 16693-700.

3. Ding, Q.; Meng, F.; English, C. R.; Caban-Acevedo, M.; Shearer, M. J.; Liang, D.; Daniel, A. S.; Hamers, R. J.; Jin, S. *J. Am. Chem. Soc.* **2014,** 136, (24), 8504-7.

4. Chen, F.; Zhu, Q.; Wang, Y.; Cui, W.; Su, X.; Li, Y. *ACS Appl. Mater. Interfaces* **2016,** 8, (45), 31025-31031.

5. Andoshe, D. M.; Choi, S.; Shim, Y.-S.; Lee, S. H.; Kim, Y.; Moon, C. W.; Kim, D. H.; Lee, S. Y.; Kim, T.; Park, H. K.; Lee, M. G.; Jeon, J.-M.; Nam, K. T.; Kim, M.; Kim, J. K.; Oh, J.; Jang, H. W. *J. Mater. Chem. A* **2016,** 4, (24), 9477-9485.

6. Zhang, H.; Ding, Q.; He, D.; Liu, H.; Liu, W.; Li, Z.; Yang, B.; Zhang, X.; Lei, L.; Jin, S. *Energ. Environ. Sci.* **2016,** 9, (10), 3113-3119.

7. Ji, L.; McDaniel, M. D.; Wang, S. J.; Posadas, A. B.; Li, X. H.; Huang, H. Y.; Lee, J. C.; Demkov, A. A.; Bard, A. J.; Ekerdt, J. G.; Yu, E. T. *Nat. Nanotechnol.* **2015,** 10, (1), 84-90.

8. Benck, J. D.; Lee, S. C.; Fong, K. D.; Kibsgaard, J.; Sinclair, R.; Jaramillo, T. F. *Adv. Energ. Mater.* **2014,** 4, (18), 1400739.

9. Warren, E. L.; McKone, J. R.; Atwater, H. A.; Gray, H. B.; Lewis, N. S. *Energ. Environ. Sci.* **2012,** 5, (11), 9653-9661.

10. Fan, R.; Mao, J.; Yin, Z.; Jie, J.; Dong, W.; Fang, L.; Zheng, F.; Shen, M. *ACS Appl. Mater. Interfaces* **2017,** 9, (7), 6123-6129.

11. Fan, R.; Dong, W.; Fang, L.; Zheng, F.; Shen, M. *J. Mater. Chem. A* **2017**, 5, 18744-18751.

12. Zhu, H.; Wang, Y.; Xiao, J.; Liu, M.; Xiong, S.; Wong, Z. J.; Ye, Z.; Ye, Y.; Yin, X.; Zhang, X. *Nat. Nanotechnol.* **2015,** 10, (2), 151-5.

13. Choi, M. J.; Jung, J. Y.; Park, M. J.; Song, J. W.; Lee, J. H.; Bang, J. H. *J. Mater. Chem. A* **2014,** 2, (9), 2928-2933.

14. Huang, G.; Mao, J.; Fan, R.; Yin, Z.; Wu, X.; Jie, J.; Kang, Z.; Shen, M. *Appl. Phys. Lett.* **2018,** 112, (1), 013902.

15. Fan, R.; Tang, C.; Xin, Y.; Su, X.; Wang, X.; Shen, M. *Appl. Phys. Lett.* **2016,** 109, (23), 233901.

16. Fan, R.; Dong, W.; Fang, L.; Zheng, F.; Su, X.; Zou, S.; Huang, J.; Wang, X.; Shen, M. *Appl. Phys. Lett.* **2015,** 106, (1), 013902.

17. Zhou, Q.; Su, S.; Hu, D.; Lin, L.; Yan, Z.; Gao, X.; Zhang, Z.; Liu, J.-M. *Nanotechnol.* **2018,** 29, (10), 105402.

18. Zhang, Q.; Li, T.; Luo, J.; Liu, B.; Liang, J.; Wang, N.; Kong, X.; Li, B.; Wei, C.; Zhao, Y.; Zhang, X. *J. Mater. Chem. A* **2018,** 6, (3), 811-816.

19. Feng, J.; Gong, M.; Kenney, M. J.; Wu, J. Z.; Zhang, B.; Li, Y.; Dai, H. *Nano Res.* **2015,** 8, (5), 1577-1583.

20. Zhao, J.; Cai, L.; Li, H.; Shi, X.; Zheng, X. *ACS Energ. Lett.* **2017,** 2, (9), 1939-1946.

21. Huang, S.; Zhang, H.; Wu, Z.; Kong, D.; Lin, D.; Fan, Y.; Yang, X.; Zhong, Z.; Huang, S.; Jiang, Z.; Cheng, C. *ACS Appl. Mater. Interfaces* **2014,** 6, (15), 12111-8.

22. Zhang, L.; Liu, C.; Wong, A. B.; Resasco, J.; Yang, P. *Nano Res.* **2014,** 8, (1), 281-287.

23. Andoshe, D. M.; Jin, G.; Lee, C.-S.; Kim, C.; Kwon, K. C.; Choi, S.; Sohn, W.; Moon, C. W.; Lee, S. H.; Suh, J. M.; Kang, S.; Park, J.; Heo, H.; Kim, J. K.; Han, S.; Jo, M.-H.; Jang, H. W. *Adv. Sus. Sys.* **2018,** 2, (3), 1700142.

24. Yin, Z.; Fan, R.; Huang, G.; Shen, M. *Chem. Commun. (Camb)* **2018,** 54, (5), 543-546.

25. Kast, M. G.; Enman, L. J.; Gurnon, N. J.; Nadarajah, A.; Boettcher, S. W. *ACS Appl. Mater. Interfaces* **2014,** 6, (24), 22830-7.

26. Lee, M. H.; Takei, K.; Zhang, J.; Kapadia, R.; Zheng, M.; Chen, Y. Z.; Nah, J.; Matthews, T. S.; Chueh, Y. L.; Ager, J. W.; Javey, A. *Angew. Chem. Int. Ed. Engl.* **2012,** 51, (43), 10760-4.

27. Hettick, M.; Zheng, M.; Lin, Y.; Sutter-Fella, C. M.; Ager, J. W.; Javey, A. *J. Phys. Chem. Lett.* **2015,** 6, (12), 2177-82.

Appendix-3

Experimental section

Fabrication of p^+-n Si: Double side polished *n*-type Si(100) wafers (WRS Materials, thickness: 254 – 304 µm; resistivity: 1 - 10 Ω·cm) were spin-coated with liquid boron dopant precursor (Futurrex, Inc.) on one side to form the p^+-Si emitter and liquid phosphorus dopant precursor (Futurrex, Inc.) on the other side to form the n^+-Si back field layer. Subsequently, the thermal diffusion process was conducted at 950 ^oC for 240 min under argon gas flow in a furnace. The residue of the precursor was removed in buffered oxide etch solution. To measure the efficiency of the solar cells, metal contacts were made on *n*-side and *p*-side by depositing Ti/Au and Ni/Au respectively using e-beam evaporator. Shown in Appendix-3.1, J_{sc} of the device is ~31 mA/cm^2, V_{oc} is ~0.52 V, and the energy conversion efficiency is ~11%.

PEC measurements: The PEC reaction was conducted in 1 mol/L HBr solution using a potentiostat (Gamry Instruments, Interface 1000) with $MoSe_2$/p^+-*n* Si, silver chloride electrode (Ag/AgCl), and Pt wire as the working, reference, and counter electrode, respectively. The working electrode was prepared by cleaving the $MoSe_2$/p^+-*n* Si wafer into area sizes of 0.2 – 1 cm^2. A Ga−In eutectic (Sigma Aldrich) alloy was deposited on the backside of the Si wafer to form ohmic contact, which was subsequently connected to a Cu wire using silver paste. The entire sample except the front surface was covered by insulating epoxy and placed on a glass slide. A solar simulator (Newport Oriel) with an AM1.5 G filter was used as the light source, and the light intensity was calibrated to be 100 mW/cm^2 for all subsequent experiments. The conversion of the Ag/AgCl reference potential to RHE is calculated using the Equation (6.3),

$$E_{(RHE)} = E_{Ag/AgCl} + E^o_{Ag/AgCl} + 0.059 \times pH \qquad \text{eq. (6.3)}$$

where $E^o_{Ag/AgCl}$ is 0.197 V, and pH of the electrolyte is nearly zero.

MBE growth of $MoSe_2$: During the growth process, molybdenum (Mo) was thermally evaporated using an e-beam evaporator (Telemark Inc.) retrofitted in the MBE reaction chamber. We have developed a two-step MBE growth process for $MoSe_2$ thin film. In the first step, the substrate was heated to temperatures in the range of 200-450 ^oC, and Mo molecular beam was introduced under Se-rich conditions (Se beam equivalent pressure (BEP) of 3.5×10^{-7} torr) for 18-180 minutes, with a deposition rate ~0.01 Å/s for $MoSe_2$. The resulting $MoSe_2$ thicknesses vary between 1nm and 10 nm. In the second step an *in situ* thermal annealing was performed under Se flux for 10 mins in the temperature range of 200-650 ^oC (see Appendix-3.2).

Appendix-3.1: **Fabrication of p^+-n Si Wafer**

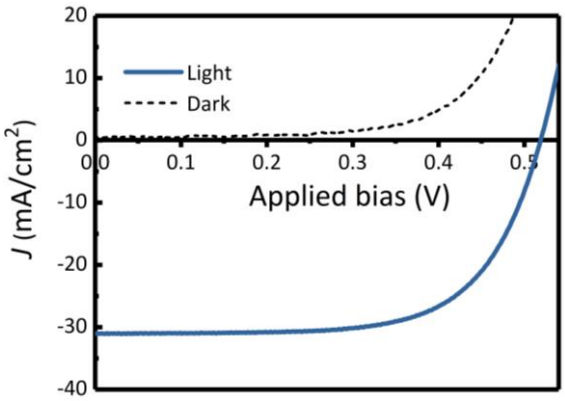

Figure 1. *J-V* characteristics of p^+-n Si solar cell under AM1.5G one sun illumination 100 mW/cm^2 (dark blue curve) and dark condition (black dashed curve). The current density shown in the figure is limited by the reflection of incident light [1, 2].

Appendix-3.2: **Effect of $MoSe_2$ Growth Conditions on the PEC Performance**

To study the effect of growth temperature (T_G) and annealing temperature (T_A) in the two step MBE growth (see Chapter-6), samples with different growth and annealing temperature

combinations were grown by keeping the same thickness of 3 nm for the $MoSe_2$ film. Shown in Figure 2, it can be observed that the best PEC performing sample, in terms of on-set voltage and photocurrent density, is with growth temperature of 250 ^{0}C and annealing temperature of 250 ^{0}C. The sample with growth temperature of 400 ^{0}C showed lower photocurrent density and the sample with growth temperature 200 ^{0}C produced a lower on-set potential compared to the sample with growth temperature 250 ^{0}C.

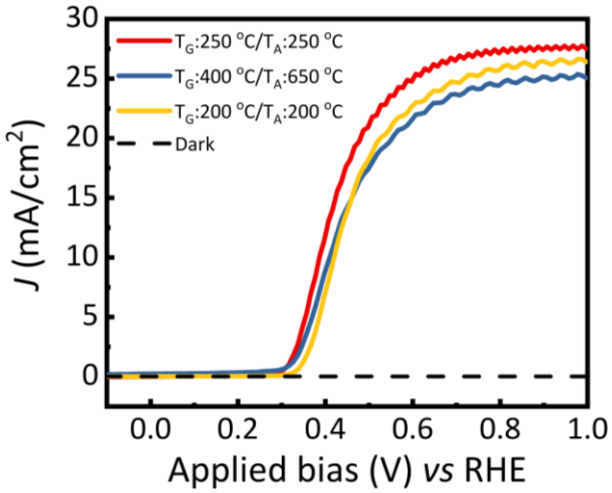

Figure 2. *J-V* characteristics of $MoSe_2$ thin films (~3 nm thick) on p^+-*n* Si wafer with different growth combinations of growth temperature (T_G) and annealing temperature (T_A) under AM1.5G one sun illumination 100 mW/cm^2 and dark condition (black dashed curve) in 1M HBr. T_G: 250 ^{0}C/ T_A: 250 ^{0}C (red curve), T_G: 400 ^{0}C/ T_A: 650 ^{0}C (blue curve), and T_G: 200 ^{0}C/ T_A: 200 ^{0}C (yellow curve).

Appendix-3.3: **Structural Characterization of $MoSe_2$**

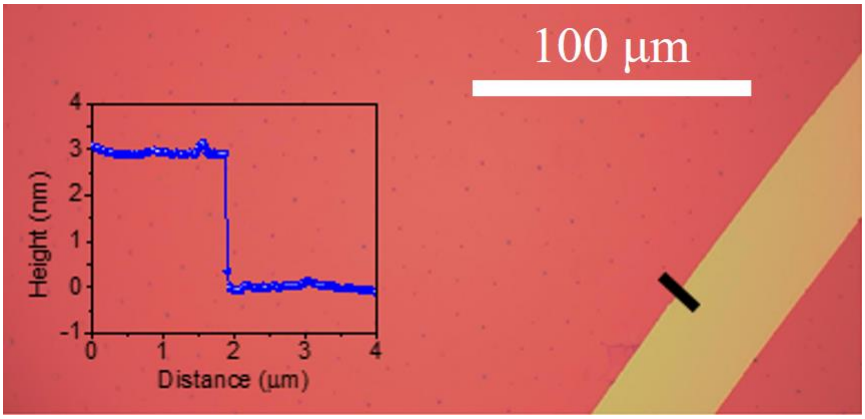

Figure 3. Optical microscopy image of $MoSe_2$ with a thickness of ~3 nm. The atomic force microscopy measurement performed near the black bar region is shown in the inset.

Appendix-3.4: **PEC Performance of p^+-n Si Photoanode**

J-V curves (see Figure 4) show that the photocurrent density for p^+-n Si photoanode (light blue curve) without $MoSe_2$ protection layer is almost negligible, compared to $MoSe_2$/p^+-n Si photoanode (red curve). This can be attributed to the fact that unprotected Si surface is highly prone to oxidation [3] in acidic solution, which results in extremely low current density and poor stability. As shown by the red curve in Figure S4, the sample with $MoSe_2$ protection layer exhibited a high saturated photocurrent density of ~30 mA/cm^2.

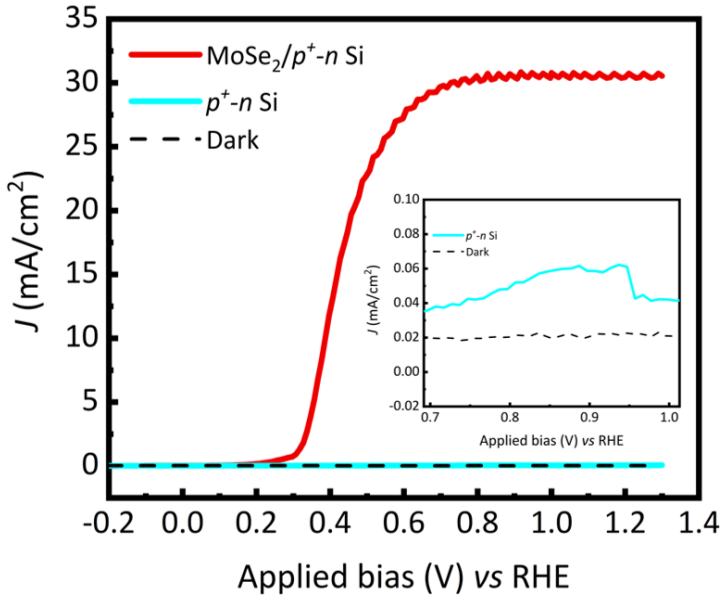

Figure 4. LSV curves showing a comparison between with (red curve) and without (light blue curve) $MoSe_2$ thin film on p^+-*n* Si photoanode in 1M HBr solution under the illumination of AM1.5G one sun (100 mW/cm^2) and dark condition (black dashed curve). Inset shows the comparison between p^+-*n* Si solar cell under AM1.5G one sun illumination (light blue curve) and dark condition (dotted black curve) in the potential range of 0.7-1 V *vs* RHE.

Appendix-3.5: **PEC Performance of $MoSe_2$/p^+-*n* Si Photoanode**

The saturated photocurrent density of ~30 mA/cm^2 is close to the maximum theoretical current density for c-Si, considering surface reflection loss of the incident light. In fact, the measured photocurrent density is nearly identical to the J_{sc} of the Si solar cell shown in Figure 1, which suggests that photo-generated holes in Si can effectively tunnel through the thin $MoSe_2$ protection layer and participate in oxidation reaction. We have further tested the PEC performance by varying the light intensity. Shown in Figure 5 are the measurements performed under different light illuminations: 0.3 Sun, 0.5 Sun, 1 Sun and 2 Suns, with the saturated photocurrent being 11

mA/cm^2, 15 mA/cm^2, 30 mA/cm^2 and 60 mA/cm^2, respectively. The photocurrent density scales linearly with the light intensity. The light-limited photocurrent density values also agree well with previous reports [4-8].

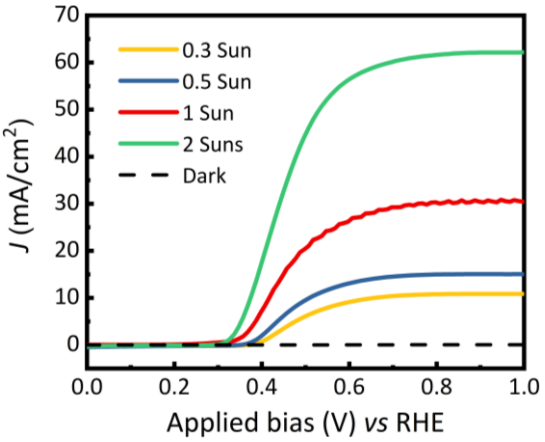

Figure 5. *J-V* characteristics of $MoSe_2/p^+$-*n* Si photoanode under different illumination conditions in 1 M HBr under various illumination intensities: 0.3 Sun (yellow curve), 0.5 Sun (blue curve), 1 Sun (red curve) and 2 Suns (green curve) and dark condition (black dashed curve).

Appendix-3.6: **Mott-Schottky Characteristics of $MoSe_2/p^+$-*n* Si Photoanode**

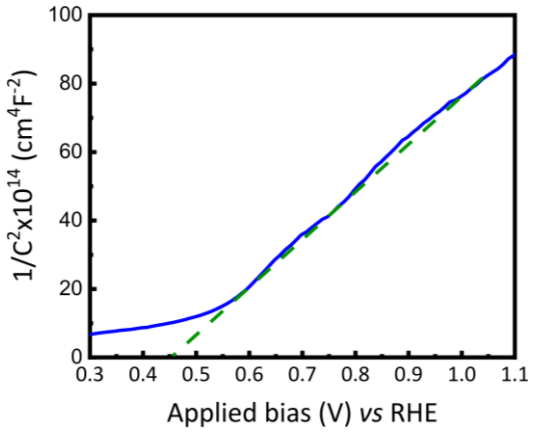

Figure 6. Mott-Schottky characteristics of $MoSe_2/p^+$-*n* Si photoanode measured at 1 KHz under dark condition (blue curve) in 1M HBr and the extrapolated linear fit (green dashed line) intercepts the x-axis at 0.46 V vs RHE. From the Figure S6, the positive slope indicates *n*-type behaviour which is characteristic of photoanode. The V_{fb} from this analysis is ~0.46 V *vs* RHE which is close to the value reported in the main text using OCP analysis.

Appendix-3.7: **Stability of $MoSe_2/p^+$-*n* Si photoanode**

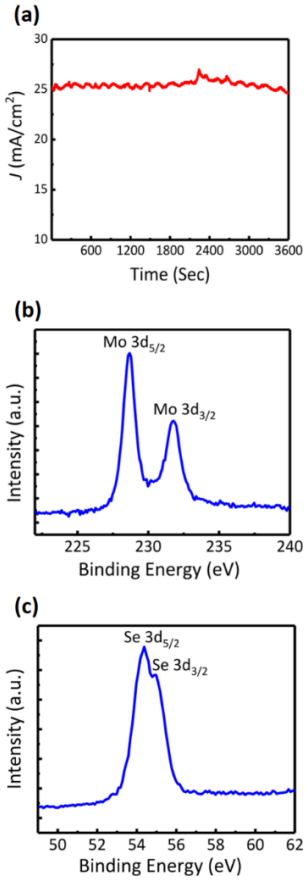

Figure 7. (a) Chronoamperometry study for $MoSe_2/p^+$-*n* Si photoanode shows stable photocurrent density of ~ 26 mA/cm^2 at 0.6 V *vs* RHE for 1 hr. XPS measurements after 1 hr chronoamperometry stability test for (b) Mo and (c) Se, showing Mo:Se ratio of ~1:2.

Appendix-3.8: **On the Hole Injection Efficiency**

The light-limited current density for $MoSe_2/p^+$-*n* Si solar cell photoanode is 30 mA/cm^2. Based on this observation, we have further calculated the hole injection efficiency for photoanodes with different thicknesses of $MoSe_2$. As seen from Figure S8, at relatively low bias ~0.5-0.6 V *vs* RHE the hole injection efficiency is ≥ 80% for $MoSe_2$ thicknesses of 3 nm and 5 nm. The shaded region in Figure 8 indicates hole injection efficiency >80%. The achievement of very high hole injection efficiency at a relatively low biasing voltage suggests the efficient tunneling of photogenerated holes from Si to solution through the $MoSe_2$ protection layer.

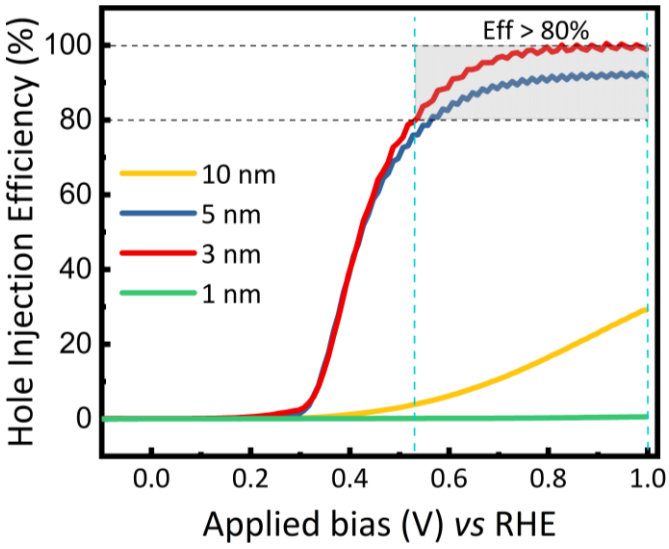

Figure 8. Hole injection efficiency for $MoSe_2/p^+$-*n* Si photoanodes with different $MoSe_2$ thicknesses under AM 1.5G one sun illumination in 1 M HBr. The shaded region indicates hole injection efficiency between >80%.

References

1. L. A. Osminkina, K. A. Gonchar, V. S. Marshov, K. V. Bunkov, D. V. Petrov, L. A. Golovan, F. Talkenberg, V. A. Sivakov, V. Y. Timoshenko, *Nanoscale Research Letters* **2012,** 7, (1), 524.

2. R. Santbergen, *Optical absorption factor of solar cells for PVT Systems*. Eindhoven University Press: 2008.

3. A. Q. Contractor, J. O. M. Bockris, *Electrochim. Acta* **1984,** 29, (10), 1427-1434.

4. S. Hu, M. R. Shaner, J. A. Beardslee, M. Lichterman, B. S. Brunschwig, N. S. Lewis, *Science* **2014,** 344, (6187), 1005-1009.

5. X. Yu, P. Yang, S. Chen, M. Zhang, G. Shi, *Adv. Energ. Mater.* **2017,** 7, (6), 1601805.

6. J. Yang, K. Walczak, E. Anzenberg, F. M. Toma, G. Yuan, J. Beeman, A. Schwartzberg, Y. Lin, M. Hettick, A. Javey, J. W. Ager, J. Yano, H. Frei, I. D. Sharp, *J. Am. Chem. Soc.* **2014,** 136, (17), 6191-4.

7. K. Sun, M. T. McDowell, A. C. Nielander, S. Hu, M. R. Shaner, F. Yang, B. S. Brunschwig, N. S. Lewis, *J. Phys. Chem. Lett.* **2015,** 6, (4), 592-8.

8. X. H. Zhou, R. Liu, K. Sun, D. Friedrich, M. T. McDowell, F. Yang, S. T. Omelchenko, F. H. Saadi, A. C. Nielander, S. Yalamanchili, K. M. Papadantonakis, B. S. Brunschwig, N. S. Lewis, *Energ. Environ. Sci.* **2015,** 8, (9), 2644-2649.

JOHN WILEY AND SONS LICENSE TERMS AND CONDITIONS

Apr 04, 2019

This Agreement between McGill University -- Srinivas Vanka ("You") and John Wiley and Sons ("John Wiley and Sons") consists of your license details and the terms and conditions provided by John Wiley and Sons and Copyright Clearance Center.

License Number	4561720804397
License date	Apr 04, 2019
Licensed Content Publisher	John Wiley and Sons
Licensed Content Publication	Solar RRL
Licensed Content Title	A High Efficiency Si Photoanode Protected by Few-Layer MoSe2
Licensed Content Author	Srinivas Vanka, Yongjie Wang, Pegah Ghamari, et al
Licensed Content Date	Jun 6, 2018
Licensed Content Volume	2
Licensed Content Issue	8
Licensed Content Pages	6
Type of use	Dissertation/Thesis
Requestor type	Author of this Wiley article
Format	Electronic
Portion	Full article
Will you be translating?	No
Title of your thesis / dissertation	Photoelectrochemical Water Splitting on III-Nitride and Transition Metal Di-Chalcogenides Nanostructures
Expected completion date	Jun 2019
Expected size (number of pages)	300
Requestor Location	McGill University 3480 University Street McConnell Room No 633 Montreal, QC H3A0E9 Canada Attn: McGill University
Publisher Tax ID	EU826007151
Total	0.00 USD
Terms and Conditions	

TERMS AND CONDITIONS

This copyrighted material is owned by or exclusively licensed to John Wiley & Sons, Inc. or one of its group companies (each a"Wiley Company") or handled on behalf of a society with which a Wiley Company has exclusive publishing rights in relation to a particular work (collectively "WILEY"). By clicking "accept" in connection with completing this licensing transaction, you agree that the following terms and conditions apply to this transaction (along with the billing and payment terms and conditions established by the Copyright Clearance Center Inc., ("CCC's Billing and Payment terms and conditions"), at the time that

Re: Permission for using STEM results in my thesis

BG Botton, Gianluigi <gbotton@mcmaster.ca>
To Srinivas Vanka

Reply | Reply All | Forward

Tue 2019-03-26 3:3

Hi Srinivas, yes, I give you my approval to use the results and the paper
Gianluigi

Sent from my iPhone

On Mar 26, 2019, at 2:54 PM, "Srinivas Vanka" <srinivas.vanka@mail.mcgill.ca> wrote:

> Hello Prof. Botton,
>
> How are you? As per McGill policy, I need your consent to submit my thesis which will contain STEM results from the manuscript as listed below:
>
> S. Vanka, E.Arca et. al., Nano Lett. 2018, 18, 10, 6530-6537
>
> Could you please reply to this email and grant me permission for using this manuscript in my thesis?
>
> Thanks,
> Srinivas

Re: Permission for using STEM results in my thesis

RH Robert Hovden <robert.hovden@gmail.com>
To Srinivas Vanka

Reply | Reply All | Forwa

Tue 2019-0

You replied to this message on 2019-03-26 2:52 PM.

Srinivas,

You may use the results in that manuscript as well as any content my lab has produced in collaboration with you or Prof Mi's group.

Robert

On Tue, Mar 26, 2019 at 2:48 PM Srinivas Vanka <srinivas.vanka@mail.mcgill.ca> wrote:

> Hello Prof. Hovden,
>
> How are you? As per McGill policy, I need your consent to submit my thesis which will contain STEM results from the manuscript as listed below:
>
> S. Chu, S. Vanka, et. al., ACS Energy Lett. 2018, 3, 2, 307-314
>
> Could you please reply to this email and grant me permission for using this manuscript in my thesis?
>
> Thanks,
> Srinivas

RE: Permission for using XPS results in my thesis

HN Haegel, Nancy <Nancy.Haegel@nrel.gov>
To Arca, Elisabetta; Srinivas Vanka
Cc Teeter, Glenn

Reply | Reply All | Forward
Tue 2019-03-26 3:0

All,

As best I can tell, this is a published manuscript, so there is not problem using data/figures from the paper in your thesis. Just reference the paper.
If you want to use additional unpublished data, that should also be fine unless Elisabetta or Glenn identify any sensitivities. If there are none, then just use standard referencing/acknowledgement for unpublished data.

Good luck with the completion of your PhD.

Nancy

From: Arca, Elisabetta <Elisabetta.Arca@nrel.gov>
Sent: Tuesday, March 26, 2019 12:45 PM
To: Srinivas Vanka <srinivas.vanka@mail.mcgill.ca>
Cc: Teeter, Glenn <Glenn.Teeter@nrel.gov>; Haegel, Nancy <Nancy.Haegel@nrel.gov>
Subject: Re: Permission for using XPS results in my thesis

Hi Srinivas

I have absolutely no problem and of course, as far as I am concern, you can use this paper in your PhD thesis.
Nancy, Glenn, is there any restriction at a laboratory level? I am not aware of any, but I am just cross-checking for correctness.

Srinivas, best of luck with your PhD, I am sure you'll do a great job!
Regards

Elisabetta

答复: Permission for using Paper in my thesis

SC Sheng Chu
To Srinivas Vanka

Reply | Repl

You replied to this message on 2019-03-18 3:09 PM.

Sure, Srinivas. Congratulations!

Thanks,
Sheng

发件人: Srinivas Vanka
发送时间: 2019 年 3 月 18 日 12:25
收件人: Sheng Chu
主题: Permission for using Paper in my thesis

Hi Sheng,

Hope you are doing well. I will soon be submitting my thesis and it will contain the following manuscript as listed below:
S. Chu, S. Vanka, et. al., ACS Energy Lett. 2018, 3, 2, 307-314

Could you please reply to this email and grant me permission for using this manuscript in my thesis?

Thanks,
Srinivas